INFORMATION TO USERS

This manuscript has been reproduced from the microfilm master. UMI films the text directly from the original or copy submitted. Thus, some thesis and dissertation copies are in typewriter face, while others may be from any type of computer printer.

The quality of this reproduction is dependent upon the quality of the copy submitted. Broken or indistinct print, colored or poor quality illustrations and photographs, print bleedthrough, substandard margins, and improper alignment can adversely affect reproduction.

In the unlikely event that the author did not send UMI a complete manuscript and there are missing pages, these will be noted. Also, if unauthorized copyright material had to be removed, a note will indicate the deletion.

Oversize materials (e.g., maps, drawings, charts) are reproduced by sectioning the original, beginning at the upper left-hand corner and continuing from left to right in equal sections with small overlaps.

Photographs included in the original manuscript have been reproduced xerographically in this copy. Higher quality 6" x 9" black and white photographic prints are available for any photographs or illustrations appearing in this copy for an additional charge. Contact UMI directly to order.

ProQuest Information and Learning
300 North Zeeb Road, Ann Arbor, MI 48106-1346 USA
800-521-0600

UMI®

DISSERTATION

SYSTEMS DESIGN OF A HIGH-RESOLUTION, LARGE-DATA SET, ULTRASONIC TIRE INSPECTION MACHINE

Submitted by
Justin Gaylord Downs III
Department of Mechanical Engineering

In partial fulfillment of the requirements
for the degree of Doctor of Philosophy
Colorado State University
Fort Collins, Colorado
Fall 2001

UMI Number: 3038629

UMI Microform 3038629

ProQuest Information and Learning Company
300 North Zeeb Road
P.O. Box 1346
Ann Arbor, MI 48106-1346

COLORADO STATE UNIVERSITY

February 6, 2001

WE HEREBY RECOMMEND THAT THE DISSERTATION PREPARED UNDER OUR SUPERVISION BY JUSTIN GAYLORD DOWNS III ENTITLED SYSTEMS DESIGN OF A HIGH-RESOLUTION, LARGE DATA-SET, ULTRASONIC TIRE INSPECTION MACHINE BE ACCEPTED AS FULFILLING IN PART REQUIREMENTS FOR THE DEGREE OF DOCTOR OF PHILOSOPHY.

Committee on Graduate Work

C. Byron Winn

Hiroshi Sakurai

Adviser

Department Head

ABSTRACT OF DISSERTATION

SYSTEMS DESIGN OF A HIGH-RESOLUTION, LARGE-DATA SET, ULTRASONIC TIRE INSPECTION MACHINE

Inspection of semi-truck tires helps ensure the safety of all highway travelers. Additionally, product transport costs can be reduced by improving tire reliability. While tire inspection can take many forms, non-destructive evaluation by ultrasound has been used for many years. In particular, a clear progression of ultrasound inspection techniques has lead from simple point testing devices to more complex systems that can automatically inspect a tire. However, the traditional methods of inspection have speed and resolution limitations.

A functionally complete, high-resolution, large data set, ultrasonic tire inspection machine was developed and represents an advancement in the way it inspects tires. The system development is motivated by the desire of a large tire retreading company to perform high-resolution ultrasound inspection of semi-truck tires. The inspection device for truck tires generates complete tire flaw maps in a timely fashion where an inspection can be performed at 1/8" resolution in under 10 minutes. This represents an improvement greater than one order of magnitude over previous techniques that required 12 hours for a partial tire scan. The system inspection capability is demonstrated and validated.

A challenge of ultrasonic inspection methods is the large system point spread causing blurring of the signal. To satisfy resolution requirements and enhance flaw imaging, an application of double Wiener filtering to recover the system point spread function in ultrasonic tire inspection imaging is also developed. The double Wiener deconvolution is performed using an algorithm developed for this application. The algorithm has the capability of directly enhancing the blurry image produced by a given tire inspection when a known flaw is present on the tire. Improvements to the tire image by the filtering provide an enhancement recovering true flaw data from an indicated flaw data over twice the spatial size of the actual flaw. So a 4x4 pixel flaw that is detected as 8x8 pixels is adequately recovered after filtering as a 4-5x4-5 sized flaw.

Contributions resulting from this work are the development of an advanced high speed tire inspection methodology and apparatus. Additionally, to demonstrate system effectiveness, a deconvolution technique was applied that recovered true flaw size information from blurry flaw images. In conclusion, this work shows that tire inspection techniques can be dramatically improved with an additional improvement possible in final image quality by proper filtering. Future work possible in this area includes the streamlining of the hardware apparatus that was developed; an in depth testing and analysis to provide ultimate flaw recognition capabilities; and certainly homomorphic deconvolution techniques could be applied to eliminate the need to include a known flaw in an image prior to filtering.

Justin Gaylord Downs III
Department of Mechanical Engineering
Colorado State University
Fort Collins, Colorado 80523
Fall 2001

TABLE OF CONTENTS

ACKNOWLEDGEMENTS

I would like to thank the members of my committee; David Alciatore, Hiroshi Sakurai, Chuck Smith, and Byron Wynn. Their efforts on my behalf became more than was ever asked of any committee member. Thank you very much. I would also like to express my deepest gratitude to my final advisor Wade O. Troxell. Without his help and support, this dissertation could not have been completed. Additionally, I would like to thank Mick Peterson despite problems that eventually arose between us.

SYSTEMS DESIGN OF A HIGH-RESOLUTION, LARGE-DATA SET, ULTRASONIC TIRE INSPECTION MACHINE

1. Introduction

A recent addition to the engineering lexicon is the use of the word 'mechatronics' to describe "the synergetic integration of mechanical engineering with electronic and intelligent computer control in the design and manufacture of industrial products and processes" [Mec96]. Design of a mechatronic system can be distinguished by the need to understand a broad range of disciplines. For instance, in this research project, a general understanding of a variety of disciplines is necessary. Among these are mechanics for ultrasound transmission principles, mechanical engineering for machine operating principles, electrical engineering principles to design controllers and electronics, and computer science to design code and interface programming.

This thesis presents an implementation of mechatronic system design. Two contributions have emerged as a result of this work. The first and most important is demonstration of an inexpensive hardware system for tire inspection that allows high data acquisition rates while performing closed loop control, processing, and display in real or near-real time. The second is improving the resolution of ultrasonic tire inspection images by a direct double deconvolution method that recovers the system point spread function and filters the acquired signal. This chapter presents a brief introduction to the

research motivation, the history of the research with prior work performed by others, and a thesis statement.

1.1 Origins and history.

Non-Destructive Evaluation (NDE) in industry utilizes many techniques for evaluation of materials. Ultrasound inspection is one method traditionally used for tire inspection. However, previous tire inspection efforts have been limited to low resolution with flaw detection sizes on the order of one inch. Recent advances in digital data-acquisition and control hardware have made possible the development of high resolution, high speed ultrasonic scanning equipment. Design and construction of a tire scanning system incorporating these advances will enhance the current state of understanding and facilitate the implementation of this type of system. In particular, design of such a system requires close hardware integration of disparate systems, an appropriate algorithm for real-time control and data-acquisition in a multi-processor system, and deconvolution of the system point spread function to enhance image resolution.

1.1.1 Motivation for Truck Tire Inspection.

Semi-truck tires are expensive. A typical new radial truck tire (size 11-22.5) costs $360 from a discount seller with larger, specialized, top of the line models costing $455 [Pre97]. The expense per tire multiplied by 18 tires on a typical '18-wheeler' is a significant working cost for truck operators. Due to the high cost of new tires, many trucking firms and independent truck operators use re-treaded tires. The cost of a similar 11-22.5 retread is $289 [Elp97]. A minimum $70 savings per tire is possible by using

retreads. Multiplied by 18 tires, there is a minimum savings of $1,260 during the life of a set of tires.

While retreading of car tires has been decreasing due to readily available, inexpensive new tires, retreading of truck tires has been increasing. Truck tires are often retreaded three times before the original casing is discarded [Cla93]. Truck tire retreading services produced an estimated 17.3 million units in 1997 (up 5% from 1996). Estimates call for a 4% increase in 1998 [Boz97]. This is in contrast to production of new truck tires in 1997 where 12.5 million units were produced, showing most truck tires being used are retreads [Boz97]. The 11-22.5 is the most popular size to retread demonstrating it as a "typical" truck tire [Boz97].

To enhance safety on the highway and diminish warranty liability, tire retreading companies would like to reduce the incidence of failure in their retreaded tires. The National Tire Dealers and Retreaders Association asserts that properly inspected retreaded tires have lifetimes and failure rates comparable to new tires [Cla93]. The incidence of catastrophic failure can be reduced by characterizing the flaws that cause failure and eventually removing tires containing critical flaws from the production process prior to retreading.

Critical flaws in tires are not yet well understood. To accomplish the characterization of flaws and removal of flawed tires, a comprehensive database of flaw types needs to be developed. Such a database would allow tires with flaw indications to be tracked while in service. Tire failures occurring in inspected tires can be correlated with the flaw indications discovered during inspection. Since there are millions of truck

tires being used on the road today, inspecting even the 17 million that are retreaded yearly would be an enormous undertaking at this time.

Developing a database to characterize flaw identifiers can be accomplished. A retread plant producing 100 retreads per day can be used with complete inspection of every tire. Inspecting 100 tires/day at 10 minutes/tire requires over 16 hours so a high-speed inspection system is required. Based on reasonable spatial resolution inspection estimates from previous work [Rog91][Rog92], defects as small as 1/8 inch can be detected. Thus an inspection system capable of both high-speed and high-resolution is required to develop the database necessary to evaluate this concept.

1.1.2 **The Need for Improvements in Truck Tire Inspection.**

The importance of non-destructive testing truck tires has been recognized for quite some time. Ortoli [Ort88] states that tire testing takes many forms including simple visual inspection and measurements of tire size. In addition, tire evaluation is accomplished by destructive testing; subjecting tires to simulated road wear. Ortoli mentions that a third method for tire testing is the use of various NDE methods. However, he does not include ultrasonic inspection despite the work of Ryan in 1977. Ortoli develops a general framework for tire evaluation shown in Figure 1.1. NDE tests, destructive tests, and fleet use contribute to a database available to engineering staff who may then better evaluate tire effectiveness in the presence of defects. Ortoli mentions that data acquisition in tire testing is usually not "user friendly" and often requires a technician be present to assist in operating such a system. One objective of the developed system is "user friendliness". This implies the system should be easy to use requiring little input from the user. In addition, the system should be capable of operation without

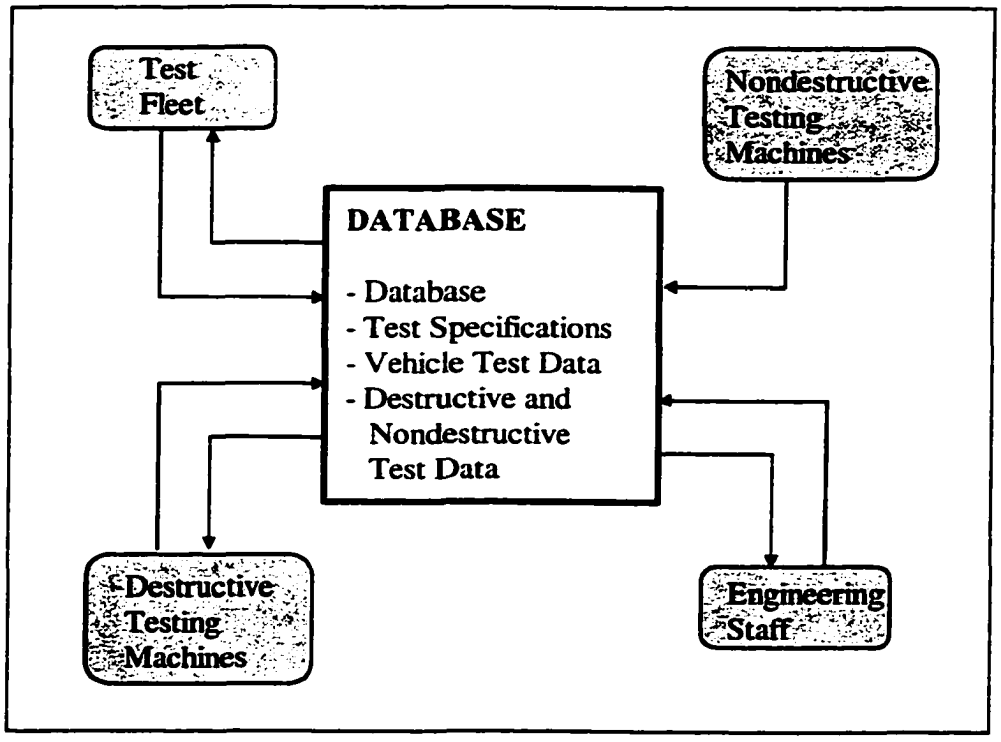

Figure 1.1: Ortoli's overall inspection system.

constant technical assistance. While Ortoli neglects ultrasonic inspection as a means for NDE of tires, his comments are pertinent to the question of NDE of tire casings.

Further demonstrating the role of inexpensive data acquisition equipment, Reader discusses the nature of non-destructive testing (NDT) in industry and suggests areas for future improvements [Rea90]. Typically, if industrial products can be 100% inspected with little additional cost, it is indisputable that such testing will have a significant impact on product quality and user satisfaction. Reader again states that inspection can be a simple visual inspection, however this requires a trained operator and probably will not detect subsurface flaws within a material. In automated NDT applications, effective image processing of large amounts of data are required for the output to be easily and quickly understood. Automated recognition of flaws needs to be incorporated into NDT image processing to promote complete effectiveness. Reader concludes that the advent

of relatively cheap microprocessors will facilitate improvements in traditional NDT techniques.

1.1.3 **Ultrasonic Tire Casing Inspection Fundamentals.**

Ultrasonic tire casing inspection is performed by pressure wave generation, transmission to the tire, and reception of a reflected or transmitted signal. The generation, transmission, and reception are influenced by physical attributes of the transducers, transmission medium, material to be inspected, and operating frequency chosen for inspection. Rogers has shown that ultrasound tire inspection can detect disbond and heat damage flaws that cause attenuation changes in the ultrasound beam detected after passing through the material [Rog91][Rog92]. Optimal frequency for this type of inspection was determined by Rogers to be 500 kHz. Examination of some tire physical attributes demonstrates necessary conditions for the tire casing inspection.

Two types of mechanical waves that can be generated in unbounded elastic solids are longitudinal and transverse waves. Longitudinal waves are also called pressure waves and are similar to sound waves. Transverse waves are also called shear waves. Both wave types as well as types generated in a bounded solid are used in NDE techniques, depending on the inspection to be performed. Mode conversion between the wave types occurs at material boundaries where the angle of incidence is not normal to the surface. The relative amplitude of mode converted waves depends on the angle of incidence and wave speeds in the materials [Kra90]. The ultrasonic tire inspection performed in this work uses only longitudinal waves. Mode conversion is unwanted and avoided by maintaining an incident wave angle less than the first critical angle where a

shear wave is generated. The close match in wave speeds between water and rubber increases the angle and helps prevent mode conversion.

Ultrasonic imaging employs two primary inspection techniques, pulse-echo and through-transmission. The first method uses a single ultrasonic transducer in a transmitting and receiving configuration. In pulse-echo inspection, the single transducer generates an ultrasound pulse that is selectively reflected from the interior or exterior surface of a sample or defect within the sample. The same transducer is used to generate an electric potential from the reflected wave. The second method uses a transmitter-receiver pair where the ultrasonic wave is transmitted through the specimen and received by a separate transducer. Both methods can be used for tire casing inspection.

The inspection methods can be performed using direct contact of the transducer with the tire; by air coupling where the transducer is placed some distance away from the tire and air serves as the propagation medium for the ultrasound beam between the transducer and the tire; or by water coupling where water propagates the ultrasound beam between the transducer and the tire. Several physical principles of ultrasound transmission must be considered for each of the coupling techniques. The acoustic impedance of the materials propagating the wave (directly related to sound velocity in the materials) influences the sound energy transferred across material boundaries during inspection. Sound velocity in the propagating medium also determines beam refraction at boundaries. Beam reflection and/or refraction at boundaries can be reduced by choice of coupling between the transducer and the material to be inspected.

The first important consideration is relative acoustic impedance of the materials propagating the ultrasound wave. The acoustic impedance is defined as the product of density and velocity of sound in the material [Kra90]:

$$Z = \rho c$$

where:

Z = acoustic impedance
ρ = density
c = sound velocity in material

The acoustic impedance of some materials relevant to this work are [Kra90]:

$Z_{air} = 4.2 \times 10^2 \text{ kg/m}^2\text{s}$
$Z_{water} = 1.5 \times 10^6 \text{ kg/m}^2\text{s}$
$Z_{rubber} = 2.8 \times 10^6 \text{ kg/m}^2\text{s}$

In general, when large acoustic impedance mismatches are present at a two-layer boundary, a significant portion of the ultrasonic wave is reflected instead of transmitted across the boundary.

Relationships for coefficients of reflection and transmission R and D can be derived so that [Kra90]:

$$R = \frac{Z_2 - Z_1}{Z_2 + Z_1} \qquad D = \frac{2Z_2}{Z_2 + Z_1} \tag{1.1}$$

where $Z_{1,2}$ are different materials and Z_1 is the material propagating the incident wave. R and D can be expressed as the fraction of incident sound pressure amplitude that is reflected or transmitted. It is evident that the reflection coefficient R becomes large as the difference between Z_1 and Z_2 becomes large. Similarly the transmission coefficient becomes small. When $Z_2 > Z_1$, the reflection coefficient R is positive indicating the incident and reflected wave are in phase. In the case that $Z_1 > Z_2$, R becomes negative and the incident and reflected wave are 180° out of phase [Kra90].

It is also evident from Eq. 1.1 that the transmission coefficient D can be larger than 1.0. This condition indicates that sound pressure in the transmission material can be greater than that in the incident material. This condition arises because the energy or intensity of the sound is proportional to the sound pressure squared and the acoustic impedance of the material. Intensity J (W/m^2) is given by [Kra90]:

$$J = \frac{1}{2}\frac{p^2}{Z}$$

where p = sound pressure. For a transmission material with high acoustic impedance in comparison with the incident material the sound pressure may be much higher even if the sound intensity is much smaller.

The transmission medium between the transducer face and the inspection material is also important. As noted, ultrasound inspection can be performed by direct contact of the transducer with the material to be inspected. However, wave amplitude reception can be unreliable due to inconsistent coupling between the transducer and material. Additionally, complex shapes such as a tire can be difficult to inspect using direct contact even when using manual scanning.

Air coupling is possible and has been used extensively for low resolution tire casing inspection [Rog92][Rog94]. Unfortunately the large impedance mismatch between air and rubber ($Z_{air} << Z_{rubber}$) causes greater reflection at the air/rubber boundary with resultant loss in transmitted energy. In addition, the refraction coefficient associated with air coupling of the ultrasonic wave causes increased alignment sensitivity. From Snell's law [Kra90]:

$$\frac{\sin\alpha_1}{\sin\alpha_2} = \frac{c_1}{c_2} \qquad (1.2)$$

where:

α_1 = angle of incidence in transmission material
α_2 = angle of incidence in receiving material
c_1 = wave speed in transmission material
c_2 = wave speed in receiving material

and from the wave speeds c in air, water, and rubber [Kra90]:

c_{air} = 343 m/s
c_{water} = 1,800 m/s
c_{rubber} = 2,300 m/s

During through transmission, even if the angle α_1 of the incident wave is small, the refracted wave as it emerges from the opposite boundary can be offset enough that

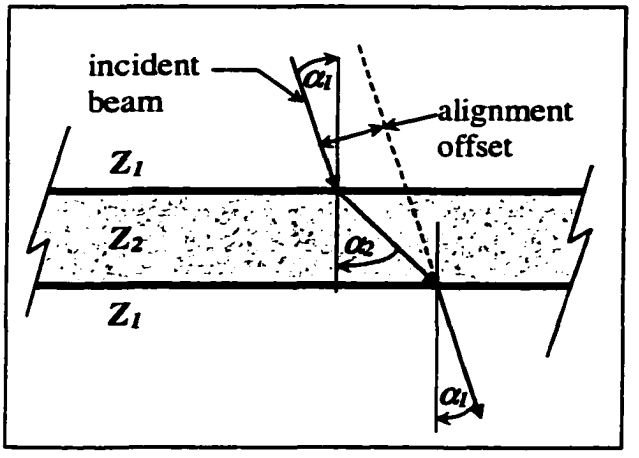

Figure 1.2: Incident beam offset by large acoustic impedance mismatches.

alignment of the receiving transducer can be difficult. Figure 1.2 demonstrates an incident beam in through transmission with angle α_1 that is refracted within the inspected material and emerges with an alignment offset.

To overcome some of the problems associated with direct or air coupling, materials are often inspected using water coupling where a water medium propagates the ultrasound beam between the transducer face and material to be inspected. During inspection, the transducer can be placed some distance away from the material to be inspected. The water medium can be implemented as total immersion of the object and

transducer or as a water stream between the material and transducer face. Wave propagation speeds in water and rubber are more closely matched so the angle of incidence for the refracted wave is similar to that of the transmitted wave. Where $\alpha_1 \approx \alpha_2$ the alignment offset shown in Figure 1.2 will not be as severe as in the air case.

Water coupling in tire inspection provides additional benefits. From Equation 1.1 $D = 0.69$ or the wave transmitted into the rubber has about 70% energy of the incident wave. Additionally, stepping a transducer pair over an entire tire in 1/8" increments, axially aligned and in direct contact to reduce attenuation, would be complex. The water coupling negates the need to move the transducer for direct contact over the entire surface [Rya77][Rog91][Rog92]. The developed system uses water coupling of the transducers to reduce attenuation and to decrease sensitivity to misalignment of transducers.

In through transmission tire inspection the receiver must be inserted into the tire so the physical size of the transducer becomes an issue. The physical size of a piezoelectric (PZT) transducer is directly related to the center frequency. Ultrasonic inspection of rubber has previously used a range of acoustic frequencies starting under 100 kHz and extending to over 10 MHz. While there is leeway in the physical size for a particular frequency, it is generally not practical to produce for instance, a 0.5 MHz transducer with a 1/8" PZT element diameter. Transducers in the 0.5 MHz frequency range are commonly found with diameters of 0.75 $\rightarrow$ 1.5 inches [Pan94] (transducer size becomes a factor when designing a sensor head discussed later).

Transducer size is constrained by physical principles. Simple PZT transducers are constructed from a disk of PZT material. Deformation of the elastic PZT solid disk when a voltage is applied to opposite surfaces generates displacement along the central axis of

the disk between the electric potentials. The deformation is proportional to the applied voltage in the linear range typically employed. The axial displacement generates pressure waves in front of the transducer (non-axial displacement generates shear waves). Conversely displacement of the piezo-electric solid generates a voltage. Due to the elastic properties of the material, any positive displacement of the material in one direction must be associated with corresponding negative displacements in other directions excluding small dilatation effects [Kra90]. So if the PZT disk is oscillating along its thickness axis to produce ultrasound, there must be a corresponding oscillation of the perimeter of the disk. For a particular diameter disk excited along its central axis, the thickness governs the center frequency or natural mode of vibration for a particular piezo-electric material [Kra90]. Producing a large amplitude pressure wave for high energy requires a large displacement in the PZT material. A transducer with a diameter of only 1/8" would not be capable of producing the large displacements necessary to generate the long wavelength ultrasound energy for the proposed tire inspection.

The ultrasound beam resolving capability determines the size of flaws that can be detected. The wavelength of the ultrasound beam, dependent on frequency and the speed of sound in the medium, in part determines the resolving capability. Additionally, the relative aperture of the transducer plays a role in resolution [Kra90]. Lower frequencies are associated with lower spatial resolution for a fixed aperture. The ultrasonic wavelength is found from the relation:

$$\lambda = \frac{c}{f} \tag{1.3}$$

where: λ = *wavelength*
c = *longitudinal wave speed in an unbounded solid*
f = *frequency of signal*

The wave speed in rubber has a range between 1,480 m/s for soft rubber up to 2,300 m/s for vulcanized rubber [Kra90]. The wavelength of a 0.5 MHz ultrasonic pulse can vary between 3.0 mm and 4.5 mm. Rogers' work shows that for a higher frequency transducer (2.25 MHz), the resolution increases sufficiently that steel belts inside the tire are resolved. Steel belt strands are typically about 0.8 mm diameter and the wavelength in rubber at 2.25 MHz is approximately 0.8 mm showing resolution in this type of inspection to be on the order of the wavelength used. Rogers reduced the center frequency for the inspection until the belts were no longer detected (to 500kHz). However, this also sets the resolving limit for flaws in the material. Thus flaws of dimension much smaller than 3.0 mm will not be resolved successfully either.

Transducers have a spatial point spread function (PSF) associated with them. The point spread function describes the sound pressure distribution moving away from the central axis of the transducer at a particular distance in front of the transducer face. From reciprocity, the PSF also describes the region of maximum sensitivity to sound pressure during reception [Kra90]. The center frequency and transducer aperture ultimately determines the area of maximum sound pressure or 'spot size' of the transducer and influences its resolving capability. The spot size is defined as the size of the region where the sound pressure is attenuated less than –6 dB. Due to the long wavelength and relatively small aperture involved, the spot size has a relatively large area for low frequency operation. For instance, a 0.5 MHz transducer with aperture 1.5" spherically focused to 2.25" has a spot size of about 1/5".

The ideal scan is a true flaw image reflecting the correct spatial dimensions of the flaw. Any image produced with an ultrasonic system will be a convolution of the ideal

scan a flaw would produce and the PSF of the transducer and system itself. (Point spread functions discussed in Sections 2 and 4 are for a transducer operating in water.) Once the beam enters the material to be inspected, additional blurring or sharpening occurs due to the ultrasound transmission properties of the material itself during refraction at boundaries. A system PSF is then a combination of the blurring induced by all components of the inspection process. For a transducer with a 1/5" spot size, the image of a flaw only 1/8" in size is convolved with the PSF. In fact, if the system is capable of only 1/8" resolution, the image developed is a reflection of the system PSF or impulse response of the system.

Since any image produced by ultrasonic scanning convolves the system PSF with true flaw information, deconvolution of the system PSF ideally recovers the true flaw information. In addition to a spatial 2-D PSF that describes the sound pressure distribution, transducers also have a 1-D temporal PSF that describes the sound pressure variation over time due to impulse excitation of the transducer. A transducer, operating in pulse-echo mode, illuminating a flaw with ultrasound, will detect a reflection of the flaw that is a convolution of the sound generation capabilities of the transducer itself and the sound reflection capabilities of the flaw. The term "signature" describes the ideal echo returned during ultrasonic examination of a flaw. Evaluating the type and size of a flaw reduces to identifying the signature of the flaw from echoes returned during inspection [Mur78].

A great deal of prior NDE deconvolution work deals primarily with examination of time signatures. Many researchers have used deconvolution of the time impulse response of the transducer to enhance the time resolution of the transducer. Chen

provides a review of spectrum based techniques for 1-D ultrasonic signal deconvolution [Chen90]. However, the Wiener filter is used by most for 1-D deconvolution as discussed in the historical review Section 4.2. An important component for using the Wiener filtering algorithm is prior knowledge of the noise power spectrum in the detected signal. Neal has examined optimization techniques for determining the noise power spectrum when it is unknown [Nea88a][Nea88b]. Neal also demonstrates use of the Wiener filter to enhance 1-D flaw signatures with prior and limited-prior knowledge of the expected flaw signature [Nea92][Nea93].

Deconvolution of the system PSF from experimental data to image 2-D flaws correctly is not well represented in the NDE literature. Frock has shown that using axial-Wiener deconvolution can enhance the lateral resolution in ultrasonic c-scan images [Fro91]. However, the axial deconvolution method used is not a 2-D deconvolution but a 1-D deconvolution performed at each individual step. Cheng has shown effective PSF recovery from 2-D pulse echo signals using a specially constructed test sample that is used to extract the system PSF [Che96]. The PSF is then used on an unrelated sample to perform deconvolution. Downs demonstrated that using the simple PSF model is not appropriate for tire image deconvolution and recovered the system PSF from the same experimental data the system PSF was to be deconvolved from [Dow96]. The recovered PSF was successfully applied to enhance data from the same image. A through transmission system where time signature of the ultrasonic pulse is ignored eliminates axial deconvolution as an image enhancement option. The 2-D spatial PSF remains as blurring influence in the ultrasound images. Flaws detected are a convolution of the 2-D

PSF of the system and the flaw signature itself (2-D convolution, deconvolution, and history in NDE is discussed in greater detail in Section 4).

Further complicating the tire inspection problem is the geometry of the tire. A cross sectional slice of a typical tire shows a large variation in tire thickness as shown in Figure 1.3. The large variation coupled with the attenuating influence of the various steel

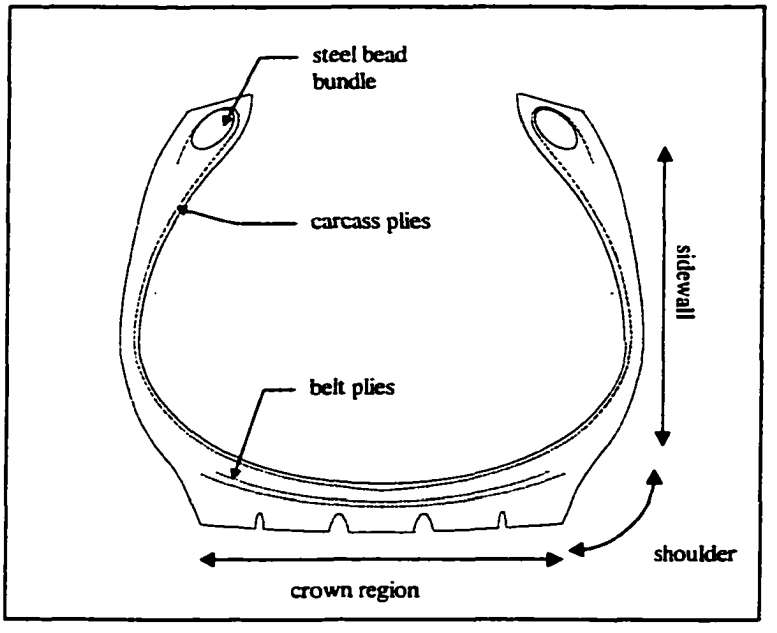

Figure 1.3: Tire profile.

belts incorporated in a tire produces a large variation in transmissibility of the ultrasound beam passing through the tire. For a fixed transmitter energy level, highly attenuating sections of the profile transmit less beam energy through the tire. To overcome this, receiver gain can be increased for the higher attenuating regions. The variation prevents scanning the complete tire profile with a fixed system gain applied to the receiving transducer. If the receiver amplification is held constant when passing from a highly attenuating region to a region of less attenuation, the received signal exceeds the dynamic range of the amplifiers during amplification. The result is that the received signal is "clipped" by the amplifiers with resultant loss in sensitivity to small variations in

attenuation. Ideally the receiver amplification is set so that the received signal is amplified to the maximum dynamic range of the amplifier. Any attenuation due to flaws will be evident. Conversely, the receiver gain can be held at a fixed level and the transmitter energy level varied as appropriate for attenuation conditions encountered. Gain control needs to be implemented so that unflawed areas are received using maximum gain without clipping.

1.1.4 Historical Review of Tire Casing NDE by Ultrasound.

Tires have been retreaded since the early 1900's. Early tires lasted only about 1000 miles so that reapplying tread to the casings became commercially viable during World War I when rubber prices were high [Pre89]. Tire casings have been inspected for as long as tires have been retreaded. For many years tire inspection was visual with the inspection being performed by a human operator. A patent search performed for the previous 26 years (to present time) revealed 49 patents in that time alone relevant to tire inspection [Pat97]. In general the patents can be divided into three types of inspection devices. The first and most prevalent are typically devices to hold and spread the tire so a human observer can visually assess the condition of the tire. The second are devices that inspect a single point on the tire in some way such as contact ultrasound. The third class are systems that use a non-destructive evaluation method such as X-ray, ultrasound, or displacement sensing in some form to examine larger portions of the tire. There are many X-ray devices extant in the patent database for inspecting tire casings. In addition, several shearography and holography systems are in evidence. Finally there are five ultrasonic systems listed for tire inspection [Pat97].

1.1.4.1 **Patents Related to Ultrasonic Inspection.**

The history of patented ultrasound devices and/or systems for tire inspection begins with a U.S. Patent issued in 1945 to W. E. Morris [Mor45]. Morris' patent uses water bath immersion and swept ultrasonic frequencies with through transmission inspection to inspect single points on a tire. Several devices of similar nature are listed with the most recent being a patent issued to Halsey in 1977 for a full contact probe to inspect a tire [Hal77]. Halsey's device uses a single probe contacting the tire with multiple receivers situated on the opposite side of the tire to detect "occlusion" (sic: Halsey's wording) of the ultrasound signal by flaws imbedded within the tire. This is the most sophisticated device patented to date.

Of particular relevance for this dissertation are ultrasonic tire inspection systems represented in patents and literature. A discussion of tire inspection systems show that the developed system is indeed a novel implementation. The first system to be patented was by McCauley in 1975 [McC75]. McCauley's system uses a single matched pair of ultrasonic transducers performing through transmission inspection. Successive scans were performed on a rotating tire using water immersion for coupling. The display was limited to an *xy* graph of successive scans. A complex mechanical gearing system provides motion of the various components. The system covers only the crown of the tire.

While McCauley's system was the first, it appears to have not been as successful as later systems. In 1981, Weiss at AMF Inc. and Dugger, et al, at Bandag Inc. both patented more advanced systems for tire inspection [Wei81] [Dug81]. A series of patents

fallow over several years by both Weiss and Dugger with improvements and novel features of their respective systems being patented.

Dugger 1981

Dugger's system used 40 kHz air-coupled, pulsed ultrasound in through transmission and compares relative magnitudes of the received signal. The tire is spun with the entire tire inspected in one revolution. An array of 15 transducers over the crown of the tire provided lateral resolution no less than 0.5". Sidewall scanning is not performed. Dugger's patent cited an "urgent need for cost-effective, efficient, non-destructive inspection (NDI) of rubber tire casings" [Dug81]. Dugger also notes there had not been a commercially viable mechanism developed to that date for mounting and moving the tire. Display of the data was by multiple *b-scan* plotting on a television monitor by location vs. amplitude.

Weiss 1981

Weiss also patented a system in 1981 that used air-coupled transducers in through transmission [Wei81]. The tire is insonified by a toneburst to transmitting transducers while using slightly different frequencies to prevent cross-talk in the elastic tire medium. Weiss' system is the first to use microprocessors to perform data analysis on digitally sampled waveforms detected during scanning. The system uses five transducers arrayed across the crown providing a minimum lateral resolution of 1.6". The tire is spun and an entire scan performed in one revolution. Sidewall scanning is not performed.

Cushman 1990

The next patented system is by Cushman for Oliver Rubber Company in 1990 [Cus90]. The system again uses air-coupled through transmission on a spinning tire. In Cushman's system, an array of 26 receivers is placed outside the tire while a single transmitter is aligned by an ultrasound mirror with each receiver in turn after one revolution. The receivers are arrayed to cover part of the sidewalls but a large section of the shoulder is left un-inspected. The lateral resolution between scan lines is approximately 0.5". Limited sidewall scanning is performed but the shoulder region is largely ignored.

Macecek, et. al., 1990

The system developed and patented by Macecek, et. al, was developed for the Vulcan Equipment Company of Scarborough, Canada [Mac90]. The system used through transmission ultrasound at 40 KHz with air as the transmission medium. The tire was mounted to a special hub that incorporated 16 ultrasonic receiving transducers. The tire was then inflated with air to 15-18 PSI. The system utilizes an array of 16 transmitter transducers in an arc around the exterior of the tire crown matched with the receivers on the inside of the tire. No effort was made to inspect the sidewall. During operation, a single transmitter is pulsed while its corresponding receiver is sampled for a short time.

A number of problems are associated with this configuration. The first is that most of the sidewalls are ignored. Alignment of the transducer pairs relative to the tire and relative to each other would be a constant problem due to variation in individual tires. Large refraction coefficients occur in air coupled systems so that when the beam incident angle departs from normal to the surface, receiver alignment can be difficult. Transducer

alignment is not addressed in the patent. No resolution is provided for the system. However, if 16 transducers are assumed to be arrayed in an arc of 10 inches around the crown of the tire, only 16 scan lines are taken in that distance. The implied minimum distance between lines is 0.6". Resolution in that direction would not be less than that.

Yovichin 1994

The latest patent for a tire inspection system is not an ultrasonic system but is included here to show further development of tire inspection systems [Yov94]. In the system, several contact displacement sensors are arranged on the sidewall. The tire is spun and the output of the displacement sensors digitized to build up a displacement map of the sidewall. Filtering algorithms sift the data for high and low spots on the sidewall that can be correlated from previous experience with damage to the sidewall belts. The crown and shoulder regions are not inspected.

1.1.4.2 **Publications.**

In relevant publications, Morris published a paper discussing the ultrasonic inspection of tires as a development of his patent from 1945 [Kra90][Mor52]. More recently, Halsey discussed ultrasonic inspection of passenger car tires [Hal68] and McConnell investigated aircraft tires using pulse-echo techniques [McC72]. Early inspection methods were all primarily single point inspection techniques and devices.

Halsey, 1968

Halsey introduced ultrasonic inspection of passenger car tires. He concentrated on the effects produced by various anomalies in tire casings such as porosity, separations, and bond quality. The inspection method used pulse-echo technique. Halsey made mention of a 1 MHz "system" for inspecting but provides no details on how such a

system may be implemented. He did reference a number of previous inspection methods demonstrating feasibility without crediting Morris as the first [Hal68][Cur55][Dun54].

Ryan, 1977

The first ultrasonic NDE tire inspection system (where a system scans more than a single point on the tire) described in literature was developed by Ryan in 1977 as part of a United States Department of Transportation project [Rya77]. Ryan's system used a pulse-echo configuration, water coupled, with the transducers located external to the tire. The tire was mounted to a rim and inflated before inspection. The entire tire was then submerged completely and spun at 6 rpm for inspection. Ryan's system was designed to inspect only car sized tires. An array of 24 transducers was arranged around a cross section outside of the tire providing inspection around the full crown and sidewalls of the tire. The system sampled 1000 points circumferentially on the tire providing approximately 1/8 inch step sizes. However, the array of 24 transducers provided radial cross section inspection point separation of about 1 inch. While circumferential step size was good, radial cross section step size was poor.

A significant problem with the pulse-echo technique, mentioned by Ryan, was the need for precise orthogonality between the transducer central axis and the interior surface of the tire. He stated that since there was significant refraction at the water-rubber boundary, without precise orthogonality the ultrasound beam exiting the tire after reflection could be directed in a completely different direction than the incident beam. A complex mechanism to address the alignment requirement was designed and needed adjustment for each tire size inspected. In fact, continuous adjustment was required even for tires of the same size.

Ryan attempted inspection at a variety of transducer center frequencies between 1.0 and 5.0 MHz but settled on 2.25 MHz for the final system citing the resolution was high enough at that frequency with adequate penetration. At higher frequencies, penetration became a problem when the ultrasound beam would not pass through the thicker sections of tire. In 1977, polyester belted tires were dominant and the close impedance matching of the cords and rubber did not cause resolution problems at this higher frequency. Operating at the same frequency on steel belted tires would resolve the steel belts in the tire and increase difficulties with identifying flaws. Extensive signal processing and display was not possible at that time. Flaws were detected using simple analog threshholding applied to the time history of reflected data.

Technic Systems

Technic Systems, based in Leicestershire, England, developed the most recent ultrasonic inspection system. The system was called the Tyrescan System and was described in their sales brochure as offering [Tec94]:

1. real time display.
2. 90 second cycle time.
3. full color display.
4. information storage.
5. accurate sizing

The system was referred to by White [Whi95] as "a new ultrasonic tyre testing system". White stated the system was a "practical, easy-to-use imaging system, at moderate cost". Rick Rogers [Rog94] of Bandag pointed out several disadvantages of the system for their purposes:

1. does not image the entire tire.
2. cannot scroll the display to look at the whole tire.
3. no real reference as to where the defect is around the circumference of the tire.

4. picture is dominated by the tread pattern rather than the defect.

In fact, the scanner imaged only the crown of the tire and not the sidewalls. Technic Systems product literature did not provide information on the resolution of the system. However, inspection of the photographs included with the literature seem to show the resolution was similar in size to the tread pattern on a large truck tire or about 1 square inch.

Reis 1997

Most recently, Reis demonstrated an acousto-ultrasonic method to detect broken cords in steel belted radial tire sidewalls [Rei94][Rei96]. His method employed a toneburst injected into the sidewall near the bead on the tire. A receiving transducer detects the signal by the shoulder of the sidewall. Wave speeds in steel are about 4 times the wave speed in rubber [Kra90]. Since the wave speeds in rubber and steel are very different, a break in the radial steel belt tire changed the speed of propagation of waves through the sidewall. Most recently, Reis demonstrated results from a prototype system to implement the inspection [Rei97]. The system inspects only the sidewall and the resolution is limited to radial bands on the tire.

1.1.4.3 **Alternative Inspection Methods.**

Alternative methods of inspection include shearography, holography, and x-ray. In holography, the tire is mounted on an airtight rim and placed in a vacuum chamber. A visible laser light is used to illuminate the tire while a CCD camera is used to acquire an image of the tire. Vacuum is then applied to the chamber. Embedded defects within the tire that encapsulate air expand and distort the outside surface of the tire. A visible laser light is again used to illuminate the tire and the image is re-acquired. The images are

combined and interference fringes are generated where the tire shows relative deformation. Shearography is a similar process to holography except the second derivative of the gradient on the interference fringes is generated and imaged.

Both of these methods have notable advantages but also have limitations. One advantage of these methods is that the full field of the tire is viewed. However, the speed of the inspection process is slow and both require a large vacuum chamber to implement. The process is slow because the tire must be mounted on an airtight rim, moved into a vacuum chamber, illuminated properly by the coherent light and then the machine begins the inspection. If the flaw of interest is open to the vacuum, such as a leaky disbond, little information is derived from holography since there will be little deformation due to expansion of encapsulated air. If the tire does not reflect the coherent light adequately, the process will not work. Additionally heat damage and rubber reversion are not detectable since deformation does not occur during the vacuum process. Due to the slow speed and vacuum chamber required, this method is not appropriate for high speed scanning.

A third alternative is x-ray. The short wavelength and high energy associated with x-rays provides very high resolution. The greatly increased resolution of x-ray images the steel belt components extremely well. However, rubber is relatively transparent to x-ray so disbond and heat damage in the rubber will be difficult to detect. X-ray is not a good alternative where small changes in the rubber material are of interest.

1.2 **Thesis Statement.**

Ultrasonic NDE techniques have been demonstrated in the laboratory, literature, and industry to be capable of detecting disbond and material property changes in rubber

steel composite tires. The previous inspection techniques have had demonstrated problems. Specifically a number of issues arise. The time required for a complete tire scan is very long. The difficult shape of the material to be inspected does not lend itself easily to automated inspection techniques. The constraints imposed by ultrasonic transducer fields have limited resolution and blurred the resultant image due to the large spatial point spread function associated with low frequency, small aperture ultrasonic transducers. Finally, the difficulty with inter-linking a number of disparate data-acquisition and control systems in near real-time have presented significant challenges to the development of such a system.

A tire inspection system design is developed for data-acquisition and control that allows high-speed, large data set, near real-time control and display of simulated flaws detected in tires by ultrasound. A scanning technique is demonstrated that overcomes the problem of inspecting the complex tire surface. High speed allows a complete tire scan to be completed in under 10 minutes. Large data set acquisition in near real time allows collection and display of data without constraining system resources. The large data-set capacity of the system permits over-sampling (or overlapping samples) to be performed. Due to the over-sampling capability, resolution limitations can be overcome using a numeric deconvolution filtering implementation to recover and apply the system point spread function on the inspected tire image. Resolution of the system is enhanced by deconvolution of the system point spread function reducing blurring in the tire flaw image.

1.3 Dissertation Organization

Chapter 2 presents limitations imposed by the inspection technique. A low noise (Electro Magnetic Interference) environment is required for sensitive electronics used in ultrasonic inspection. Ultrasonic generation and reception transducers are limited by the size of tires further constraining the design. Additionally, real-time data acquisition and control in a system requires timely handling of signal processing and control. These constraints are reviewed Chapter 2.

Chapter 3 presents a review of how the limitations discussed in Chapter 2 were handled. Truck tire specifics are reviewed and then an inspection technique is presented. The system can be characterized into three major sub-systems; ultrasonic, motion control, and data acquisition. Each of the sub-system designs is reviewed. A description of the hardware used in the design is given with a review of the software architecture used in the system. Finally, the system capabilities are demonstrated.

2-D ultrasonic inspection at low frequencies introduces significant blurring in the acquired image due to the large point spread function. Chapter 4 presents a review of the point spread function and its effects. Deconvolution technique is reviewed and applied to the acquired image to enhance the resolution of the system.

Chapter 5 presents a discussion of the system and its performance. Additionally, improvements that could be made are discussed.

Chapter 6 provides a conclusion to the work and suggestions for future work.

Chapter 7 lists the references cited.

Chapter 8 (the appendix) contains an explanation how the tire co-ordinate system used in Chapter 3 was developed. The MATLAB code for the tire setpoint program is listed.

2. Design Motivation.

Aspects of the system design are motivated by the need to overcome constraints imposed by system components. The design must ensure that operation of one component is not inhibited by the operation of another. Ultrasound beam generation, detection, and amplification for non-destructive evaluation purposes depends on selecting transducer operating conditions to match the required inspection. In this chapter, the constraints imposed by system components are described.

This chapter presents an overview of low EMI (electro-magnetic interference) motor drives and then describes the constraints imposed by the use of low EMI drives. The chapter continues with an examination of ultrasonic transducer operating conditions and the ultrasound beam field. Transducer conditions and constraints imposed by the specific conditions for the system are specified. Finally, study of the high-resolution criteria introduces constraints established by the need to perform high speed, large data set, data acquisition and control.

2.1 Low-noise drive required for low EMI.

Many types of mechanical motion actuators are available. For precision motion control, the choice is usually to use stepper or servo motors. Servo and stepper motor drivers typically use a 'chopper' type power supply to drive the motor. The chopper supply differs from a linear supply by using a chopping frequency, typically in the 50 to 100 kHz range, to simulate a DC voltage by providing a series of high voltage pulses instead of a constant DC voltage source. Figure 2.1 shows an example. The motor

response is similar whether the driving voltage is chopped or steady state as long as the voltage rating of the motor is not exceeded. A chopped DC pulse with amplitude of 10V

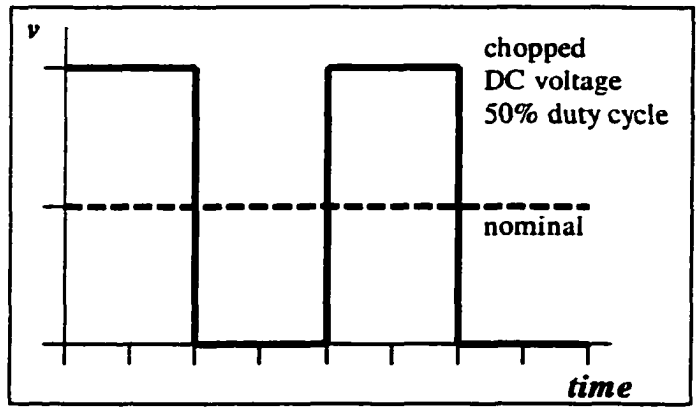

Figure 2.1: DC vs. chopped voltage.

and duty cycle of 50% has the same effective power as a steady DC voltage of 5V. Chopper drives are used extensively due to their low cost compared to linear drives.

Chopper type motor drivers generate large amounts of electro-magnetic interference (EMI) during operation. The EMI generated can interfere with sensitive electronic measurement systems such as that needed for ultrasound reception and amplification. In the machine design for tire inspection, EMI interference is unacceptable. To overcome this problem, linear drives need to be used instead of chopper drives. The linear drive supplies the motor with a constant voltage eliminating the chopping frequency and reducing EMI to acceptable levels.

However, there is a trade-off that exists when using linear drives. The drives are usually more expensive and are able to output less effective power than a comparable chopper drive. This means that the size of motor a linear drive can run is significantly smaller than standard chopper drives. Chopper stepper motor drives can often drive motors with torque outputs in lb/ft. Linear drives will instead operate motors in the oz-in range. For instance, one vendor provides medium sized stepper motors with chopper

drives that have torque ranges between 960 – 4500 oz-in. The same vendor offers higher cost, low EMI drives with matching stepper motors. The largest available low EMI torque range is 150 oz-in [Com93].

2.2 Mechanical limitations due to drive limitations.

The low torque capability of the linear drive imposes a design constraint on a mechanical system. Accelerations and/or component sizes are limited by the maximum torque available for rotational motion or transfer to translational motion. Low-noise, linear motor drives are available that have torque ratings equivalent to chopper drives however the cost can be very high ($50,000 surplus). To avoid high drive costs, mechanical limitations are imposed upon the design.

2.2.1 System throw weight and speed severely constrained.

A cost effective, low noise drive can be purchased with a maximum torque range of 150 oz-in [Com93]. The low torque available limits the accelerative force that can be applied to large components. For instance, if four transducers weighing 1.5 lbs. each where mounted to a 20 lb. carriage on frictionless bearings driven by 2.5" radius low-loss belts, the force applied to the system is:

$$\tau = fd$$

where:

τ = torque
f = force applied
d = distance of lever arm

so force available is:

$$f = \frac{150}{2.5} = 3.75\ lbs force$$

Knowing that:

$$f = ma$$

where: m = mass
a = acceleration

then the maximum acceleration able to be applied to the example system is only about 1.75 in/s^2. High-speed set point motion of heavy components requires large accelerations at the beginning and end of motion. The low acceleration force available effectively prevents high-speed set point motion of system components. This limitation will become important when examining scanning techniques in Chapter 3. However, the constraints on possible sensor acceleration due to the limitations of low-noise drives are evident.

2.3 **Transducer size and frequency limitations.**

For a through transmission ultrasonic tire scanner to detect small defects, the transducer resolving capability is a penetrating issue. As previously noted, transducer size, frequency, and focusing influence the resolving capability of a transducer. While PZT ultrasonic transducers are commercially available in a large variety of sizes, frequency ranges, and wave mode generating capability (pressure or shear wave discussed later), additional limitations are imposed on transducer size and frequency by the inspection to be performed. This section discusses the sound field characteristics of flat and focused circular, immersion type transducers as used for this inspection.

Figure 2.2 shows a simple diagram of a circular flat transducer. The central axis is defined as a line down the center of the transducer extending out in front of the transducer. The face of the transducer that emits the ultrasound pulse is referred to as the radiator for modeling purposes. The diameter of the radiator face also characterizes the aperture. 'Operating conditions' in the following sections will refer to the size, frequency,

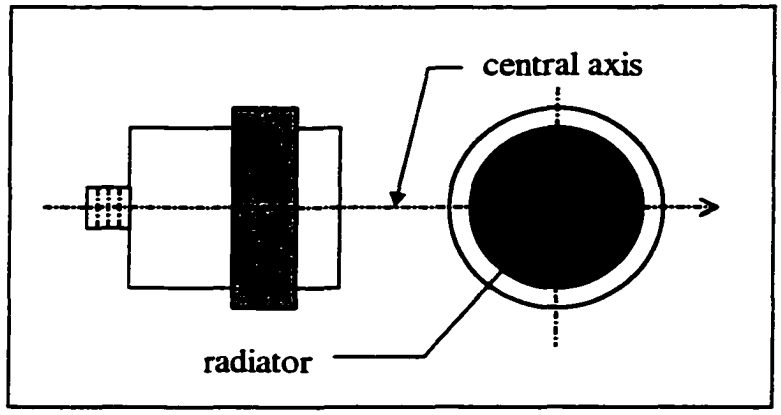

Figure 2.2: Simple circular transducer.

and medium of operation for a transducer. The frequency and medium determine the wavelength as per Equation 1.1.

2.3.1 Sound field physics.

Sound field physics at small wavelength are somewhat analogous to those of optical light fields. The sound beam can be focused, refracted, and reflected. For the range of operating conditions where the wavelength is much smaller than aperture, such as 1:100 wavelength/aperture ratios, geometric optics will serve for a description of the sound field propagation from an orifice, slit, etc. However, at lower frequencies or smaller apertures where the wavelength is closer to the aperture size, diffraction effects begin to dominate the wave field [Kra90]. The diffraction effects are still similar to those of optical light fields but geometric optics are no longer sufficient for characterization of the sound field.

2.3.1.1 Axial pressure distribution.

A circular flat radiator generates pressure waves in front of the face by planar displacement of the surface. Typically the diameter of the radiator will be close to the

wavelength in the medium. For instance, 0.5 MHz ultrasound in water has a wavelength of approximately 0.143" so a 1.5" transducer is only about 10x the size of the wavelength. Diffraction phenomenon occurring in front of the radiator face cause an interference pattern that dominates the sound field in front of the radiator. Waveforms in front of the radiator face can be developed generally by applying Huygens principle for most simple cases [Kra90]. For ultrasound generation from a flat circular radiator, interference in front of the radiator causes a series of maxima and minima in the sound pressure along the central axis of the transducer. The location of the last maxima at a distance *N* from the face of the transducer is known as the near field distance and is the natural focus of the transducer shown in Figure 2.4. The location of the maxima and minima can be calculated by [Kra90]:

$$p = \left| p_o \, 2 \sin\left(\frac{\pi}{\lambda} \left\langle \sqrt{\frac{D^2}{4} + a^2} - a \right\rangle \right) \right| \qquad (2.1)$$

where:

p_0 = *initial acoustic pressure, (usually* $p_0 = 1$*)*
λ = *wavelength*
D = *diameter of radiator*
a = *distance along central axis*

Figure 2.5 shows pressure maxima and minima values, moving away from the face, for a sample 0.5 MHz, 1.5" transducer diameter. Pressure is normalized so $p_0 = 1$ in Equation 2.1. The transducer face is taken to be at position 0 at the origin of the graph. A series of maxima and minima occur moving away from the axis due to interference effects until a final maximum is reached at N. The point N determines the near field distance or natural focal point of the transducer. The distance N can be calculated by [Kra90]:

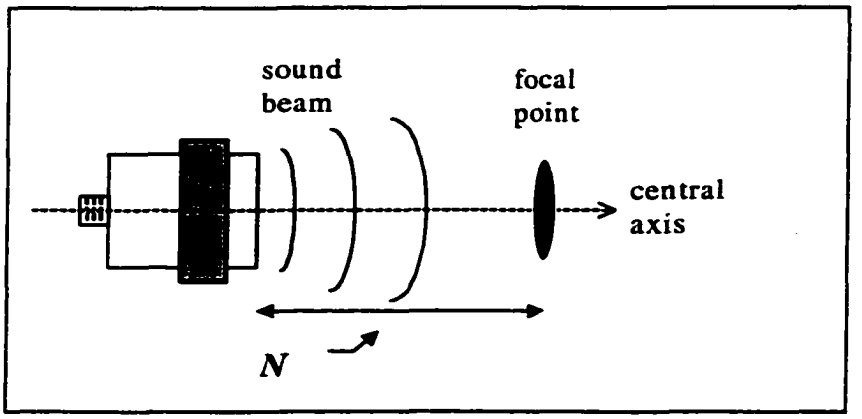

Figure 2.4: Near field distance *N*.

$$N = \frac{D^2 - \lambda^2}{4\lambda} \tag{2.2}$$

The natural focus is a result of diffraction effects caused by the long wavelength and small relative aperture. An additional result of the long wavelength and small relative aperture is the long depth of field or 'focal zone'. If the half-power point is defined as a pressure of 1.5 in Figure 2.5, the depth of field is a relatively long 15 cm or almost 6" (for a flat transducer operating in water).

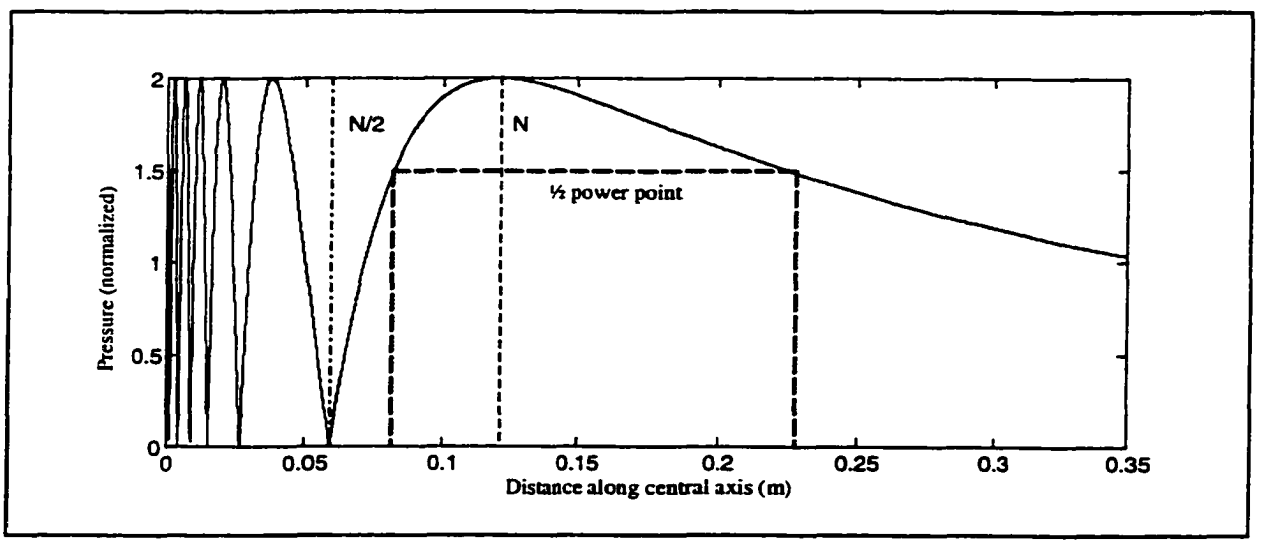

Figure 2.5: Acoustic pressure along central axis, flat transducer.

Focusing the sound beam can achieve higher sound pressure along the central axis and reduces the spot size during transmission. The higher pressure and smaller spot size contribute to increased sensitivity to small flaws since a greater percentage of the total sound energy transmitted will be concentrated and reflected from a small flaw. A curved radiator or a contact lens on a flat radiator are two methods of achieving a fixed focus. A contact lens is constructed of a material that causes little attenuation of the ultrasound beam. The lens must also be acoustically matched to the inspection medium, flat on one side for contact with the transducer face, and spherically curved on the other to focus the ultrasound beam. For a focused transducer the regions of maximum sound pressure in front of the transducer are given by [Kra90]:

$$p = p_0 \left| \frac{2}{1 - \frac{a}{r}} \right| \left| \sin\left[\frac{\pi}{\lambda} \left(\sqrt{(a-h)^2 + \frac{D^2}{4}} - a \right) \right] \right| \tag{2.3.1}$$

$$h = r - \sqrt{r^2 - \frac{D^2}{4}} \tag{2.3.2}$$

where: r = *radius of curvature of the radiator.*

Figure 2.6 shows an example of how focusing affects the near field and maximum power of the acoustic beam. Figure 2.6A shows the sound pressure moving away from the radiator face for a 1.5" diameter flat transducer operating at 0.5 MHz and is equivalent to that shown in Figure 2.5. The maximum sound pressure is 2 times the mean pressure. Figure 2.6B shows the sound pressure along the central axis for a similar transducer focused at 2.25". The focused transducer exhibits maximum sound pressure almost 8 times the mean enhancing the ability of the transducer to insonify a small part of the inspection zone.

The focal zone is located along the central axis between the points where the acoustic pressure drops by -6dB (half-power) from the pressure at the focal point. Figure 2.5 shows the location of the half-power or focal zone for the flat transducer. In Figure 2.6B, the maximum pressure is about 7.5 so the –6dB points would be where the pressure drops to one-half that or 3.75. The pressure is above 3.75 between 0.03 m to 0.1 m so the focal zone is located and about 7 cm long. The length of the focal zone can be estimated by [Pan95]:

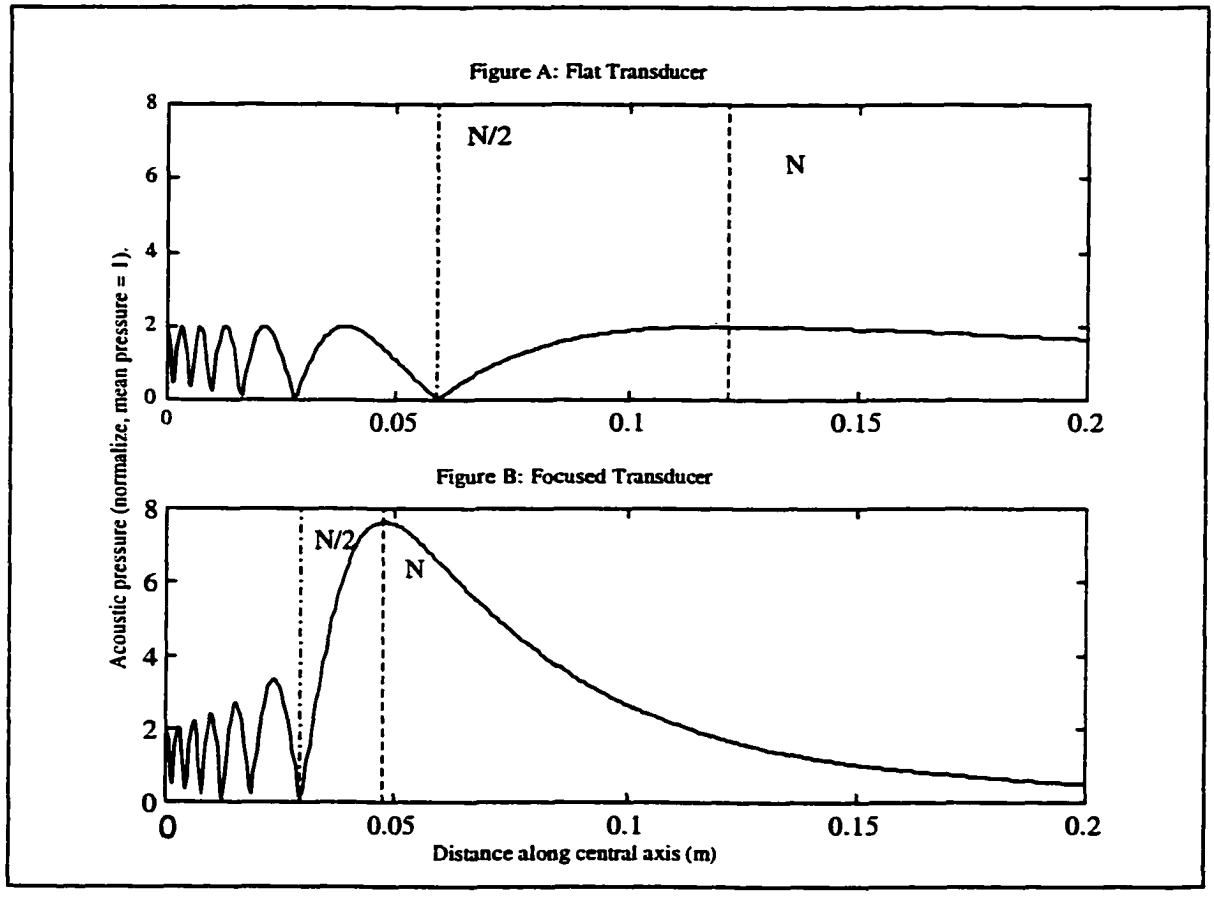

Figure 2.6: Sound pressure along central axis; flat vs. focused transducer.

$$F_z = NS_F^2\left[\frac{2}{(1+0.5S_F)}\right] \tag{2.4}$$

where: F_z = *length of focal zone*
N = *near field distance from Eq. 2.2*
S_F = *normalized focal length* = $\frac{\text{focal length}}{N}$

With focused transducers, the beginning and end of the focal zone usually must be determined iteratively using Equations. 2.3.1 and 2.3.2 [Kra90]. The long length of the focal zone is critical in this application for high-speed inspection to be possible.

There are tradeoffs associated with focusing. Comparison of Figures 2.6 A and B clearly show that the location of the near field is shifted closer to the radiator face. In addition, the length of the maximum pressure field is shortened. The interference fringe generated in the near field classically prohibits its use for effective measurements and most measurements will be made using the far field after the *N/2* point [Kra90].

2.3.2 **Lateral pressure distribution (transducer spot size).**

The size, wavelength in medium, and focusing also determine the beam diameter of a particular transducer. The 'spot size' of the transducer describes the beam diameter in the lateral direction away from the central axis where the acoustic pressure has not been attenuated more than -6dB. Figure 2.7 shows a cross section slice, rotated out of plane, at some distance away from transducer face greater than the near field distance. The cross section slice shows concentric rings with the area of maximum acoustic pressure in the center. Moving laterally away from the central axis, the sound pressure drops until an attenuated region –6dB point is reached.

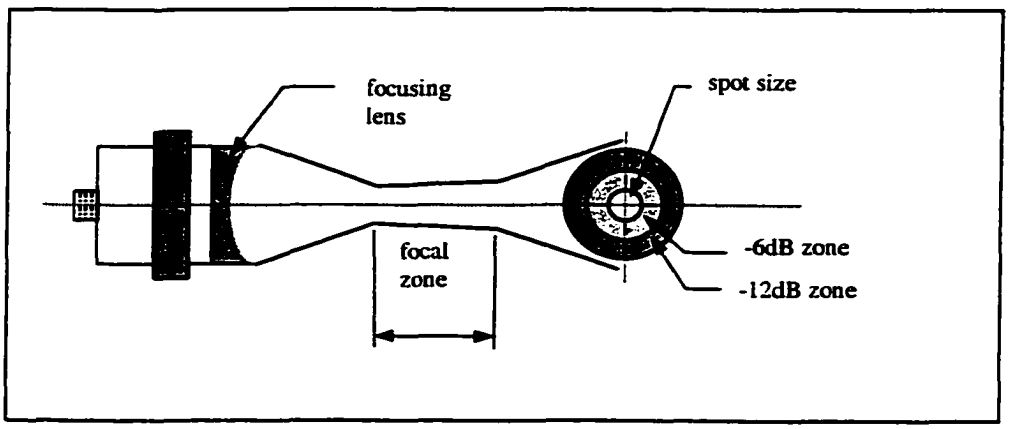

Figure 2.7: Focused transducer spot size.

The sound pressure distribution moving away from the central axis is also a series of maxima and minima, arranged in concentric rings as in Figure 2.7, and can be calculated with a simple model for a focused transducer from [Kra90]:

$$p_t = \left| p_{\max} \frac{2J_1(x)}{x} \right| \tag{2.5.1}$$

$$x = \frac{\pi D q}{\lambda} \tag{2.5.2}$$

where: p_t = *pressure transverse to the central axis*
p_{max} = *maximum sound pressure at axis from Eqs. 2.3.1 and 2.3.2*
q = *distance at right angles to the central axis*
J_1 = *first order Bessel function*

This relationship describes the point spread function (PSF) of a transducer and will be examined in detail in Chapter 4. The spot size of a spherically focused transducer can be estimated by [Pan93]:

$$BD_{(-6dB)} = \frac{1.028Fc}{fD} \tag{2.6}$$

where: F = *focal length*
f = *frequency*
c = *sound velocity in transmission medium*
D = *diameter of transducer*

The spot size for the 1.5", 0.5 MHz transducer transmitting in water is estimated using Equation 2.6 to be $BD_{(-6\,dB)} \approx 1/6"$.

2.3.3 **Transmitter–receiver reciprocity.**

The previous sections describe the axial and lateral pressure distributions due to interference effects moving away from the radiator face for flat and focused ultrasound transmission. From the distributions, there is a relatively cylindrical region in front of a flat transducer where the sound pressure is 1.5→2 times the value of the ambient pressure. In front of the focused transducer, there is a region 3.75→7.5 times the ambient. Focusing the transmitter delivers greater power to a smaller area. During pulse-echo inspection, the increase in power delivered to a small area enhances the ability of the transducer to detect small flaw by reflection of the more powerful beam. Because of this, the focused transducer is more sensitive to small flaws.

The sensitivity of the flat and focused transducers when operated as a receiver is important. Krautkramer states that according to the reciprocity theorem, a flat transducer operated as a receiver has the same sensitivity in reception as the transmission beam field described earlier. Due to reciprocity, the receiver characteristics equal the transmitter characteristics [Kra90]. This implies that within the confines of the focal zone and spot size, the flat transducer is up to 2 times as sensitive to detecting ultrasound as outside the zone.

The same reciprocity relationship should hold for focused transducers. This implies that a focused transducer operated as a receiver will be 4 times as sensitive as a comparable flat transducer. There is very little literature discussing reciprocity relationships for focused transducers suggesting this field may be ripe for investigation.

However, in preliminary tire scanning research prior to this effort, Rogers used flat receivers during initial efforts [Rog91] He later switched to focused transmitters and receivers noting the increased sensitivity during reception [Rog92]. Achenbach extended the preliminary results of Rogers using flat transmitters with focused receivers and notes that Rogers preliminary work indicated that the small beam diameter associated with focused receivers increased sensitivity to small flaws [Ach94]. Achenbach also demonstrated flat-vs.-focused receiving transducer characteristics obtained by pulse-echo scanning that supported the focused receiver reciprocity concept.

While the reciprocity relationship for focused transducers has not been thoroughly established, the relationship is ultimately unneeded for this work. Experimental recovery of the system PSF for deconvolution obviates the need to establish reciprocity. Regardless if reciprocity is correct, the actual sensitivity of the system to flaws can be well established after a particular scan has been performed.

2.3.4 **Transducer operation.**

Commercial ultrasonic transducers use piezo-electric ceramics to generate finite length ultrasonic pulses. The most common piezo-electric material used for ultrasound generation and reception is lead zirconium titanate (PZT) [Kra90]. PZT transducers are commonly available and the system design uses only PZT transducers. The inverse piezoelectric effect is used to generate the ultrasonic wave. When an electric potential is applied to opposite faces of a piezoelectric disk, deformation occurs [Kra90]. Figure 2.8 illustrates deformation of a PZT disk when electric potential is applied to faces of the disk. The thickness of the disk will determine its natural frequency of vibration. For natural crystals such as quartz, the direction it is cut and then coupled to a material will

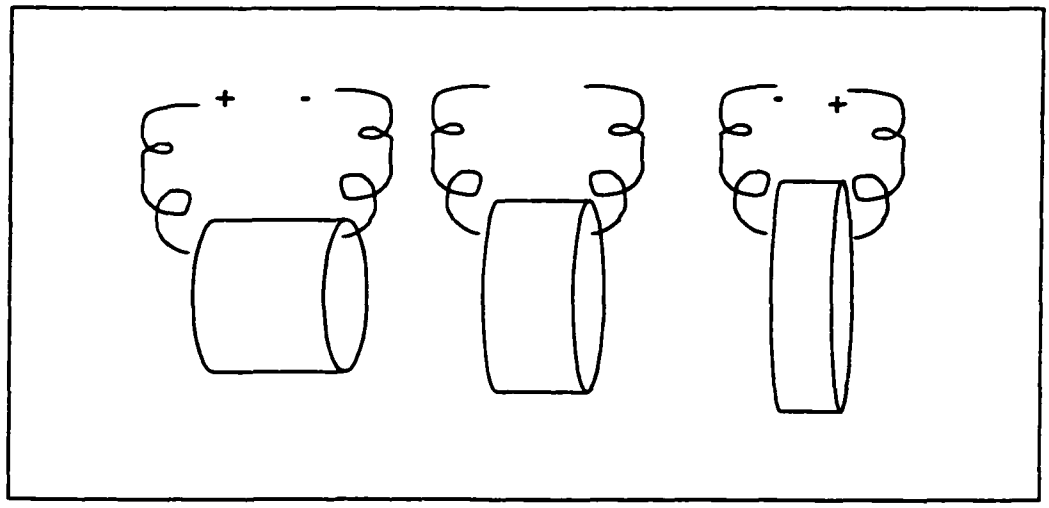

Figure 2.8: PZT displacement with electric potential applied.

determine whether pressure or shear waves are transferred to the material. Longitudinal motion with respect to the material generates pressure waves and transverse motion generates shear waves in the material. Piezo-ceramics are polarized during manufacture to set the direction of contraction when excited. After polarization the ceramic is oriented like a natural piezo-electric material so the excitation axis generates the desired wave type in the material.

Ultrasound is generated by single or repeated contractions of the PZT disk. To contract the PZT disk, an electric potential in the form of a voltage pulse is applied to the disk. The voltage pulse duration is limited to less than one-half the natural frequency period of the disk. Repeated excitation at the natural frequency will set up continuous ultrasound generation. However, pulse excitation is typically more advantageous for the detection of flaws within materials when echoes or signal attenuation is the desired result. Due natural harmonic resonant frequencies and to transient conditions set up in the disk at the beginning and end of the excitation pulse, a small range of frequencies is generated. The frequency bandwidth is adjusted by mechanical and electrical tuning or

damping. The damping applied determines the length of the generated pulse. Higher damping produces shorter pulses with a broader band signal. Narrow and broadband transducers are available depending on the application. The center frequency of the transducer refers to the average frequency of the transducer spectrum above the –14 dB level [Pan95]. The center frequency is a measure of the transducer's maximum power output frequency.

2.3.5 **Transducer limitations.**

To perform tire inspection with resolution of at least 1/16", the acoustic field must be sufficiently small to resolve characteristics of that size in the tire. In general, as transducer center frequency rises, the resolving capability of the transducer becomes smaller. The center frequency to be used for the inspection is limited to a frequency where flaws are detected but the steel belts within the casing are not. In addition, the physical size of the receiving transducer needs to fit within the tire. Finally, a long focal zone is required so the tire casing need not be a fixed distance in front of the transducer. These design limitations are discussed in the following sections.

2.3.5.1 **Center frequency requirements.**

Rogers [Rog92] has shown that tires can be inspected for disbond and material property changes using through transmission ultrasound imaging. Belt disbonds and material property changes produce attenuation of the ultrasound beam due to reflection at disbonds and material interfaces. Tire inspection can be performed by comparing the relative attenuation of a transmitted elastic wave at different points on the tire. To provide high spatial resolution, a large number of inspection points must be acquired

while the ultrasound beam field must provide sufficient resolution to detect features of interest.

Steel belts in truck tires are typically constructed using twisted steel wire with a diameter of about 1/32" for the twisted strands. To characterize defects in the tire rubber without detecting the steel belts themselves, the spot size must be of sufficient area so the steel belts are not resolved. Rogers' use of 500 kHz ultrasound provides sufficient resolution to detect flaws while not resolving the belt wires [Rog92]. Use of the lower frequency (and subsequent longer wavelength) reduces the attenuation due to scattering from the belt wires. The reduced attenuation increases the signal to noise ratio of the received ultrasonic signal. Alternative inspection methods, in particular x-ray, are well suited for detection of belt wire failure.

2.3.5.2 **Transducer size.**

Transducer size influences the system design. For a through transmission transducer configuration, it is necessary to place either the transmitting or receiving transducer within the tire. Additionally, to inspect the required number of tires, data acquisition must be performed quickly. Sampling two transducers concurrently can halve the inspection time. However, two transducers aimed in separate directions must fit within the tire profile for concurrent sampling.

The selection of 500 kHz center frequency places a practical limit on the transducer element diameter. A small spot size and large depth of field are desired. From Eq. 2.6 it is evident that for a fixed transducer frequency, the spot size diameter can be altered by varying either the transducer diameter or the focal length. Additionally, from Eqs. 2.2 and 2.4, long focal zones require a large diameter element. Since the tire

profile is too small to allow a long focal length transducer, the largest transducer diameter possible must be used for maximum sensitivity, resolution, and depth of field. At the bead, (see Figure 1.2) the smallest truck tire opening is about 4.5". The length of a 1.5" transducer with coaxial cable connector is about 4" which barely fits into the bead opening allowing for a small clearance.

2.3.5.3 **Focal zone requirements.**

The focal zone depth of field determines the transducer proximity and location accuracy necessary relative to the tire surface. The transducer spot size remains relatively constant throughout the depth of field maintaining resolution in the focal zone. Long focal zones are possible due to the long wavelength and relatively small aperture of the radiator surface. If the focal zone is long with a close focal point, the transducer need not be held at a fixed distance from the tire to maintain resolution.

To achieve efficient scanning, it is necessary to simultaneously inspect both sidewalls. A sample transducer configuration for simultaneous scanning is shown in Figure 2.9. The transducers need only be stepped vertically into the tire while taking advantage of the large depth of field. Because of sidewall curvature, the focal zone of the transducers must have a depth of field greater than the depth of curvature of the sidewall. The transducer faces must be less than 4.5" apart to fit between the beads. Using two transducers, the gap between the transducer face and the tire sidewall may be as large as 3 inches. Thus the focal zone of the transducers must be deep enough to remain within the thickness of the sidewall without moving the transducer closer to the sidewall. Ideally, the focal zone for the transducer should extend from approximately 0.25" to more

than 3.0" beyond the face of the transducer to make it possible to inspect both sidewalls without a loss of spatial resolution.

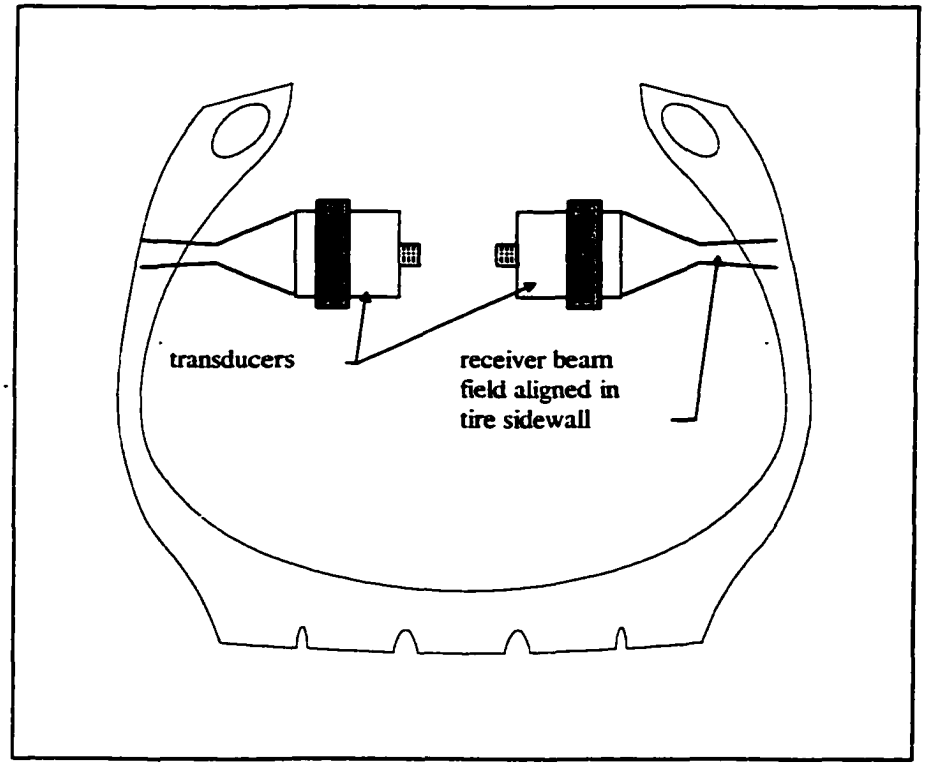

Figure 2.9: Concurrent inspection with two transducers.

2.4 High resolution large area tire scanning.

Previous tire inspection methods discussed in Chapter 1 inspected the tire at low resolution and accomplished only partial inspection of the tire. The complex shape and/or limitations in the number of transducers used prevented scanning the full tire. Additionally, large immobile transducer arrays are inherently unable to inspect every portion of the tire at high resolution due to their physical size. However, high resolution is necessary for detecting small flaws within the tire. Small flaw detection depends on scanning many points in close proximity where, ideally, the step size between scan points is less than the resolution of the receiver.

The tire surface area is large in comparison with the small step size desired during inspection. Large data set data acquisition is necessary to provide high resolution over the large surface area. The surface area of a standard 42" diameter truck tire is over 3200 sq.in. (22 sq.ft.). A tire inspection with 1/8" resolution produces over 200,000 data points. (Inspecting at 1/16" resolution produces over 800,000 data points.) Inspecting this large surface area in near real time results in very high I/O demands on the system design. For an 8 minute scan time, data must be acquired at 2.4 ms intervals (about 420 Hz). This data acquisition rate is not high. However, hardware control and data processing with display must occur concurrently.

2.4.1 **Real time data acquisition and control.**

The complex tire shape presents a surface that cannot be covered using a planar *xy* coordinate scan. Inspection of the tire surface requires 3 axis motion. The motion of each axis needs to be coordinated with the data acquisition. A number of scanning techniques are possible. The worst case design would require the sensor system and/or tire to be repositioned after each data point was acquired. Traditionally, asynchronous interrupt handling would be used to acquire the data and move the sensors. If an interrupt were generated at each data position, a simple program could execute the data acquisition and move the sensor in preparation for the next data point. However, assuming an average interrupt handling of 100 μS was possible, data would then need to be acquired after an interrupt and a move made before the next target point. Table 2.1 shows typical times required for the CPU to perform each task required in a single CPU control system.

Theoretical Data Acquisition and Control	
Task	**Time (s)**
position interrupt	0.0001
data acquisition	0.0001
move sensor (CPU time only)	0.001
Total	**0.0012 s**

Table 2.1

The estimate of CPU response time is based on simple algorithms implemented on an Intel 80486 PC running at 120 MHz. While the time for the system to actually move is excluded, over half of the allowable time is used in data acquisition and the processing of move commands. With additional processing needed and display required data acquisition and control is not possible in the time available.

2.5 ISA bus limitations.

In addition to the timing problems, the PC ISA bus itself poses additional real time control constraints. PC's add functionality to the computer system by adding additional peripheral control through the use of serial line controlled hardware, parallel port controlled hardware, or in particular, plug in cards that are inserted internally into the PC ISA bus. While the PCI (Peripheral Component Interconnect) bus is rapidly becoming standard, nearly all data acquisition cards, and motion control cards (during this development, 1995-97) use the older ISA (Industry Standard Architecture) bus. Adding functionality by using the ISA bus dramatically increases the CPU workload. The ISA bus standard was set by IEEE to run at an 8 MHz clock rate [Gil94][Nat97].

However, given CPU cycle times for all operations, it is difficult to provide closed loop control across an ISA bus above 1000 Hz. The 1000 Hz implies only 1 ms for a closed loop interrupt latency and handler.

In 1989, with slower computers, closed loop control was performed at only 100 Hz with a "high-speed" controller at 250 Hz requiring special coding for efficient software [Bol89]. This has changed somewhat with a common industry 'yardstick' to assume 500 Hz control is possible and speeds greater than 500 Hz will require special coding. Single I/O execution speed for an 80486-25 MHz computer was benchmarked at 0.2 ms for one analog I/O operation without closed loop control of the output [Lof93]. Update times for closed loop control range as high as 100 ms [Lof93]. A review of commercially available real time operating systems (RTOS) timer resolutions show 1 ms resolution to be normal [Lan96]. The resolution of the RTOS timer sets the upper frequency of handling at 1000 Hz. From the previous discussion it is evident that 500 Hz is barely fast enough to run the proposed system and offers no additional time for processing and display. Nearly all of the available processor time would be used for data acquisition in the single processor configuration.

An alternative to real time closed loop data acquisition and control by a single processor is to design a multi-processor system. In a multi-processor system, sub-systems are individually controlled by an embedded processor to perform various functions such as motor control and data acquisition. A new approach to tire scanning hardware using the multi-processor concept is presented in the next section.

3. Development of a Large Scanned Area, High Resolution, Ultrasonic Scanning System.

The previous chapter described some system requirements for a large area, high resolution, tire scanning system. The constraints on the system must be overcome while remaining cost effective. This chapter describes a series of design compromises that allow the system to satisfy design objectives and to overcome the constraints.

This chapter presents an overall system description and descriptions of independent subsystems. The first section presents solutions to the low noise drive problem and concurrent data acquisition and control. The second section covers the theory of operation for the ultrasonic system, motion control, and data acquisition systems. A description of the hardware used is covered followed by an examination of control flow for inspection. Finally, examples of data and control display systems are shown with experimental data showing some results from the use of the tire inspection system.

3.1 Tire sizing and inspection description.

To describe the inspection operation a tire coordinate system is used to estimate sensor head motion during inspection. For the coordinate system to be generally applicable, all tires should be able to be mapped into the system using only the tire size. The inspection procedure itself is detailed showing how a tire is inspected using circumferential scanning. Section 3.2.1.1 shows how circumferential scanning

overcomes the constraint of using low noise drives. A new approach to large data-set, data acquisition and control is discussed for this application.

3.1.1 **Tire profile and size.**

Tires can be characterized by their cross-sectional profile. The tire size itself provides a set of descriptors for the tire profile. For example, the tire size **275/80R22.5** provides the following information shown in Figure 3.1. The cross section width is 275 mm, the height is 80% of the width, and the tire rides on a 22.5" rim. Mixing Metric and common English units is common in the tire industry and remains unexplained. If the aspect ratio is not listed the tire is assumed to be 100%. For example, tire size 10.0-22

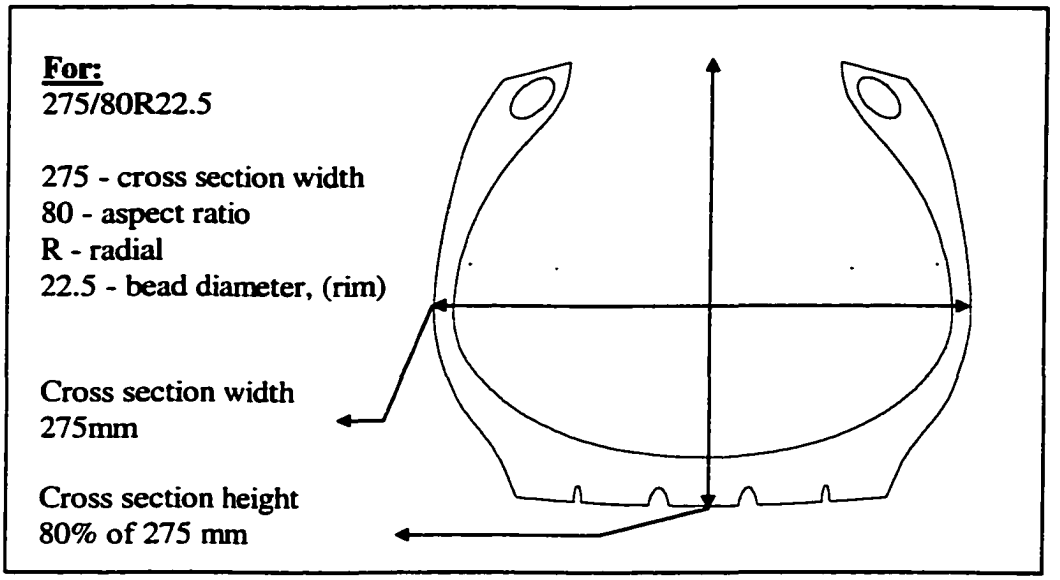

Figure 3.1: Tire sizing.

has a 10" height and width on a 22" rim. Table 3.1 shows a set of common truck tire sizes that will be used for further development later.

Table 3.1 Tire sizing.

Tire Size Table			
Tire size	**Rim diameter (in)**	**Height (in)**	**Width (in)**
8R17.5	17.5	8	8
10.00-20	20	10	10
11R22.5	22.5	11	11
295/75R22.5	22.5	8.71	11.61
275/80R22.5	22.5	8.66	10.83
285/75R24.5	24.5	8.4	11.22
275/80R24.5	24.5	8.66	10.83

3.1.2 Using the coordinate system.

A cylindrical coordinate system, described in the Appendix, is used to locate points defined on the tire and determine the motion profile for the sensor head to cover all parts of the tire. Truck tires typically have a 42" outside diameter at the tread. The circumference of the tire is about 132". Inspecting at 1/8" resolution would require 1,056 data points around the tire. Inspecting at 1/16" resolution would require 2,112 data point. However, the resolution of the system will not be changed drastically if 2,048 points are used instead of 2,112. 2,048 resolution was chosen since encoders with 2^n resolution are readily and cheaply available. It is also a simple matter to convert from 1/16" to 1/8" or 1/4" resolution using multiplication and division by 2. In the coordinate system, it is necessary to define an angle relative to a starting point. With 2,048 separate points arrayed on a 360° tire, it is convenient to think of the location as a number between

0→2048 instead of an angle in degrees. A simple conversion can give the angle in degrees if necessary with:

$$\alpha = \frac{num}{2048} 360$$

where: α = *angle in degrees*
num = number of points around tire (ex: 496)

Any point on the tire can be described by using the (r, θ, z) coordinate system. The coordinate system is also used to determine the motion of the sensor head for each tire size as described in Section 3.2.2.

3.1.3 **Solving low noise drive limitations.**

Low noise drive limitations were discussed in Section 2.2. In particular, system throw weight is severely constrained because relatively inexpensive low-noise drives are not capable of developing a large torque. There are two methods of inspection available for examination.

The first method is to raster scan the tire where the tire is held fixed while the sensor head scans over the tire profile. The tire is then moved one step (1/16") and the sensor head scans the profile again. Repeating the scan around the entire perimeter will produce a complete inspection. There are drawbacks to this method. In particular, to scan 2048 separate profiles in 8 minutes implies 0.23 seconds per raster scan. Assuming the scan can be made with a single pass reading two transducers concurrently over a 16" path implies the sensor head needs to move at over 5 feet per second. One limitation of the drive was the low force available for acceleration. It is not possible to accelerate a sensor head to 5 ft/s and stop it again in 0.23 seconds. In addition, moving the huge rotary inertia of the tire and stopping it within the same time is difficult.

The second method for scanning is to perform a perimeter scan with the tire spinning constantly and the sensor head stepping after each revolution to scan a new perimeter. This method has tremendous advantages over the raster method. The tire can be set in motion and need only be kept at speed so controlling the rotary inertia during start-stop motion is not a factor. Incrementing motion of the sensor head need only be done over 1/8" (or 1/16") step sizes reducing the travel required of the sensor head.

It should be noted that previous systems have employed both techniques for inspection and the most recent system built by Technics (discussed in Chapter 1) uses a combination of raster and tire spinning. One problem with this is that the scan does not cover the entire surface but instead runs a sort of zig-zag pattern over the tire tread. The zig-zag pattern occurs when the tire is spun while the transducer is moved at the same time, much as a sewing machine produces a zig-zag pattern on cloth.

For this system, the perimeter scan shows additional benefit because it has low requirements for motion control. Instead of the high speeds, and high torque control necessary with raster scanning, the sensor head motion needs to be accurate and repeatable over very short distances. Figure 3.2 shows tire perimeter scanning. The tire is set into motion and a speed controller holds the speed relatively constant. If an encoder is attached to the shaft, precise position of the tire is known and the speed need not be controlled with high accuracy.

3.1.4 **A new approach to large-data set, real-time data acquisition and control.**

Large-data set, real-time data acquisition and control has traditionally implied expensive hardware such as VXI bus products [Nat97]. The advent of relatively inexpensive data acquisition and control plug-in cards for PC compatibles has spawned a

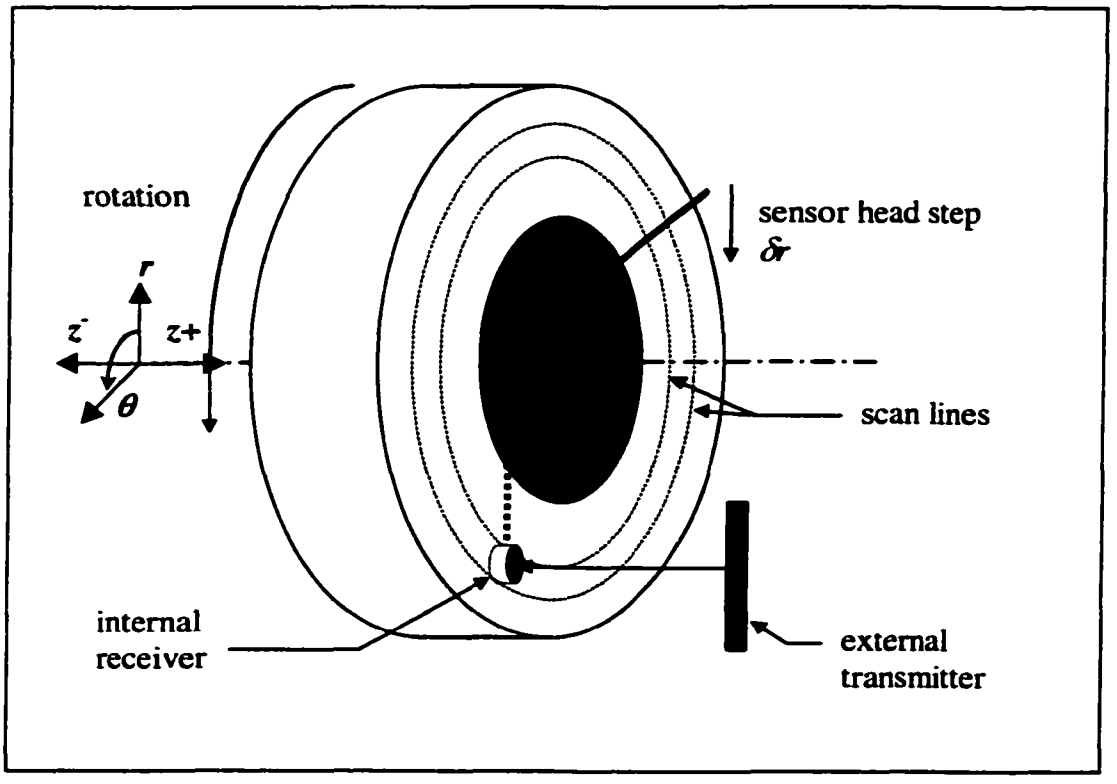

Figure 3.2: Tire perimeter scanning.

new era in non-destructive evaluation systems [Jac93]. It is a simple matter to plug in a data acquisition card and almost immediately begin taking data [Mar93][Jac93]. However, use of typical laboratory data acquisition cards means using them to sample a single waveform at moderate to slow speed for later analysis. The same is true for a simple plug-in I/O board. Using simple boards requires the host PC to continually provide commands for data-acquisition or I/O.

Limits to the speed of transfers across a PC ISA bus were discussed in Chapter 2. The large data set and concurrent control required by the scanning system places high demands on ISA bus closed-loop control. To overcome the ISA bus limitations, the system is designed using a series of embedded processors and separate digital intercommunication lines to relieve the host PC from complex data acquisition and control in real-time.

An embedded multi-processor system uses separate processors for each general category of tasks necessary for system operation. By decomposing the tasks, each processor is accountable for only its specific task. In this design there are several task subdivisions:

1. Motion control.
2. Data acquisition.
3. Display of data.

It is possible to dedicate at least one embedded processor for each area. The host PC then need not concern itself with the details of task implementation and deal only with task scheduling. Such a system is easily extensible. Additional embedded processors can be added at will until the task scheduling capabilities of the host are exceeded.

Real-time operating systems (RTOS) that guarantee timely handling of events are designed to ensure timeliness by using a small kernel with programmable task scheduling properties. The small kernel prevents undue time and memory use by the operating system while most I/O functions are run as tasks instead of being embedded in the kernel. The task scheduling properties available are typically: defining tasks (processes), setting a priority for the task, and setting the amount of time a task can maintain control of the CPU [Cra97]. Windows NT has been shown to be an appropriate RTOS when configured properly [Car97]. One commonly used RTOS is iRMX from Intel. A single license for one '486 PC machine was over $4000.00 in 1993 [Irm93]. Other RTOS's such as QNX are similarly priced. To avoid the high cost of purchasing an RTOS, the embedded processor approach coupled with Windows NT was adopted for the system control design. In this way, Windows NT is used to mimic an RTOS by scheduling tasks

as needed to perform the inspection. Timely handling of events is handled below the main operating system level.

Real-time, multi-tasking operating systems are used on all embedded processors to provide real-time handling of asynchronous events. In the inspection system, almost all data-acquisition and control needs to be handled asynchronously. However, this new approach to handling asynchronous events by embedded CPU's can be expensive since several embedded processors need to be purchased. Embedded processors for this application cost $1,700.00 for the data acquisition board and $2,600.00 for the motion controller. However, the benefits far outweigh the disadvantages. One single processor does not need to handle all data acquisition, control, and display. Capacity can be added at will by adding more embedded processors until the I/O port limit or the task scheduling capability of the main CPU is exceeded. While the embedded processors are expensive, the use of Windows NT instead of an expensive RTOS helps negate the expense.

3.2 **Theory of Operation.**

This section details the operation of each subsystem. Three subsystems are covered:

1. Ultrasonic system.
2. Motor control system.
3. Data acquisition system.

A section presents the hardware used to implement the subsystem design and a section on the Master Control Program (MPC) presents how the subsystems are governed. A short section provides an overview of the Display system.

3.2.1 **Ultrasonic system.**

Section 2.3 presented size and frequency limitations applied to the transducers. Using relatively low frequency 0.5 MHz transducers made necessary the use of the largest possible transducer to reduce the spot size. 1.5" transducers are the largest possible that will still fit within the tire inside profile and are still easily obtainable. Section 3.1.4 showed that using a perimeter scan while stepping the sensor head met the requirement resulting from using low noise drives.

3.2.1.1 **Covering the entire tire.**

To make the perimeter scan most effective, several sensors should be sampled concurrently. Section 2.3.1 demonstrated the large depth of field available by proper transducer selection. The depth of field can be used to great advantage for concurrent scanning. Figure 3.3 shows a simple example of the first step in concurrent scanning. In

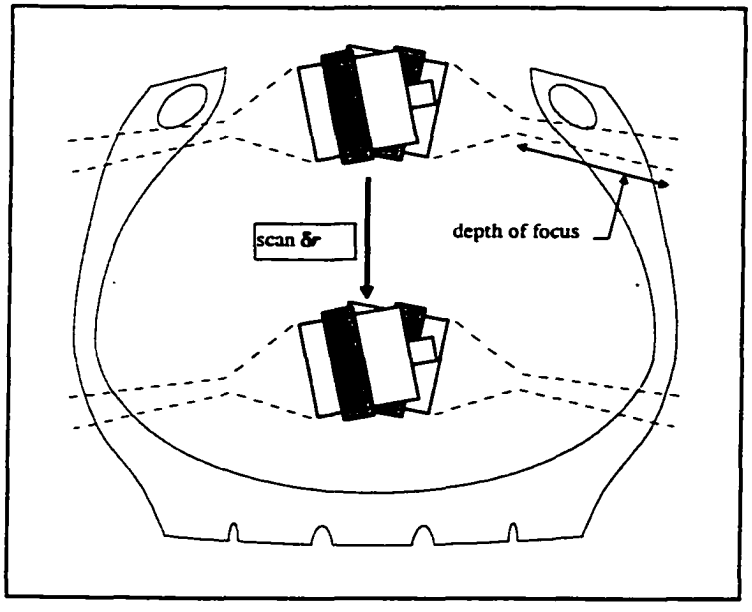

Figure 3.3: Concurrent sidewall scanning.

the figure, two transducers are used to look at both sides of the tire at the same time. Stepping the transducers along the *r* direction while performing circumferential scans allow the scan to cover all of the sidewalls. The same idea can be used for scanning the crown. Figure 3.4 shows two transducers set up to cover the entire crown of the tire with

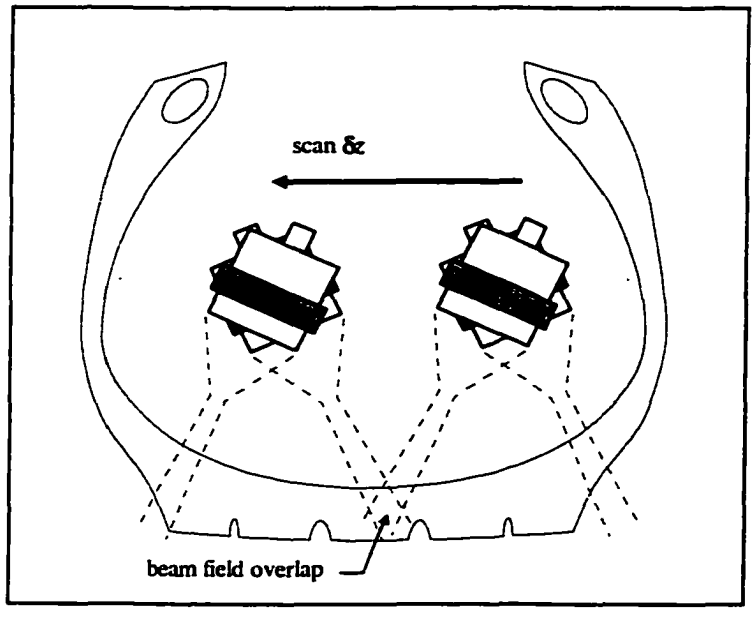

Figure 3.4: Concurrent crown scanning.

one pass. In the figure, overlap of the beam field at the center of the crown is used to ensure that the entire crown is inspected. A combination of the two scanning types is used to ensure complete coverage of the tire during an inspection. Figure 3.5 shows an example of beam field overlap at the shoulder of the tire. Careful selection of the *r* and *z* axis placement and the angles the transducers are mounted at will ensure complete inspection. A sensor head can then be designed, incorporating the overlap idea that uses four transducers lined up in a row along the *z* plane. The head has two sidewall facing transducers arranged as in Figure 3.3 and two crown facing transducers arranged as in Figure 3.4. For through transmission inspection, the receivers inside the tire must

be paired with external transmitters. The receiver and transmitter must have the radiator surface normals parallel and aligned. The external transducer can be similar in design to the internal ones, but they would then need to be moved with the internal receivers to provide continual axial alignment.

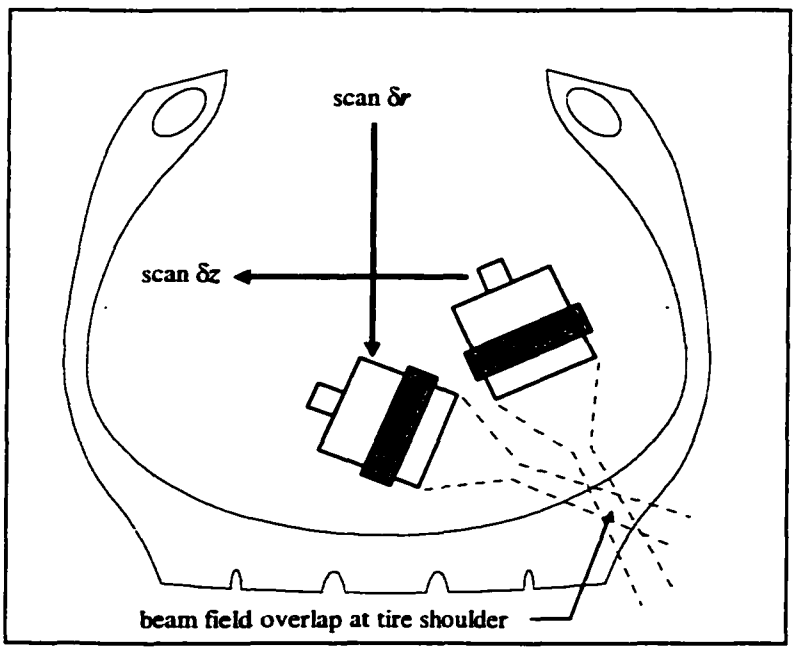

Figure 3.5: Beam overlap at tire shoulder.

To avoid needing to move the external transducers, 'paintbrush' transducers can be used. Paintbrush transducer are constructed using multiple PZT crystals emitting simultaneously through a long rectangular face that is the radiating surface as shown in Figure 3.6. A larger acoustic field is radiated from the face than out of a smaller circular transducer insonifying a large section of material at one time. By pairing one paintbrush transmitter with each internal receiver, the entire tire profile can be inspected with the configuration shown in Figure 3.7. The external paintbrush transducer and its complementary receiver must have their radiator surface normals parallel and the receiver central axis inline with the paintbrush long axis shown in Figure 3.6.

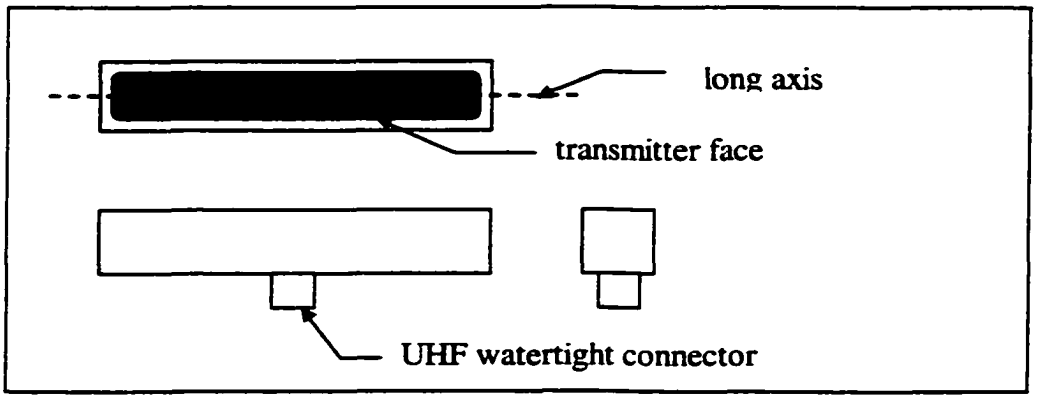

Figure 3.6: Paintbrush transducer.

If the transducers were lined up in a row the sound fields could interfere with each other. To prevent sound field interference and provide clearance in between transducers, each transducer pair is offset from the sensor head centerline. A top view of the sensor system is shown in Figure 3.8 and shows an example demonstrating how the transducers are be offset to prevent interference and provide clearance.

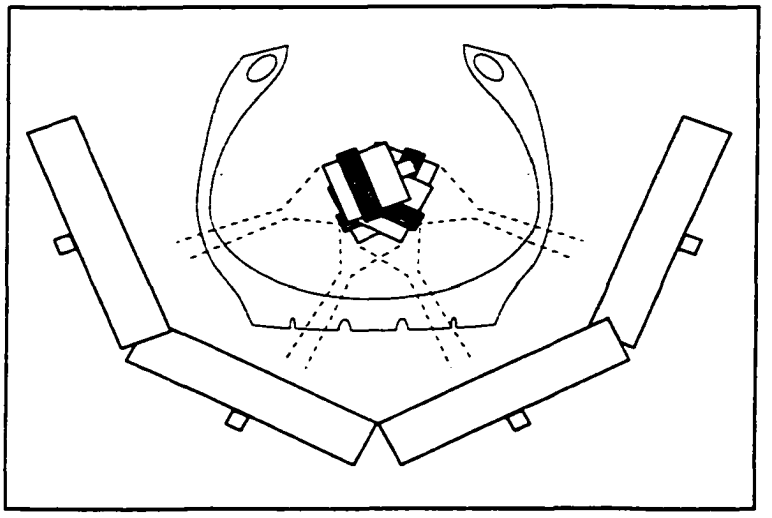

Figure 3.7: Transmitter and receiver setup.

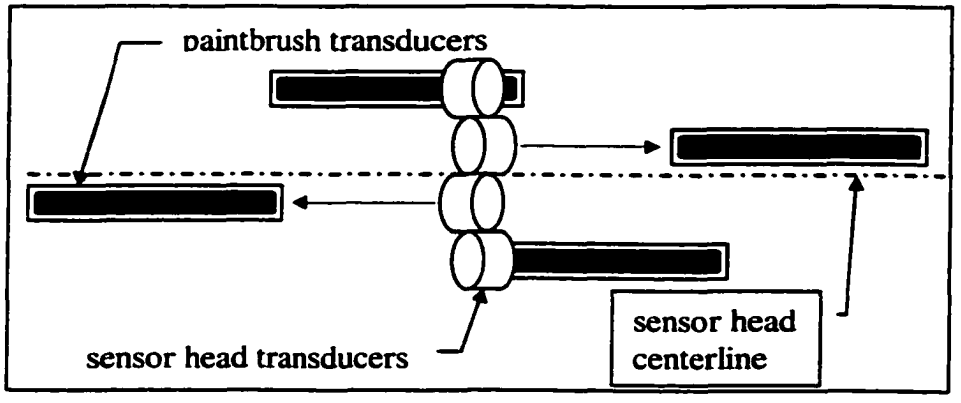

Figure 3.8: Transducer offsets.

3.2.1.2 **Determining sensor head specifics.**

The sensor head angles are determined analytically and confirmed using scale model drawings of the system transducers and representative tires. Identically sized tires do not always have the exact same cross sectional profile after use. The sensor head discussed in Section 3.2.1.1 is large enough to bump into the tire if its motion profile is not characterized properly. The motion profile is discussed in Section 3.2.1.3. However, to prevent unwanted impact of the sensor head with the tire during rotation inspection, an imaginary inspection zone is postulated 1" inside the inner liner of the tire. This is reasonable since the focal zone with highest sensitivity during receiving starts over 1" away from the radiator face and there is no need for the transducers to be closer to the liner. Figure 3.9 shows the inspection line. The transducers can travel only inside the inspection zone. Recalling the tire width w from Section 3.1.2, the width of the inspection zone w_i will be:

$$w_i = w - 2 \tag{3.3}$$

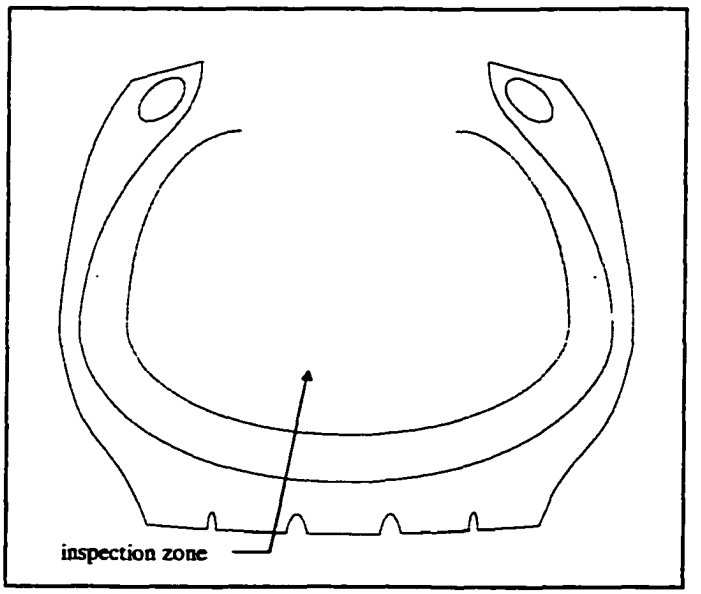

Figure 3.9: Inspection zone.

To inspect concurrently as shown in Figure 3.3, the sidewall receiving transducers must be arrayed about the centerline of the tire with the radiator faces equidistant from the z-plane. Assuming a 4.5 inch maximum bead opening in the tire, the maximum spread, shown in Figure 3.10, on the sidewall transducers must be less to allow the sensor head to fit within the tire. To allow ¼ inch leeway on each side of the transducer head, a maximum spread of 4 inches is allowed when designing the sensor head.

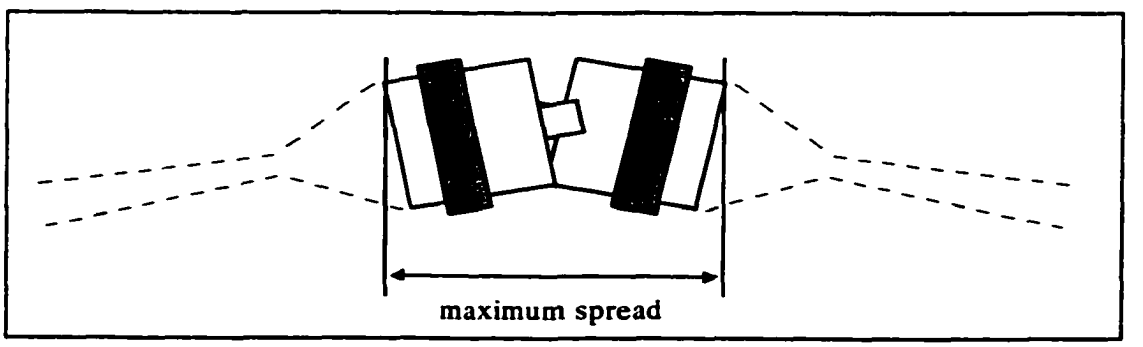

Figure 3.10: Maximum transducer spread.

Truck tires to be inspected have widths of 10 inches or greater so w_i will be greater than 8 inches. The maximum spread of 4 inches leaves 2 inches on each side of the transducer head before the inspection zone border. The transducer head can travel a total of 4 inches along the δ direction without impinging on the inspection zone. It is evident that the full width available should be used for design of a sensor head. Figure 3.11 shows a sensor head that can fit within the confines of a cylinder 4" in diameter.

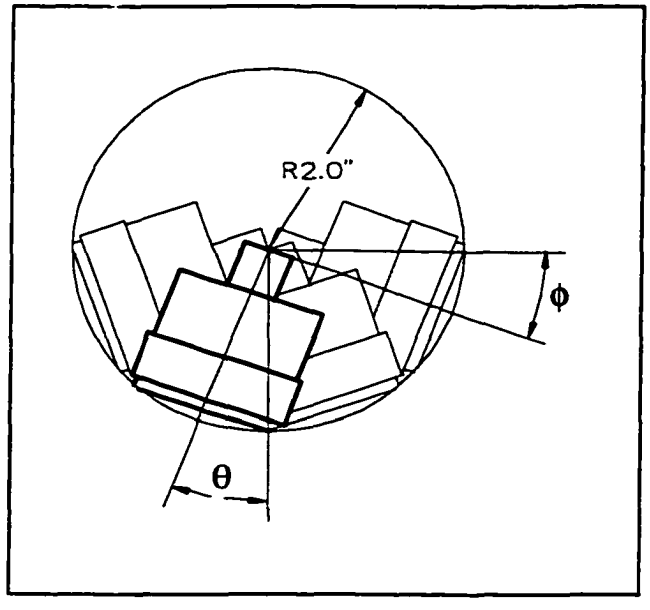

Figure 3.11: Crown and sidewall transducer angles.

The angles ϕ and θ are to be determined to assure coverage of the entire tire by overlap as discussed earlier.

It is noted by observation that the tread width w_t is typically 70-80% of the tire width w as shown in Figure 3.12. The tread width w_t can be used as the limits of the crown transducer inspections. If a sensor head is designed using a cylinder with diameter 4" and transducers arrayed within the diameter as shown in Figure 3.11 the ideal angle depth of focus of the transducer begins at about 2" along the central axis away from the

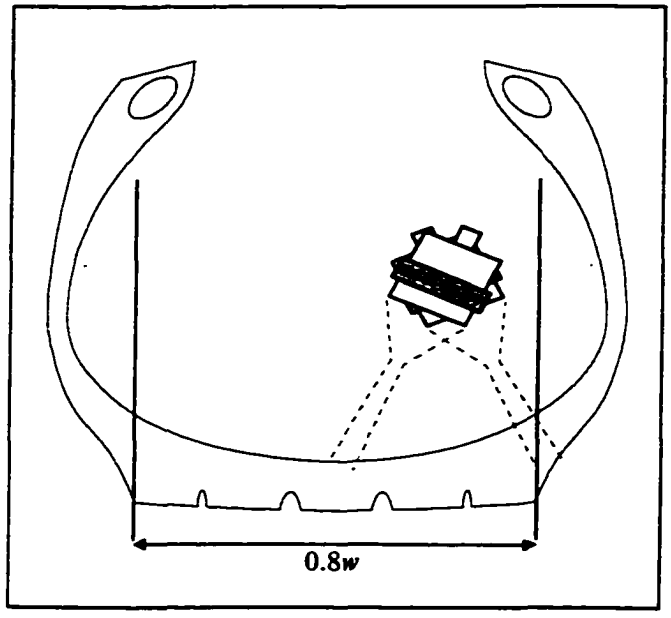

Figure 3.12: Tread width.

transducer face. In Figure 3.13, the total width to be inspected by transducer T_2 during a δz scan is $0.5w_t$. The angle θ can be derived as shown in the figure where the sensor head diameter has radius 2". In the figure it is evident that:

$$0.5w_t = d_1 + d_2 + 2 \tag{3.4}$$

and:

$$\begin{aligned} d_1 &= 2\sin\theta \\ d_2 &\approx d_1 \end{aligned} \tag{3.5}$$

The minimum tire size to be inspected is w = 4.5" (corresponding to a 9-xx tire). Letting the tread width equal 75% of the tire width w_t = 3.375" so:

$$\begin{aligned} 0.5w_t &= 2(2\sin\theta)+2 \\ \sin\theta &= \frac{0.75(0.5w)-2}{4} \\ \theta &\approx 20° \end{aligned} \tag{3.6}$$

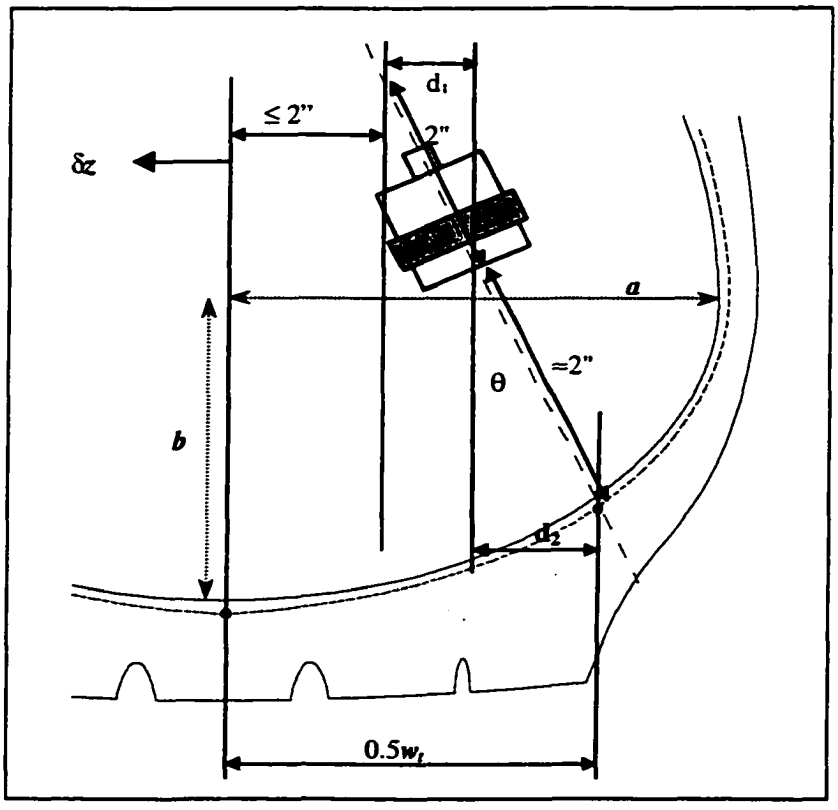

Figure 3.13: Sensor head crown transducer angles

Similarly, the angle ϕ shown in Figure 3.11 can be derived. Figure 3.14 shows the relationship so that using similar constraints:

$$0.5w_t = 2\cos\phi + 2\cos\phi$$
$$\phi \approx 20° \tag{3.7}$$

With the sensor head specifics set, motion of the sensor head to cover all sections of the tire can be determined. Knowing only the tire size, a motion profile can be generated to cause overlap at all sections of the tire profile as covered in Section 3.2.2. The sensor angles calculated here were checked using scale drawings of the components. A sensor head designed to these parameters was drawn and cut out of paper. Tires of several sizes where drawn to scale. The sensor head cutout was placed over the tire and moved along the projected motion path to determine if the angles calculated were adequate.

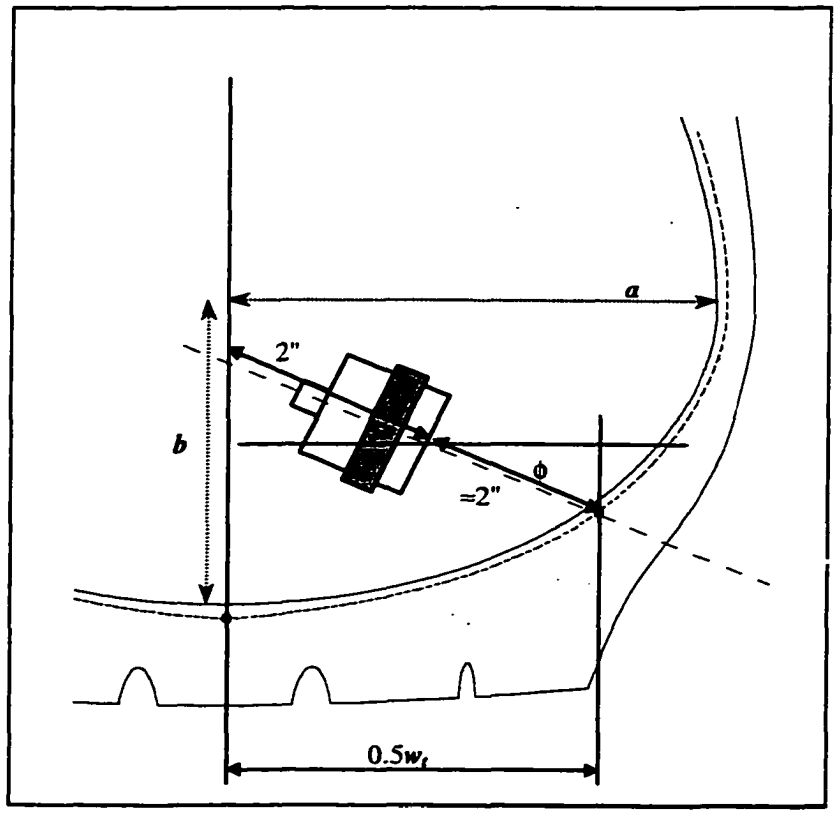

Figure 3.14: Sidewall angle (drawing not to scale).

Results of the analytic calculation and scale model experimentation of the angles show the angles given to be adequate for this type of tire inspection. The angles will be used later for determining sensor head motion to ensure coverage of the entire tire.

3.2.2 Motion Control System.

Motion for a complete inspection is accomplished using three axes. The tire is spun at constant speed along the central axis of the tire. The sensor head is moved in and out of the tire and circumferential scans performed (while the tire is spinning) by motion along the tire coordinate system r and z directions as shown in Figure 3.15. During operation, a tire is held fast at one bead by a mount fashioned to allow access to the tire

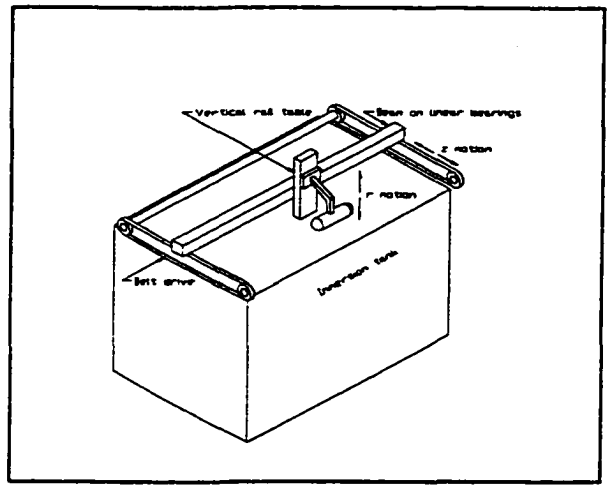

Figure 3.15: Sensor head motion axes.

interior. The mount is fastened to a shaft with an encoder attached to the end. The shaft is held in bearings mounted to a frame on a rotating air cylinder (see Figure 3.16).

Using the air cylinder, an operator lowers the frame to the floor and mounts a tire. The tire is raised and rotated into the tank and lowered onto bearings that hold the mounting shaft. A simple motion profile moves the sensor head into the tire to begin

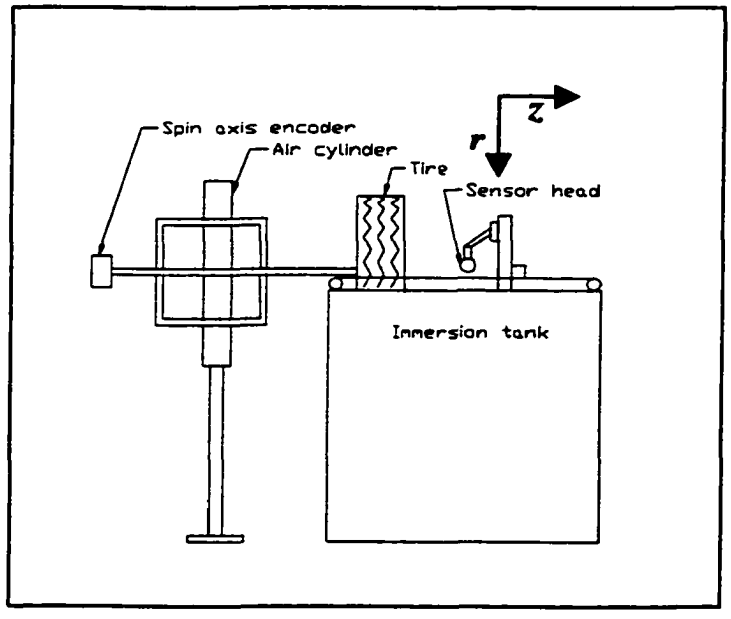

Figure 3.16: Tire mounting in tank.

scanning. During scanning, the sensor head is stepped vertically in the r direction into the tire while circumferential scans are performed on the sidewalls concurrently (as discussed in Section 3.2.1). At the end of the sidewall scans, the sensor head is retracted to cause overlap at the shoulder region and crown scanning begins with the sensor head being stepped in the z directions.

The tire is spun using a DC motor belt drive attached to the shaft. An embedded processor speed controller governs the rotational velocity. During scanning, data is acquired during one complete revolution. The sensor head is stepped during the next revolution and another scan begins at the next 0° point from the encoder.

To assure the entire tire is scanned, overlap points have been defined at the center of the crown and on the shoulder at the tread width extremities. The sensor head motion profile must be developed to force overlap at the points. Figure 3.17 shows the path followed by the sensor head to cause overlap as discussed earlier. The overlap can be calculated using the tire size information, the tire coordinate system developed earlier, and the sensor head path shown in Figure 3.17. Figure 3.18 shows a diagram of a sample sting holding the sensor head at the start of a scan at the bead.

All locations in or on the tire can be described in the r,z,θ coordinate system introduced earlier. Sensor head motion need only use r and z components since the θ component is handled by tire rotation in the θ direction. An origin O is defined at the center of the tire as discussed earlier and shown in Figure 3.18A. A center C is defined at the center of the scanning head. The scanning head would ideally start along the tire central axis at $r = 0$, $z = 0$. However, the sting arm supporting the sensor head needs to be long enough to allow the sensor head to extend into the tire. The length of the sting

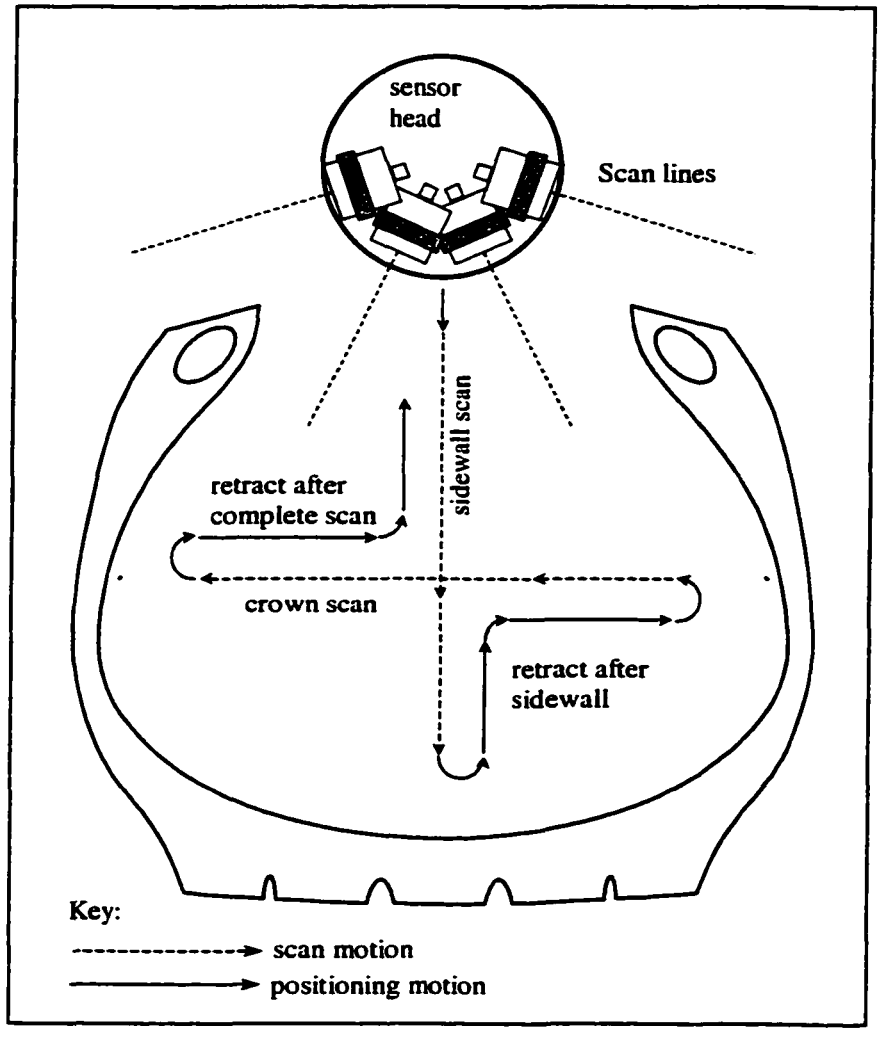

Figure 3.17: Sensor head path.

arm prevents the sensor head from entering the tire with its center C on the central axis of the tire.

The location of the tire origin O is dependent on the tire size and bead opening z_{bd}. The tire mount is fastened to a rotating shaft that is fixed in the z direction. All tires need to be mounted to the same position at the bead as seen in Figure 3.18A. However, since there is variation in bead openings and tire sizes, the location of the origin O will vary with tire size. The sensor head motion can be determined in the tire coordinate

system using the sensor head center point C and mapped into a machine coordinate

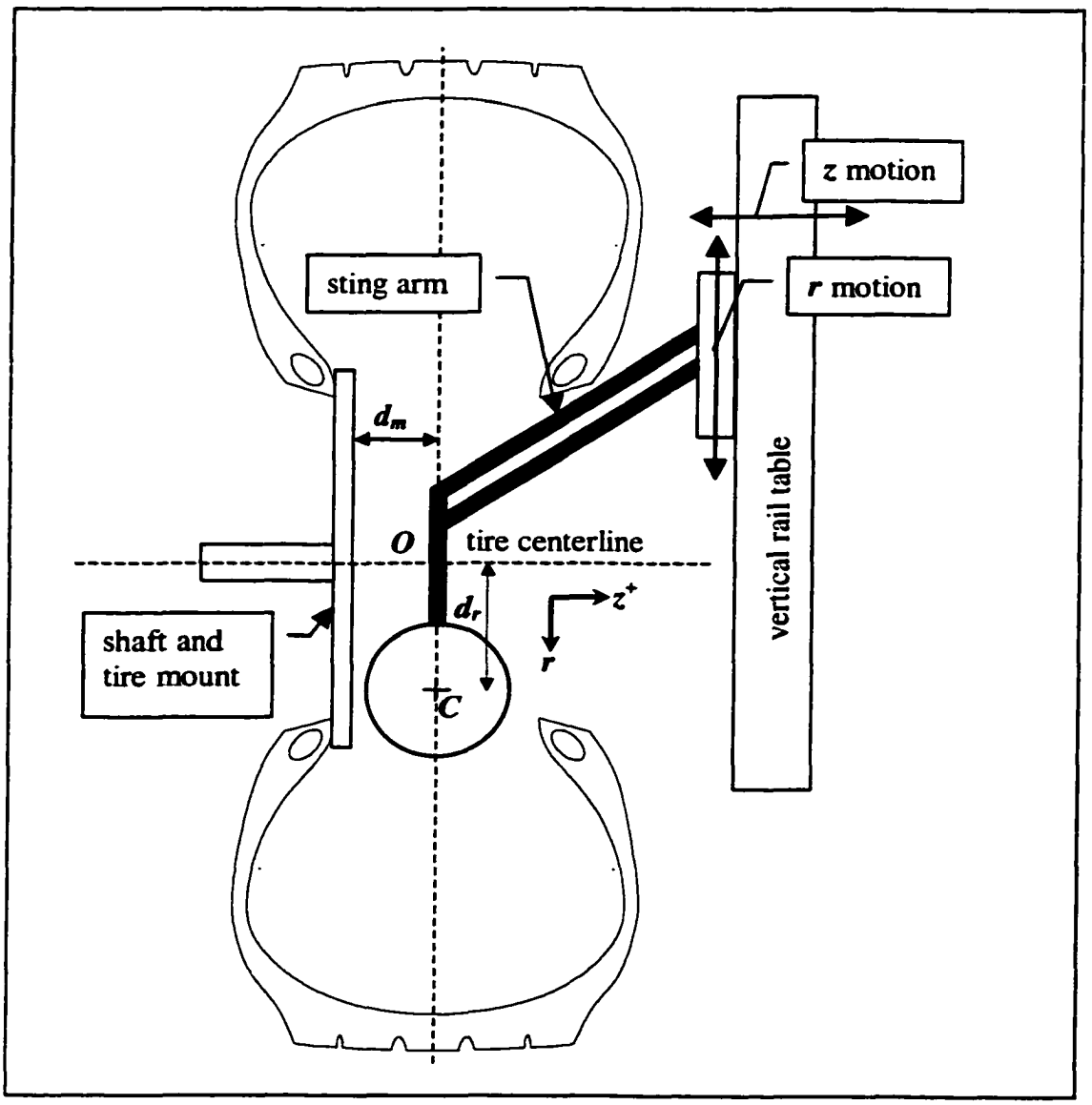

Figure 3.18A: Sensor head positioning.

system later.

The length of the sting arm vertical section and sensor head combination must fit inside the tire between beads as shown in Figures 3.18A and 3.18B. In Figure 3.18B, the length l_l also must be long enough to insert the sensor head completely into the tire during sidewall inspection. If the diameter of the sensor head is 4", the length of l_l, the

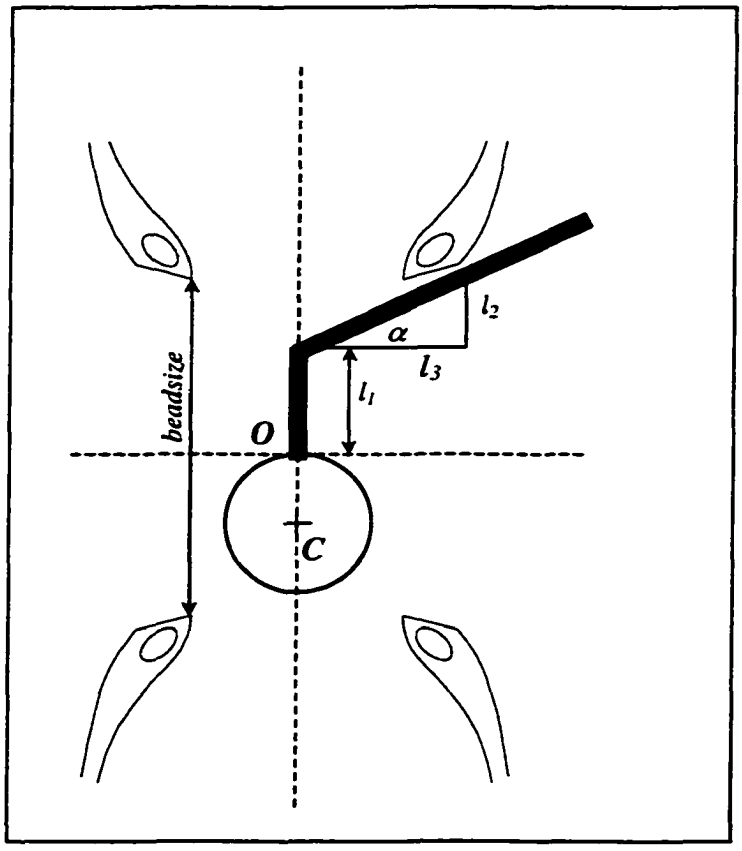

Figure 3.18B: Sting arm clearance.

sensor head and the 1" inspection zone buffer should be greater than or equal to the height:

$$l_1 + 4" + 1" \geq height \tag{3.8}$$

Using Table 3.1 for common tire sizes, the maximum height of the common tires is 11" so the length of l_1 must be greater than 6". On a 22.5" rim, letting l_1 equal 8" for added clearance at maximum extension into the tire, leaves a maximum of 10" for l_2 in Figure 3.18B. Allowing 1" of clearance under the sensor head and over the sting arm sets l_2 = 8". Knowing the bead opening, l_3 = ½*(bead opening)*, the angle α is:

$$\alpha = \arctan\left(\frac{l_2}{l_3}\right) \tag{3.9}$$

With an minimum bead opening of 4.5" $\alpha \approx 75°$. This size sting arm will be adequate for inspecting tires with 22.5" rims and heights no greater than 11". It is obvious from Table 3.1 that the sting arm sized for this tire will not work in a rim size 17.5" tire since $\sum(l_1, l_2, 4")$ is longer than the rim opening. However, the size would be acceptable for the 24.5" rim size tire with height less than 11". Conversely, a sting arm sized for the 17.5" rim with height 8" would not inspect the 22.5" tire with height 11" (although it probably could inspect the 22.5" tire with height of 8.71").

An inspection set point is defined so that the bottom of the sensor head clears the bead by 1.0" as the sensor head moves into the tire and sets up to start a scan, (see Figure 3.19). At the set point, the center of the sensor head *C* will align along the middle of the

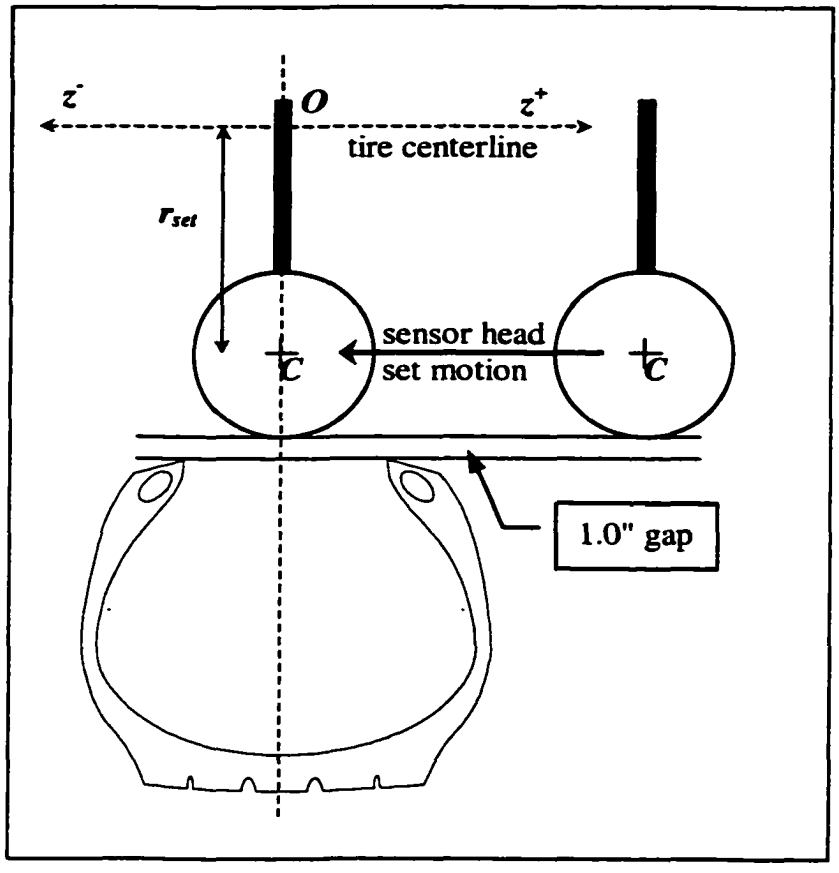

Figure 3.19: Sensor head set point.

tire at the z-plane line z_0 and will be ***1.0" + sensor head radius*** above the bead. The location can be described in terms of the tire size. Given a tire with width ***w***, bead diameter ***rimsize***, and sensor head radius R_{sh}; the ***r,z*** coordinates for the set point will be at:

$$r_{set} = \frac{rimsize}{2} - 1.0" - R_{sh} \qquad (3.10)$$
$$z_{set} = z_0$$

With sensor head radius $R_{sh} = 2.0"$ the set point coordinates in the tire coordinate system can be given knowing only the tire size:

$$r_{set} = \frac{1}{2} rimsize - 3.0" \qquad (3.11)$$
$$z_{set} = z_0$$

From the set point the sensor head moves in the ***r*** direction into the tire. The sensor head center ***C*** moves to an inspection point r_{insp}, z_{insp} where the tire bead just enters the transducer focal zone as shown in Figure 3.20. This can be calculated easily from the

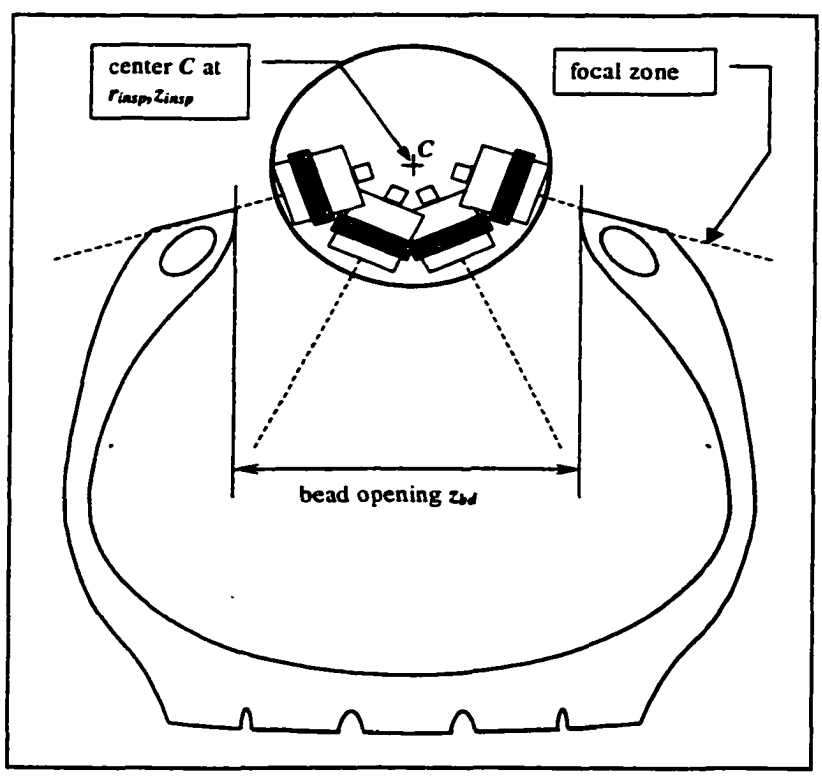

Figure 3.20: Sensor head inspection start point.

transducer head geometry and since:

$$z_{insp} = z_0$$

then:

$$r_{insp} = 0.5(rimsize - z_{bd} \tan 20) \tag{3.12}$$

So the inspection start point relative to the tire origin O can be described knowing only the tire size and the bead opening.

From the start point r_{insp}, z_{insp} the sensor head moves vertically into the spinning tire in 1/8" or 1/16" steps while sampling the sidewall ultrasonic transmission amplitude at encoder pulses. The limit of travel for the sidewall inspection is determined by the point where the focal zone intersects the shoulder overlap point shown in Figures 3.5 and 3.4. The overlap point is calculated knowing where the tire tread width w_t intersects the elliptical section.

Figure 3.21 shows a sample transducer mounted in a sensor head with 20° angle as calculated in Section 3.2.1. At the end of sidewall scanning, the center of the sensor head C will be located at some point below the center of the elliptic section located at O'. The shoulder overlap point is located along the ellipse section relative to O' at r_1, z_0 so that:

$$\frac{w_t}{2} = a\cos\varphi$$
$$r_1 = b\sin\varphi$$

Giving:

$$r_1 = b\left[1 - \frac{1}{4}\left(\frac{w_t}{a}\right)^2\right]^{\frac{1}{2}} \tag{3.13}$$

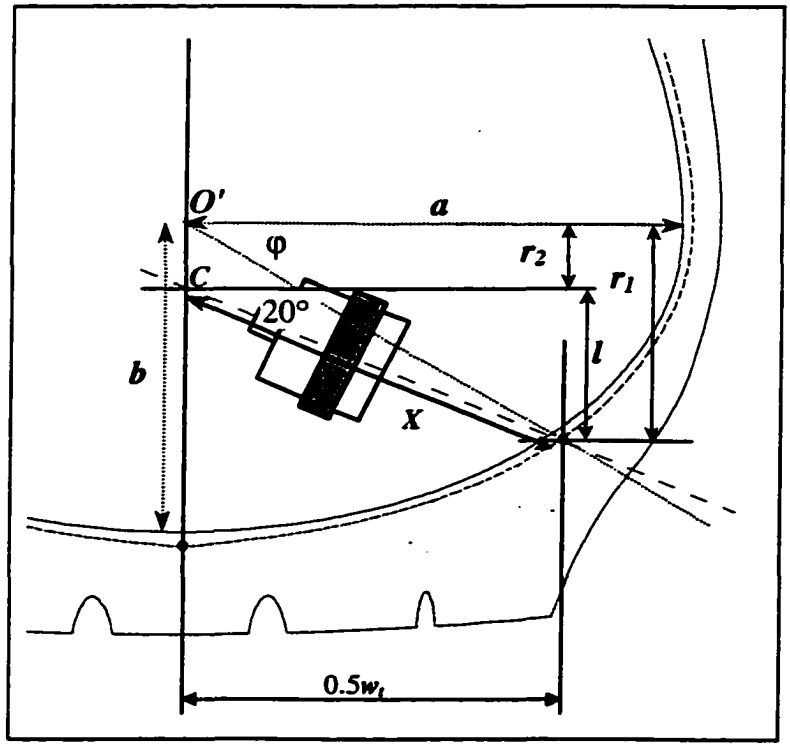

Figure 3.21: Sidewall inspection end point.

Then the distance l can be calculated from:

$$\frac{w_t}{2} = X\cos 20$$
$$l = X\sin 20$$

So that:

$$l = \frac{w_t}{2}\tan 20 \tag{3.14}$$

The center of the sensor head C will travel to a point relative to O' at $r_1,0$ equal to:

$$r_2 = r_1 - l$$

Returning this to the tire coordinate system O gives:

$$r_{int} = r_{ic} + r_2$$
$$z_{int} = z_0 \tag{3.15}$$

where O' is located at

$$r_{ic} = \frac{1}{2} rimsize + \frac{2}{3} h_{ply}$$
$$z_{ic} = z_0$$

and by substitution:

$$r_{int} = \frac{1}{2} rimsize + (h-1)\left\{\frac{2}{3} + \frac{1}{3}\sqrt{1-\left(\frac{w_t}{w}\right)^2}\right\} - \frac{1}{2} w_t \tan 20 \qquad (3.16)$$
$$z_{int} = z_0$$

giving the coordinates of the sidewall scan endpoint in terms known from only the tire size and tread width. So during sidewall inspection the scanning head center C steps from the start point $r_{insp}z_0$ to the intermediate ending point $r_{int}z_0$.

At the end of the sidewall scan, the sensor head is retracted in the r and z^+ directions to begin the crown scanning path as shown in Figure 3.22. The beginning of the path is set using the bead opening, tire size, and tread width. The sensor head can be moved in the z- direction until the sting arm is within 0.125" of the tire mount to avoid contacting the tire mount during spinning. The tire mount is 0.5 inch thick limiting the travel it can move in the z- direction relative to the centerline along $z = z_0$. The sensor head center C can move in the z- direction by:

$$z_1 = 0.5 z_{bd} - 0.125" - 0.5 armwidth - 0.5" \qquad (3.17)$$

Where: $armwidth =$ width of sting arm

To make the scan symmetric about the centerline, motion in the z+ direction is set equal to z_1. The z coordinate for crown scan start using the inspection center O' is then:

$$z_{crown} = z_0 + z_1 \qquad (3.18)$$

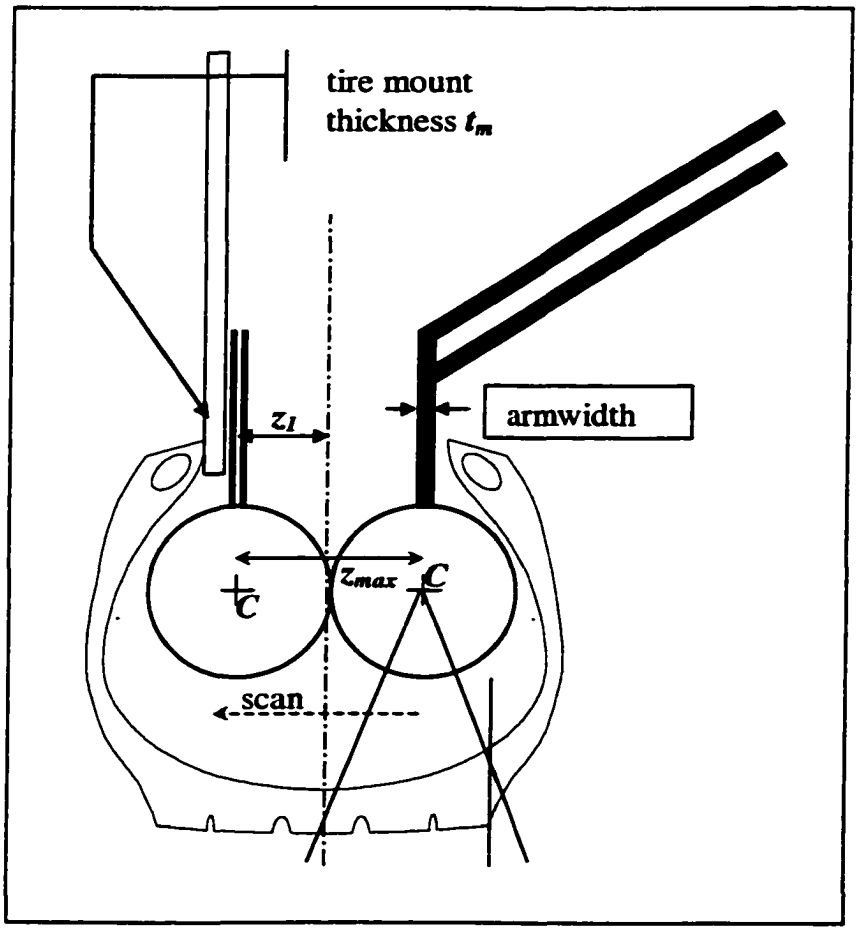

Figure 3.22: Crown scan path.

The r coordinate relative to O' is determined in a similar manner to the sidewall coordinates. It is important that the sensor head retract far enough that the sound fields of transducers cause overlap at the shoulder and middle of the crown. From Figure 3.23 it can be shown that:

$$\frac{w_t}{2} - z_1 = X \sin 20$$
$$l = X \cos 20$$

so that:

$$l = \cot 20 \left[\frac{w_t}{2} - z_1 \right]$$

and: $$r_2 = l - r_1$$

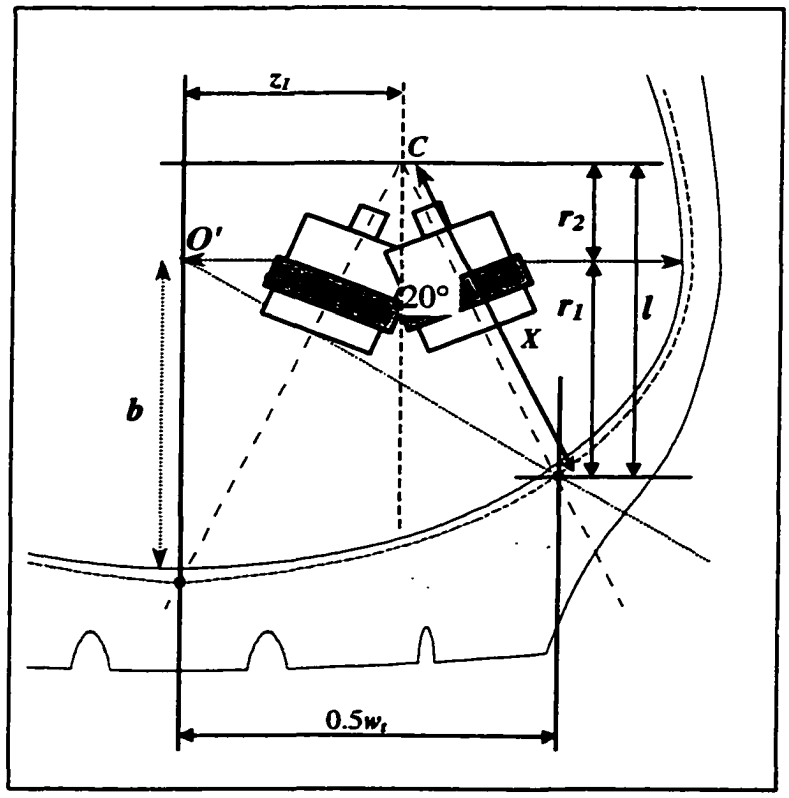

Figure 3.23: Crown inspection end point.

So the sensor head center C must be retracted by lengths r_2 in the r direction and z_1 in the z^+ direction to begin a crown scan. returning to the tire coordinate system:

$$r_{crown} = r_{ic} - r_2$$
$$z_{crown} = z_0 + z_1$$

so that:

$$r_{crown} = \frac{1}{2} rimsize + \frac{2}{3} h_{ply} - \left\{ \cot 20 \left(\frac{w_t}{2} - z_1 \right) - b \left[1 - \frac{1}{4} \left(\frac{w_t}{a} \right)^2 \right]^{\frac{1}{2}} \right\}$$

$$z_{crown} = z_1 \qquad (3.18)$$

$$z_1 = \frac{1}{2} z_{bd} - 0.125" - \frac{1}{2} armwidth$$

During the crown inspection r remains constant and the sensor head center C moves to:

$$z_{end} = z_0 - z_1 \qquad (3.19)$$

It is possible for the tire bead opening to be wide so that the length of z_1 will cause undue retraction in the r direction to force overlap at the middle of the crown as shown in Figure 3.24. This can be overcome by retracting in the r direction only enough to bring

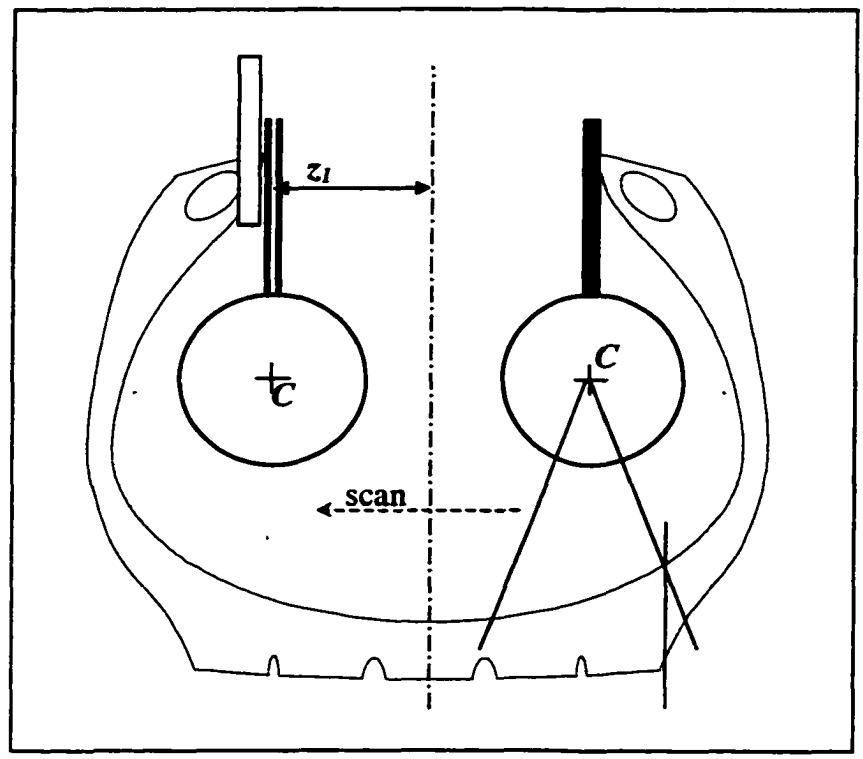

Figure 3.24: Large tire crown scan path.

the shoulder overlap point into the sound beam focus and acquiring data on only one transducer until the second reaches the midpoint of the crown.

Sensor head motion has been defined relative to any tire given only the tire size, bead opening, and tread width. For most tire sizes, the bead opening and tread width will remain constant for a particular size. It is only in the event that narrower or wider tread has been applied or the tire was mounted on the wrong rim size that information about more than the tire size would be required.

As noted earlier, the sensor head motion is relative to a tire size where the center of the tire O is the coordinate system origin. However, the design of the machine required that a fixed shaft be mounted forcing the location of O to be dependent on the tire size. The location of the sensor head center C is known relative the machine and fixed shaft. Figure 3.18 shows the location of O relative to the tire mount fixture. The location of O will be distance $d_m = (\frac{1}{2} z_{bd} - 0.5") = z_0$ along the z^+ direction in front of the tire mount. The z axis is coincident with the centerline of the rotating shaft.

During a scan, the sensor head follows a path, shown in Figure 3.25 to enter the tire and begin scanning. The vertical rail table and horizontal beam have home positions that the sensor head center C is retracted to when moving tires in and out of the tank. The

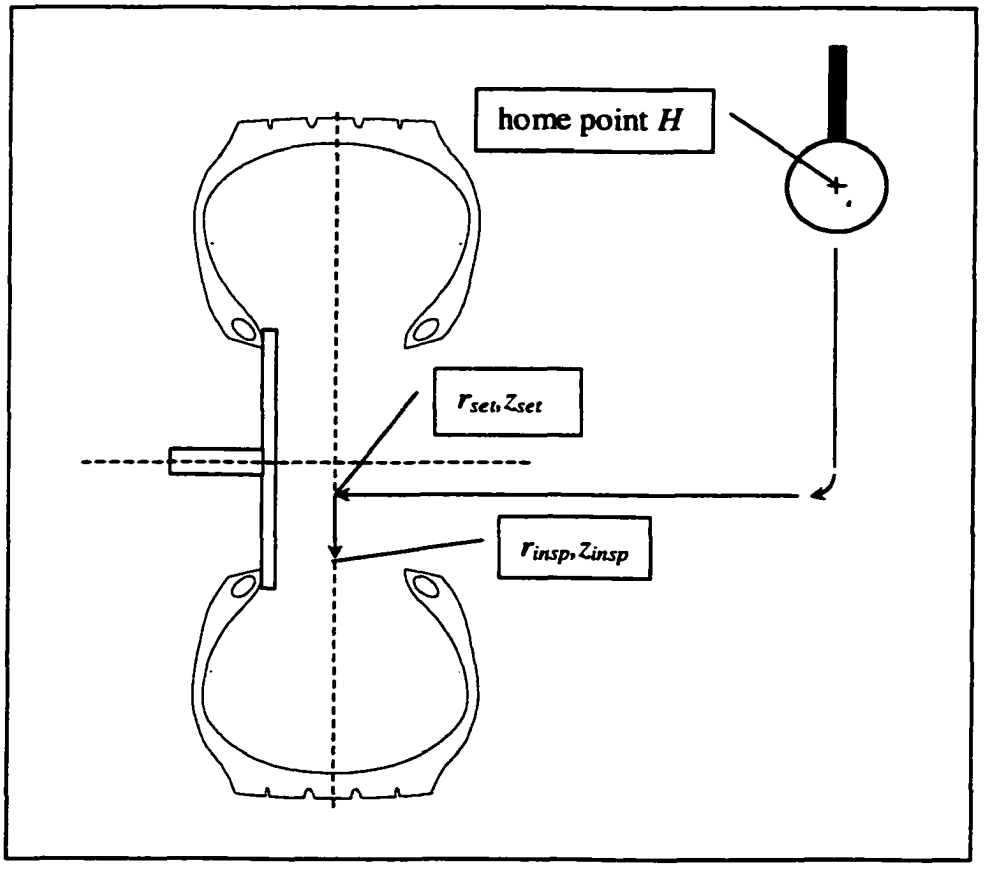

Figure 3.25: Sensor head position setup.

location, called H, is known relative to the tire mount. When a scan begins, the sensor head center C leaves H and moves as shown to the z_0 point of the tire located at distance d_m in front of the tire mount face as noted above. The r distance is at r_{set}. From point $r_{set}z_{set}$, the sensor head center C moves to $r_{insp}z_{insp}$ and begins the tire inspection as shown in Figure 3.18 and discussed previously. At the end of the inspection, the center C is retracted to $r_{set}z_{set}$ and finally to H in preparation for the next inspection.

An interactive, animated MATLAB program listed in Appendix Section 9.1 is used to simulate the tire profile and sensor head motion described in this section and Section 3.1. The program calculates the sensor head motion profile and displays the number of 1/8" steps needed for the setpoints previously discussed. The program then animates the tire inspection for a visual test of the inspection. Figure 3.26 shows single frames from the simulation. An 11R22.5 tire was used for the simulation shown, however, any tire profile can be modeled by the simulation to determine coverage.

In Figure 3.26, the tire profile is generated using the coordinate system developed in Section 3.1 and displayed with the zero axis at the tire coordinate system origin O. A treadline is place above and below the tire to simulate the true width of the tread. The sensor head in 3.26A is located at its home position. In 3.26B, the sensor head is moved to $r_{insp}z_{insp}$ for the start of the sidewall scan where diagonal dotted lines represent the sidewall ultrasound receiver direction. Figure 3.26C shows the sensor head at $r_{int}z_{int}$ or the end of the sidewall inspection. At this point the sidewall transducer inspects the tire profile at the treadwidth. In Figure 3.26D the sensor head has retracted in to $r_{crown}z_{crown}$ to start the crown scan. The dotted lines now represent the crown ultrasound receiver direction. The receiver starts at the same point the sidewall scan finished. Figure 3.26E

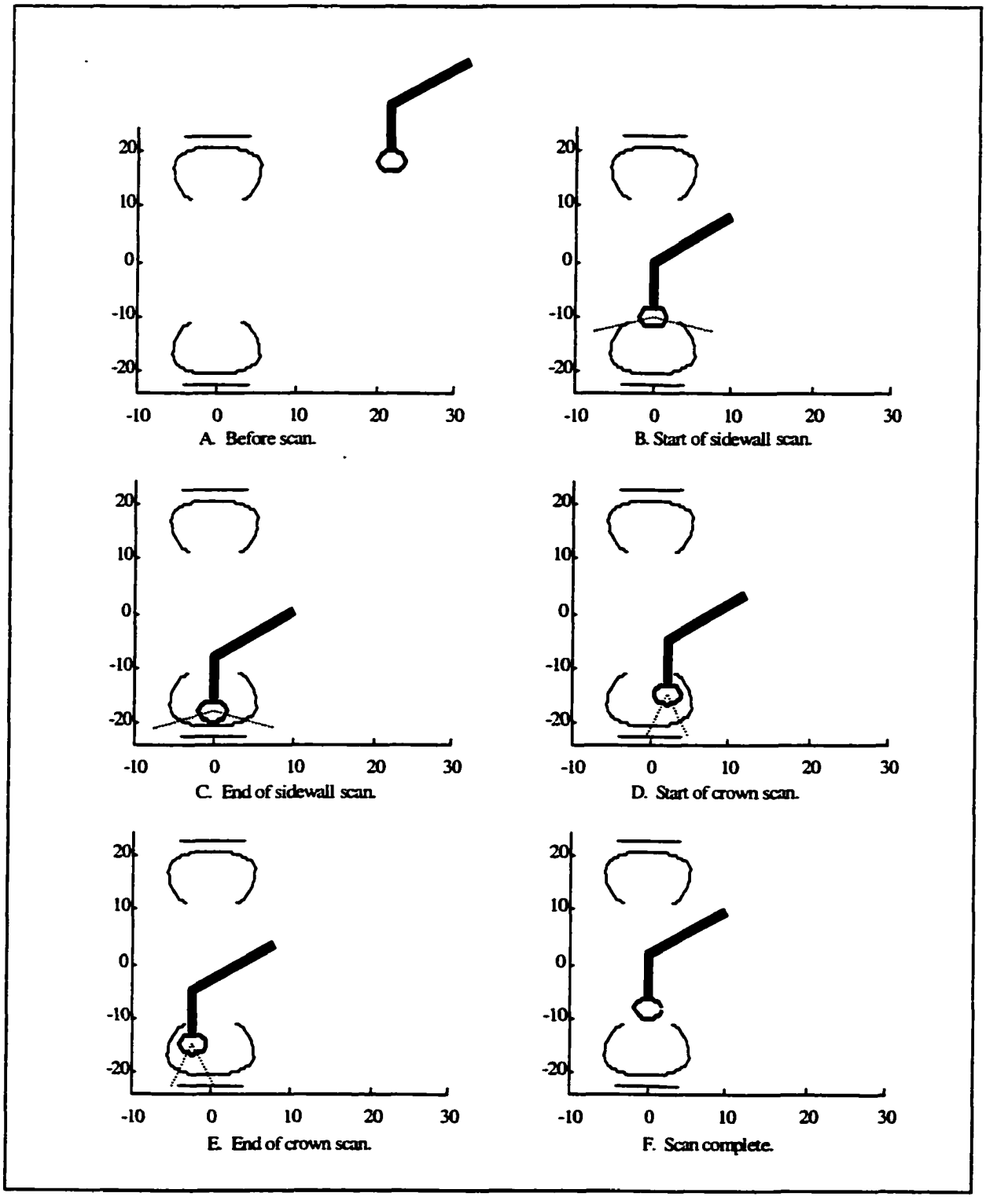

Figure 3.26: Tire inspection simulation.

shows the end of crown scanning and 3.26F shows the scan completed prior to sensor head retraction to its home position.

The MATLAB program generates step motion data for the tire size. Table 3.2 shows an expansion of Table 3.1 with set points for common tire sizes from the table. Prior to inspection, the bead opening must be measured by hand since the same size tire can have different bead openings after use.

Table 3.2

Sensor head motion set points for inspection.							
Tire size	***bead opening(in)***	$O_{location}$ z	r_{set},z_{set}	r_{insp},z_{insp}	r_{ins},z_{ins}	r_{crown},z_{crown}	z_{end}
8R17.5	5	2.50	5.75,0	7.84,0	13.87,0	10.84,1.50	-3.00
10.00-20	6	3.00	7.00,0	8.91,0	16.62,0	13.18,2.00	-4.00
11R22.5	6.5	3.25	8.25,0	10.07,0	18.62,0	14.97,2.25	-4.50
295/75R22.5	7	3.50	8.25,0	9.98,0	16.51,0	12.99,2.50	-5.00
275/80R22.5	7	3.50	8.25,0	9.98,0	16.57,0	13.76,2.50	-5.00
285/75R24.5	7	3.50	9.25,0	10.98,0	17.30,0	14.14,2.50	-5.00
275/80R24.5	7	3.50	9.25,0	10.98,0	17.57,0	14.76,2,50	-5.00

Table 3.3 shows the same tire sizes with the number of steps require to travel to each of the set points. This data can be used to easily change tire sizes during scanning.

Table 3.3

Sensor head steps to set points, 1/8" step size.						
Tire size	r_{set} steps below r_0	r_{insp} steps below r_{set}	r_{int} steps below r_{ins}	r_{crown} steps retract from r_{insp}	z_{crown} steps in z+ direction	z_{end} steps in z- direction
8R17.5	46	17	48	24	12	24
10.00-20	56	15	62	28	16	32
11R22.5	66	15	68	29	18	36
295/75R22.5	66	14	52	28	20	40
275/75R22.5	66	14	53	22	20	40
285/75R24.5	74	14	51	25	20	40
275/80R24.5	74	14	53	22	20	40

3.3 Data Acquisition system.

Central to the tire inspection machine concept is a method to acquire large data sets. The data acquisition system is an embedded sub-processor incorporated in the system using currently available plug-in cards. It is designed to relieve the central computer of the burden of concurrent, high-speed, data-acquisition and control. Regardless of the state of the motion control system, the data acquisition sub-processor can acquire data independently and transfer it to the master CPU during motion control. The master CPU commands the system to begin and polls it occasionally when a data transfer is expected. This section details the system design to acquire data during scanning.

Signal analog to digital conversion is performed by the data acquisition processor (DAP) card. The DAP is a stand alone embedded processor running its own real-time, multi-tasking operating system. The DAP communicates with the master control PC through the ISA bus. A master control program on the central CPU loads a series of

programs to the DAP during initialization before scanning. The programs control setup and data acquisition by the DAP.

The sensor head has four ultrasound transducers operating as receivers but only two are sampled at one time as per the scanning technique discussed in Section 3.2. Figure 3.27 shows the layout of the data acquisition system. There are four transmitters

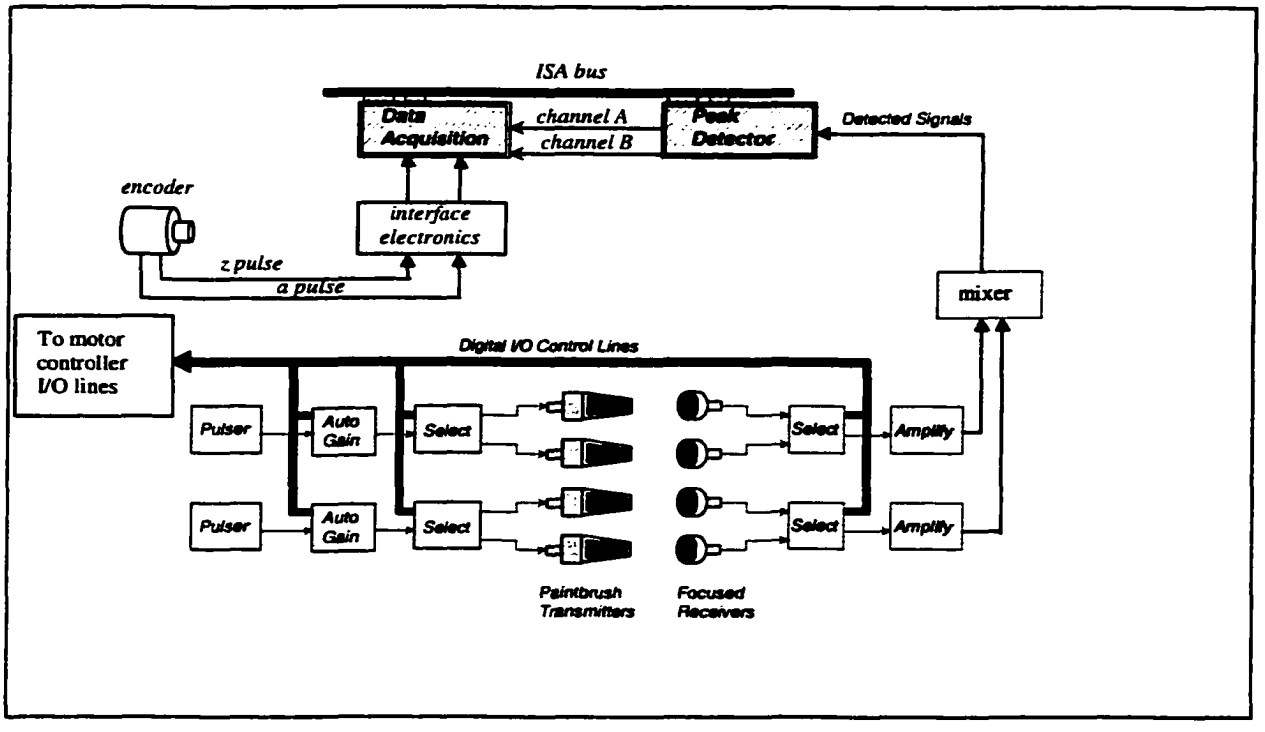

Figure 3.27: Data acquisition system.

and receivers as discussed in Section 3.2 paired into channels A and B. Only two are used at any given time. A set of four RF (radio frequency) relays labeled *Select* in the figure are controlled by digital I/O lines from the motor controller card. The relays select whether the crown transducers or the sidewall transducers are being used. The transmitters are driven by standard ultrasonic pulser/receivers discussed in Section 3.4. The receiving section of the pulser/receivers is set to a constant gain (typically 35 dB for this inspection). The signal amplitude is varied for auto-gain purposes by an 8-bit

programmable attenuator in-line between the pulser and the transmitter. In this way, signal amplitude received can be varied by the amount of attenuation applied to the driving pulse sent to the transmitters. The programmable attenuators are connected to digital I/O lines on the motor controller card.

The pulsers operate at a repetition rate of 1000 Hz to prevent unwanted decay in the peak detector stages. Figure 3.28 shows peak detector output for two frequencies. At

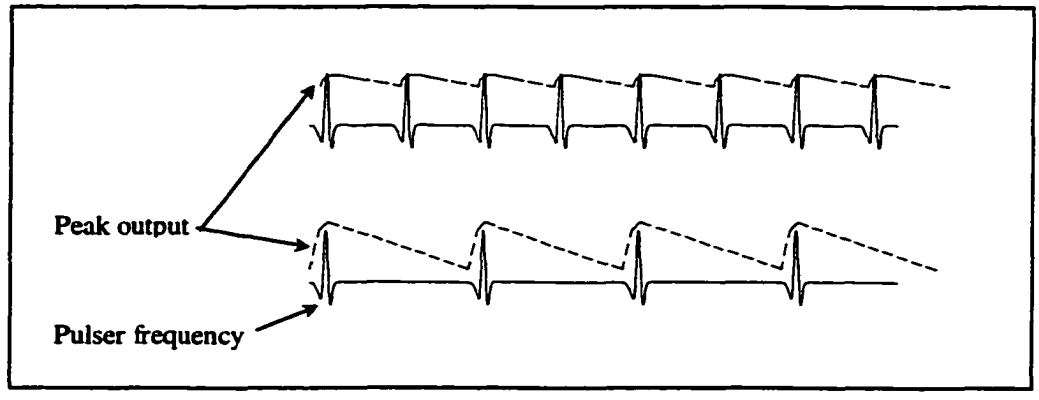

Figure 3.28: Peak detector output decay.

the higher frequency, decay between peaks is small so that the output reflects true peak values. At a lower repetition rate, the decay between peaks is significant and can lead to incorrect data acquisition. The repetition rate of 1000 Hz was selected to prevent decay during asynchronous sampling that occurs at encoder pulses that have no correlation with the pulser repetition rate.

The Channel A pulser operates as a master and Channel B is slaved to operate after a delayed trigger from the Channel A. The delayed trigger is an adjustable delay set on the interface electronics board. Figure 3.29 shows sample timing in the system. Channel A transmits followed by B after a delay. A transmission time allows for the ultrasound pulse to pass through the water and tire to the receiver. The outputs of the receivers are combined in a Mixer as shown in the receiver flow chart Figure 3.30. The

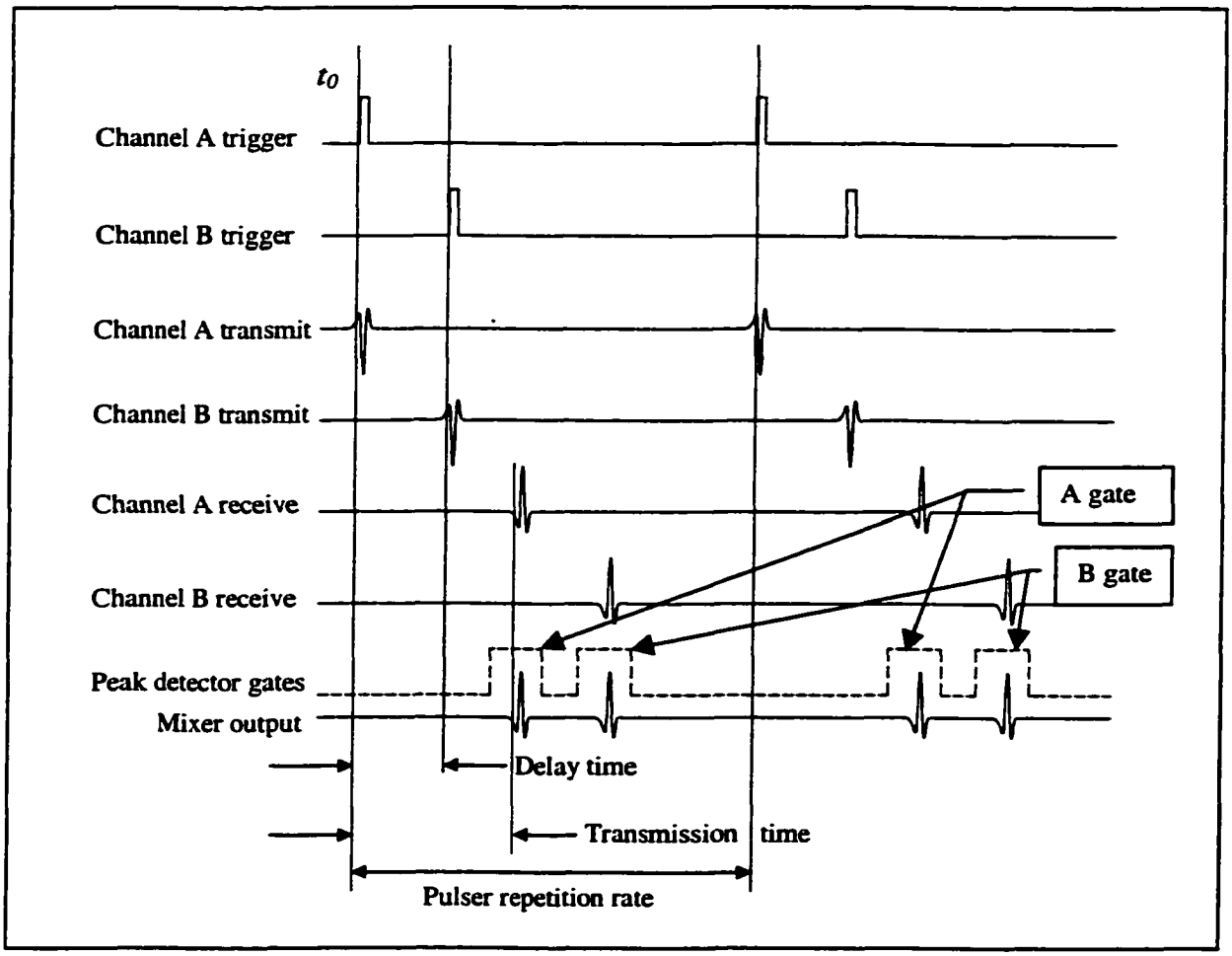

Figure 3.29: Pulser timing.

peak detector gates are set up to separate the peak values received. The delay time is set long enough to separate the receiver values and allow separation between the gates. The reason for the delay is to enable the use of a single peak detector card with dual gates. The peak detector can be set to read the receiver signal only during gated periods.

As described earlier, an encoder with 2048 pulses/revolution is attached to the rotating shaft with the tire mount. The encoder also features a zero pulse for actual position information. The encoder pulse output is connected to an input line on the DAP. The DAP is able to perform hardware or software triggering. Using software triggering, a task running on the DAP processor generates a data acquisition on any line or lines

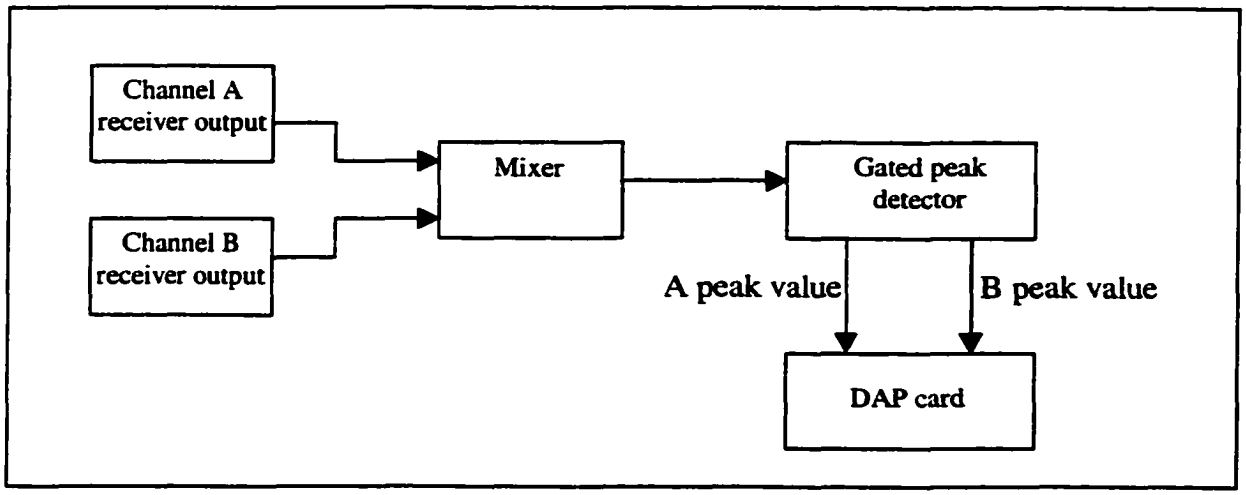

Figure 3.30: Receiver signal flow chart.

when there is a logic change on the triggered input line. Software triggering has advantages since the system is not dependent on a hardwired line that can be difficult to modify for future needs. The task running a software trigger can be modified easily by writing new or additional tasks. The real time nature of the DAP operating system guarantees the trigger will be handled within 10 μs providing adequate resolution for this system design. With the tire rotating at 20 rpm, the difference in location for a 10 μS span is less than $1/1000^{th}$ inch. Little resolution is lost in the system by using software triggering.

Data is acquired on every other revolution of the spinning tire. This allows a full revolution to move the sensor head, transfer data, calculate and set auto-gain parameters and update the b-scan display. A simple circuit is set up to alternate a binary output with each revolution using the encoder zero pulse as input. The binary output is directed to an input line on the DAP processor. The software triggering samples both the binary output line and the encoder pulse line and generates a data acquisition when both are high. This prevents data acquisition during the off revolution.

2048 data points are acquired during a full revolution and stored onboard the DAP card. At the end of a revolution the master control program checks to see if all 2048 points were acquired and downloads the data if good. If 2048 were not acquired, the DAP reacquires the same data at the next revolution before the sensor head is stepped by the master control program.

During a single circumferential B-scan at 1/8" resolution, 2048 data points are acquired and down sampled by the master control program saving alternate points (at 1/16" resolution all 2048 data points are saved). The data is stored in an Mx1024 (2048 for 1/16") matrix where m is the number of circumferential scan lines necessary to cover the tire profile. For a typical 275/80R22.5 tire, 208 circumferential B-scans are necessary to cover the entire tire at 1/8" step size. The storage matrix is then 208x1024. After a full scan is complete, the data stored in the Mx1024 (2048) matrix is post-processed by the master control program and put in a form to be sent for data acquisition.

From a known 0° point on the tire where the encoder passes its own 0° or **z** point, the 1024 points can be transformed into degrees. The location of the point along the cross section can be derived from the scan line $M_{current}$ divided by 8 (or 16) and measured in inches from the inner bead around the tire. In this way, the location of defects can be determined on the tire itself by a degree coordinate and a length from the bead.

3.4 **System Hardware.**

The overall system is comprised of two main sections, a central controller and an immersion, ultrasonic scanning tank shown in Figure 3.31A. The central controller is housed in a ½ height rolling rack. The controller contains the PC with embedded

subsystems mounted onboard. The scanning tank with external frame holds the mechanical assemblies and electromechanical drives for tire and sensor head motion.

Figure 3.31B shows a diagram of the system hierarchy. The system hierarchy uses a PC master with an embedded processor controller connected to the internal ISA bus for motion control, data acquisition, and peak detection (of the receiver signal). A serial line embedded processor controller governs the rotational velocity of the tire during scanning. A TCP/IP link with a separate display computer transfers data for display. Each embedded controller has digital and analog I/O capability. The motor controller I/O is also used to control attenuators, relays, and water pumps. In addition, communication between embedded controllers is possible by direct I/O links rather than communicating across the master PC ISA bus.

The master PC runs Windows NT that has been shown to be adequate for real-time control of systems [Car97]. The master PC uses a National Instruments LabView interface. Each embedded processor also runs its own real-time operating system allowing constant real-time control over events without the need for continual interrupt servicing by the master PC. The master LabView interface also provides real-time display of the B-scans acquired after every other revolution.

The scanning tank allows partial immersion of the tire. Motion in the z and r direction is accomplished using a vertical rail table for the r axis and a floating beam on twin rails with a belt drive for the z axis (shown in Figure 3.31A). A frame mounted on an air cylinder holds a horizontal shaft with a tire mount at the end as in Figure 3.31A. The frame can be moved above the tank height or lowered to ground level for ease in mounting a heavy truck tire. After mounting a tire, the frame is raised with the air

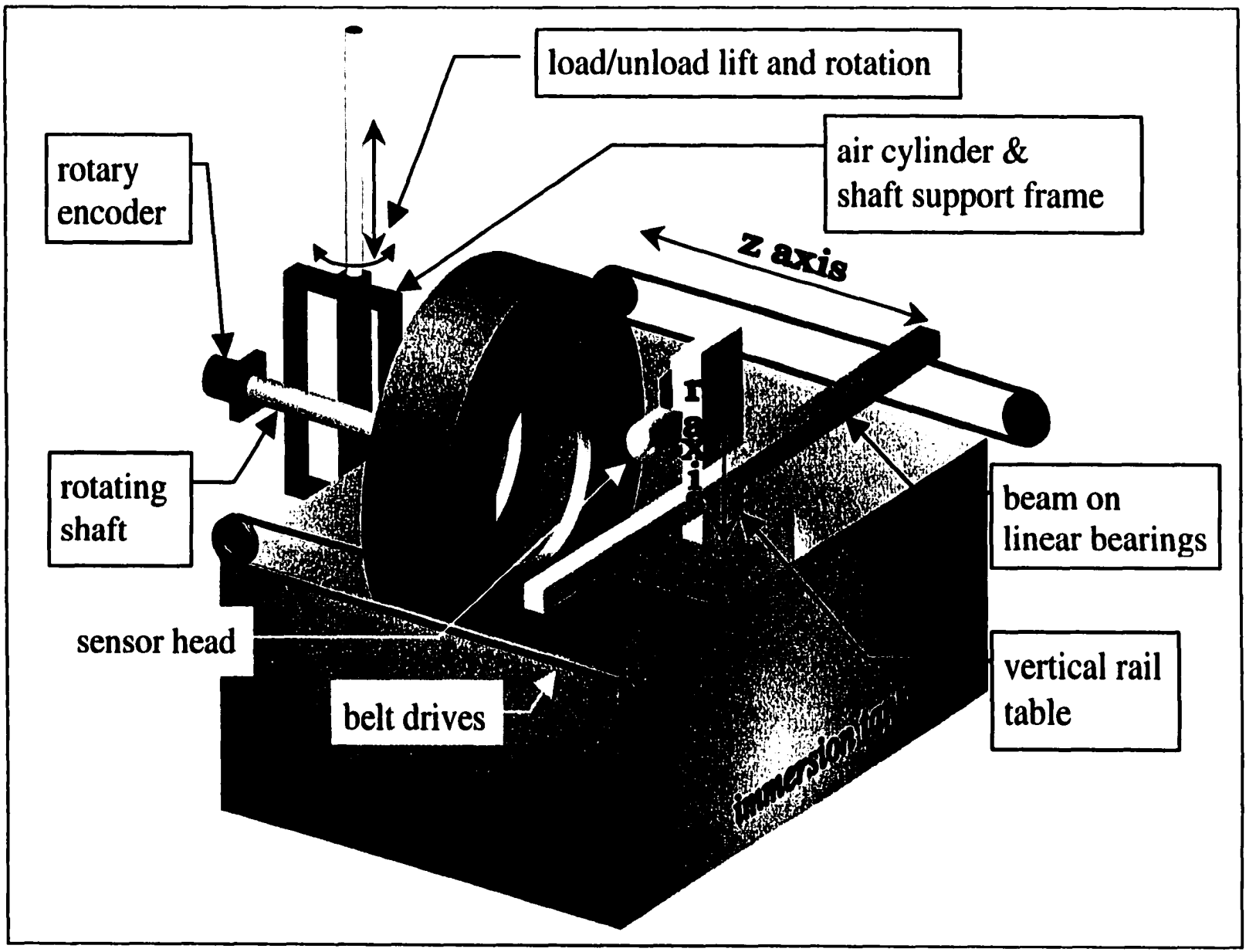

Figure 3.31A: System Hardware.

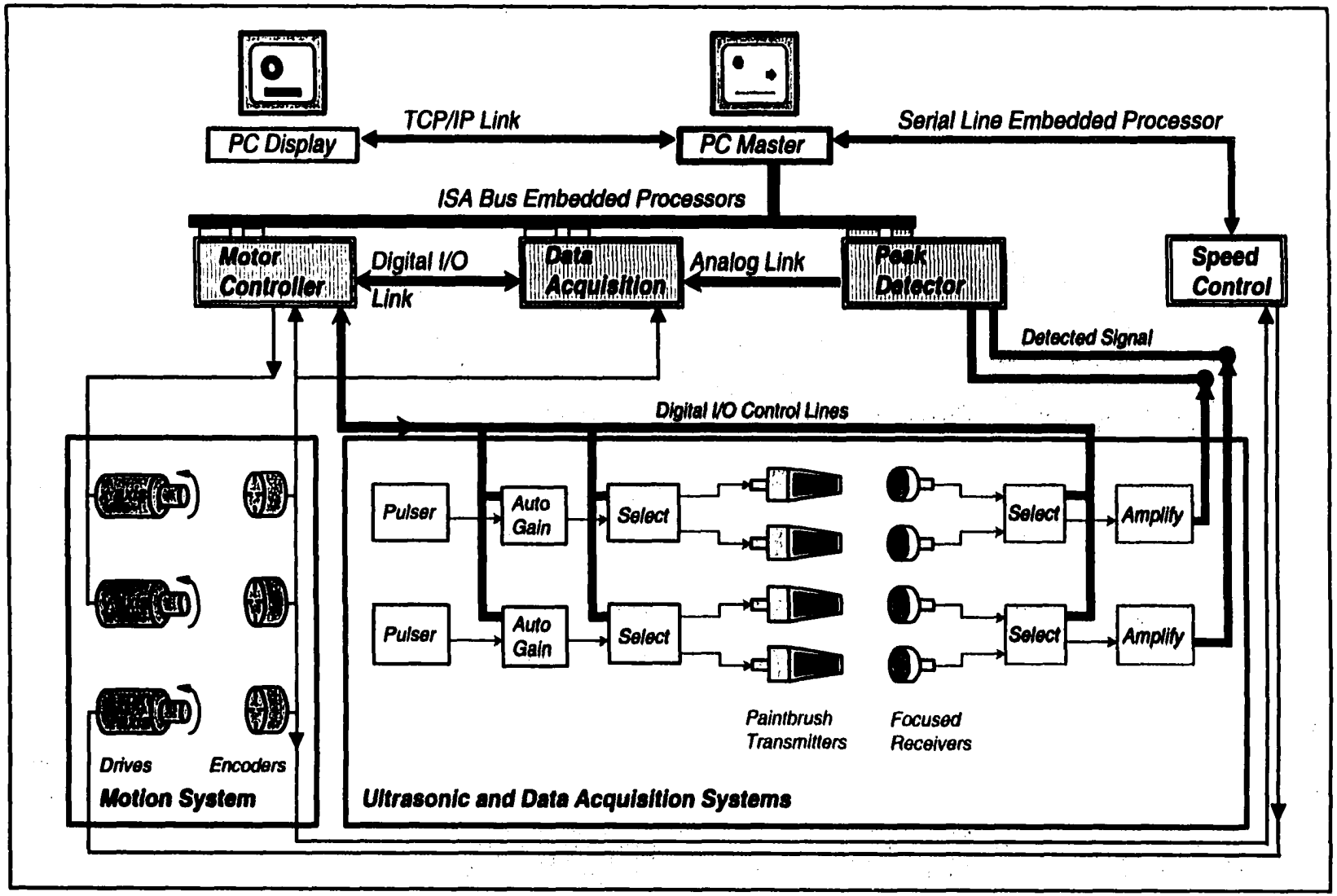

Figure 3.31B: System organization.

cylinder and the tire rotated into the tank. Fixed paintbrush transducers within the tank follow the exterior contour of the tire as shown in Figure 3.7. The sensor head is moved into the tire by r and z axis motion. Scanning proceeds until the entire tire has been inspected and then the process is reversed and the tire removed from the tank.

Embedded subsystems on the rack include:

1. Data acquisition – Microstar Laboratories - DAP 1200e/4.

   This data acquisition card is Windows NT compatible and offers a National Instruments LabView interface. The card uses an 80C186 onboard processor, 1 megabyte onboard RAM, 16 analog inputs, 16 digital inputs, 2 analog outputs, and 16 digital outputs. Maximum sample rates are 166,000 samples/second. The card runs an onboard DAPL operating system with data acquisition and analysis incorporated in the language. Custom programming is also available. It interfaces to the PC across the ISA bus.

2. Motion control – Compumotor (Parker) - AT6400 4-axis controller.

   The motion control card offers a built in 68000 processor with four axis motion control including encoder feedback. The processor runs its own AT6400 operating system and is programmable with its own motion control language including I/O. The card is Windows NT compatible and offers a LabView interface. The board offers 24 programmable inputs and outputs in addition to joystick control. It interfaces to the PC across the ISA bus.

3. Peak detection – Matec Instruments Inc. - PD2000 gated peak detector.

   The gated peak detector provides 2 channel peak detection. Controllable gates with delay and 10 nanosecond resolution are individually programmable. The peak detector provides peak detector outputs. The card interfaces to the PC through the ISA bus. Windows NT drivers and LabView interfaces were developed explicitly for this application.

4. Speed controller – Dart Controls Inc. – MD30P

   The speed controller is mounted external to the PC. However, it is an embedded system and incorporates an MC68HC11 microcontroller. It offers digital closed loop control of DC permanent magnet motors. The controller governs the spin speed of the tire in the tank. Communication with the PC is through an RS232 serial line.

In addition, the rack holds:

1. 2 – Ultrasonic Pulser/Receivers - Panametrics model 5072PR

   The pulser section provides selectable pulse energy output of 13, 26, 52, and 104 μJoules. Variable repetition rates are available between 100 and 5000 Hz. The receiver section offers selectable gain of 0 to 59 dB (or attenuation). Additionally, high and low pass filters are available and variable damping for the pulser section of 15 to 500 ohms. For this system the pulser was operated at maximum output and no damping. The receiver was operated without filtering and typically 35 dB amplification.

The amplification was varied depending on the attenuation properties of a particular tire.

2. 2 – TTL Logic Programmable Attenuators - Alan Industries model 50TTL31.5

   The attenuator offers steps of .5,1,2,4,8,16, and 31.5. The attenuator was controlled directly by a custom module constructed with standard TTL 7204 gates as an interface the output of the AT6400 motor controller. The attenuator was adjusted so the energy sent to the transmitters prevented clipping of the receiving amplifiers set at a fixed gain for a tire scan.

3. Custom interface board.

   Interfacing between encoders, board I/O lines, ultrasonic relays, water pump relays is handled by a custom designed interface circuit board. The board also incorporates timing components to set the delay needed to run two ultrasonic circuits using only a single peak detector.

4. Standard DC power supply.

The immersion tank is a separate unit consisting of:

1. The immersion tank.

   The tank is 4'x6' by 4' deep, larger than necessary for this purpose to accommodate future expansion for unrelated research.

2. Motion control hardware.

Horizontal rails are mounted at each end of the tank to provide X motion. A belt drive system at each end is connected by a shaft to provide movement. The shaft is driven by single stepper motor microstepped at 25,000 steps/revolution. Positional accuracy is 0.003". A ParFrame beam is connected to belts at each end. On the beam, a Parker-Daedel 500000PD belt drive rail table is mounted to provide Z axis motion.

3. Interface electronics.

   Several breakout enclosures are mounted external to the tank to hold interface circuitry, RF relays, and stepper drive electronics. The stepper drives are Parker-Compumotor LN57-102 low EMI drives. Low EMI drives are required to prevent chopping frequency interference with sensitive ultrasonic receiver amplifiers.

4. Tire mount and spin hardware.

   Externally mounted on the tank is an air cylinder with frame attached. On the frame a shaft is held in bearings. The shaft has an encoder mounted to one end and a tire mount at the other. The entire frame moves up and down and spins on the air cylinder.

3.5 **Master Control Program.**

The system design incorporates three embedded processor systems as discussed in Section 3.3 and shown in Figure 3.31. However, the embedded systems are not stand alone in the traditional sense of autonomous operation. A master control PC governs the embedded sub-processors with independently running software and hardware. This section presents a review of the master control PC program operation.

Each embedded processor runs its own proprietary operating system with programming language. The programming languages are high level so that extensive programming skills to understand nuances are unnecessary. The motor controller card and the data acquisition card require extensive programming before operation. The rotation speed controller requires only setup and speed sets. In addition, the peak detector card without an embedded processor requires a programmed setup prior to inspection or changing tire sizes.

The master control program (MCP) is designed as a LabView executable running in Windows NT. LabView offers a robust, graphical programming environment greatly enhancing the ability of a programmer to perform complex programming functions [Nat97]. Built in data acquisition and control interfaces are standard.

Before the system can be used for inspection, individual subsystems must be initialized and setup. Figure 3.32 shows a block diagram of the initialization procedure. The master LabView program establishes communication with the motor controller card and downloads the card operating system. A system check determines if the card accepts the operating system. If communication is not correct, the LabView program terminates until the problem is solved. Following the motor controller, the master program establishes communication with the data acquisition processor (DAP). A second check terminates execution if communication is faulty. The DAP loads its own operating system from BIOS during power up. Communication is then established with the tire rotation speed controller (DART) via serial line. Peak detector initialization and operating parameters are setup and checked. If not correct, the master program again terminates execution. After communication with all subsystems are enabled, the master

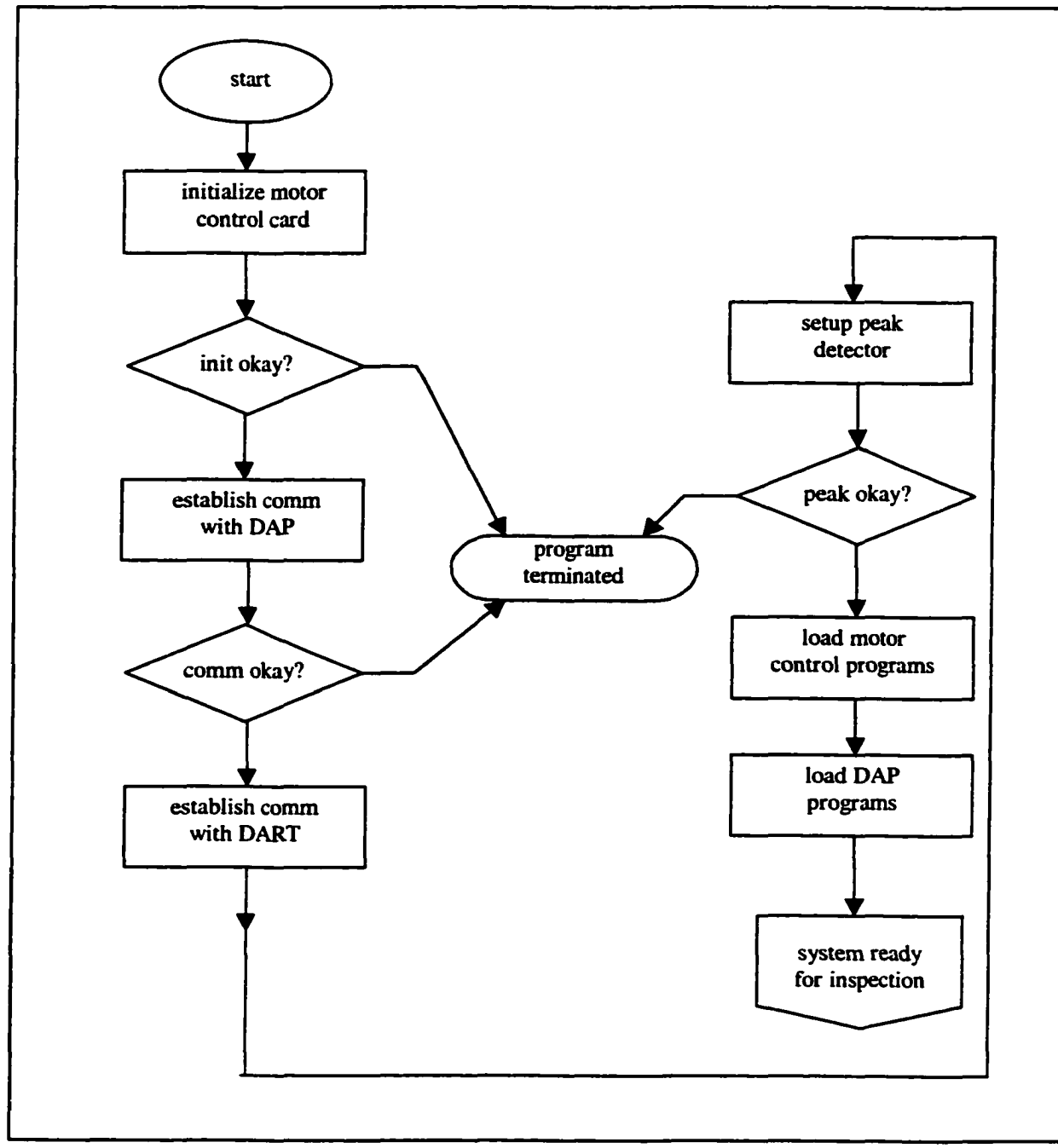

Figure 3.32: System initialization and setup diagram.

program loads subprograms to the individual processors. The system is then ready to begin inspection.

To begin inspection, the tire must be mounted and swung into the tank. Figure 3.33 shows a flow chart of the scan process. The MCP commands the motion controller

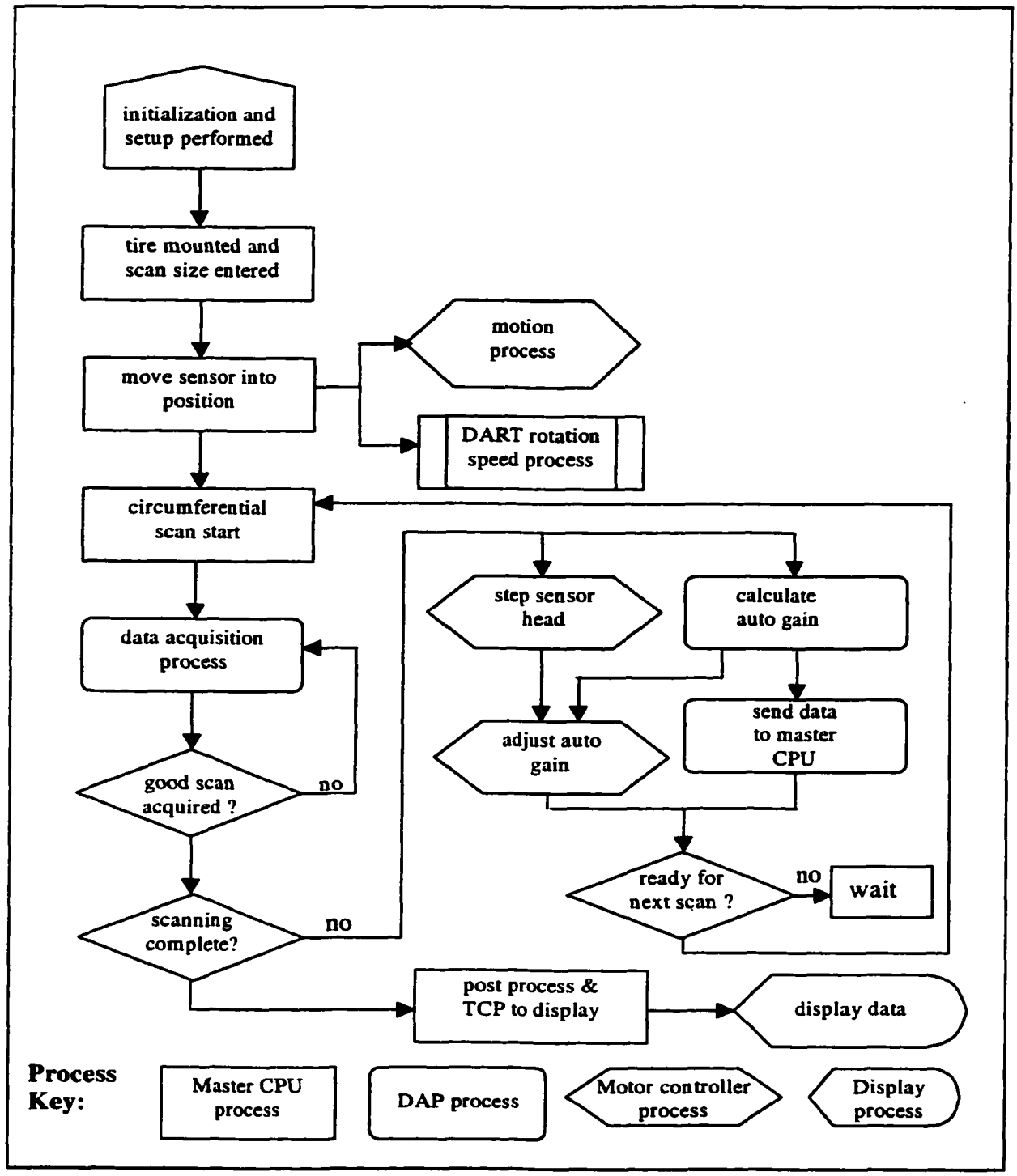

Figure 3.33: Scan flow chart.

to move the sensor into position and the rotation speed controller to set the scanning speed. A circumferential scan is started at the next encoder zero pulse. The data acquisition processor acquires data during a full revolution of the tire. The number of

points acquired is checked by the MCP. If the data points are not correct, the program acquires a new set of data at the next encoder zero pulse. If the data set is good, the sensor head is stepped by the motor controller and the DAP calculates auto gain parameters to send to the motor controller. The motor controller adjusts the auto gain, the DAP sends the data set to the MCP and the cycle is reset and ready for the next encoder zero pulse. Intermittent b-scans are displayed on the MPC computer between each circumferential scan. At the end of a complete scan, the MCP post processes the data set and maps it to a format for the display program. The data set is sent to the display computer by TCP/IP link.

At the end of a complete scan, the MCP commands the motor controller to retract the sensor head to its home position so a new tire can be mounted and scanned. The MCP program polls the embedded processors to check status occasionally but otherwise does not command the embedded processors unless preconditions are met.

3.6 **Data and Control Display System.**

As noted by Ortoli in Section 1.2.2, the 'user friendliness' of an inspection technique is important to assure acceptance of the technique. With the exception of the Technic system, previous inspection systems were limited to analog signal display on an oscilloscope or TV monitor. The Technic system moved one step beyond the analog display by providing a flat map of inspection points on a computer monitor. The Technic system, however, was low resolution and imaged only the tire crown. The system design presented here is capable of data acquisition with over 800,000 samples on a single tire. Display of this large amount of data in an intuitive manner is critical for the inspection system to be viable. To allow for ease of use, the inspection system features an easy to

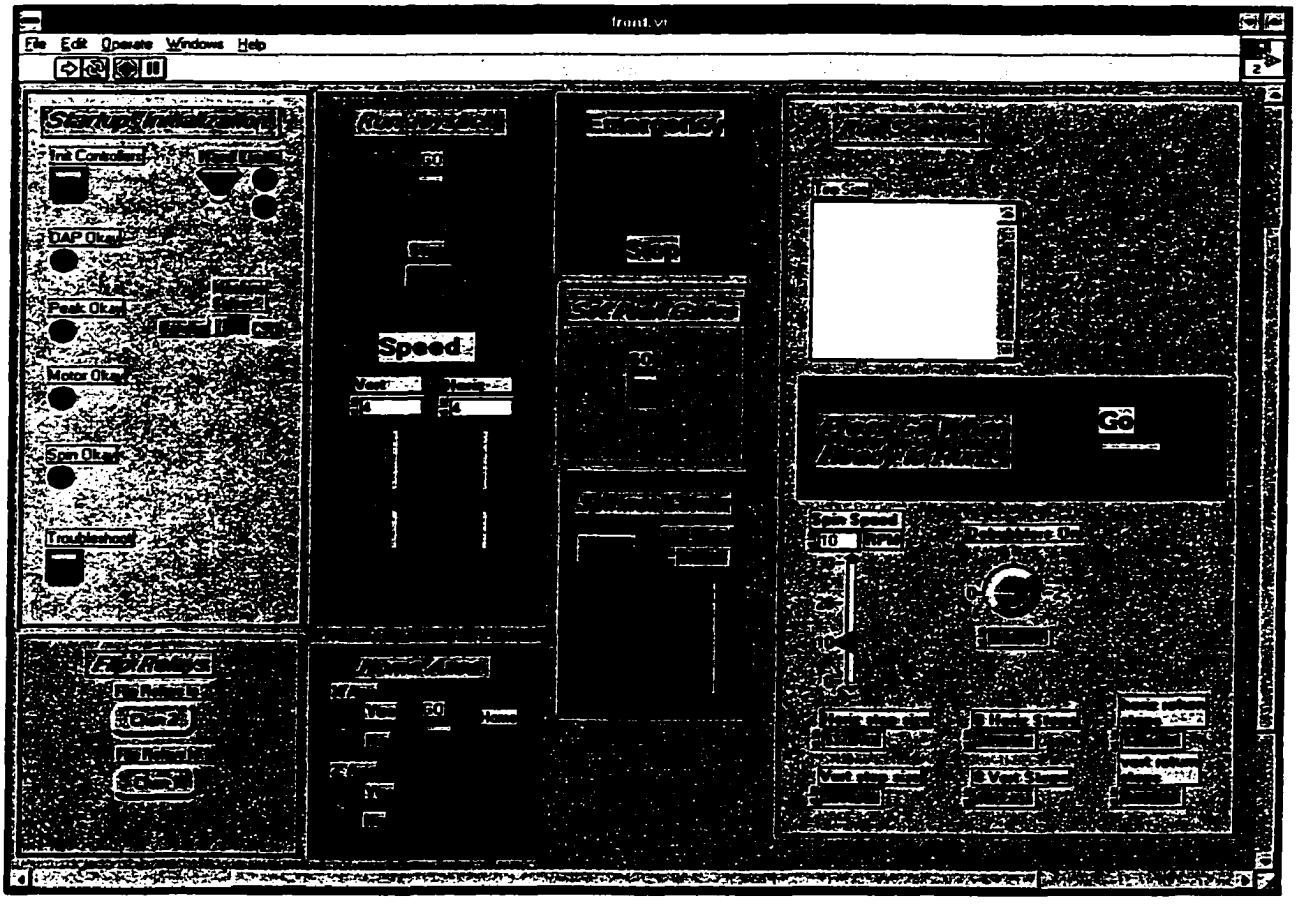

Figure 3.34: Scanner master control program panel.

use graphical interface for the operator and an intuitive map of the data. The graphical display offers point and click operation for running the system and inspecting tires. Additionally, b-scan information is displayed after each circumferential scan is complete. Figure 3.34 shows the user control panel used to set up a scan. The user selects and/or sets parameters for a scan by point and click operation. Peak detector gates are typically set at this point using an oscilloscope and manually moving the scanner head into the tire by a joystick.

Figure 3.35 shows the interface that appears during scanning. Intermediate b-scans are displayed along with autogain information. The user is able to monitor receiver

gain settings to determine if signal clipping is extant in near real time. At the end of the scan, the display reverts to that shown in Figure 3.34 to set up the next scan.

Display of the data acquired uses an intuitive means shown in Figure 3.36. The display was developed by Ellis as a portion of his MS thesis work [Ell96]. Ellis uses

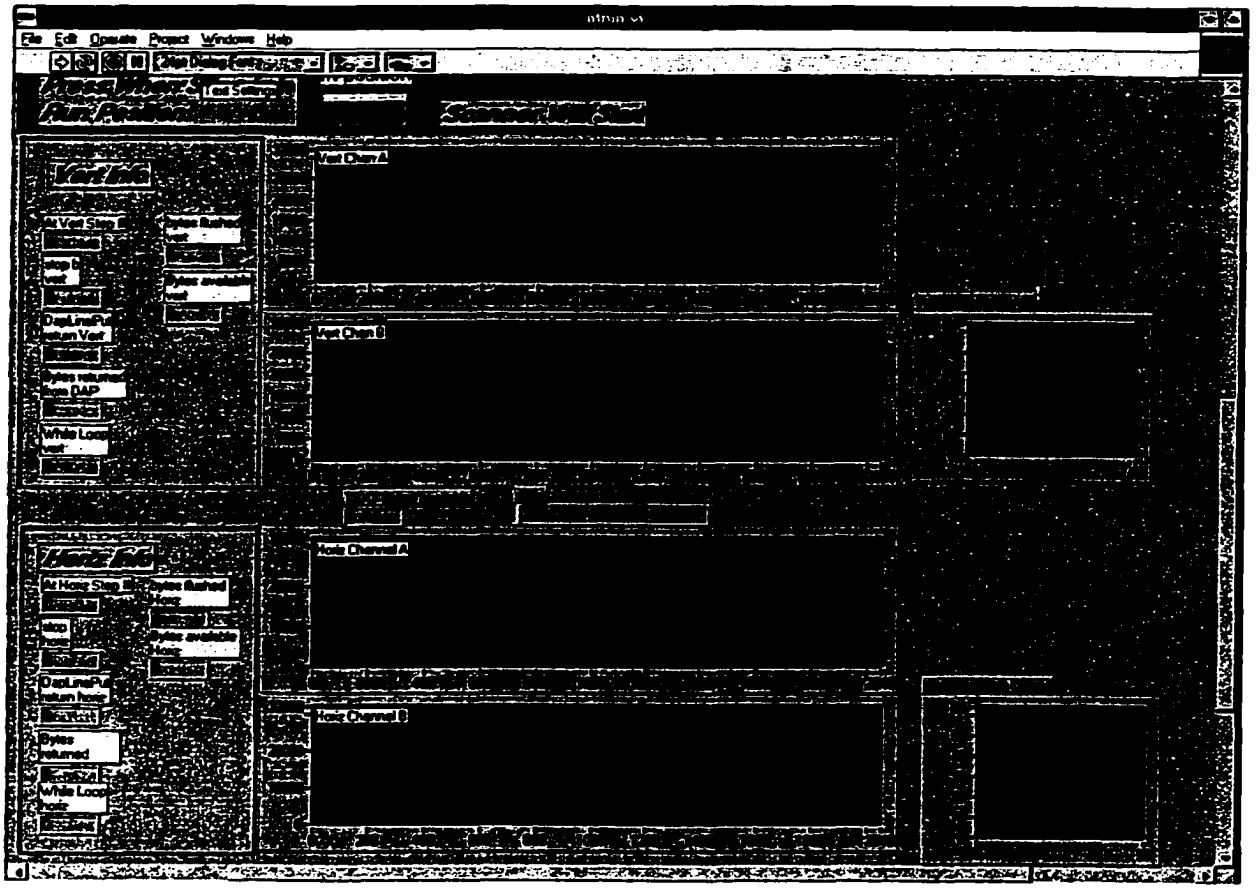

Figure 3.35: Scanning interface with b-scan graphs.

texture mapping to image the data set on a virtual tire. In the figure, data from the scan are mapped onto a virtual tire and also displayed as a flat image below the tire. The operator can zoom into specific areas or rotate the tire at will to examine specific details. Cursors and co-ordinates also provide location information so scan locations can be correlated to the tire itself.

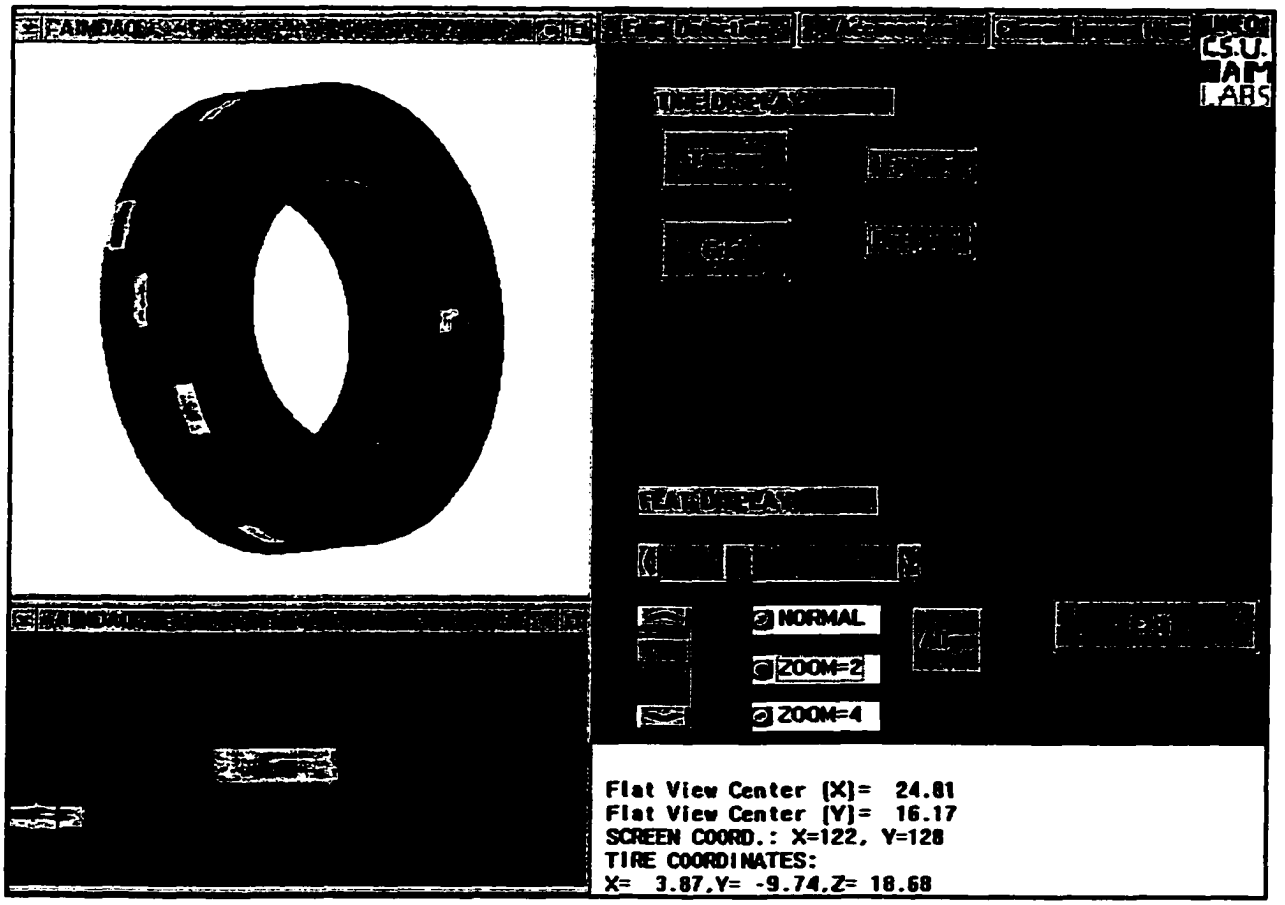

Figure 3.36: Data mapped onto virtual tire.

3.7 System demonstration.

Previous sections have described the tire inspection machine hardware and software implementation. This section presents tire scan images performed using the inspection machine developed for this work at CSU and a second machine constructed for the Bandag tire company that featured a complete set of transducers. The CSU machine used only 3 paintbrush transducers due to cost constraints and thus a full tire scan could not be made. The 3 transducers were considered adequate for development purposes. However, the Bandag machine was constructed using a full array of

transducers to inspect the entire profile. The tire images are compared with known flaws on the tires to demonstrate the system performance. Reproducibility results are presented and finally, detecting real flaws in unknown tires is discussed with limited results.

Bandag tire company provided two embedded defect tires for testing the inspection system. The tires are specially constructed with lead flaw defects inserted between layers of the tire plies to mimic actual flaws in the tires. The lead flaws act as ultrasound attenuators. A map of the embedded flaw sizes and locations was also provided to use for system response and accuracy testing. One tire was constructed with predominately large flaws and the second with small flaws and large flaws. However, prior to construction of the embedded defect tires, a method was required to begin system testing. To accommodate this need, attenuating material such as a penny or foam tape was applied to a tire to mimic the ultrasound attenuating properties of a flaw. The tire was then scanned and the image examined to determine if the attenuating material dimensions were reproduced.

Sections 3.2.1 and 3.2.2 described design of a sensor head and a motion profile to move the sensor head that ensured coverage of the entire tire. The sidewalls were to be scanned concurrently by two transducers as the tire rotated and the sensor head performed 1/8" or 1/16" steps into the tire. Since the system was design to accommodate 1/16" scans, there are 2048 data steps along each scan line in the raw data sets. (1/8" scanning is accomplished by removing every other step from the scan.) Following the sidewall scan, the sensor head was moved to a position to begin scanning the crown. The crown was scanned by two sensors concurrently as the sensor head stepped across the crown. Scanning in this way, four different data sets were recorded. Each data set was

offset by the distance of the transducer from the centerline of the sensor head as shown in Figure 3.8. Additionally, scanning the sidewalls concurrently meant one sidewall data set produced a 'flipped' image of its actual orientation since the transducer was pointed in the opposite direction. A simple diagram of the raw data sets produced by the system is

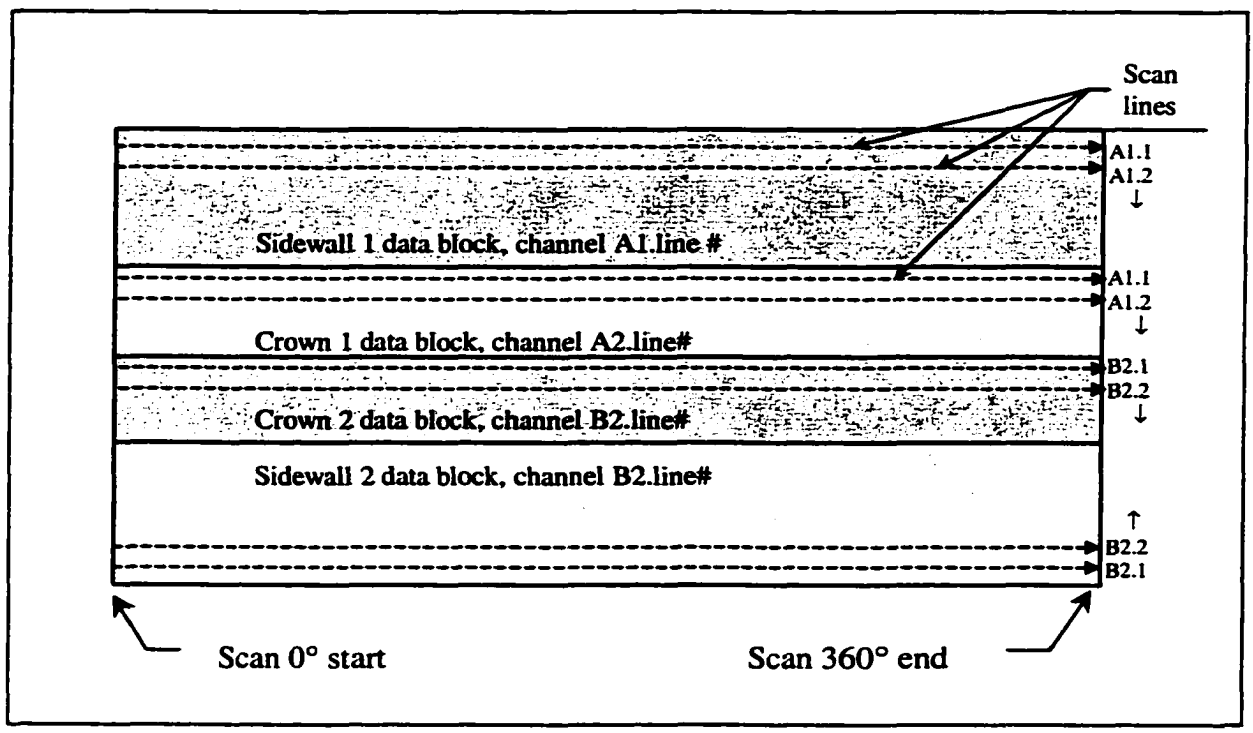

Figure 3.37: Signal block diagram.

shown in Figure 3.37. If it was possible to flatten the tire out, then each section of the tire could be thought of as a flat block of material (or data). From a 0° start, each spin of the tire produced one scan around the circumference. Each block shown in Figure 3.37 is built up of multiple scan lines.

Figure 3.38 shows an unprocessed image of a tire scan performed on August 18, 1996 using the Bandag scanner. The tire was an arbitrary sample tire selected from the Bandag retreading assembly line. As such, no flaw information was available for the tire. The figure demonstrates the raw data file format from Figure 3.37. Prior to scanning, a

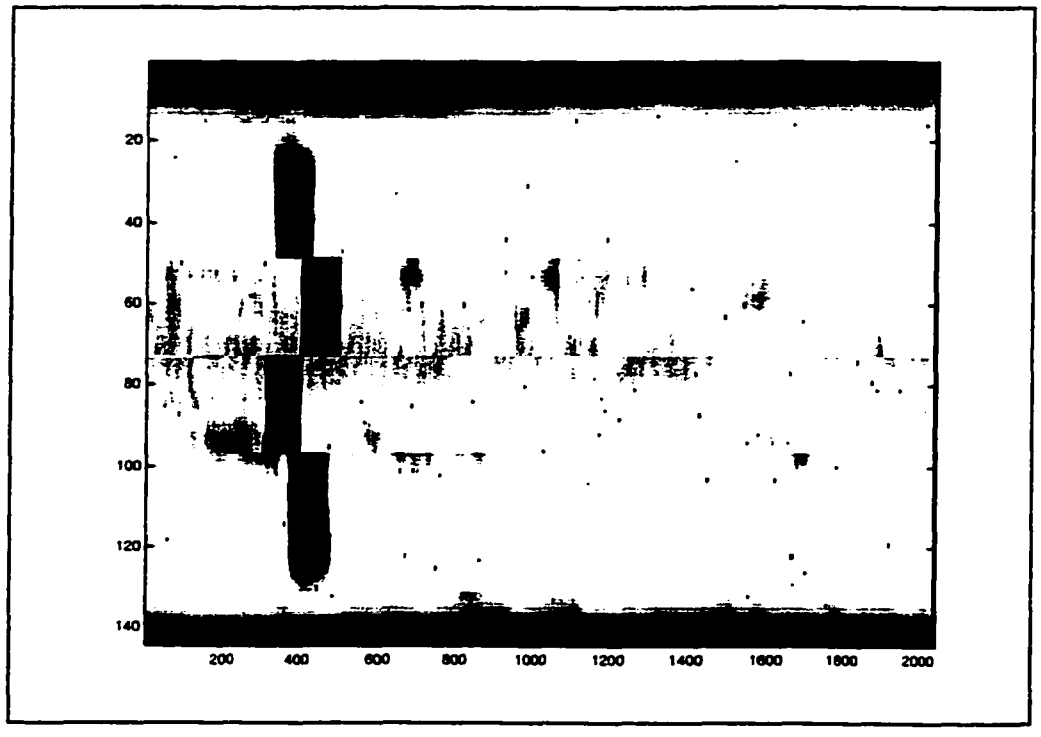

Figure 3.38: Raw output tire image.

3" strip of duct tape was fastened to the tire to use as an alignment indicator. The duct tape acts as an ultrasound attenuator whose edges are easy to locate in the image. The image pixel values have been normalized to lie between 0→1 and then adjusted for a maximum of 65 on a 0→255 grayscale. Dark areas represent regions of high attenuation.

In Figure 3.38, the duct tape is easy to see and the misalignments due to sensor head transducer offsets are apparent. Speckle noise is evident in the image. The noise is introduced into the system when peak detector gates switched on and off this was a problem on the Bandag machine (but not the CSU machine) that was not solved by this work, see Future work in Section 6.1. The dark areas at the top and bottom of the image correspond to ultrasound attenuation when the sensor head was next to the tire bead. Some additional areas of attenuation are also apparent in the tire. Figure 3.39 shows the

same image after re-alignment to correct for the transducer positions and median filtering

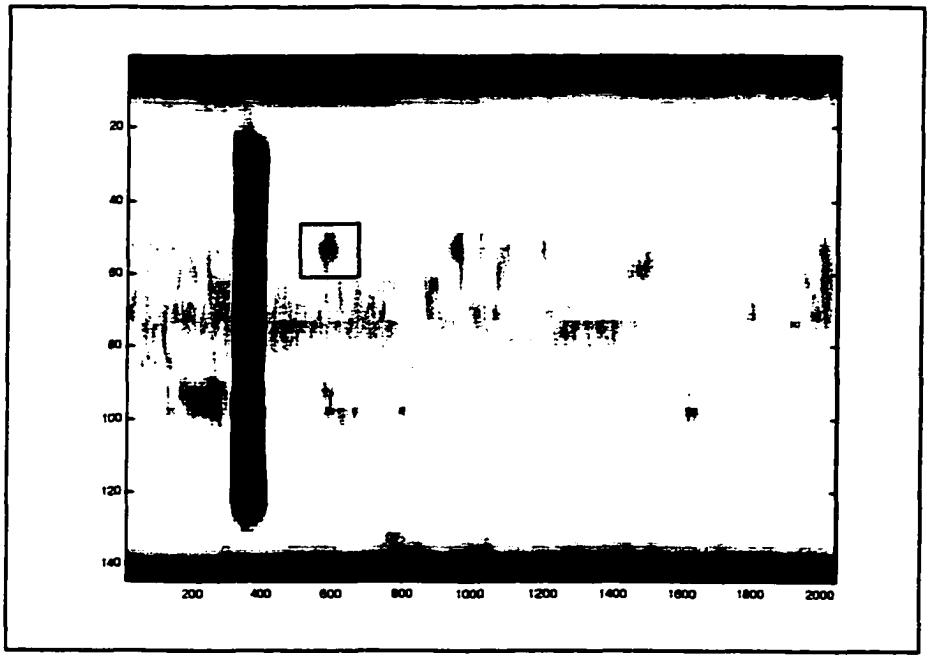

Figure 3.39: Raw data re-aligned and filtered.

to remove speckle noise.

Re-alignment should be performed for all scans prior to image analysis. Once the re-alignment is performed, flaws on the tire appear in their actual locations. Figure 3.40 shows an ultrasonic scan performed using the Bandag machine on July 11, 1996. For this inspection, the large defect tire provided by Bandag was used. The scan was performed with 35 dB amplification applied to the receivers to locate only large defects and prevent tire lugs from being detected as small attenuation changes. The data set has been median filtered to remove speckle in the scan prior to display.

The scan in Figure 3.40 shows one of the embedded defect tires described previously. A comparison of the scan with a map of the embedded defects in the tire crown, shown in Figure 3.41, demonstrates the effectiveness of the scanner at detecting

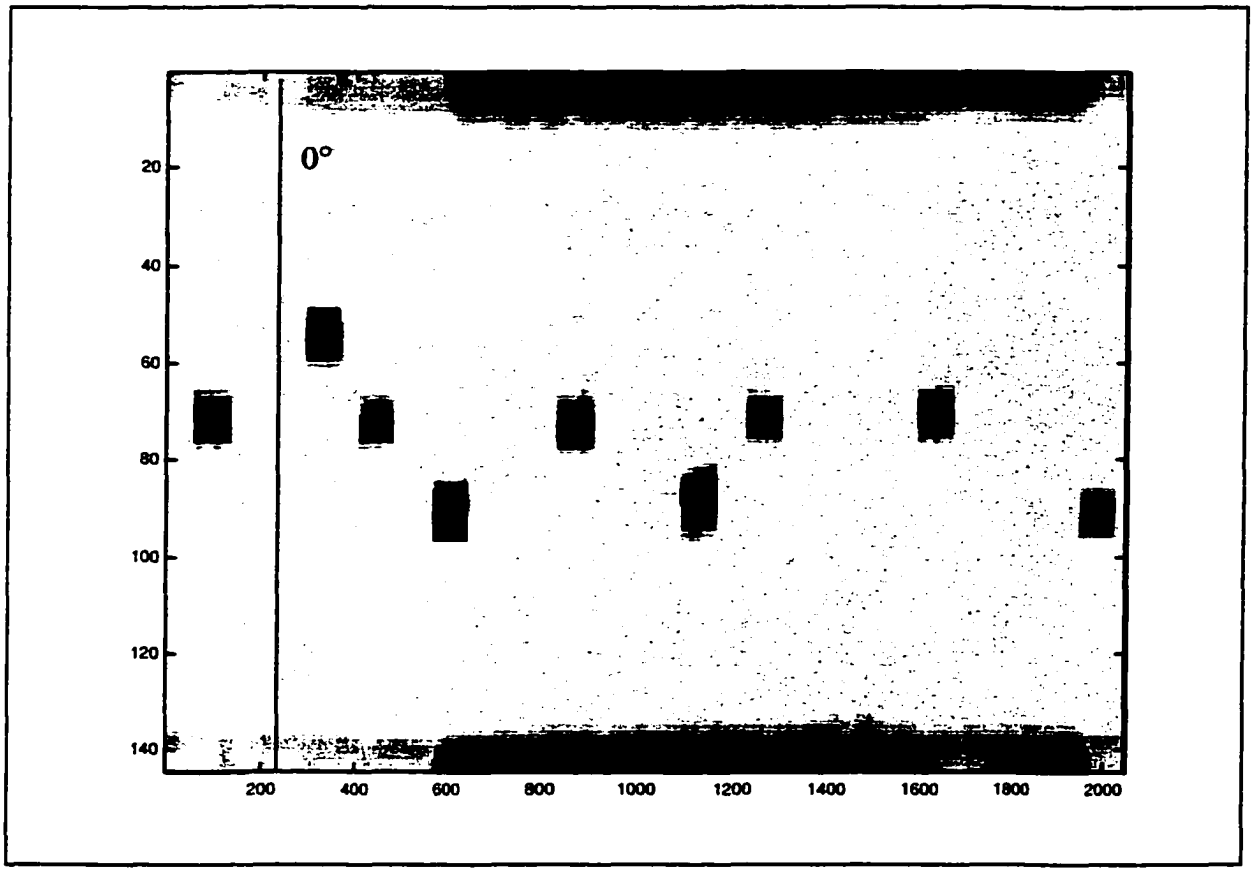

Figure 3.40: Full tire scan with embedded flaws.

gross flaws within the tire. All of the large embedded defects are detected easily. There is significant blurring of the edges due to the effects of the large ultrasonic point spread

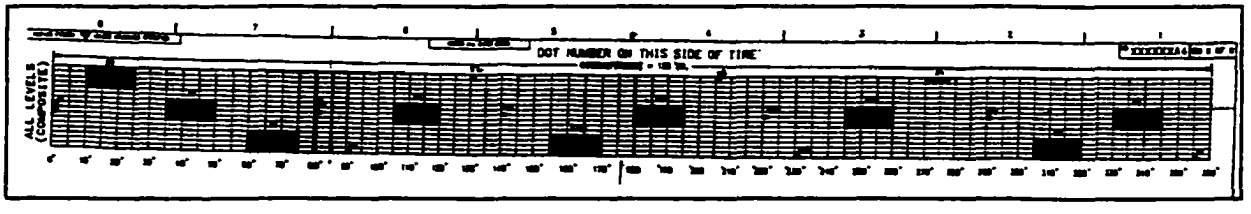

Figure 3.41: Large defect tire crown flaw map.

function (discussed in detail in Section 4). The flaw image is shifted slightly to the right side of the image since the 0° points in the image are not coincident with those in the flaw map. A 0° line has been inserted into the image and corresponds to the 0° point on the flaw map for comparison.

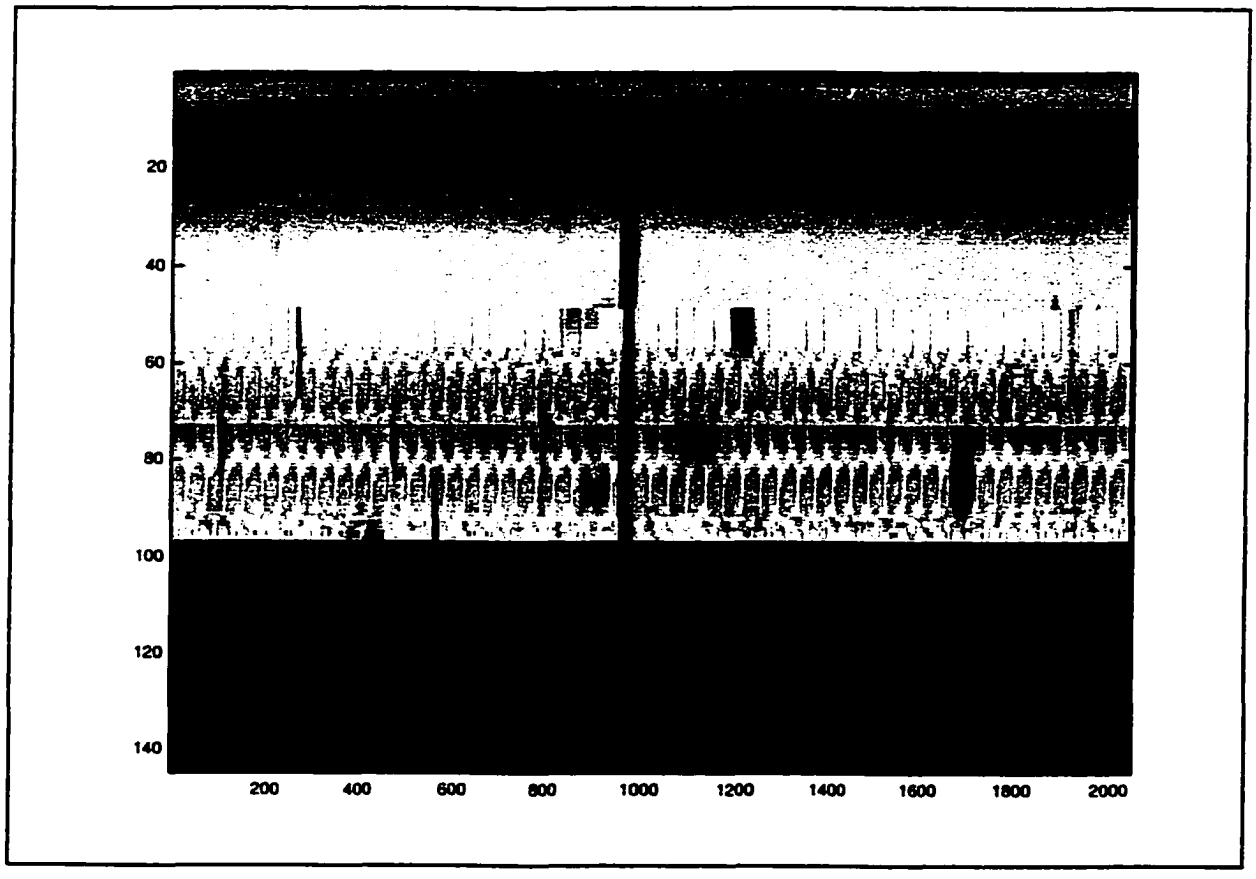

Figure 3.42: Small flaw defect tire scan (3/4 scan).

Figure 3.42 shows a scan performed using the CSU machine on February 3, 1997.

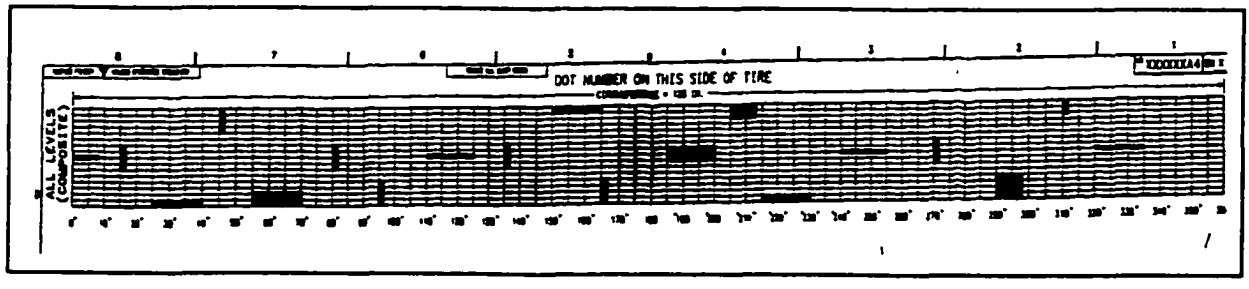

Figure 3.43: Small defect tire crown map.

The scan shows the second embedded defect tire with produced with small flaws as described earlier. (The scan is not complete on the sidewall since the CSU machine was not outfitted with a complete set of transducers due to the expense involved in purchasing

them.) Figure 3.43 shows the flaw map for the small defect tire. During scanning, the receiver amplifier gain was set to 25 dB to help accentuate the smaller flaws. Lower gain helped to accentuate small flaws by reducing the amount the relatively small differences in signal amplitude were amplified. However, tire lugs become evident in the image as minute attenuation changes. Still, all the flaws in the map are detected although blurring is evident.

Figure 3.44 shows the same images as Figure 3.42 and 3.43 combined so scanned flaws are coordinated with the flaw map and identified. Each flaw is assigned a number that identifies it with the flaw size information shown in Figure 3.45. The flaw size information chart, shown in Figure 3.45, was provided by Bandag with the specially constructed tires. (It should be noted however, that not all flaws sizes listed on the chart are included in the constructed tires. Only the sizes noted in Figure 3.44 are included. The chart is shown to provide flaw sizing information.) While all the flaws in the map are visible in the scanned image, it is evident that the flaws oriented horizontally in the display are blurred significantly more than the vertical flaws. This effect is partially due to the image dimensions where the horizontal dimension is over 10x the size of the vertical dimensions. However, the effect is also due to the paintbrush transducer insonifying a large section of tire along its long axis (see Figure 3.6). The greater insonification in one direction compared to the other contributes to a larger system PSF along the paintbrush long axis. Section 4 of this dissertation demonstrates some deconvolution techniques that can be applied to remove the blurring inherent in the system.

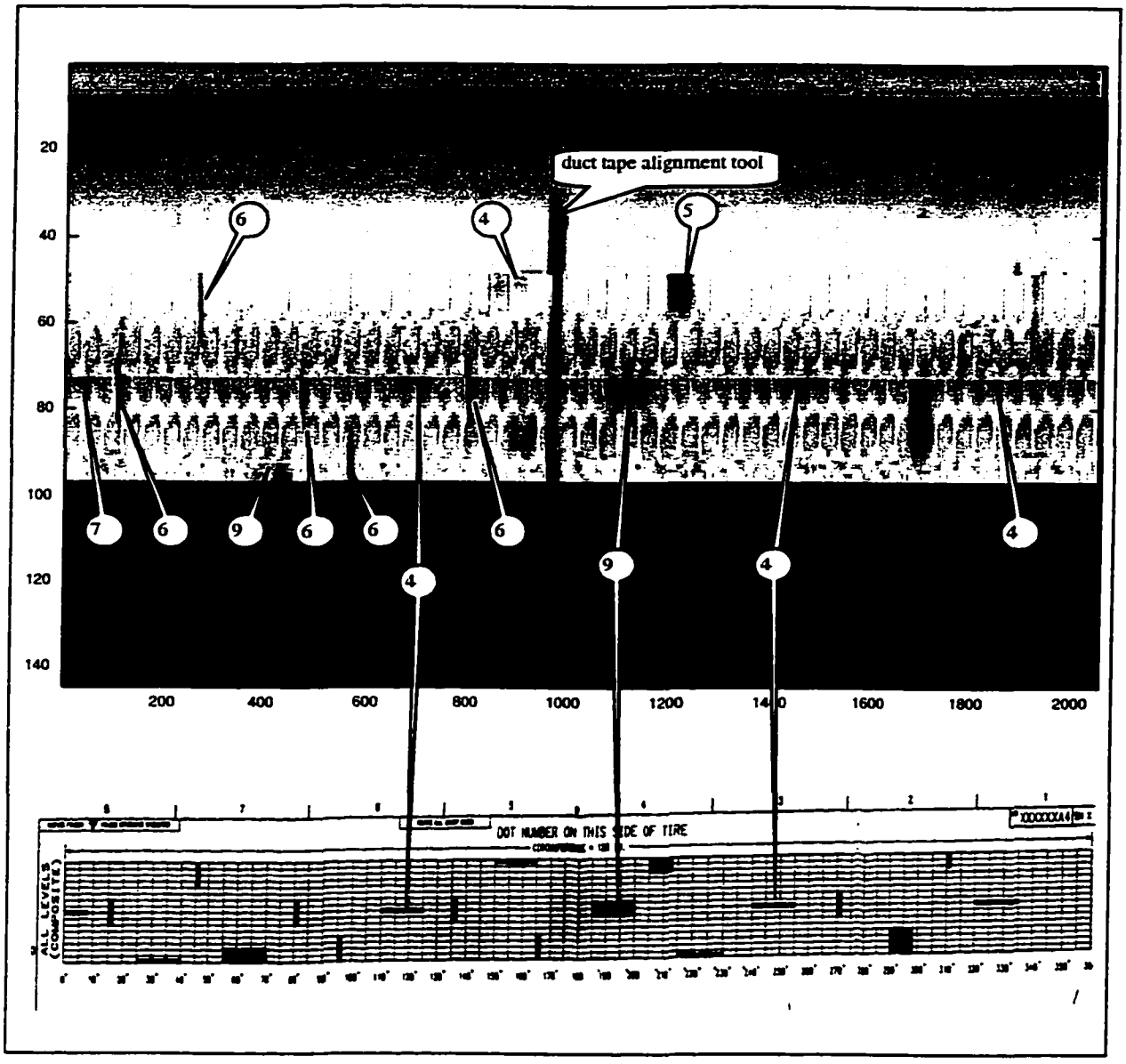

Figure 3.44: Tire scan and flaw map comparison.

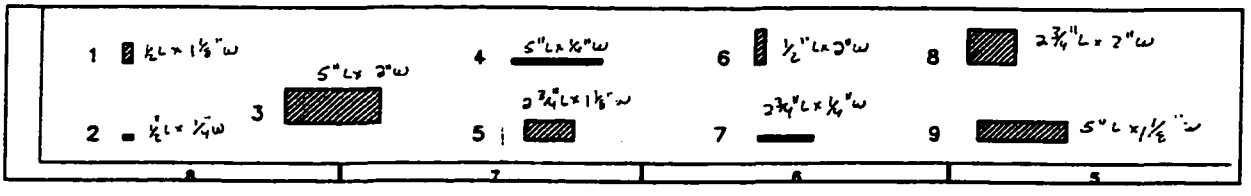

Figure 3.45: Flaw map sizing.

To examine the effects of the system PSF blurring, Figure 3.46 shows a close-up of the flaw labeled #6 in the upper left corner of Figure 3.44. Using the flaw

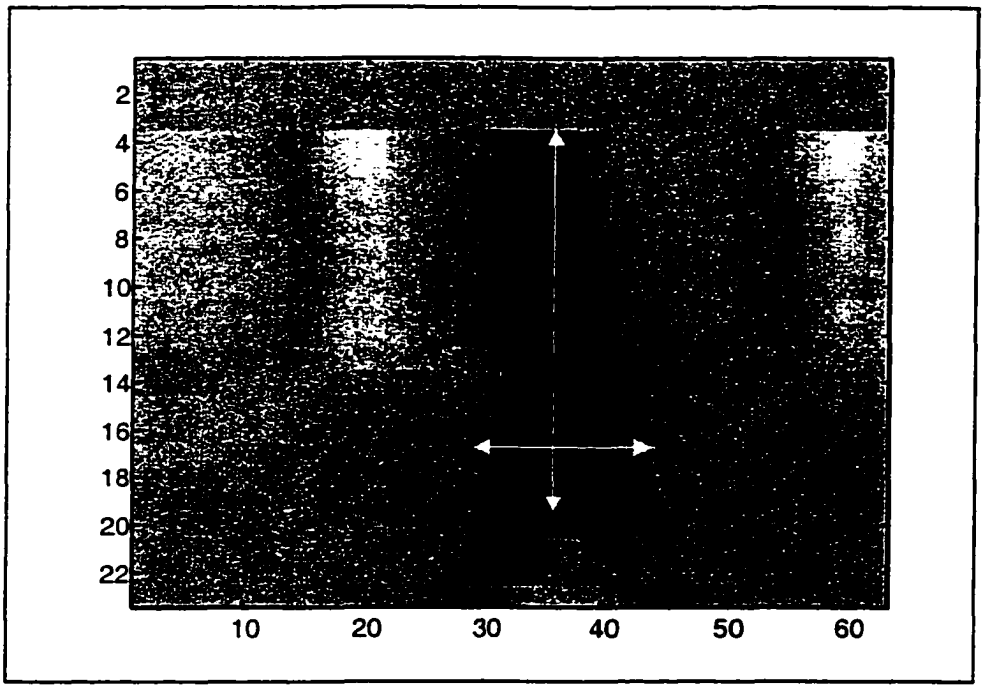

Figure 3.46: Flaw close-up.

size map in Figure 3.45, a #6 flaw is ½"x2". In the close-up image, the flaw appears with dimension of approximately 16 vertical corresponding to the 1/8" step size of the transducer motion. There are approximately 14 steps horizontal corresponding to the 1/16" resolution of the encoder generating pulses. Conversion to inch dimensions gives about 2"x1/2" as expected from the known flaw size chart.

Some informal testing of real tire flaws was performed during system test at the CSU facility and the Bandag facility. Using the CSU scanner and several tires acquired from a local tire dump, one tire appeared to have a 1" wide flaw that ran the circumference of the tire at the shoulder. Slicing the tire open showed that there was indeed a zipper defect where the tread itself was peeled away from the casing completely around the tire. During testing at the Bandag facility, another tire that showed flaw indications, shown in Figure 3.39, was sliced open for visual inspection. It was thought by Bandag engineers that the region highlighted by the square box in Figure 3.39 may be

a possible void in the material. After slicing the tire open, the material was found to not be separated but was spongy as if incomplete vulcanization had occurred. The engineers commented that proper analysis would require sending the material for testing and was not necessary at that time. These examples showed the scanner was able to detect changes in material properties as well as material disbond.

3.8 System Repeatability

An inspection system intended for use in developing the tire database requires the inspection to be highly repeatable. To demonstrate system repeatability, an ensemble average was compared against individual images to determine the 2-D cross correlation of each image relative to an average image. A set of scanned images was produced by repeated inspection of the same tire 15 times using the Bandag scanner. The images were then combined into an ensemble average $f_{avg}(m,n)$ by:

$$f_{avg}(m,n) = \frac{\sum_{i=1}^{i=15} f_i(m,n)}{15} \tag{3.20}$$

A 2-D cross correlation C_{fg} was then calculated between each individual image $g(m,n)$ and the ensemble average $f_{avg}(m,n)$ by:

$$C_{fg} = \frac{\sum_{m=1}^{M}\sum_{n=1}^{N} f(m,n)g(m,n)}{\sqrt{\sum_{m=1}^{M}\sum_{n=1}^{N} f(m,n)f(m,n)\sum_{m=1}^{M}\sum_{n=1}^{N} g(m,n)g(m,n)}} \tag{3.21}$$

Figure 3.47 shows a plot of the 2-D correlation coefficients for all 15 images. Coefficients are all within a narrow range between 0.94 to 0.96 where 1.0 is perfect correlation. This demonstrates that the system inspections are highly repeatable. Figure

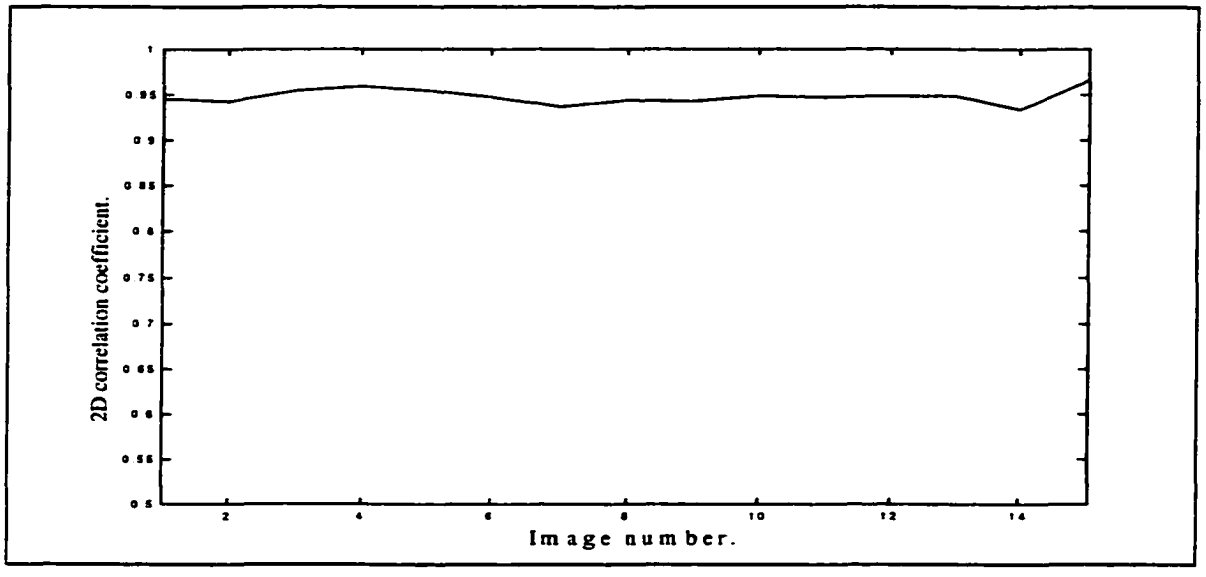

Figure 3.47: 2D correlation coefficients between ensemble average and images.

3.48 also shows the crown region of a typical image and the crown region of the ensemble average for comparison purposes. The inspected tire was a heavily lugged tire and the tire lugs are easy to discern in the examples in addition to the embedded defects.

3.9 Chapter Conclusion

This chapter has presented a method of inspecting tires that allows for high speed, high resolution inspection. Implementations of inspection system design for motion control, ultrasonic system, and data acquisition were presented. Motion control of the sensor head to cover the entire tire was shown. And finally, the chapter has shown results of scanning two embedded defect tires provided by Bandag to be used for scanner testing. The scanner is shown to be capable of resolving all the flaws in the embedded defect tires. The scanner design is shown to be highly repeatable by comparisons of repeated inspections. Unfortunately, the ultimate resolution of the scanner is uncharacterized at this time (see Section 6, Future Work). A working scanner was produced in the Advanced Inspection and Monitoring laboratory at CSU (shown in Figure 5.1) that was

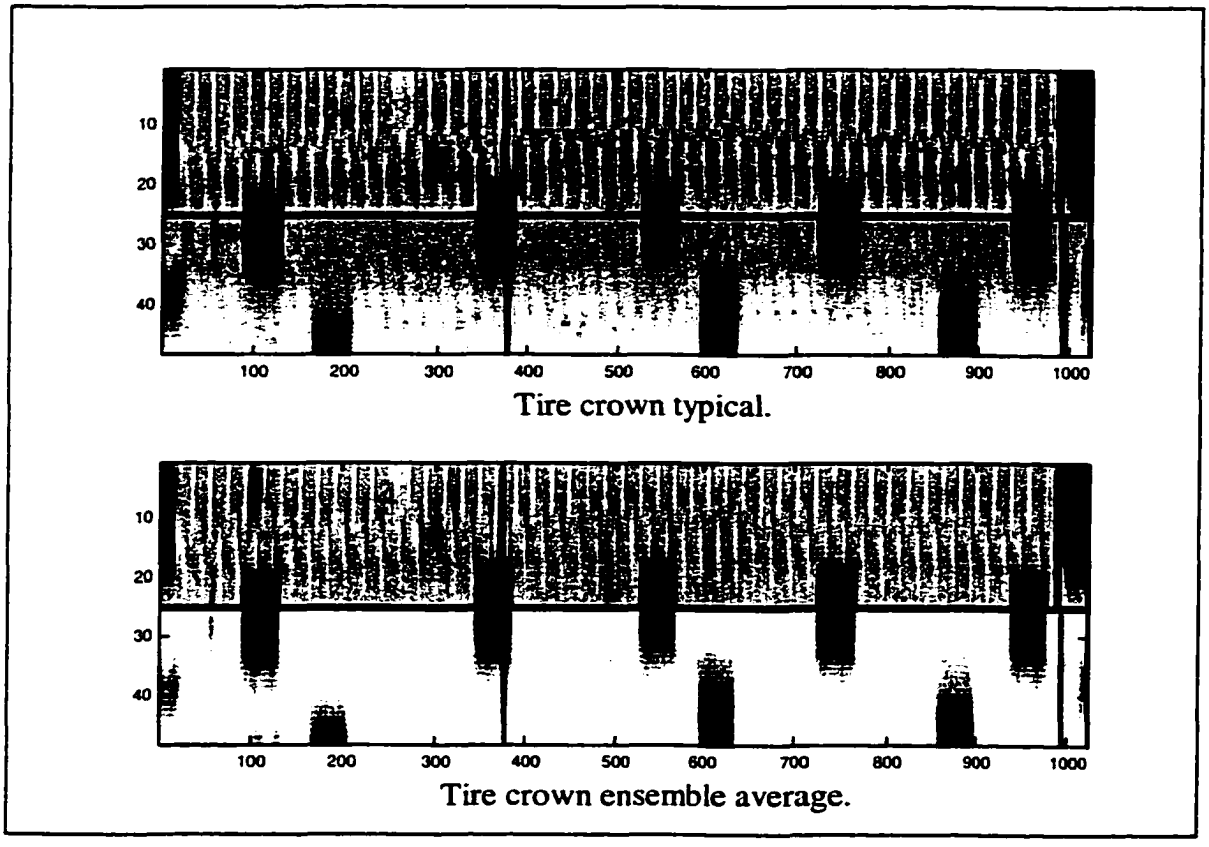

Figure 3.48: Ensemble average and typical crown scan.

used as a model to produce a second industrial scanner. The second scanner (shown in Figure 5.2) was installed on the Bandag factory floor in Muscatine Iowa for use in developing a tire database. Results from both scanners were presented in previous sections.

4. Increasing the Resolution of the Ultrasonic Tire Scanning System by a Double Deconvolution of the Spatial Point Spread Function.

Ultrasound images generated by the step and scan, through-transmission technique discussed in Chapter 3 are inherently blurred due to the effects of the system point spread function. Recovery of true flaw information by processing to eliminate the blur has been subjected to extensive analysis. One technique for removing the blur is to use a Wiener deconvolution filter. To apply the Wiener filter, prior information is necessary describing the nature of the system point spread function and any additive noise that may be present in the data acquisition system. However, if a feature in the ultrasound image can be positively identified, a double deconvolution can be performed using the prior feature information. This technique leads to a simple, direct method for enhancing the resolution of ultrasonic tire images. With additional processing, recovery and display of the system point spread function can be performed. This implementation of a double Wiener filter is novel to current tire inspection methods.

This chapter presents the need for deconvolution in this system with a short review of the PSF and blurring for a hemispherically focused transducer. A partial history of relevant deconvolution in ultrasonic NDE applications is presented. Review of deconvolution presents the mathematical foundation of some deconvolution techniques with emphasis on Wiener filtering. The theoretical PSF is applied to enhance an

ultrasound image and shown to be inappropriate. Then, experimental recovery of the system PSF by double deconvolution is demonstrated using a known flaw. The system PSF for a particular tire is used to enhance unknown features in the same tire. Using the technique, a known flaw can be placed onto a tire prior to inspection for PSF recovery. Finally, a simple direct deconvolution algorithm is derived and demonstrated.

4.1 Need for Spatial Deconvolution in the Tire Scanner.

Every transducer has a spatial point spread function (PSF) associated with it. The spatial PSF describes the sound pressure distribution moving laterally away from the central axis at some distance in front of the radiator surface. The transducer is not a perfect point focus and additional beam spread occurs in the tire material. Because of this any spatial imaging performed using the transducer is inherently a convolution of the transducer's PSF, the flaw signature that is inspected, beam spread in the material, and any additive noise that may be intrinsic to the inspection system. The PSF's of ultrasonic transducers can be relatively large, due to the small aperture relative to the wavelength, contributing significantly to blurring in an ultrasound image. The blurring becomes particularly noticeable as the flaw signature size approaches the spot size. If the PSF can be determined analytically or experimentally, the image can enhanced by deconvolution of the PSF from the experimental data.

It was desired to produce an inspection system capable of 1/16" resolution inspection. The fine resolution would allow the system to characterize very small flaws in tires. However, in Section 2.3, the operating constraints for the transducers were detailed and from Equation 2.6, the spot size for a 0.5 MHz, 1.5 inch diameter, 2.125 inch focused transducer in water yield a spot size of approximately 1/6 inch. The estimated

spot size is also the area of maximum acoustic pressure. The acoustic pressure does not decay to zero outside the spot size but degrades, in the ideal case, in a pattern modeled in the simple case by Equations 2.5.1,2.5.2. Figure 4.1 shows a plot of the PSF calculated from the equations. The plot shows a 2-D slice of the transducer pressure distribution mapped into a 3-D display for clarity. The pressure distribution is oriented laterally from the central axis at some distance x away from the radiator face. The central cone shows the region of maximum sound pressure. However, the spot size is defined at the ½ power point (-6 dB) or less than ½ the size of the central cone. While the transducer is ideally sensing only in the spot size, there is actually a large area of attenuated sound pressure

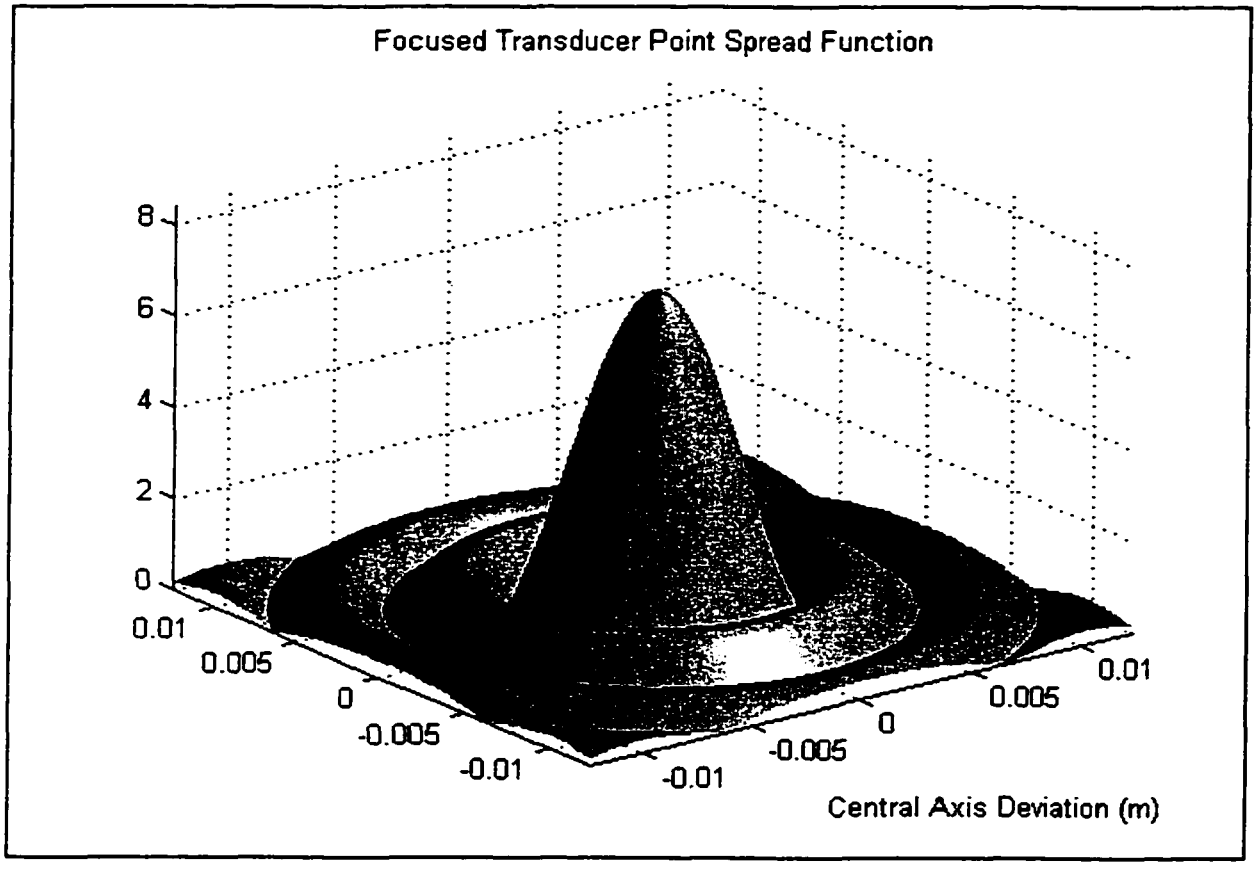

Figure 4.1: Point spread function mapped into 3-D view.

outside the theoretical spot size that contributes to the received signal.

4.2 Historical Review of Deconvolution Techniques for Ultrasonic Signals.

The importance of deconvolution in ultrasonic signal processing has long been recognized since the large PSF's associated with ultrasonic transducer systems degrade the acquired signal. Two authors well represented in relevant literature, Steven Neal and Donald Thompson, state that "The use of prior information is an important component in the detection, classification, and characterization of flaws using ultrasound. In order to take full advantage of advanced digitally-based approaches to flaw detection, classification, and characterization, use of prior information will be critical." [Nea92]. Neal further notes in a separate paper that "Digital signal processing will play a prominent role in ultrasonic NDE as the application of digital data acquisition and processing systems becomes more prevalent. A common digital signal processing step will be to deconvolve the measurement system response out of the measured signal in the presence of acoustic noise." [Nea93]. These points are well taken and are critical to the deconvolution application represented by this work. Deconvolution of the measurement system response is the prime motivation of this section.

Deconvolution of ultrasound signals has been studied for many years. A large body of work has already been performed for deconvolution in the 1-D case, with some work for the 2-D case. Ultrasonic signal deconvolution represents a broad range of problems and no single technique is applicable to more than a small range. In particular, many ultrasonic deconvolution applications target specific examples where deconvolution has been successful at enhancing one type of ultrasonic signal [Mur78][Fro91][Jen93][Zha95][Tax95][Che96][Bec97]. However, the prior efforts of

many others contributed to their ability to target specific applications with deconvolution techniques.

While Wiener first derived the deconvolution filter named for him in 1942 [Wie42], Oppenheim notes in 1975 that homomorphic filtering is used for deconvolution of signals [Opp75]. He continues that deconvolution problems can be broadly grouped into two classes: (1) estimation of speech parameters, and (2) de-reverberation. Apparently, at the time of Oppenheim's publication in 1975, little work was yet being performed in 2-D deconvolution techniques or application of deconvolution outside the above mentioned problems. However, seismologists were aware of deconvolution techniques and employed them for resolution enhancement of seismic signals [Ulr71][Ber77][Tre82].

Ultrasonic imaging has been employed for many years in medical diagnostics [Vol82][Jen93]. Vollmann seems to have pioneered the use of deconvolution techniques in ultrasound imaging in 1982 [Vol82]. His work is cited by many others as being one of the first users of deconvolution in ultrasonics. Medical ultrasonics though are dominated by the use of the *B-scan* or multiple pulse-echo techniques. The image is built up using a series of time-of-flight signatures. Since the tire scanner builds an attenuation map from step and scan techniques, the ideas used in medical ultrasonic deconvolution are fundamentally different than those used for the lateral deconvolution of the tire scanner.

This work is primarily interested in prior and current use of deconvolution applied to ultrasonic NDE techniques. A series of publications are extant detailing the gradual development of deconvolution techniques first for the 1-D case and later for the 2-D case. As noted above by Neal and Thompson (and many others), modern data acquisition

systems and digital analysis by computers have enabled significant enhancement techniques to be developed. It is apparent in the literature that while at one time just detecting a flaw using ultrasonics was sufficient, now a finer qualitative estimate of flaw characterization is desired. This is evidenced by several items. First, the seminal volume on ultrasonic inspection, *Ultrasonic Testing of Materials* [Kra90], ignores significant digital data enhancement techniques. The original volume was published in 1969 before extensive data enhancement techniques were available but the latest edition from 1990 still contains little information. Second, yearly or biennial conferences organized within the past 15 years, such as *Review of Progress in Quantitative Non-Destructive Evaluation*, are addressing the issue of further and finer characterization of ultrasonic inspection. Many inspection techniques are well understood at this time and further refinement can be addressed by increased enhancement of the acquired data. For instance, inspection of tires by ultrasound has a long history (over 50 years) as noted in Section 1.2.4. However, deconvolution has not been applied to enhance the resolution of signals acquired during ultrasonic tire inspection.

4.2.1 **NDE Ultrasonic Deconvolution Publications.**

NDE deconvolution applications can be divided into two broad categories. Axial-Wiener deconvolution refers to 1-D deconvolution using the transducer temporal response as a point spread function. Axial deconvolution is primarily concerned with time-of-flight (TOF) blurring in pulse-echo inspection. 2-D Wiener deconvolution refers to using a transducer's lateral point spread function to reduce spatial blurring in ultrasonic images. A combination of the techniques is used occasionally when TOF and spatial

blurring is possible such as in a pulse-echo, x-y scanner. It should be noted that in the tire scanner, TOF characteristics are not an issue, only the spatial blurring is a concern.

Terminology common to NDE ultrasonics applications are the use of *A-scan*, *B-scan*, and *C-scan*. The term *A-scan* refers to a single pulse-echo record. *B-scan* refers to a series of *A-scans* performed in a row to provide a sectional slice of the material to be examined. *C-scan* refers to a series of *B-scans* performed to provide a 2-D image of the material to be examined. Pseudo filtering refers to the use of constant estimates for noise and PSF parameters when the actual parameters are unknown.

As previously noted, a series of deconvolution publications exist that chronicle the development of applied deconvolution in NDE ultrasonics. Probably the first is Murakami *et al*, who applied Axial-Wiener filtering to deconvolve the "transducer response signal" (now referred to as the PSF) from a single *A-scan*. It is interesting to note that their measurement and analysis apparatus consisted of a "sampling" (not digitizing) oscilloscope that outputs a slowed down version of the pulse received. The slowed pulse is digitized by a separate digital to analog converter whose digital output is then used in a PDP 11-10 minicomputer for Fourier transform and deconvolution [Mur78]. The PDP 11-10 probably used a significant amount of time to perform the single scan deconvolution. While this was state of the art at its time (only 20 years ago), this type of analysis would now be considered simple with only a small PC and could be performed in milliseconds.

Hundt 1980

The work of Hundt *et al* is frequently cited in NDE literature as an important contribution to the development of using deconvolution in ultrasonic signal processing.

The work uses a 1-D deconvolution to process *B-scan* data and improve lateral resolution by removing the lateral impulse response of the transducer from the acquired scan. A 'kernel' is recovered from a point reflector target and used for deconvolution. The kernel is actually an experimentally recovered 1-D slice of the 2-D PSF shown in Figure 4.1 showing the first use of experimentally recovering the PSF. Hundt is the first to note that digital signal processing of ultrasonic signals is increasingly important [Hun80].

Vollman 1982

Vollman's work is also cited by many subsequent authors as one of the beginning steps in ultrasonic signal deconvolution. He recognizes Hundt's previous work noting the resolution enhancement and analyzes the degree of enhancement possible by Hundt's technique for various signal to noise ratios. Vollman's work assumes a fixed Gaussian point spread function and provides results showing a fixed enhancement parameter R can be derived for given signal to noise ratios [Vol82].

Clark 1986

Clark *et al* uses a semi-homomorphic deconvolution technique involving spectrum extrapolation to enhance *A* and *B-scans*. He casts the deconvolution problem as a *systems identification* problem where the PSF of the transducer-measurement system must be determined. He notes that for this purpose, system identification and deconvolution are identical. The method is essentially an application of PSF recovery where the PSF is eliminated from the image. He notes in conclusion that the novelty of his approach is that actual experimental NDE data are used for the first time to attempt deconvolution [Cla86]. His final comments demonstrate that applied deconvolution in NDE applications is relatively new.

Neal 86-88

Neal and Thompson published a series of papers in this time that examined the effects of prior flaw information on the outcome of Axial-Wiener filtering [Nea86a][Nea86b][Nea88b]. Neal notes that the Wiener filter requires some form of prior information about the PSF of the transducer and some estimate of the noise included in the signal. However, some prior referenced work including Marakami above has used what he refers to as a 'desensitization' form of the Wiener filter. The form is so called because of the use of a constant term that estimates noise parameters to 'desensitize' Fourier domain division where the denominator may approach zero. Neal's work focuses on the use of the 'classic' Wiener filter where prior noise information is required. In particular he examines the effects of various amounts of prior noise information and concludes that for poorly characterized flaws, a prior knowledge based filter shows improved results relative to the desensitization filter. Neal concludes this period in his Ph.D. dissertation that demonstrates an optimal prior knowledge filter for 1-D deconvolution [Nea88a].

Chen 1988

Chen *et al* in a very short paper (2 pages) compares several 1-D deconvolution types. The methods considered are Axial-Wiener filtering, spiking filter deconvolution, time domain deconvolution, and L1 norm deconvolution. Mathematical details are not presented in the paper. Chen concludes that there is no clear choice as a deconvolution technique but that Wiener filtering works as well as any and is less computationally expensive and so should be the logical choice [Che88].

Hayward 1989

Hayward and Lewis provide a second comparison of 1-D deconvolution techniques. The techniques examined are:

1. the Wiener pulse shaping filter
2. the two-sided Wiener filter
3. the weighted Least Squares filter
4. Mendel's minimum variance deconvolution
5. Oldenburg's frequency domain deconvolution
6. L1 norm deconvolution

Assessing the performance of each technique, they conclude that the L1 norm deconvolution technique offers the best resolution enhancement. However, computation times to implement the deconvolution were 1,250-7,500 times that of the Wiener filtering methods. Other than the L1 deconvolution, no others showed clear superiority in resolution enhancement[Hay89].

Chen 90

Chen and Sin's next paper provides a review of the need for deconvolution in NDE systems and present a survey of deconvolution algorithms for 1-D deconvolution. In particular, the work uses the Wiener desensitization deconvolution noted earlier by Neal, spectral extrapolation similar to Clark, L2 least-squares deconvolution (Wiener with optimal parameters known), L1 least absolute error and MVD, all discussed in Hayward's work above. Simulation results are presented and show that the use of spectrum based deconvolution is superior [Che90].

Frock 1988-91

Earlier works of Frock [Fro88][Kar89] [Fro90] are cited by Cheng [Che96] as being instrumental in the development of Axial-Wiener deconvolution and later in the development of 2-D deconvolution techniques. Frock specifically proposed using the 2-D lateral pressure distribution (PSF) of a focused transducer in deconvolution to enhance

the resolution of a 2-D ultrasound image. In 1990, Frock proposed using pseudo 3-D Wiener deconvolution to enhance image resolution. Pseudo 3-D deconvolution is a technique that employs a combination of Axial and 2-D Wiener deconvolution. In 1991, Frock demonstrated the effects of Axial-Wiener deconvolution on the lateral resolution of *C-scan* images [Fro91]. Simple 1-D Wiener deconvolution is used throughout with the PSF's simulated and noise modeled as a constant. Frock's work is demonstrated in later publications to be seminal in the development of 2-D ultrasonic deconvolution.

Kechter 1991

Kechter and Achenbach combine linear and homomorphic deconvolution in a new 1-D technique to recover flaw impulse response. The technique requires both flawed and unflawed ultrasonic signals and is essentially a PSF recovery from the unflawed signal that is later used to deconvolve the flawed signal and determine true flaw characteristics [Kec91].

Jensen 1992

Jensen has a long publication record primarily applicable to medical *B-scan* imaging where temporal deconvolution is being performed. However, the temporal techniques developed to enhance medical ultrasound images are also applicable to NDE *B-scan* inspection. Ultrasound in the human body is scattered tremendously by small density changes and corresponding velocity changes. The techniques presented by Jensen would also be applicable to NDE fine grained composite material inspection where material property changes are common throughout the material [Jen91].

Mitchell 1992

Mitchell and Gilmore present one of the first true applications of 2-D Wiener deconvolution to real data. Scans are in pulse-echo mode by a step and scan technique. Periodogram and autoregressive estimates are made for noise parameters and compared. They are the first to implement recovery of the 2-D PSF using a small flaw as representative of the system impulse response. The recovered PSF is then used to deconvolve an ultrasound 2-D scan. The work focuses on specially constructed targets without attempting to deconvolve a field scan. They do note that while the autoregressive estimate provides a good noise parameter, good estimates for the PSF are still unknown [Mit92].

Neal 1992

Neal notes here that "prior information is an important component in the detection, classification, and characterization of flaws". The work presented is a continuation and development of previous work and establishes a methodology for analyzing ultrasonic scattering amplitude as a random variable. The result of random variable analysis show that the scattering amplitude distribution cannot be determined analytically. This by necessity means that some prior knowledge needs to be included in Wiener filtering for an optimal solution [Nea92].

Sin 1992

Sin now with Chen provides yet another comparison of deconvolution techniques. Little new ground is broken over the 1988 and 1990 papers although there is a sprinkling of new simulation information[Sin92].

Neal 1993

Neal *et al*, and with previous partners, ranks with Frock and Vollman in their contributions to deconvolution technique. This paper describes another extension to his previous work and details true flaw signature estimation using a Wiener filter with limited prior information. This work is effectively a culmination of all the previous effort. While Neal's work is devoted entirely to the 1-D temporal case, his conclusions in this paper state that his previous and current work will be extended to the 2-D case. Unfortunately, no results have been forthcoming on deconvolution from Neal since this effort [Nea93].

Jensen 1993

As previously noted, Jensen's work is primarily relevant to medical ultrasonics. There is still some crossover between medical and NDE ultrasonic applications. Jensen uses Axial-Wiener deconvolution for *B-scan* images and develops a procedure for estimating the covariance of the noise and signal. This is critical in Wiener filtering as noted by all other authors and in particular Neal [Jen93].

Xin 1993

Xin and Bilgutay develop 1-D L1 norm deconvolution and demonstrate a simple application. They note previous techniques are capable of providing high resolution enhancement but require complete *a priori* knowledge of the system PSF. This knowledge is generally not available. However, information can be recovered from a spectral histogram that can lead to estimation of the system PSF. They do also note that their technique is particularly sensitive to noise [Xin93]. Previous authors have noted though that the L1 norm deconvolution while superior to other techniques is computationally expensive. This is not discussed in the Xin paper.

Cheng 1995

Cheng *et al* derive a pseudo-inverse filter similar to a standard Wiener filter. Image generation is by synthetic aperture ultrasonic holography and so is slightly different than using standard transducer in pulse-echo or through transmission. However, their filter uses an estimated constant for noise parameters showing the common use of this technique [Che95].

Subbarao 1995

This paper, while unrelated to NDE, does develop a technique for focused image recovery from two unfocused images. The requirement for the method is that the camera settings, such as focus, be different and distinct for the two unfocused images. 2-D Wiener deconvolution is used in the technique. This paper implies that if ultrasonic images were produced using different focuses, the system PSF could be recovered directly without any prior knowledge [Sub95].

Taxt 1995

Taxt's work is primarily related to medical ultrasound. Homomorphic deconvolution is used while ignoring noise in the system. The work is included here to provide background in homomorphic filtering as discussed later [Tax95].

Unluturk 1995

This paper presents an interesting application of Neural Networks to the deconvolution problem. While not directly related to the work presented in this thesis, his investigation of a new deconvolution technique demonstrates the recent expansion in deconvolution investigation. The work focuses particularly on detecting and resolving flaw signatures in noisy data [Unl95].

Zhao 1995

Zhao *et al* investigate standard Wiener deconvolution using a fixed noise constant, block filtering to remove low-frequency components from a high-frequency signal, and a combination of the two approaches. High-frequency ultrasound is attenuated to a greater extent than low-frequency signals in an elastic medium so that undue blur may be introduced when the low frequency signals are recorded with a higher amplitude than the high frequency. The block filter ideally removes the lower frequency components. The PSF is estimated analytically. This study uses 8 MHz ultrasound for inspection of an ideal target immersed in water. Standard deconvolution techniques are also used with typical results. A combination of the two techniques shows greater improvement than either one alone [Zha95].

Cheng 1996

One of the most recent investigations and probably closest to the work presented in this thesis is that of Cheng *et al*. The technique involves recovery of the PSF by pulse-echo scanning a point reflector target in an ideal sample. The recovered PSF is then used for deconvolution of *C-scan* images in unrelated samples. The technique uses temporal and lateral PSF information available from the pulse-echo scan to perform a 3-D deconvolution using Wiener deconvolution and a fixed noise constant [Che96]. Differences in Cheng's technique from those presented here are the use of separate materials to recover the PSF and then apply it, the contrived laboratory setup for data collection as opposed to using experimental data from multiple targets, and use of two deconvolutions instead of the direct deconvolution presented here.

Downs 1996

Downs and Peterson presented a review of convolution and deconvolution for a 2-D through transmission ultrasonic inspection, simulated results, and initial results of using a known flaw signature for experimental recovery of the PSF. The recovered PSF was then used to enhance the resolution of real data images. Using a simply modeled PSF derived from classic equations proved not be a viable technique when applied to real data, necessitating the need to recover the actual system PSF. The technique shows that recovering the PSF for use in deconvolution is an acceptable technique to enhance the resolution of through transmission inspection *C-scan* images [Dow96].

Bechou 1997

The most recent deconvolution study available is an applied study of deconvolution techniques in an industrial setting to inspect solder joints on a printed circuit board. The study derives an analytic PSF and deconvolves images using a Lucy-Richardson algorithm that is not explained. Iteration during deconvolution minimizes blur [Bec97].

It is evident that there is a long history of deconvolution in ultrasonic NDE. With the exception of Bechou, it can be observed that all the 2-D studies to date are carefully setup laboratory experiments. PSF recovery from experimental data is demonstrated only by Mitchell, Cheng, and Downs [Mit92][Che96][Dow96]. In general, the PSF recovery techniques work for the one experiment they are used in. With the exception of Downs, the recovery techniques demonstrated in the literature determine a PSF on one object and then apply the recovered PSF to a different object. It should not be assumed that the PSF

from one object can be applied directly to another unless inspection conditions are identical. However, as noted by Andrews, if there is reason to assume a point reflector is available in an image, the point reflector can be used as a PSF [And77]. The same idea can be extended to any known entity in an image. It is possible to derive the PSF from a known entity and the convolved entity image. This technique s demonstrated in the preliminary paper by Downs [Dow96]. Recovery of the inspection system PSF in ultrasound tire inspection images using a known entity in the ultrasound image has not been demonstrated in the literature. The system PSF is not only a function of the transducer PSF but also the operating conditions of the system as noted earlier.

4.3 **Convolution and Deconvolution.**

The raw output of any sensing system will always be a convolution of the sensor impulse response and the ideal signal itself [Ros82]. Convolution is often overlooked since the impulse response of the sensor is benign when combined with the ideal signal itself. As noted, the impulse response of an ultrasonic transducer is a large PSF with side lobes that contribute significantly to inaccuracies in measurement of an ideal signal. This section presents how convolution occurs in the 1-D case and extends to the 2-D case. Methods of deconvolution are examined with noise inclusion covered. Limitations of the technique are discussed. A numeric simulation is presented justifying the technique and then experimental testing of deconvolution on actual tire data is performed. The data are analyzed using a classically modeled PSF for deconvolution and then experimental recovery of the PSF is presented with results.

4.3.1 **Convolution.**

To examine the 2-D case, a simple model of 1-D convolution serves to begin exploration of the concepts. Mathematically, the 1-D continuous case is represented by the convolution integral [Sil87]:

$$g(x) = \int_{-\infty}^{\infty} h(x) f(x - x')dx' = h(x) * f(x) \tag{4.1}$$

where:
$h(x)$ = sensor impulse response (PSF)
$f(x)$ = ideal signal
$g(x)$ = convolved signal

The variable x is classically time for the 1-D case but can be thought of in terms of a 1-D position vector. Equation 4.1 shows that at any point x', the output signal is a sum of input signal $f(x')$ combined with the impulse response of the sensor $h(x)$ for all x. The meaning of this becomes more apparent by an example from the discrete case. For a discrete, finite length 1-D ideal signal $f(m)$ of length M and a PSF function $h(i)$ of finite length I, convolution can be represented as [Ros82]:

$$g(p) = \sum_{k=0}^{P-1} h(p - k)f(k) = h(p) * f(p) \tag{4.2}$$

where:
P = $M+I-1$
$g(p)$ = discrete convolved signal
$h(i)$ = discrete PSF
$f(m)$ = ideal signal

Figure 4.2 shows a graphic representation of the meaning of Equations 4.2. In the figure, two discrete signals are convolved forming a third. Below the figures are discrete values representing signal levels. The convolved signal bears little resemblance to the ideal signal.

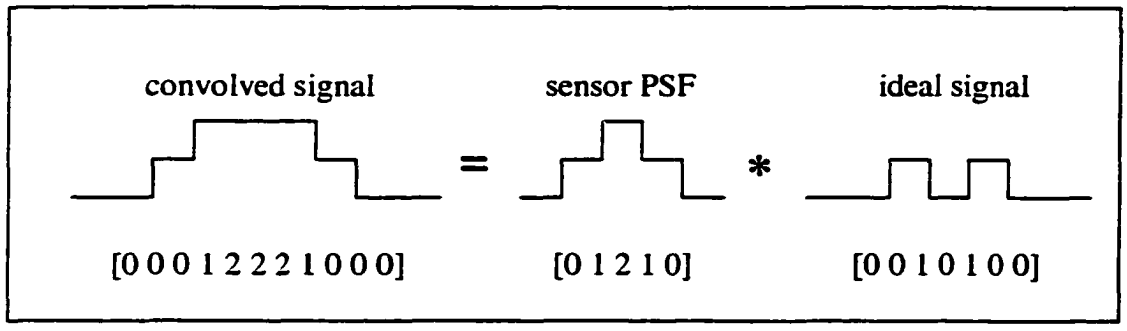

Figure 4.2: Convolved signal.

An example of how the signal becomes convolved in a spatial domain is presented in Figure 4.3. In the figure, at position A, the transducer "sees" some attenuation due to the flaw but only through the –6 dB zone of the PSF. At position B, the transducer sees attenuation due to both flaws through the –6 dB zone and through the spot size. Finally, at position C, while it is starting to move out of the flawed area, both flaws are still detected. The two small flaws appear as one large flaw as shown in the convolved scan in Figure 4.3. The PSF is actually continuous but the stepped motion of the receiver discretizes the data acquired.

For the tire inspection system, the paintbrush transmitter continuously insonifies the tire surface. The receiver scans the flawed sample in discrete steps. As noted, the step size will discretize the received signal. It is possible in the system to step the receiving transducer in increments that are smaller than the PSF of the transducer. The presence of a flaw will be detected in more than one increment as shown in Figure 4.3. Because of this, the flaw appears to be larger than the actual size. A 2-D image that is produced by combining a series of scans as above will incorporate flaw information from adjacent scans in the same fashion. It is necessary for the receiver steps to be smaller than the PSF to exploit the overlapping nature of the PSF for deconvolution to enhance the resolution of the image.

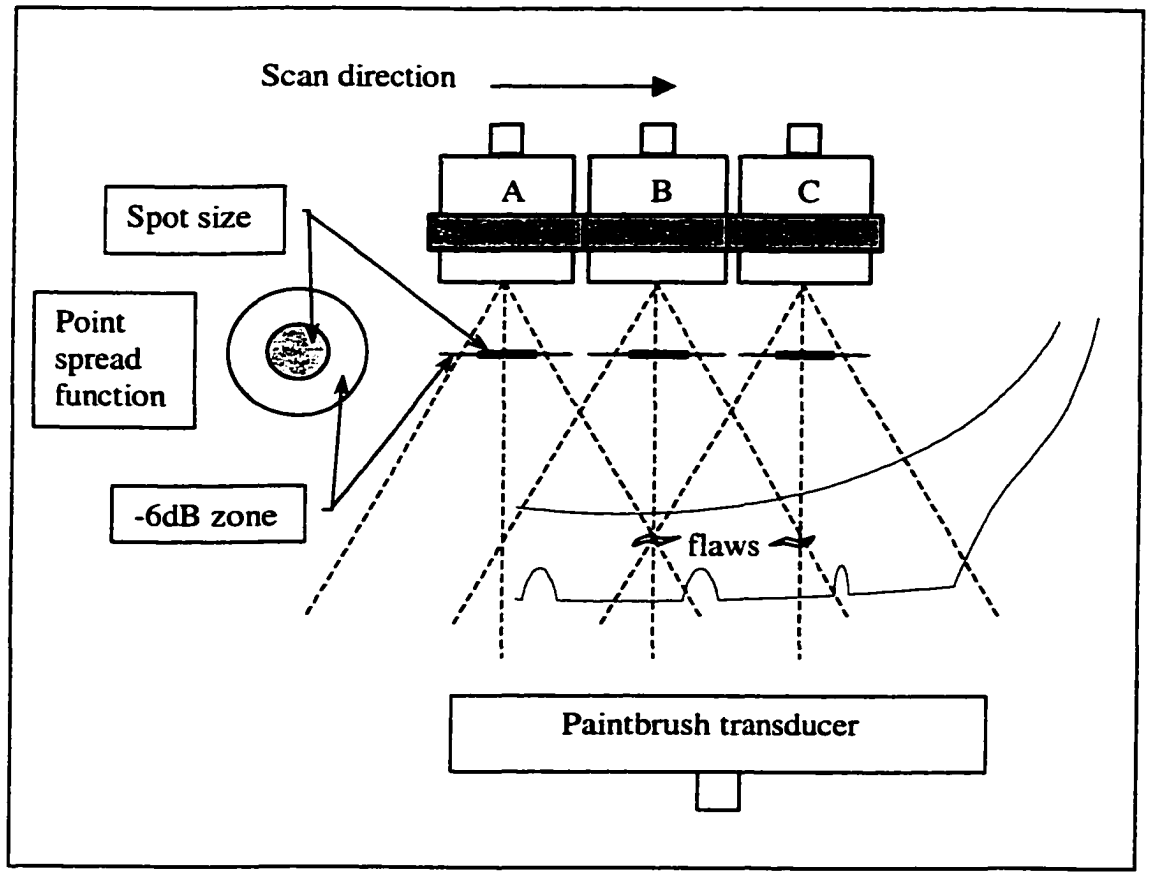

Figure 4.3: 1-D spatial convolution.

For 2-D convolution of continuous functions, Equation 4.1 can be extended so that [And77]:

$$g(x,y) = \int_{-\infty}^{\infty}\int_{-\infty}^{\infty} h(x,y)\, f(x-x', y-y')dx'dy' = h(x,y) * f(x,y) \qquad (4.3)$$

and Equation 4.2 can be extended so the convolution $g(p,q)$ of an MxN ideal image $f(m,n)$ and an IxJ PSF $h(i,j)$ can be expressed as [Ros82]:

$$g(p,q) = \sum_{k=0}^{P-1}\sum_{l=0}^{Q-1} h(p-k, q-l) f(k,l) = h(p,q) * f(p,q) \qquad (4.4)$$

where:

$P = M+I-1$
$Q = N+J-1$
$g(p,q)$ = discrete convolved signal
$h(i,j)$ = discrete PSF
$f(m,n)$ = ideal signal

Equation 4.4 denotes the basic convolution sum that causes blurring of the images presented in this section. This can be numerically represented in an example as:

$$\underset{g(p,q)}{\begin{bmatrix} 0 & 0 & 0 & 0 & 0 & 0 & 0 \\ 0 & 0 & 1 & 0 & 1 & 0 & 0 \\ 0 & 1 & 4 & 2 & 4 & 1 & 0 \\ 0 & 2 & 6 & 4 & 6 & 2 & 0 \\ 0 & 1 & 4 & 2 & 4 & 1 & 0 \\ 0 & 0 & 1 & 0 & 1 & 0 & 0 \\ 0 & 0 & 0 & 0 & 0 & 0 & 0 \end{bmatrix}} = \underset{f(m,n)}{\begin{bmatrix} 0 & 0 & 0 & 0 & 0 \\ 0 & 1 & 0 & 1 & 0 \\ 0 & 2 & 0 & 2 & 0 \\ 0 & 1 & 0 & 1 & 0 \\ 0 & 0 & 0 & 0 & 0 \end{bmatrix}} * \underset{h(i,j)}{\begin{bmatrix} 0 & 1 & 0 \\ 1 & 2 & 1 \\ 0 & 1 & 0 \end{bmatrix}} \tag{4.5}$$

It is easy to see that the ideal scan $f(m,n)$ is blurred significantly by the PSF $h(i,j)$. However, while the convolution sum $g(p,q)$ indicates it is theoretically possible to perform a signal convolution with values as high as 6, in an actual system gain limiting in the system will prevent high values. This is due to the fact that the system clips signals that are beyond the dynamic range of the sensors and amplifiers. If the maximum dynamic range of the example was 3, all values higher than 3 would be clipped to 3.

The equations and examples show convolution to be a form of image degradation that appears as blurring of the edges of well defined signals. The blurring in ultrasonic signals is particularly noticeable since the long wavelengths involved tend to produce large PSF's. Examples of the blurring will be introduced later.

4.3.2 **Signal Representation.**

A 1-D discrete system can be represented with vector and matrix notation. Using the same signals shown in Figure 4.2, spatial vectors can be defined:

$$\begin{aligned} \underline{f}(m) &= [0\,0\,1\,0\,1\,0\,0] \\ \underline{h}(k) &= [0\,1\,2\,1\,0] \\ \underline{g}(p) &= [0\,0\,0\,1\,2\,2\,2\,1\,0\,0\,0] \end{aligned}$$

Defining a square matrix operator H composed of the PSF such that:

$$H = \begin{bmatrix} 2 & 1 & 0 & 0 & 0 \\ 1 & 2 & 1 & 0 & 0 \\ 0 & 1 & 2 & 1 & 0 \\ 0 & 0 & 1 & 2 & 1 \\ 0 & 0 & 0 & 1 & 2 \end{bmatrix} \tag{4.6}$$

The convolution sum can be written as:

$$\underline{g} = [H]\,\underline{f}$$

$$\begin{bmatrix} 1 \\ 2 \\ 2 \\ 2 \\ 1 \end{bmatrix} = \begin{bmatrix} 2 & 1 & 0 & 0 & 0 \\ 1 & 2 & 1 & 0 & 0 \\ 0 & 1 & 2 & 1 & 0 \\ 0 & 0 & 1 & 2 & 1 \\ 0 & 0 & 0 & 1 & 2 \end{bmatrix} \begin{bmatrix} 0 \\ 1 \\ 0 \\ 1 \\ 0 \end{bmatrix} \tag{4.7}$$

Then Equation 4.7 can be solved to show:

$$\underline{f} = [HH^T]^{-1} H\,\underline{g} \tag{4.8}$$

Or the inverse filter M can be defined as:

$$[M] = [HH^T]^{-1} H$$
$$\underline{f} = M\,\underline{g} \tag{4.9}$$

The 2-D case becomes more complex. While Equation 4.4 defines 2-D convolution of any size image matrix, it can be noted from the results of Equations 4.7-9, that the use of square matrices allows easy matrix manipulations to be performed. Additionally, the use of square matrix manipulation convolves the signal without zero padded output associated with Equations 4.2 and 4.4. If a linear mapping of $f(p,q)$ results in the convolution sum $q(p,q)$ as shown in Equation 4.4, the mapping can be represented in discrete square scalar notation as [And77]:

$$g_{i,j} = \sum_{k=1}^{N}\sum_{l=1}^{N} f_{k,l} h_{i,j,k,l} \tag{4.10}$$

Since $h_{I,j,k,l}$ is a four-index operator working on a two-index matrix a tensor notation can be developed as [And77]:

$$[G] = [[H]]\{[F]\}$$

However to retain easily usable notation without resorting to tensor notation, lexicographical ordering can performed on the input and output matrices. For an ideal image matrix $\boldsymbol{F}$, lexicographical ordering re-orders the matrix so that each column vector is stacked on top of the other columns:

$$fv(mxn) = Lex\{F\} = \begin{bmatrix} F(m,1) \\ F(m,2) \\ \vdots \\ F(m,n) \end{bmatrix} \tag{4.11}$$

and similarly for the convolved image $\boldsymbol{G}$:

$$gv(pxq) = Lex\{G\} = \begin{bmatrix} G(p,1) \\ G(p,2) \\ \vdots \\ G(p,q) \end{bmatrix} \tag{4.12}$$

Using the effect of the stacking as a tool, a matrix PSF operator $\boldsymbol{H_2}$ can be defined to perform 2-D convolution on the ideal image vector $\boldsymbol{fv}$. For example, from Equation 4.5 a PSF matrix $h(i,j)$ is lexicographically re-ordered to define:

$$hv(i,j) = \begin{bmatrix} h(i,1) \\ h(i,2) \\ \vdots \\ h(i,j) \end{bmatrix} = [0 \quad 1 \quad 0 \quad 1 \quad 2 \quad 1 \quad 0 \quad 1 \quad 0]^T \tag{4.13}$$

When $m \neq n \neq p \neq q \neq i \neq j$, it is evident that the matrices will not be square leading to problems with direct inversion. To overcome this, zero padding is performed where $P = maximum\{(mxn),(ixj)\}$ so that [Ros82]:

$$f(i) = \begin{cases} f(i) & for \quad 1 \le i \le (mxn) \\ 0 & for \quad (mxn) \le i \le P \end{cases}$$
$$h(i) = \begin{cases} h(i) & for \quad 1 \le i \le (ixj) \\ 0 & for \quad (ixj) \le i \le P \end{cases} \qquad (4.14)$$
$$g(i) = \begin{cases} g(i) & for \quad 1 \le i \le (pxq)+(mxn)-1 \\ 0 & for \quad (pxq)+(mxn) \le i \le P \end{cases}$$

It should be noted that Rosenfeld stresses that P should be $P>(mxn)+(i,j)$ [Ros82]. This is to prevent "wrap-around" convolution of the convolving matrix at the edges of the ideal image matrix that has been re-ordered. For this work, the ideal image $\boldsymbol{F(m,n)}$ and PSF $\boldsymbol{H(i,j)}$ are imbedded in the center of a larger zero matrix so "wrap-around" introduced by convolution at the matrix edges is non-existant. This effectively reduces the size of the padded matrix to (mxn). Additionally, the size of the PSF operator $\boldsymbol{H_2}$ will be only $(mxn)^2$ instead of $\{(mxn)+(ixj)\}^2$ aiding the inversion process for testing.

For this work, Equations 4.14 were adapted to fit the problem. The PSF function matrix $h(i.j)$ was embedded in the center of a zero matrix of size (m,n) for simplicity in matching the size of the ideal image. For example, for an (m,n) matrix of $(5,5)$, $h(i,j)$ from Equation 4.5 becomes:

$$h(m,n) = \begin{bmatrix} 0 & 0 & 0 & 0 & 0 \\ 0 & 0 & 1 & 0 & 0 \\ 0 & 1 & 2 & 1 & 0 \\ 0 & 0 & 1 & 0 & 0 \\ 0 & 0 & 0 & 0 & 0 \end{bmatrix} \qquad (4.15)$$

That is lexicographically re-ordered so:

$$h(m,n) = Lex\{h\} = h(i) =$$
$$[0 \ \cdots \ 0 \ 0 \ 0 \ 1 \ 0 \ 0 \ 0 \ 1 \ 2 \ 1 \ 0 \ 0 \ 0 \ 1 \ 0 \ 0 \ 0 \ \ldots \ 0]^T \tag{4.16}$$

This representation further simplifies Equation 4.14 so that, using Eqs. 4.11-13:

$$\begin{aligned} f(i) &= fv(mxn) \\ h(i) &= hv(mxn) \\ g(i) &= H_2(mxn) \end{aligned} \tag{4.17}$$

where $\boldsymbol{H_2}$ is to be defined.

Circulant matrices offer advantages in representing the PSF operator matrix $\boldsymbol{H_2}$ due to ease of inversion, simplicity in generating the matrix itself for computational purposes, and convolution is a direct matrix-vector product motivating the re-ordering previously discussed [Ros82][Gol96]. A circulant matrix is a symmetric, positive definite, Toeplitz form constructed as follows:

$$C = \begin{matrix} c(1) & c(P) & c(P-1) & \cdots & c(2) \\ c(2) & c(1) & c(P) & \cdots & c(3) \\ \vdots & \vdots & \vdots & & \vdots \\ c(P) & c(P-1) & c(P-2) & \cdots & c(1) \end{matrix} \tag{4.18}$$

The PSF matrix operator can be constructed from a re-ordered version of Equation 4.16 so that:

$$h'(i) =$$
$$[2 \ 1 \ 0 \ 0 \ 0 \ 1 \ 0 \ 0 \ 0 \ 0 \ 0 \ 0 \ 0 \ 0 \ 0 \ 0 \ 0 \ 0 \ 0 \ 1 \ 0 \ 0 \ 0 \ 1] \tag{4.19}$$

then letting $c(i) = h'(i)$ in Equation 4.18 the $\boldsymbol{H_2}$ matrix becomes:

$$H_2 = \begin{matrix} 2 & 1 & 0 & 0 & \cdots & 0 & 0 & 1 \\ 1 & 2 & 1 & 0 & \cdots & 0 & 0 & 0 \\ 0 & 1 & 2 & 1 & \cdots & 1 & 0 & 0 \\ 0 & 0 & 1 & 2 & \cdots & 0 & 1 & 0 \\ 0 & 0 & 0 & 1 & \cdots & 0 & 0 & 1 \\ 1 & 0 & 0 & 0 & \cdots & 0 & 0 & 0 \\ \vdots & \vdots & \vdots & \vdots & & \vdots & \vdots & \vdots \\ 0 & 0 & 0 & 0 & \cdots & 0 & 0 & 1 \\ 1 & 0 & 0 & 0 & \cdots & 0 & 0 & 0 \\ 0 & 1 & 0 & 0 & \cdots & 1 & 0 & 0 \\ 0 & 0 & 1 & 0 & \cdots & 2 & 1 & 0 \\ 0 & 0 & 0 & 1 & \cdots & 1 & 2 & 1 \\ 1 & 0 & 0 & 0 & \cdots & 0 & 1 & 2 \end{matrix} \qquad (4.20)$$

The 2-D convolution problem can then be recast as:

$$gv = [H_2]fv \qquad (4.21)$$

The vector gv is re-ordered to matrix form to reproduce the convolved image. The simple inverse filter $[H_2]^{-1}$ will recover the ideal scan fv assuming knowledge of the PSF is available to produce H_2:

$$fv = [H_2]^{-1} gv$$

Or letting: $$[M] = [H_2]^{-1}$$

$$fv = [M]gv \qquad (4.22)$$

This section presented some elementary matrix formulations for signal representation and manipulation that will be used for discussion in the following sections. It is evident that if the image sizes are large, the matrix H_2 is very large. For an image with dimension N, the H_2 matrix will be N^2xN^2. Inversion of large matrices can become difficult.

4.3.3 **Simple Deconvolution.**

As noted earlier, deconvolution to enhance the resolution of ultrasonic and other signals and images has been subjected to a significant body of investigation. Several of

the techniques are presented here with the Weiner filter utilized as a preferred method of recovering the PSF of the system and using it to enhance the resolution of images. To avoid the difficult inversion necessary to use a pure inverse filter, linear transformations can be used to transfer the signal to a space where the desired processing operations can be accomplished.

One property of the Fourier transform for an integral such as given in Equation 4.3 is that convolution in the spatial domain *(m,n)* is equivalent to multiplication in the frequency domain *(u,v)* [Ros82]. This property can be exploited to produce a filter that does not involve the large matrix inversion from the previous Section. In the absence of noise, the Fourier transform of Equation 4.3 is:

$$\int_{-\infty}^{\infty}\int_{-\infty}^{\infty} h(x,y)\, f(x-x', y-y')dx'dy' = H(u,v)F(u,v)$$
$$G(u,v) = H(u,v)F(u,v) \qquad (4.23)$$

where:
$G(u,v)$ = Fourier transform of the convoloved signal
$H(u,v)$ = Fourier transform of PSF function
$F(u,v)$ = Fourier transform of ideal image

It is easy to see that the Fourier transform of the ideal image can be easily recovered by division so that:

$$F(u,v) = \frac{1}{H(u,v)}G(u,v) \qquad (4.24)$$

or letting:
$$M(u,v) = \frac{1}{H(u,v)} \qquad (4.25)$$

the filter for restoration:
$$F(u,v) = M(u,v)G(u,v) \qquad (4.26)$$

An inverse transform of $F(u,v)$ restores the original image. The method here is simple, however, implementation of a simple filter requires that the PSF must be known and that

additive noise in the system does not contribute significantly to the image degradation. The discrete case for simple deconvolution is demonstrated in Equation 4.22.

4.3.4 **Deconvolution and Noise.**

The inverse filters of Equations 4.9 and 4.16 and the restoration filter in 4.19 are for an ideal signal with no additive noise from the data acquisition system introduced during acquisition. If additive noise is introduced during data acquisition, Equation 4.3 becomes:

$$\begin{aligned} g(x,y) &= \int_{-\infty}^{\infty}\int_{-\infty}^{\infty} h(x,y)\, f(x-x', y-y')dx'dy' + n(x,y) \\ &= h(x,y) * f(x,y) + n(x,y) \end{aligned} \tag{4.27}$$

where: $n(x,y)$ = additive noise introduce by the system

Using the Fourier transform to implement a filter:

$$\begin{aligned} G(u,v) &= H(u,v)F(u,v) + n(u,v) \\ F(u,v) &= \frac{1}{H(u,v)}\big(G(u,v) - N(u,v)\big) \end{aligned} \tag{4.28}$$

The matrix formulation from Equation 4.15 becomes:

$$\begin{aligned} gv &= [H_2]fv + nv \\ fv &= [H_2]^{-1}(gv - nv) \end{aligned} \tag{4.29}$$

The deconvolution problem suddenly becomes more complex since not only does the PSF need to be known, but some information about the nature of the additive noise in the system. Almost all the work discussed in the history section has been performed to provide estimations for the PSF and/or noise models.

The Wiener filter is derived as a least-squares filter where it is assumed that some knowledge of the noise signal statistical properties may be known or measurable *a posteriori* from the image [And77][Ros82]. Additionally, the PSF is assumed to be

known (if the PSF is unknown, homomorphic deconvolution techniques discussed later can sometimes estimate the PSF by complex cepstrum filtering).

For the continuous case of the integral Equation 4.3, let $\hat{f}(x,y)$ represent the *least squares estimate* of the ideal image *f(x,y)*. The objective of least squares analysis is to find $\hat{f}(x,y)$ so that the mean square error:

$$e^2 = E\left\{\left[f(x,y) - \hat{f}(x,y)\right]^2\right\} \tag{4.30}$$

is minimized. Rosenfeld demonstrates an in depth derivation of minimizing Equation 4.30 and shows a least squares or Wiener filter to be [Ros82]:

$$M(u,v) = \frac{1}{H(u,v)} \frac{|H(u,v)|^2}{|H(u,v)|^2 + \left[S_{vv}(u,v)/S_{ff}(u,v)\right]} \tag{4.31}$$

where:
$M(u,v)$ = frequency domain filter as in Equation 4.25
$H(u,v)$ = frequency domain PSF
$S_{vv}(u,v)$= spectral density of the noise
$S_{ff}(u,v)$ = spectral density of the ideal image

The filter is applied as in Equation 4.26 to recover the ideal image *F(u,v)*. Inverse Fourier transform restores the image. It should be noted that in the absence of noise, the Wiener filter reduces to the simple inverse filter of Equation 4.25. If a useful approximation of the noise-to-signal power density ratio $S_{vv}(u,v)/S_{ff}(u,v)$ (NSR) can be determined then it is common to estimate with a suitable approximation called Γ [Mur78][Ros82][Che88][Hay89][Fro91][Sin92][Sub95][Che95][Zha95][Dow96][Ler96] so that Equation 4.31 can be re-written as:

$$M(u,v) = \frac{1}{H(u,v)} \frac{|H(u,v)|^2}{|H(u,v)|^2 + \Gamma} \tag{4.32}$$

Rosenfeld provides a similar derivation for the discrete case with one notable exception; transforms other than Fourier transforms can be used to implement the deconvolution. Using the convolved and re-ordered image *gv* from Equation 4.21, a transform sequence is defined where [Ros82]

$$\hat{fv} = [A]^{-1}[M][A]gv$$

where: *[A]* = a linear transform matrix for *gv* that can be Fourier, Eigenvalue, etc.

Rosenfeld shows that the transform filter can be derived to be [Ros82]:

$$[M] = [S_{ff}][H]^{*T}\left([H][S_{ff}][H]^{*T} + [Svv]\right)^{-1} \tag{4.33}$$

Equation 4.33 again reduces to the simple discrete inverse filter of Equation 4.22 when noise is not present in the degraded image *gv*. However, Equation 4.33 again introduces a difficult matrix inversion when *gv* is large.

As noted earlier, homomorphic deconvolution is used frequently for image enhancement. This type of deconvolution uses homomorphic mappings from one space to another until the desired processing operations are more easily accomplished than in the spatial domain. It has been shown to be possible to estimate the behavior of an unknown PSF by homomorphic operations on a recorded image [Col73][Can74]. Specifically, for a discrete convolved signal ***F(m,n)*** of finite length, the *z*-transform (z_1,z_2) again changes convolution to multiplication as in the Fourier transform:

$$\int_{-\infty}^{\infty}\int_{-\infty}^{\infty} h(x,y)\, f(x-x', y-y')dx'dy' = H(z_1,z_2)F(z_1,z_2) \tag{4.34}$$
$$G(z_1,z_2) = H(z_1,z_2)F(z_1,z_2)$$

This property is used in combination with homomorphic mapping operations to estimate the PSF $H(z_1,z_2)$ (and possibly noise content) if the signal and the PSF are located in different 2-D complex cepstrum bands [Tax95]. The cepstrum, defined as the Fourier

transform of the log of the power spectrum, is called complex cepstrum to associate it with the output of complex homomorphic transfer functions [Opp75]. Ignoring noise, the complex cepstrum is [Tax95]:

$$\hat{G}(z_1, z_2) = \log|H(z_1, z_2)| + \log|F(z_1, z_2)| + j\arg(H(z_1, z_2)) + j\arg(F(z_1, z_2)) \tag{4.35}$$

where: $\hat{G}(z_1, z_2)$ = complex cepstrum

Using an estimate of H from Equations 2.5.1, 2.5.2, the complex cepstrum of H can be calculated. Using information from the complex cepstrum for H, the cepstrum $\hat{G}(z_1, z_2)$ can then be band-pass filtered in the general vicinity to recover the PSF. The recovered PSF can then be used to perform deconvolution on the signal G. Note that noise is ignored in this technique.

A similar homomorphic filter is motivated by using a power spectrum equalization. A linear operator *[L]* is desired that operates on the convolved image Fourier transform ***G(u,v)*** to produce the same power spectrum as the power spectrum of the ideal image Fourier transform ***F(u,v)***. In the discrete frequency domain [And77]:

$$L(u,v)G(u,v) = \hat{F}(u,v) \tag{4.36}$$

where: $\hat{F}(u,v)$ = estimate of $F(u,v)$

so that the power spectrum criterion is:

$$P_{\hat{f}}(u.v) = P_f(u.v) \tag{4.37}$$

leading to:

$$|L(u,v)|^2 P_g(u,v) = P_f(u,v)$$

or:
$$|L(u,v)| = \left[\frac{P_f(u,v)}{P_g(u,v)}\right]^{\frac{1}{2}} \tag{4.38}$$

Then for:

$$P_g(u,v) = |H(u,v)|^2 P_f(u,v) + P_n(u,v)$$

so that the estimation filter *[L]* becomes:

$$|L(u,v)| = \left[\frac{P_f(u,v)}{|H(u,v)|^2 P_f(u,v) + P_n(u,v)}\right]^{\frac{1}{2}} \tag{4.39}$$

This model again assumes prior knowledge of the PSF power spectrum and the noise power spectrum. The image estimate $\hat{F}(u,v)$ is calculated and the image is recovered by inverse Fourier transform.

This section has demonstrated deconvolution algorithms in the traditional sense using simple inverse, Wiener, and homomorphic filters. While other techniques are extant, these three have received a majority of investigation in the literature. Inverse filtering assumes total knowledge of the PSF and no noise extant in the data acquisition. Wiener filtering assumes some prior knowledge of the PSF and noise model for use. Homomorphic deconvolution attempts to recover the ideal image without complete prior knowledge of the PSF or noise model. In the event that noise is a significant addition to the image, Wiener filtering compensates for the additive noise adequately as will be shown.

To improve the resolution of the tire scanner, a simple PSF theoretical model was used with a noise estimation parameter Γ in Equation 4.32 to attempt image restoration. However, as will be shown, the simple PSF model did not work well at recovering the

ideal image F even over a large range of Γ values. However, for this application it was easy to introduce a known artifact into the tire before scanning and use the known dimensions of the artifact to experimentally recover the PSF. The recovered PSF was later used to perform image restoration.

4.3.5 **Signal to Noise Ratio.**

As seen earlier, the Wiener filter is dependent on prior knowledge of the PSF and some knowledge of the noise introduced by the measurement system. A large body of work has been performed to determine noise parameters from the image itself or by using some form of *a priori*, or *a posteriori* knowledge of the noise function [And77][Ros82][Nea88a][Nea88b][Hay89][Che90][Jen92][Mit92][Nea92][Jen93] [Nea93]. However, as noted earlier it is very common to simply estimate the noise-to-signal power density ratio (NSR) $S_{vv}(u,v)/S_{ff}(u,v)$ by a suitable constant. Many deconvolution publications even ignore the noise problem altogether and use simple inverse filters [Hun80][Cla86][Sin92][Tax95][Che96][Bec97]. In general, the techniques use some form of the image variance or covariance for estimation of the NSR.

To use the Wiener filter from Equation 4.32 a noise estimation parameter for the constant Γ needs to be made. As noted, the variance or covariance of the image matrix is generally used to provide an estimate of Γ. A common SNR description and used for the deconvolution performed here is[And77]:

$$SNR = \frac{\sigma_g^2}{\sigma_n^2} \tag{4.40}$$

where: σ_g^2 = convolved image variance
σ_n^2 = noise variance

Inversion of the SNR then provides an estimate for Γ if needed. In addition to estimating Γ for deconvolution, the parameter is also experimentally determined by iteration [Sub95]. An image with a known PSF and unknown additive noise is deconvolved for a variety of values for Γ until a "best" recovery is reached. Sin and Lerch also cite a common "rule-of-thumb" for determining a Γ estimate is setting Γ equal to about 1% of $max\{|F(u,v)|^2\}$ [Sin92][Ler96]. However, Lerch and others also note that the value of Γ is chosen to stabilize the division process in Equation 4.32 [Ler96]. While Γ does tend to stabilize division when $|H(u,v)|^2 \rightarrow 0$, its prime motivation is to reflect some knowledge of the noise inherent in the degraded signal.

For most techniques, the noise intrinsic to the image is assumed to be Gaussian white noise. Additive noise introduced in the simulations later are all modeled as Gaussian white noise with SNR calculated as per Equation 4.40.

The tire scanner deconvolution described here uses the iterative technique to find the "best" value of Γ that will deconvolve a known flaw. The best Γ is then used to deconvolve unknown flaws. Equation 4.30 is used for SNR calculations in the simulated and actual data testing shown in later sections.

4.3.6 **Simulated Deconvolution.**

The preceding sections presented deconvolution techniques for continuous and discrete signals. To test the deconvolution techniques, a simulation study was performed. The simulation uses a noiseless test image matrix to perform simple inverse filtering and later adds noise to the image matrix to show the results of additive noise and possible deconvolution parameters in the presence of noise.

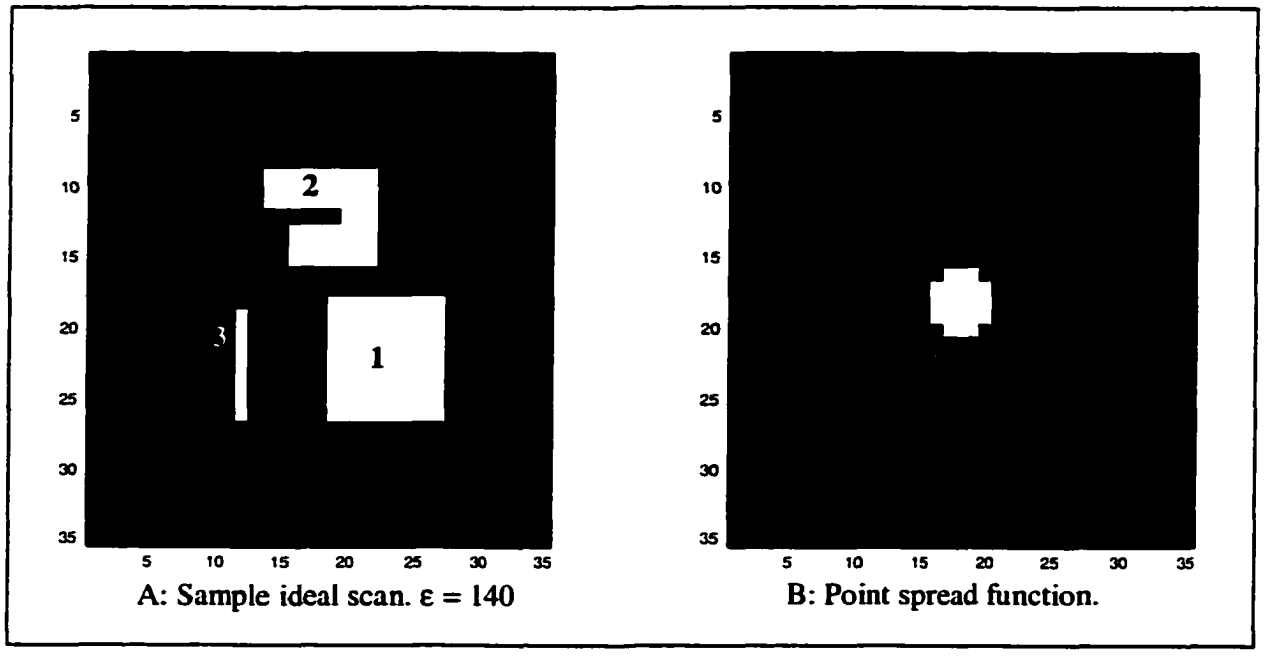

Figure 4.4: Simulated images.

A noiseless test image matrix mimics an ideal scan $F(x,y)$ as shown in Figure 4.4A. The matrix is 35x35 pixels square where the size of the matrix was chosen to simulate a system with step size of 1/16" inch. Embedded in a zero matrix are three flaws at value one. Flaw 1 one has size 9x9 pixels or 9/16"x9/16". Flaw 2 has size of approximately 7x9 pixels but includes a line of zeros only one pixel wide, and Flaw 3 is a vertical line of pixels 1x8. Figure 4.4B shows a PSF $h(x,y)$ generated using Equation 2.3.1 and 2.3.2. The parameters used to calculate the PSF were set to generate a model PSF for the 1.5" diameter, 2.125" spherically focused, 0.5 MHz transducer operating in water. It is evident that the spot size of the PSF is larger than some of the finer details of the ideal image. Maximum gain of the PSF is set to one. A convolution of the ideal image f and the PSF h is shown in Figure 4.5 that demonstrates the severe degradation of the original image associated with convolution of the image and the transducer PSF. In the simulated convolution, gain limiting has been applied to remove convolution values

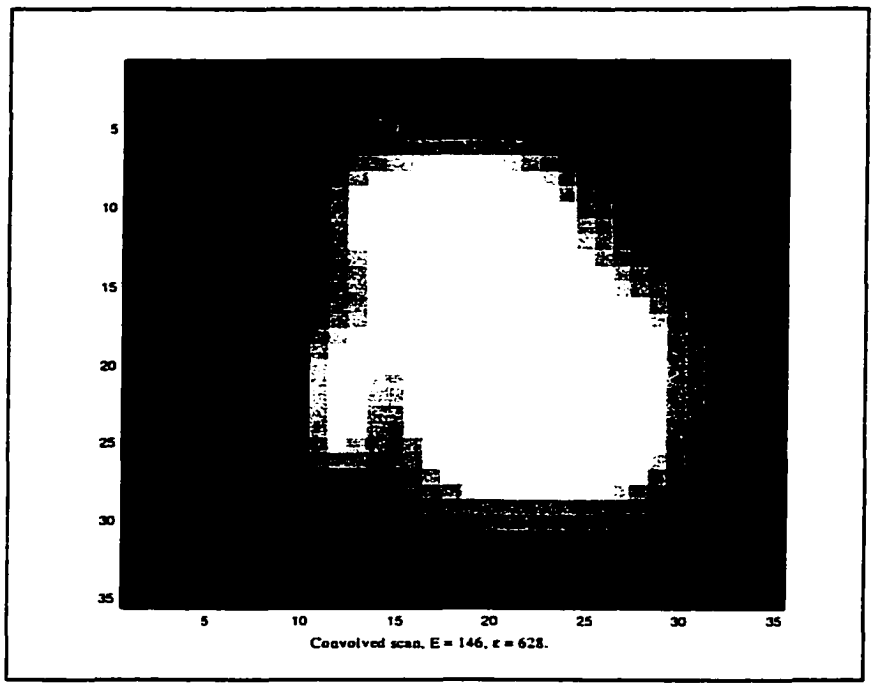

Figure 4.5: Convolution of ideal image and point spread function.

higher than one so the convolution matrix has values only between 0→1. The convolution is imaged by scaling the convolution matrix to grayscale values between 0→255.

Flaw sizing accuracy must be defined to quantify the efficacy of the deconvolution. A number of methods are available to determine flaw sizing in ultrasonic testing [Zha95]. The most common method is by using a 6 dB drop method where the edges of a flaw are estimated by the position where the reflected signal attenuation is –6 dB less than the maximum reflection [Zha95][Kra90] (other methods such as Distance Gain Size - DGS are available [Kra90]). The difference between the –6 dB flaw size estimate and an actual circular flaw would be characterized as error such as [Zha95]:

$$F_f = \frac{\sum_{i=1}^{i=n} |d_i - r|}{n} \tag{4.41}$$

where:

F_f = flaw size error
d_l = distance to –6 dB drop point
r = radius of actual flaw
n = number of –6 dB drop points

If the –6 dB criterion is applied to the image in Figure 4.5, the result is a flaw mapping shown in Figure 4.6. The general outlines are similar but finer details apparent in the

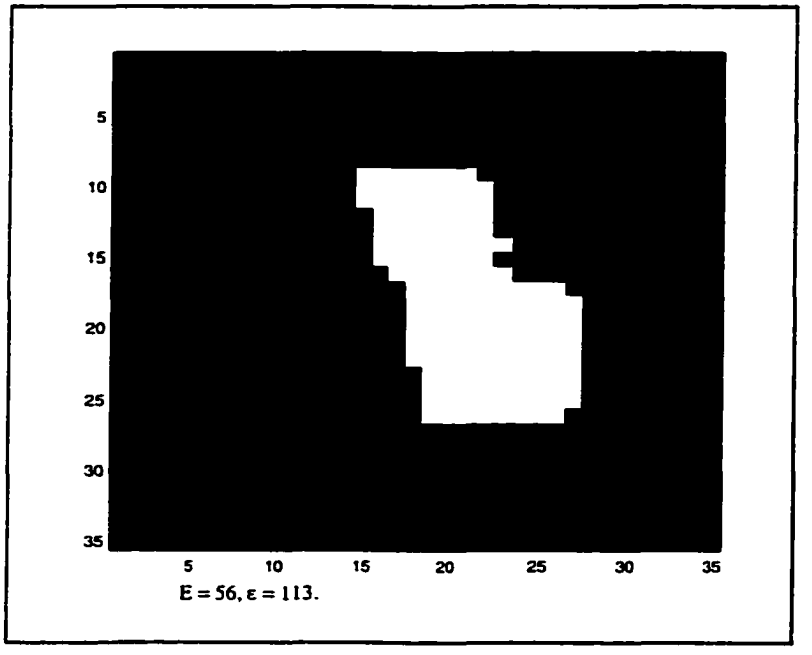

Figure 4.6: -6 dB flaw size criteria.

ideal image are not estimated correctly. This shows the –6 dB estimation to introduce its own errors. Instead of using the –6dB accuracy estimating from Equation 4.40, this work uses a similar error estimate to determine deconvolution error. For a fixed 35x35 array image, the error E is:

$$E = \sum_{y=1}^{y=35} \sum_{x=1}^{x=35} |g(x,y) - f(x,y)| \tag{4.42}$$

where:

$\hat{f}(x,y)$ = image estimate (convolved or deconvolved scan)
$f(x,y)$ = ideal image

E can be calculated for convolved on deconvolved images for comparison. The error E is useful as a means of evaluating the effectiveness of the deconvolution when the ideal image is known. When the ideal image is unknown, a measure of the effectiveness is still needed and Equation 4.42 will not suffice. To answer this need, a simple energy estimate ε is defined. In the 1-D case, the energy of an infinite sequence is defined as [Opp75]:

$$\varepsilon = \sum_{n=-\infty}^{\infty} |x(n)|^2$$

For this work the concept is extended to the finite 2-D case so that:

$$\varepsilon = \sum_{m=1}^{M} \sum_{n=1}^{N} \left| \hat{f}(m,n) \right|^2 \tag{4.43}$$

where: $\hat{f}(m,n) =$ 2-D signal
MxN = 2-D matrix size

Ideally, the energy ε will be minimized at the best deconvolution. The ideal image in Figure 4.4A has an energy level ε=140. After the convolution shown in Figure 4.5, the error E has jumped to 146 and ε jumped to 628 (recall the matrix maximum is also clipped to one). To demonstrate the veracity of this estimate, a numeric simulation is demonstrated later that shows close agreement of the two error estimate methods from Equations 4.42 and 4.43.

Figure 4.7A shows the convolution from Figure 4.5 with low pixel values enhanced so all pixels greater than zero are imaged. Figure 4.7B shows deconvolution of the PSF by the simple matrix inverse filter from Equation 4.9. Since the convolved image is noiseless, the SNR is effectively infinite. The simple matrix inverse recovers the ideal image completely with the error E = 0 and the energy ε = 140 as in the ideal

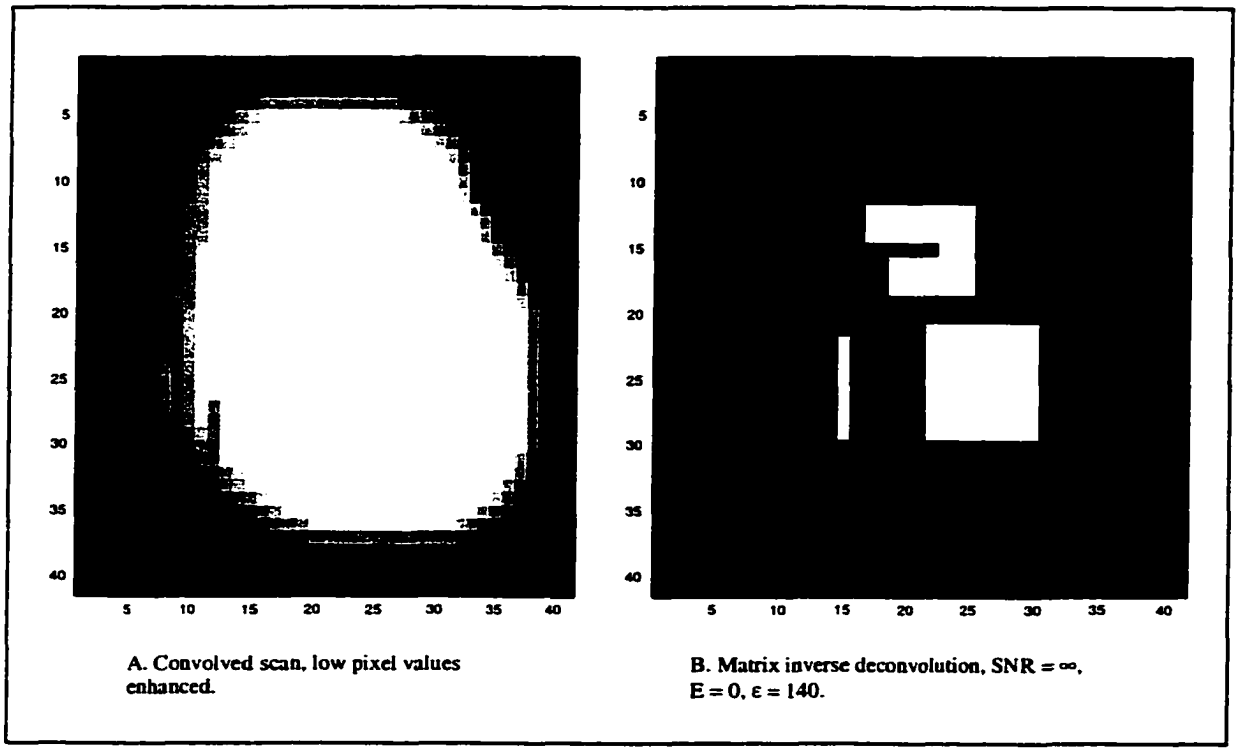

Figure4.7: Convolved and deconvolved images.

image. In a noiseless environment with small image sizes, the matrix inverse filter is appropriate. Larger images still face a difficult inversion process as matrix size grows.

As noise is introduced into the convolved image, the matrix inverse method fails rapidly. Figure 4.8A shows the same convolution as Figure 4.5 only with additive Gaussian white noise. The added noise has 0 mean value, 0.0000001 variance, and a maximum value of 0.001. The SNR calculated using Equation 4.40 is over 1.0×10^6 indicating very little additive noise is introduced. However, the deconvolved image shown in Figure 4.8B shows very poor recovery of the ideal image. The error $E = 398$ is large and the energy in the image has grown very large where $\varepsilon = 894$. Visually, a vague outline of the ideal flaw is apparent, but only because the ideal image is known to the observer. Very little information about the ideal image could be surmised if the ideal

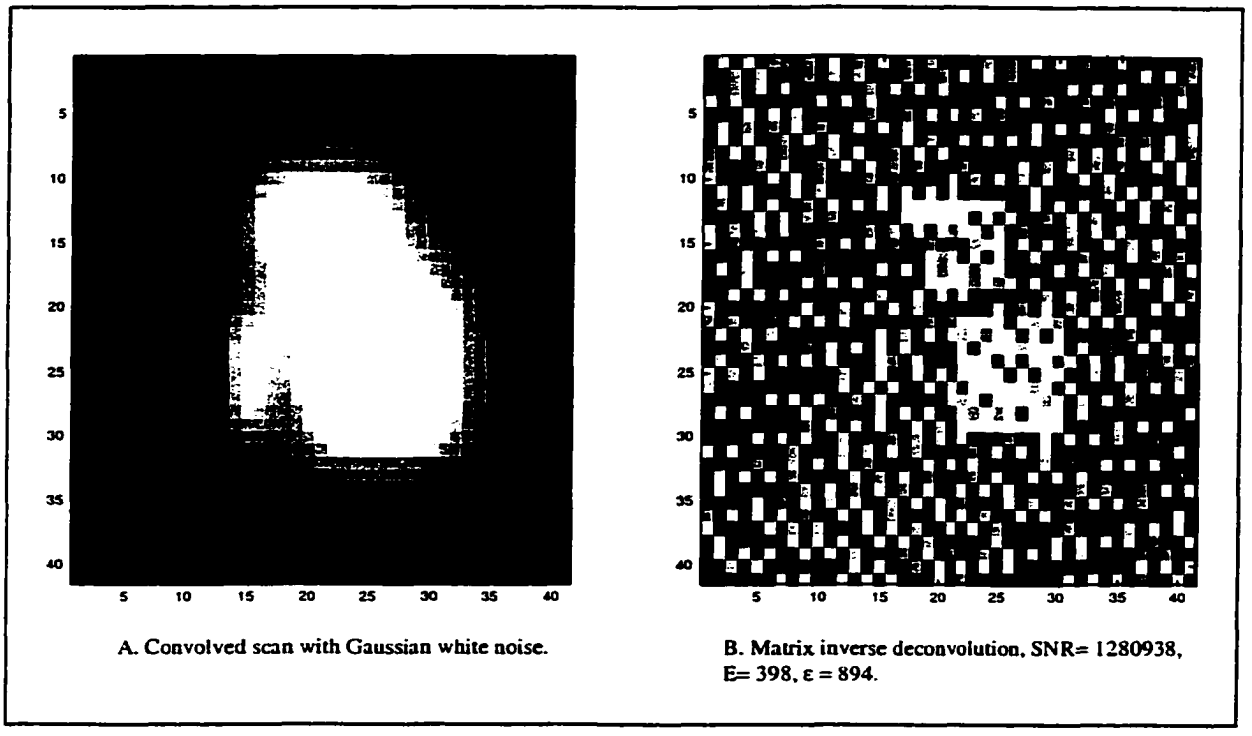

A. Convolved scan with Gaussian white noise.

B. Matrix inverse deconvolution, SNR= 1280938, E= 398, ε = 894.

Figure 4.8: Matrix inverse deconvolution in the presence of noise.

image were unknown. As the SNR decreases, the simple matrix inversion method fails completely.

Wiener filter deconvolution can recover the ideal image efficiently if prior information is known about the noise. As noted, the Wiener filter can be implemented as a matrix inverse problem as in Equation 4.33, but this can again introduce a difficult inversion problem when the image matrix becomes large. The Fourier Wiener deconvolution from Equation 4.32 reduces the computational complexity since a large matrix inversion is not required but does introduce numeric round-off errors from the transform and inverse transform. These errors show up as an additional form of noise in an image matrix. A Fourier Wiener filtering of the noise augmented image matrix from Figure 4.8 is shown in Figure 4.9. In the figure at high SNR, the error E=12 is low and the image energy ε=129 is close to that of the ideal image. The noise parameter Γ from Equation 4.32 was estimated as 0.0005 reflecting the high SNR. Figure 4.9 shows low

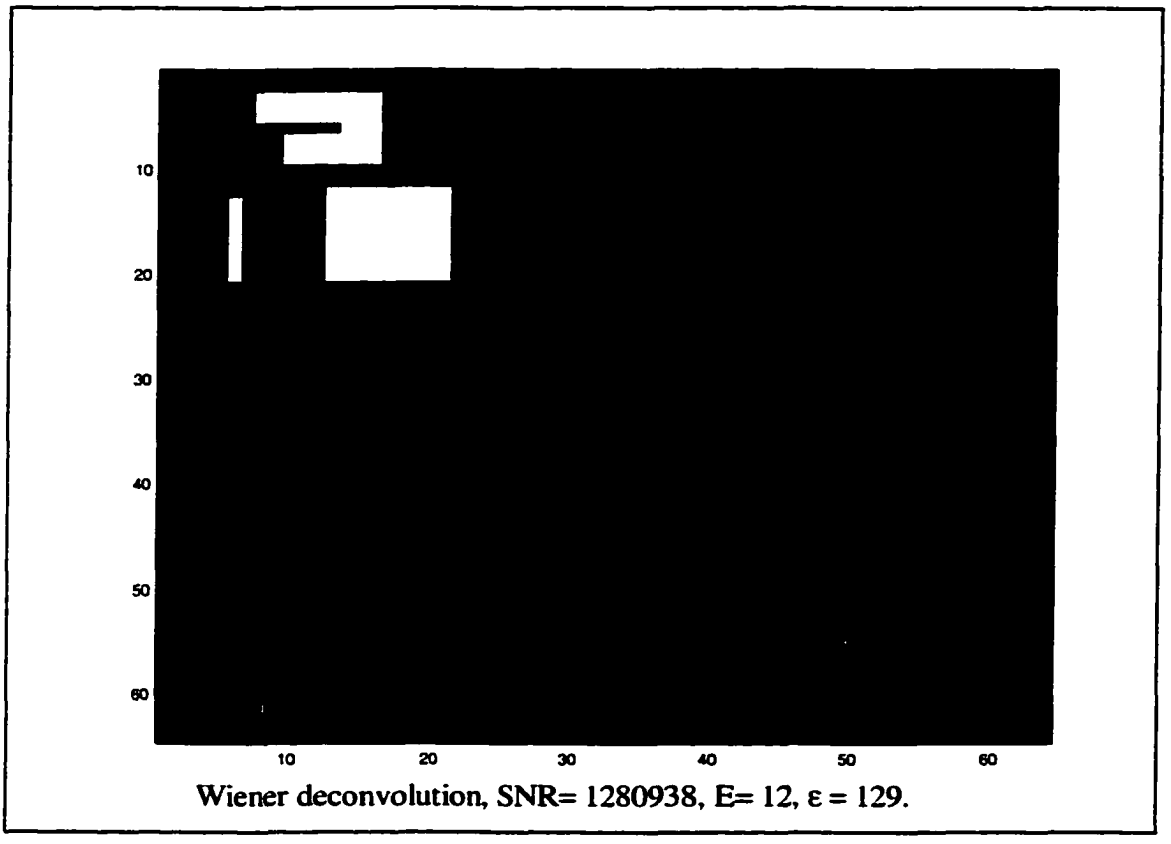

Figure 4.9: Fourier Wiener deconvolution.

level speckle throughout the image that is associated with numeric error and the original noise in the image itself. Including the speckle information in error E and energy ε estimations would contribute to error in the estimations. However, the speckle can be removed prior to error and energy estimations. A histogram of the image is shown in Figure 4.10 showing the low level speckle to be completely separable from the actual flaw information. Removing the speckle is simple to augment by performing a binary cutoff at the top of the speckle region where pixel levels below 0.1 are set to zero. Primarily flaw information remains.

The Wiener filter performs well even at low SNR ratios. For instance, Figures 4.11 and 4.12 show a series of deconvolved images with decreasing SNR's. In the figure series, section **A** shows the convolved image with additive noise and the SNR. Section **B**

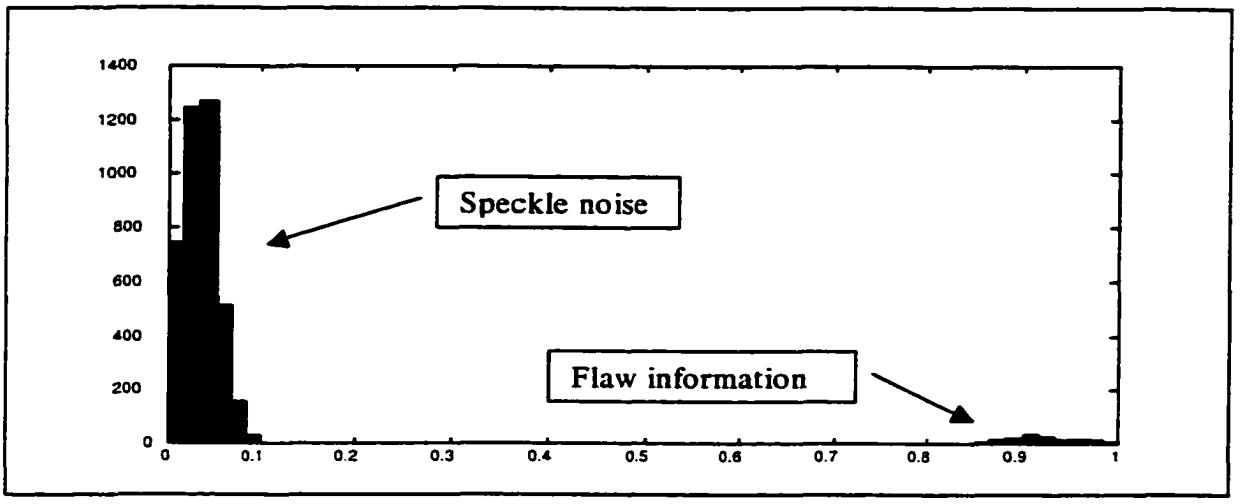

Figure 4.10: Intensity level histogram of Figure 4.9 (maximum = 1).

shows the image deconvolved by Fourier Wiener filter and lists the error E, the energy ε, and the Γ required for deconvolution. The Γ value was calculated by iterating over a series of Γ values and finding Γ that yielded the lowest energy ε. To further enhance the result, a histogram cutoff was performed as discussed above and the image binary converted (conversion to zeros and ones) where pixels >0 were converted to one. The series demonstrates that perfect reconstruction is possible at SNR's equal or lower than 139. At SNR = 14, reconstruction is possible but finer details have become lost in the noise. SNR = 2 is approaching or at the limit of Wiener filtering capability, only a coarse approximation of the ideal image can be estimated from the deconvolved image.

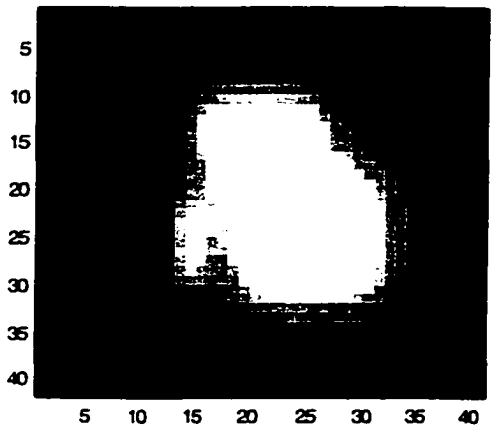

A1. Convolution with noise, SNR=1369.

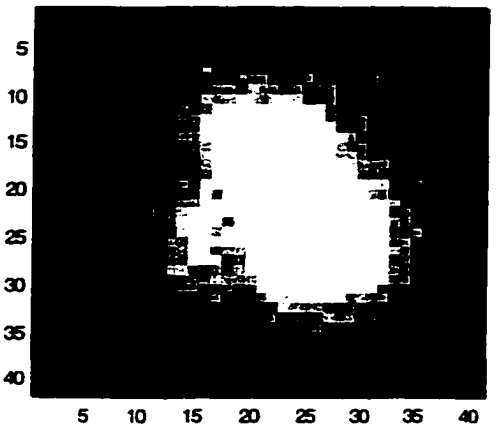

A2. Convolution with noise, SNR=135.

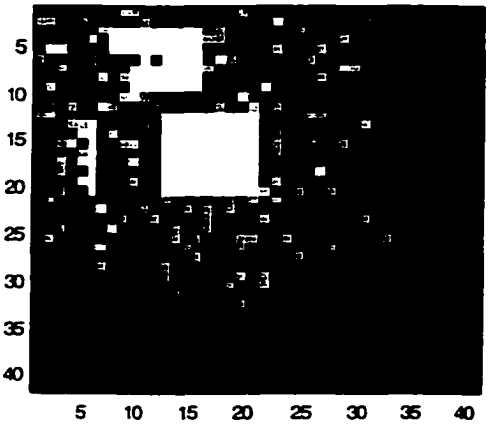

B1. Wiener filter, E= 1, ε=139, Γ=0.25.

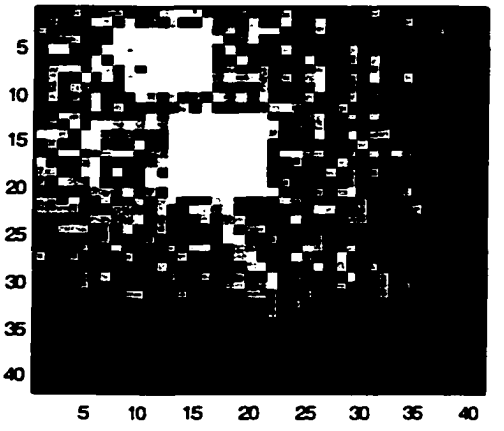

B2. Wiener filter, E= 1, ε=139, Γ=0.7.

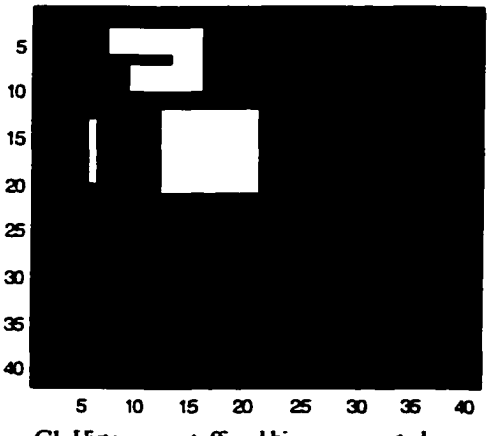

C1. Histogram cutoff and binary converted.

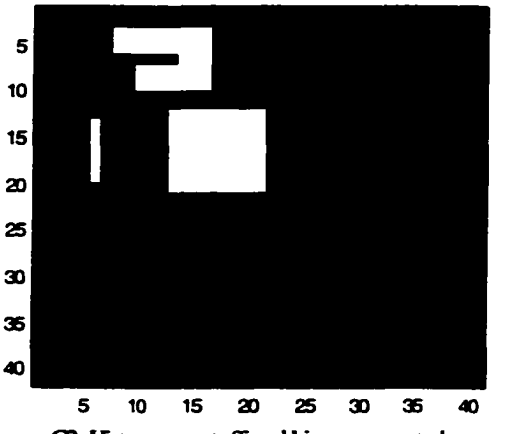

C2. Histogram cutoff and binary converted.

Figure 4.11: Deconvolved images.

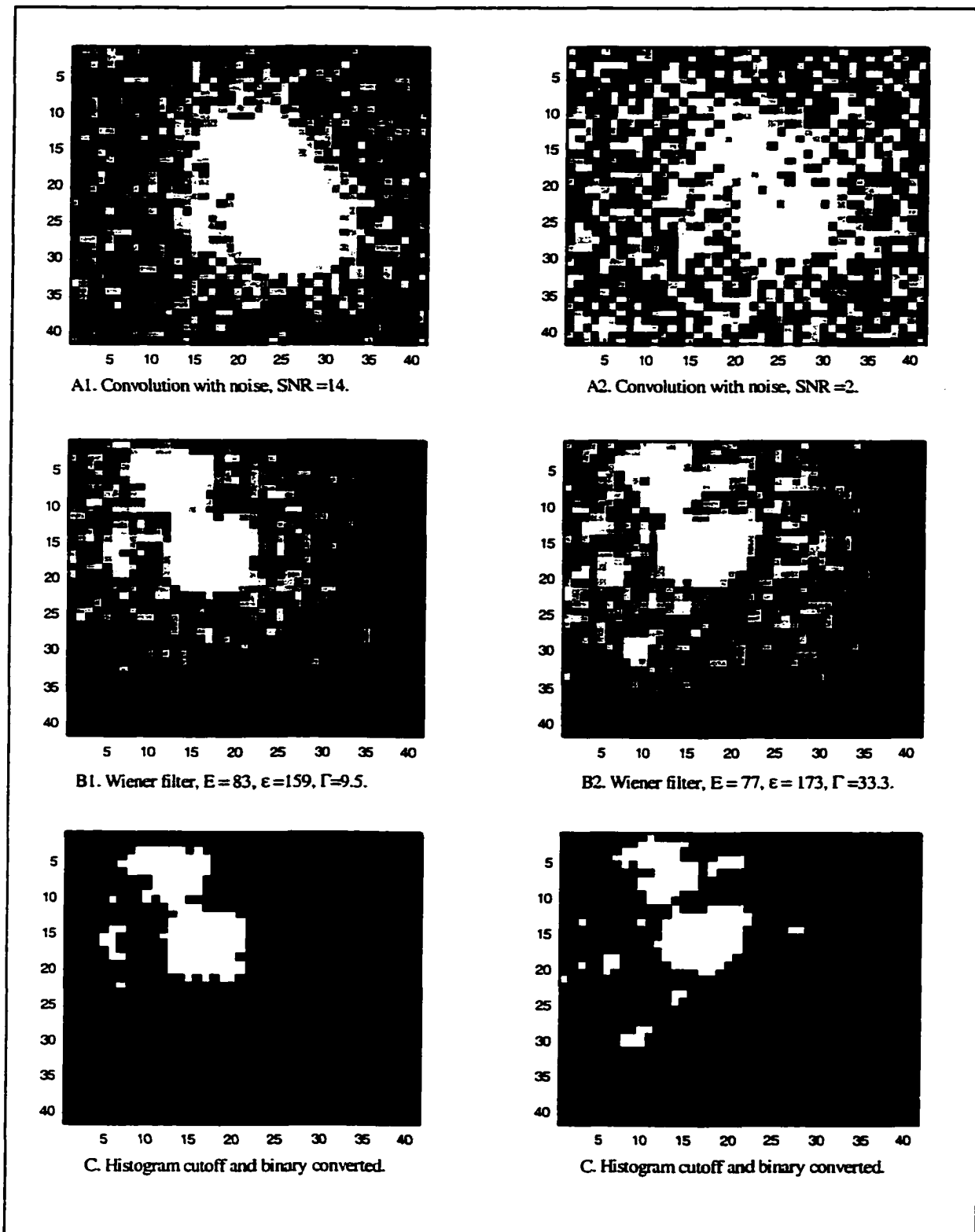

Figure 4.12: Deconvolved images.

The SNR comparisons demonstrate that Wiener filtering is appropriate for deconvolving ultrasonic images with excellent recovery of the ideal image when SNR does not approach 2. The comparisons where generated using a model of the tire inspection system. When the filter began to fail at SNR = 2, it can be noted that the maximum of the additive noise equaled the maximum of the convolved image and the energy sum of the noise was 250 while the energy sum of the convolved signal was 350. So the additive noise was almost as strong as the signal itself.

Before attempting to apply the deconvolution to actual test data, it must be shown that minimizing the energy estimate ε, can be used in place of the error estimate E that will not be available when using actual data. A numeric comparison of E and ε is made and shown in Figure 4.13. A series of error and energy estimates are performed for a wide variety of SNR's and Γs. In the simulation, a series of SNRs are tested and shown in Figure 4.13B. The noise estimate Γ,shown in Figure 4.13A is varied over a wide range ($0.000001 < \Gamma < 5$) while the SNR is held constant. The error and energy estimates are calculated at each Γ. The error estimate E and energy estimate ε are plotted in Figure 4.13C and D respectively. The simulation shows there is a very close correlation between error that is calculated from a known quantity and image energy that is calculated just from the deconvolved image. The energy estimate will be used later to determine the best deconvolution on experimental data.

This section has presented a simulation study of deconvolution. Simple inverse deconvolution was demonstrated and shown to not be capable of deconvolving in the presence of noise. The Wiener filter was demonstrated to deconvolve efficiently in the presence of noise with SNR $< \approx 150$. Speckle noise in the deconvolved image introduced

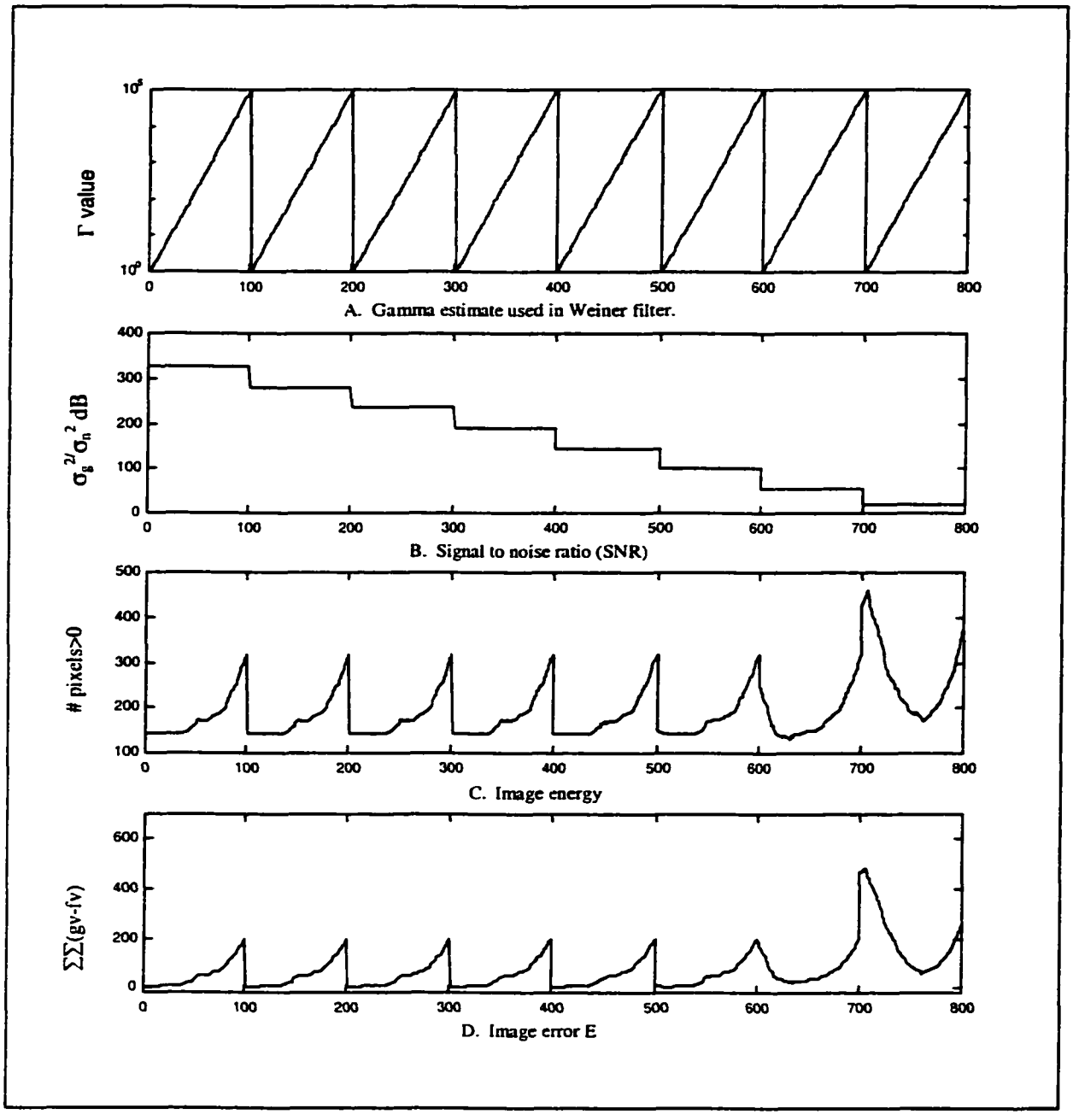

Figure 4.13: Image error and energy comparisons.

by numeric error and included noise was shown to be separable by histogram cutoff. Finally, the image energy estimate ε was shown to be a reliable indicator of the efficiency of deconvolution. The energy estimate will be used later for experimental data.

4.4 Results with comparison to theoretical PSF showing simple model not appropriate.

This section presents a practical application of deconvolution techniques to through transmission, ultrasonic inspection *C-scan* images. The previous sections have reviewed a history of deconvolution in NDE applications. Then, partially reviewed deconvolution theory with a particular emphasis on Wiener deconvolution using iteration to recover noise estimates. Numeric simulations demonstrated the veracity of deconvolution to be implemented here. An image energy estimate that does not require prior knowledge was defined and shown to correspond well with known image error estimates. With a demonstration of the efficacy of the technique, an image energy estimate can be used as a measure of deconvolution effectiveness and experimental data can be analyzed. First the theoretic PSF will be used for deconvolution. Then, experimental recovery of the PSF will be demonstrated and applied.

4.4.1 Theoretical PSF deconvolution.

The simulations were developed to exactly mimic the operating conditions of the tire scanner. If the theoretical model is correct, the PSF developed should be able to be used for deconvolution of experimental images. The image energy parameter ε is used as a basis for comparison of deconvolution.

Simulated flaws were attached to a tire and inspected by scanner. The simulated flaws were materials that served to attenuate the ultrasound signal so that the signal passed through the tire was lessened through the flaw. Rogers used pennies at Northwestern as an attenuating material and experimentation on the scanner constructed here showed foam tape to also be a very good attenuator (and much easier to attach than

pennies) [Rog92]. Figure 4.14 shows a used tire mounted in the scanning tank with several rows of pennies (diameter ¾") attached in chevrons followed by a single chevron of 1/2" diameter foam tape circles for comparison. Very little tread remains on the tire.

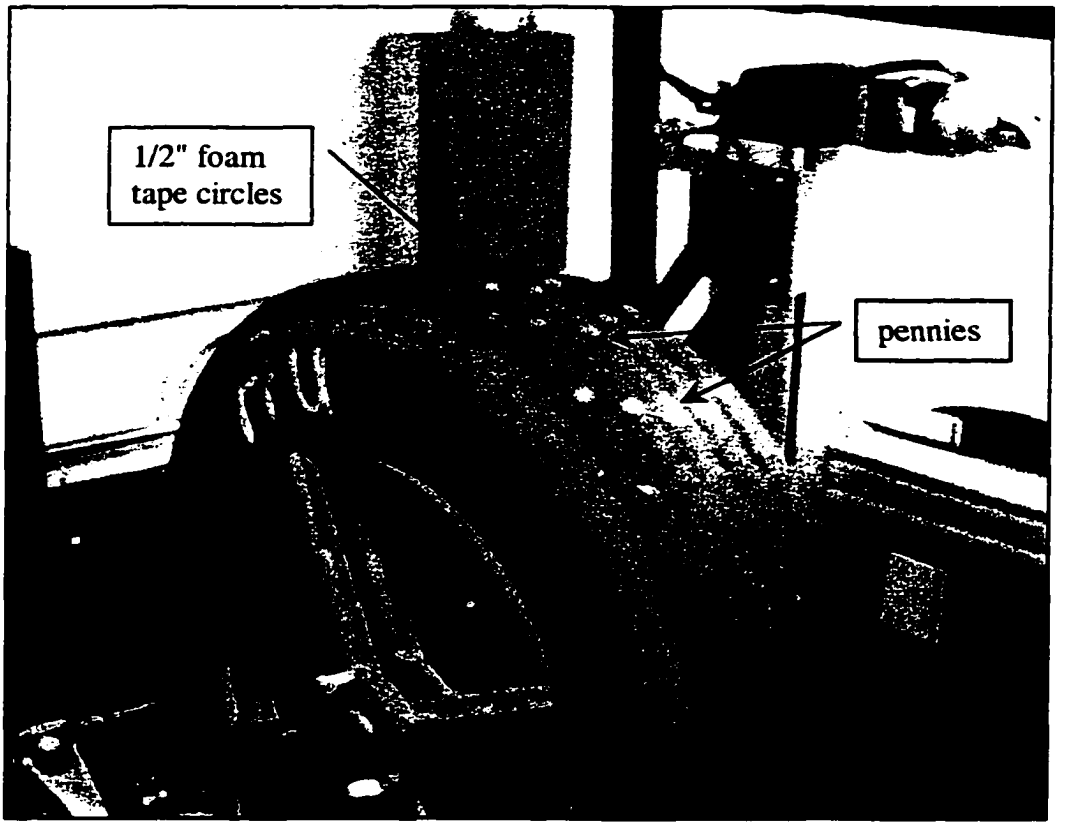

Figure 4.14: Tire with simulated flaws attached.

Figure 4.15 shows a partial crown scan of the tire using the ultrasonic scanner. During scanning, good areas of the tire offer relatively low attenuation of the ultrasound beam so high signal levels are received and amplified. Flawed areas of the tire cause signal attenuation. The simulation studies assumed flaws were associated with high signal levels with the maximum signal output equal to one. To structure the experimental examination in the same way, the ultrasound images produced by the scanner are inverted and normalized to one. Figure 4.15 has been processed by inversion and normalization and then imaged on a 0→255 grayscale. In the figure, the penny chevrons are easy to

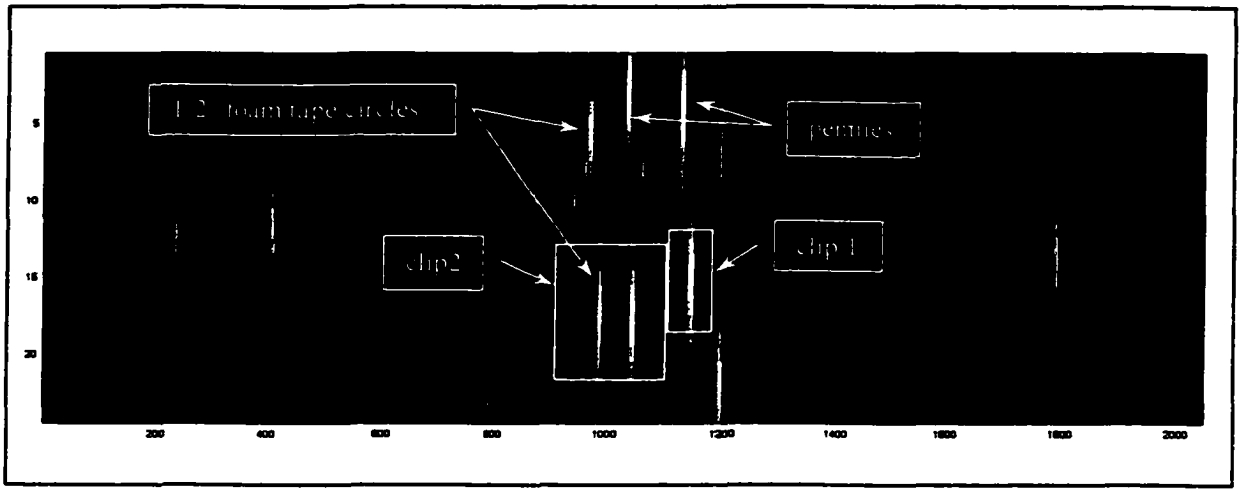

Figure 4.15: Partial crown scan with defects.

discern and also the foam tape defects. The long undulations are caused by signal attenuation due to the tread grooves seen in Figure 4.14. Several regions are defined as Clip 1 and Clip 2 that will be used later in the deconvolution investigation.

Figure 4.16A shows a close-up image of Clip 1 from Figure 4.15. A ¾" penny imaged at 1/16" step size should show a maximum diameter 12 pixels wide. In the

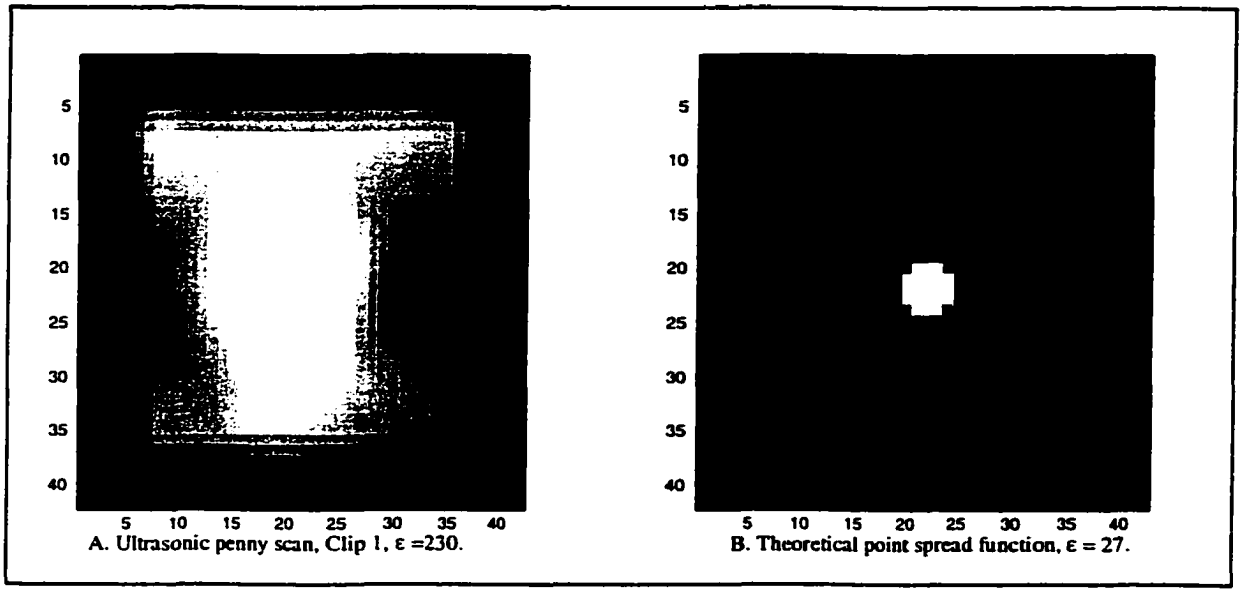

Figure 4.16: Ultrasonic scan and relative PSF.

figure, the penny has been scanned as an unfocused blob with central dimensions of over 21x25 providing a good demonstration of the convolution effects of a large ultrasonic

PSF. The clip has been embedded in a zero matrix and an averaging filter applied to smooth abrupt level changes at the edges of the image prior to Fourier transform. Abrupt level changes at steep or infinite gradients can cause severe ringing during Fourier transform rendering the transform unusable [Ros82]. Figure 4.16B shows the theoretical PSF calculated using Equations 2.3.1 and 2.3.2.

The simulations were performed using a noise free ideal scan that then had noise added to it. In practical scanning, the received signal level never reaches zero attenuation or full range output of the receiver. The acquired ***c-scan*** that is inverted and normalized then exhibits low level attenuation changes in a range between 0.0→0.1. The low signal levels changes are not indicative of flaws in the material and are instead treated as noise in the scanning system. From the results in the simulation studies, it can be inferred that since the noise in the image is high, relatively high values for the deconvolution parameter Γ must be used.

Energy estimates from the deconvolution simulations are used to adjust the relative energy in the experimental data. For instance, if the image to be deconvolved has an energy of $\varepsilon = 50$, attempting to deconvolve a PSF with $\varepsilon = 150$ will not be possible. The PSF would need to be scaled before deconvolution. The simulated signal shown in Figure 4.11 A2 has an energy content of $\varepsilon = 222$, the noise added to it is $\varepsilon = 33$, and the PSF used in deconvolution for Figure 4.11 C2 has $\varepsilon = 27$. Since deconvolution was successful during numeric simulations at these energy levels, deconvolution of the experimental data will be performed at similar relative energy levels.

The energy level of the penny scan Clip 1, shown in Figure 4.16A, is $\varepsilon = 230$. Attempting to deconvolve the theoretically calculated PSF shown in Figure 4.16B with $\varepsilon = 27$ reflects similar energy levels as the simulation studies. Figure 4.17 shows the result

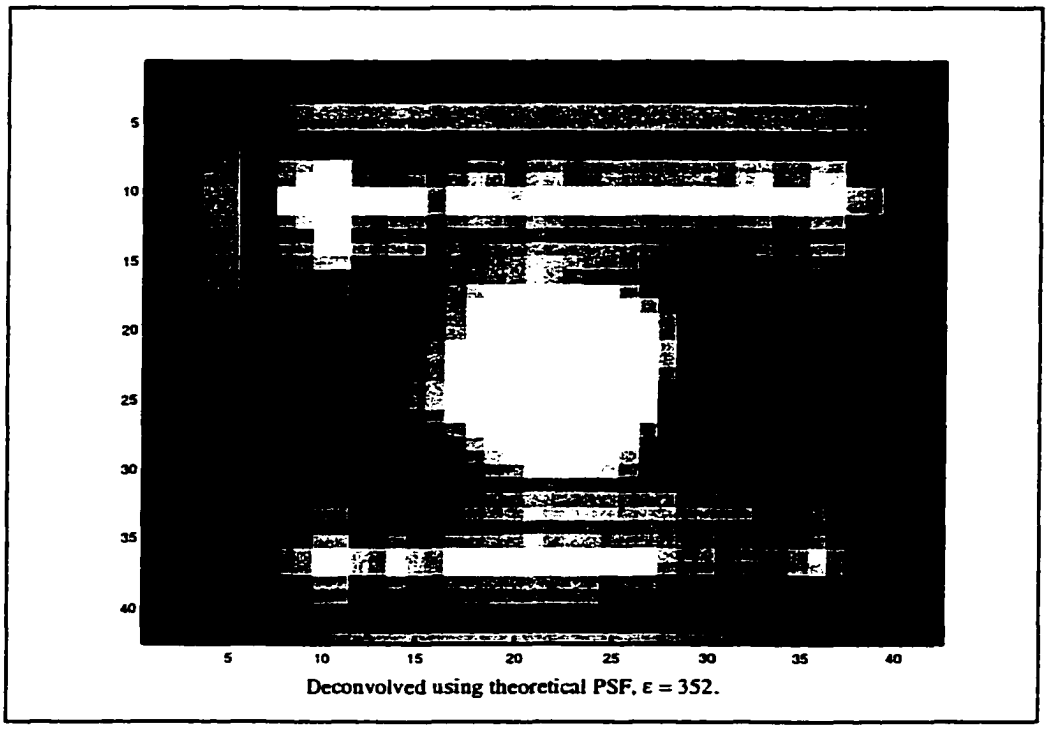

Figure 4.17: Attempted deconvolution using theoretical PSF.

of the deconvolution. The noise estimate Γ was set to 1.0 following the relatively high SNR deconvolved successfully in Figure 4.11A2. In Figure 4.17, the central region of the deconvolution image that should be representing the penny is about 15x 5 pixels, or slightly larger than the size of the ideal penny of 12 pixels diameter. However, the image energy is $\varepsilon = 352$ or greater than the energy of the original penny *c-scan* showing little deconvolution has been performed. To be certain that the noise estimate Γ is not incorrect, the deconvolution was performed over a range of Γ values with the same

result. This outcome shows the simple theoretical PSF model to not be appropriate for this type of deconvolution.

4.4.2 **Double deconvolution for PSF recovery.**

To overcome the failure of the simple PSF deconvolution, a technique of direct recovery of the PSF from a known flaw in the image is investigated. With the penny scans, the size of the penny is known. If the size is known, the PSF can be recovered directly from the convolved scan. Rosenfeld noted that if a sharp point is known in an image, then the image of the point can be assumed to be an estimate of the PSF [Ros82]. Extending this concept, if a blurred object in an image is known, the PSF can be estimated by deconvolution of the actual object from the blurred object. The recovered PSF can then be used for image enhancement. For through transmission ultrasound inspection, implementing the technique can be as simple as placing a small known flaw on the object to be inspected prior to inspection. A first deconvolution recovers the system PSF and a second deconvolution is performed to enhance unknown features. Double deconvolution from a known flaw holds the possibility to easily enhance through transmission inspection NDE images.

Mathematically, the first deconvolution is represented as a variation of Equation 4.32. A Fourier domain deconvolution filter $M_1(u,v)$ is defined so that:

$$M_1(u,v) = \frac{1}{I(u,v)} \frac{|I(u,v)|^2}{|I(u,v)|^2 + \Gamma} \tag{4.44}$$

where: $I(u,v)$ = Fourier transform of ideal scan of an actual object

The deconvolution is then performed so that:

$$H(u,v) = M_1(u,v)G(u,v) \tag{4.45}$$

where: $H(u,v)$ = Fourier transform of PSF
$G(u,v)$ = Fourier transform of convolved object

The PSF transform is then used for deconvolution and/or the PSF recovered by inverse Fourier transform.

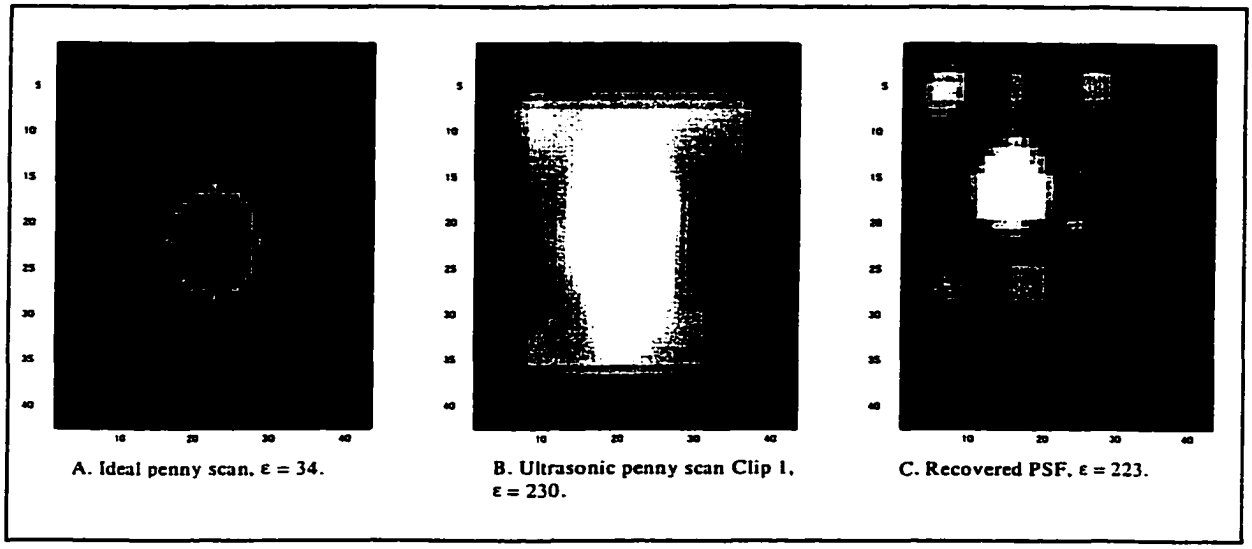

A. Ideal penny scan, ε = 34.

B. Ultrasonic penny scan Clip 1, ε = 230.

C. Recovered PSF, ε = 223.

Figure 4.18: First deconvolution for PSF reovery.

Figure 4.18 shows the first step of the double deconvolution technique. Figure 4.18A shows an ideal scan of a ¾" penny. The penny was constructed as a circular array of ones embedded in a noiseless zero matrix. The maximum diameter is 13 pixels instead of 12 since on odd number is needed for it to be symmetric about a center pixel. The ideal scan is modified by the reduction of the ones to 12% of the original value and addition of constant white noise at 0.02% image energy. The ones were reduced to limit the ideal image energy and approximate the energy ratio between ideal and convolved images from the simulation study. This sets the ratio at 34/230 or close to the simulation studies. Additive noise was introduced to maintain a similar ratio between the convolved image and its background noise. (As previously noted, no *c-scan* can be completely free of noise.) So the ideal image of the penny should also contain a similar ratio of noise.

Figure 4.18B shows the convolved penny scan from Figure 4.16. A deconvolution of the ideal scan from the convolved penny scan using Equations 4.44, 4.45 leaves the recovered PSF shown in Figure 4.18C. The noise estimation parameter Γ = 0.7 reflecting a moderate SNR of about 140 as shown in the simulation study. A comparison of the theoretical and recovered PSF's is shown in Figure 4.19. The

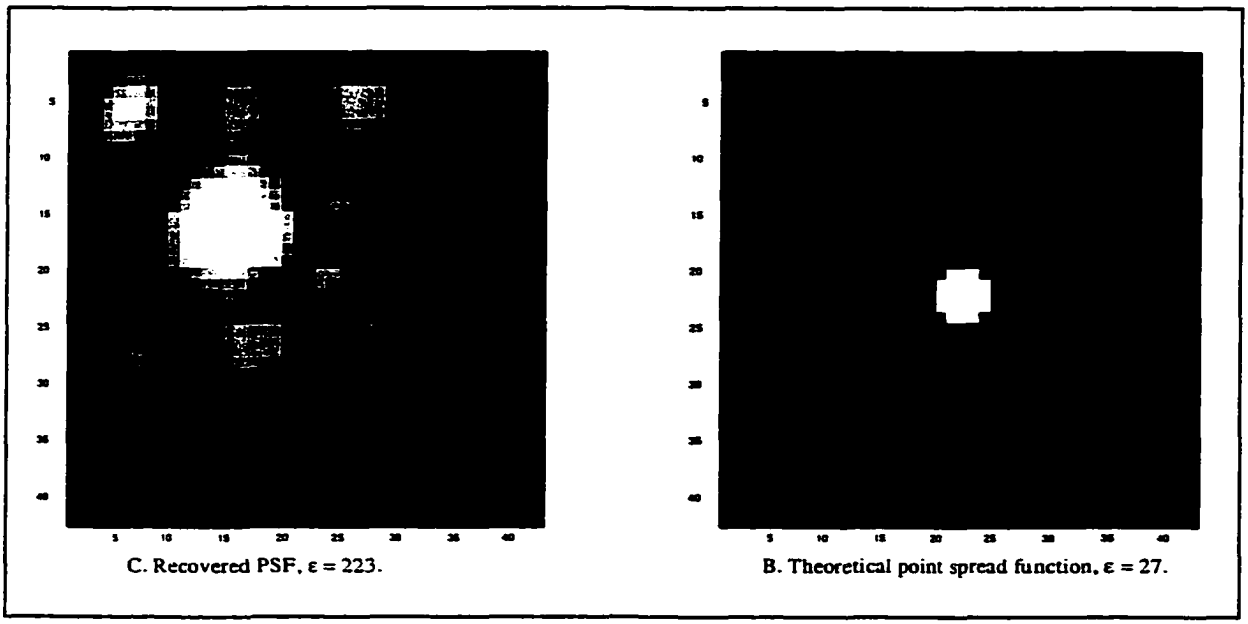

Figure 4.19: Point spread function comparison.

theoretically calculated PSF is far smaller and exhibits far less energy than the recovered PSF and is actually a measure of sound pressure distribution for a focused transducer operating in transmission. The recovered PSF is a true reflection of the system PSF function that includes the transmitter, water medium, tire, and receiver. Recovery of the system PSF then obviates the need for complex modeling of the true receiver operating conditions in this system.

The recovered PSF is used in a second deconvolution to enhance the actual image data. Since the recovered PSF energy is ε = 223, the PSF energy is reduced before

deconvolution. As demonstrated in the simulations and the previous PSF recovery, the energy level of the PSF works well at values around $\varepsilon = 30$. Figure 4.20A shows Clip 2 from Figure 4.15 enlarged. The object on the right is a penny similar to that used in Clip 1 to recover the PSF. The object on the left is a ½" foam tape circle. Ideally, the penny

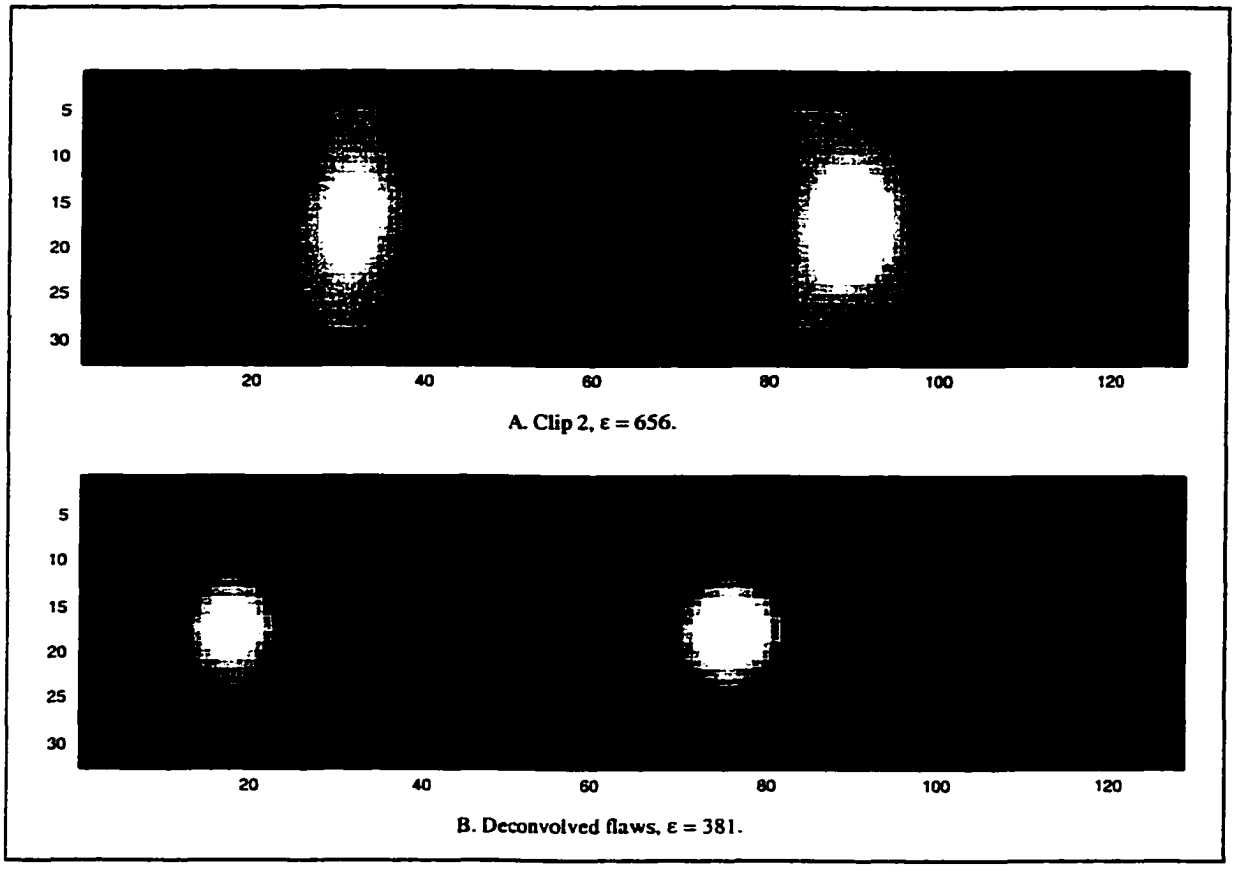

Figure 4.20: Flaws and deconvolution.

flaw should have energy $\varepsilon \approx 130$ and the ½" foam flaw should have $\varepsilon = 70$ calculated as approximately the number of 1/16" pixels that can fit inside a circle of that radius. Deconvolution using the recovered PSF was performed using Equation 4.26 where the restoration filter $M(u,v)$ was calculated from Equation 4.32 using the recovered PSF from above.

Figure 4.20B shows Clip 2 deconvolved. Before energy calculations where performed, the images were histogram filtered as discussed in Section 4.1.6 so the noise inherent in the image would not be a large factor in energy calculations. Figure 4.21A shows a zoomed view of the foam flaw on from the left side of Figure 4.20 with image energy $\varepsilon = 184$. Figure 4.21B shows the deconvolved flaw now with energy $\varepsilon = 73$. Figure 4.21C shows the penny flaw from Clip 2 with energy $\varepsilon = 258$ and 4.21D shows the penny deconvolved with energy $\varepsilon = 97$. It is evident from the deconvolved images and the energy estimates that the double deconvolution significantly enhances the image resolution. In both deconvolutions the ideal flaw size is recovered almost exactly.

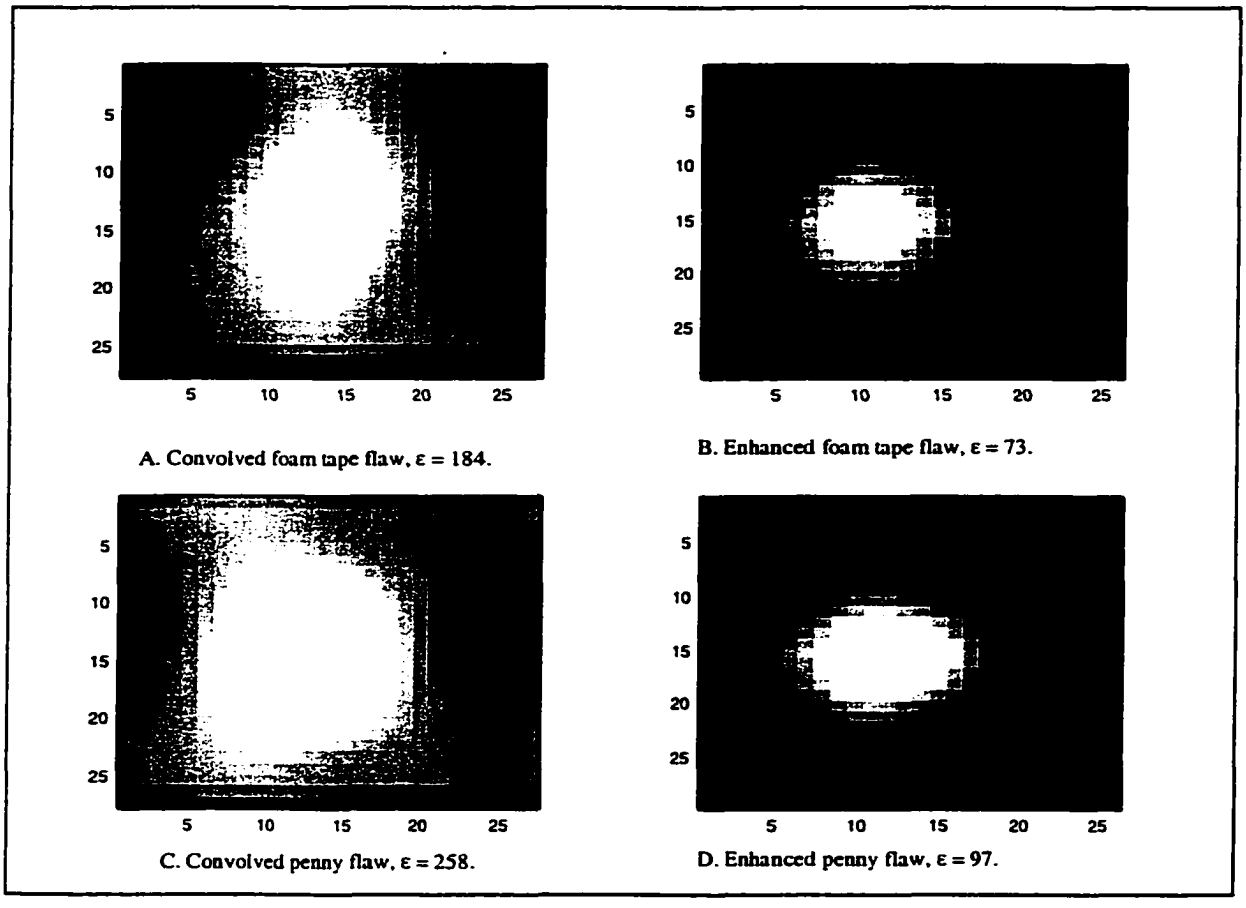

Figure 4.21: Deconvolved flaws.

4.4.3 A through transmission deconvolution filter.

With the authenticity of this technique demonstrated, a further simplification of the technique can be performed. There is little reason to recover the PSF if it is not necessary to display it. Recovery of the PSF entails unnecessary computational complexity with resulting numeric error. Instead of recovering the PSF, a deconvolution filter can be derived that directly enhances an unknown image using a known flaw in the image. In Equation 4.44, the power spectral density is:

$$|I(u,v)|^2 = I(u,v)I^*(u,v)$$

where: * = complex conjugate transform

Substitution into Equation 4.44 gives:

$$M_1(u,v) = \frac{1}{I(u,v)} \frac{I(u,v)I^*(u,v)}{I(u,v)I^*(u,v)+\Gamma} \tag{4.46}$$

Assuming the ideal flaw image $I(x,y)$ is associated with a known feature in the ultrasonic scan $G_1(x,y)$, then Equation 4.45 becomes:

$$H(u,v) = M_1(u,v)G_1(u,v) \tag{4.47}$$

For an unknown flaw $G_2(x,y)$ in the same image that $G_1(x,y)$ is embedded in, the reconstruction from Equation 4.26 is:

$$F(u,v) = M_2(u,v)G_2(u,v) \tag{4.48}$$

where from Equation 4.32 the Wiener filter can be rewritten as:

$$M_2(u,v) = \frac{1}{H(u,v)} \frac{H(u,v)H^*(u,v)}{H(u,v)H^*(u,v)+\Gamma}$$

Substitution of Equation 4.47 into 4.48 gives:

$$M_2(u,v) = \frac{1}{M_1(u,v)G_1(u,v)} \frac{M_1(u,v)G_1(u,v)[M_1(u,v)G_1(u,v)]^*}{M_1(u,v)G_1(u,v)[M_1(u,v)G_1(u,v)]^*+\Gamma} \tag{4.49}$$

With immediate simplification to:

$$M_2(u,v) = \frac{[M_1(u,v)G_1(u,v)]^*}{M_1(u,v)G_1(u,v)[M_1(u,v)G_1(u,v)]^* + \Gamma} \tag{4.50}$$

Let a shorthand notation for $M(u,v)$, $G(u,v)$, *etc.* be:

$$M(u,v) = M$$
$$G(u,v) = G$$
$$etc.$$

Then substituting Equations 4.46 and 4.50 into Equation 4.48 gives:

$$F = \frac{\left[\frac{1}{I}\frac{II^*}{II^*+\Gamma}G_1\right]^*}{\frac{1}{I}\frac{II^*}{II^*+\Gamma}G_1\left[\frac{1}{I}\frac{II^*}{II^*+\Gamma}G_1\right]^* + \Gamma}G_2 \tag{4.51}$$

Letting:

$$R(u,v) = \frac{I(u,v)I^*(u,v) + \Gamma}{I^*(u,v)G_1(u,v)}$$

Equation 4.51 can be simplified to:

$$F(u,v) = \frac{1}{R^*(u,v) + \frac{\Gamma}{R(u,v)}}G_2(u,v) \tag{4.52}$$

Inverse Fourier transform of $F(u,v)$ in Equation 4.52 provides reconstruction of the blurred image $G_2(x,y)$. The noise parameter Γ is assumed constant throughout the image that $G_1(x,y)$ and $G_2(x,y)$ are embedded within. An unknown flaw in an image can then be enhanced by using a known flaw within the same image for system PSF recovery. This is simple to implement by placing a known flaw estimate (such as the penny or foam tape flaws) onto the material to be inspected prior to inspection.

To demonstrate the ability of Equation 4.52 to deconvolve flaws, the same data used for the previous double Wiener PSF recovery is used. Figure 4.22A shows Clip 2

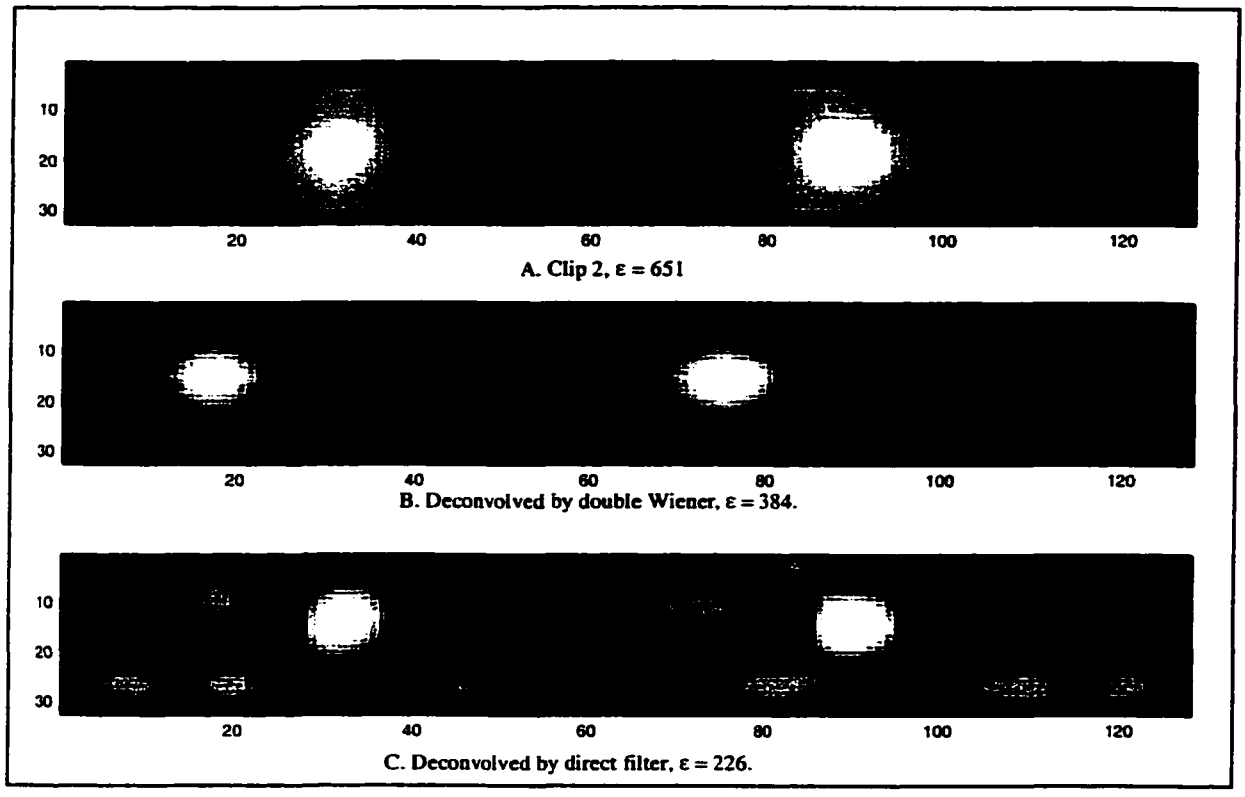

Figure 4.22: Clip 2 comparisons.

used for deconvolution. Figure 4.22B shows the previous double Wiener deconvolution from Figure 4.20B. Figure 4.22C shows the deconvolution performed using the direct enhancement filter from Equation 4.52. The image energy for the direct enhancement is $\varepsilon = 226$ showing similar enhancement to the double deconvolution Wiener filter.

Figure 4.23 shows a series of close-up comparisons of the flaws from Figure 4.22. Figure 4.23A1-C1 show the ½" foam tape flaw. A1 shows the original convolution, B1 shows the double Wiener deconvolution and C1 shows the direct deconvolution algorithm. For the ½" flaw, the direct deconvolution shows similar deconvolution with energy $\varepsilon = 83$ or still close to the expected value for the flaw. The penny scan energy $\varepsilon =$ 118, still close to the expected value. Visually, the direct penny deconvolution appears to be closer to the actual flaw size of 12 pixels wide. For the ½" foam tape flaw, the flaw

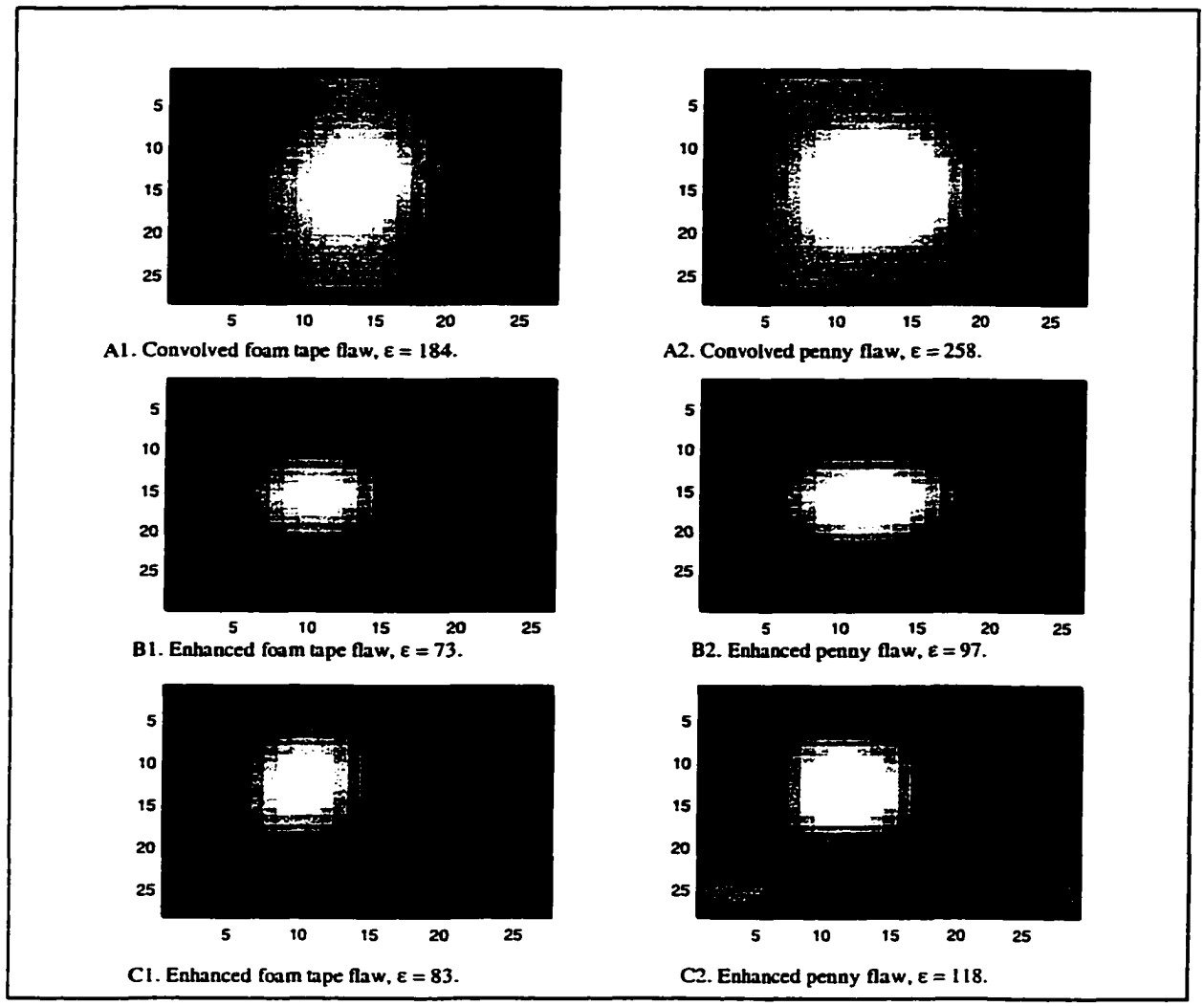

Figure 4.23: Deconvolution comparisons.

size is similar but some blurring is apparent. The direct method appears to deconvolve as effectively as the double deconvolution. Additionally, the decreased complexity of the direct method is simpler to implement.

With the direct method of enhancement demonstrated to provide adequate reconstruction of blurred images, the technique is applied to a new unrelated image. A new set of scans using an aircraft tire serves to further test the method. In research unrelated to this work, an aircraft tire was inspected using the scanning machine constructed for this research [Dow97]. The scans were performed using with 0.75"

diameter, 2.25 MHz transducers. The receiver was focused at 2.0". The transducers were stepped at 1/16" intervals during scanning. However, the 2048 step resolution in the θ axis corresponds to 1/32" resolution in the θ direction on a 20.0" diameter tire. Figure 4.24 shows an aircraft tire with foam tape flaws attached. The foam tape strips are 0.5" wide and the squares are 1.0" and 0.5" square for the large and small squares.

Figure 4.24: Aircraft tire with foam tape flaws attached.

Aircraft tires are constructed with nylon plies and belts instead of steel belts as used in truck tires. The tires typically have many more plies than a standard truck tire causing increased dispersion of the ultrasound beam in the material. The increased dispersion contributes significantly to blurring in ultrasonic images produced by scanning the tire. Since part of the blurring is due to the nature of the material itself and not only the transducer PSF, the system PSF must be recovered to successfully enhance the image resolution.

Figure 4.25 shows a partial scan of the tire in Figure 4.24. The scan was produced using a series of experimental fixtures that did not provide complete coverage

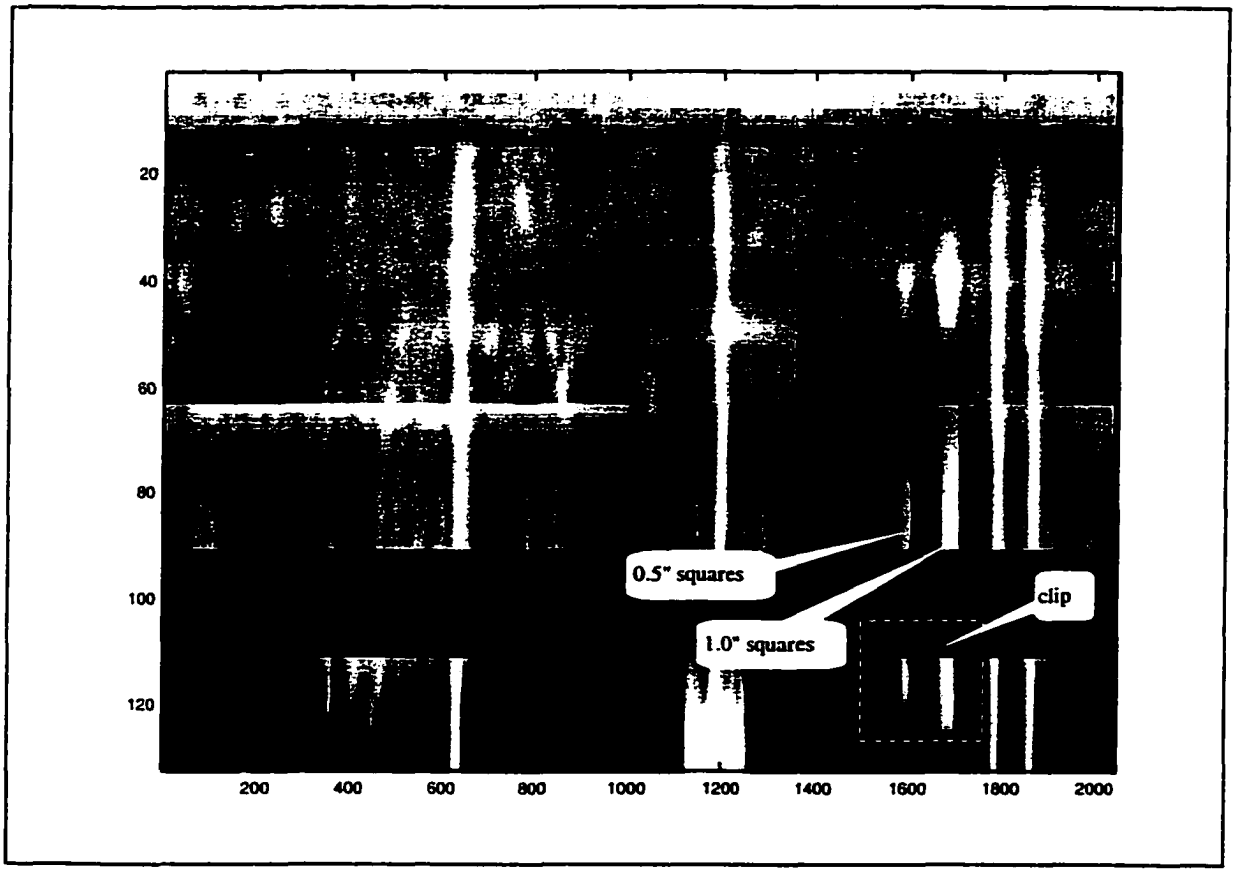

Figure 4.25: Ultrasonic scan of aircraft tire.

of the tire. The area of coverage is from the bead at the top of the figure to approximately halfway across the crown at the bottom of the figure. To place the foam flaws in proper relative position, a black strip is inserted to mark the location where data were not collected. In Figure 4.25, the strips of tape are easily discerned in addition to the large and small squares.

Figure 4.26 shows a close up view of the two square flaws labeled 'clip' in the lower left corner of Figure 4.25. The flaw on the left corresponds to the 0.5" square foam tape and the flaw on the right corresponds to the 1.0" square foam tape. Deconvolution by the direct method described earlier using the filter in Equation 4.52 is performed to enhance the image. No attempt is made to recover the system PSF, only to enhance the

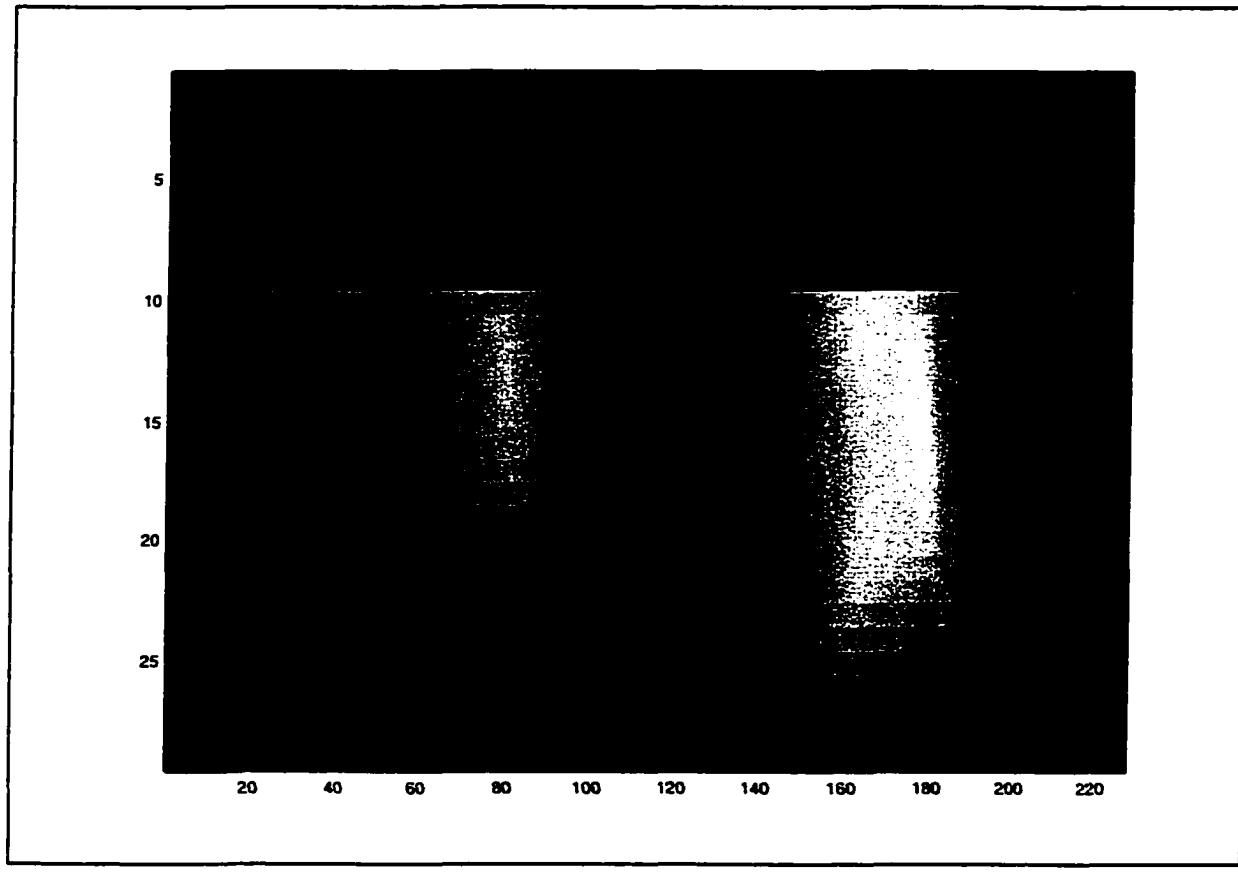

Figure 4.26: Known foam tape flaws.

image as per Equation 4.52. Both flaw sizes are known. The 0.5" flaw was selected as a known flaw in the image and used to enhance the 1.0" flaw. Since the step size in the m direction is 1/16" and the step size in the n or θ direction is 1/32" due to the encoder resolution, the step size in the m direction is artificially increased by linear interpolation to 1/32".

After the linear interpolation to match the step size in both directions, an ideal 1.0" square flaw will have an energy content of $\varepsilon = 1024$ (32^2). Figure 4.27A shows the convolved 1.0" square flaw and Figure 4.27C shows the same image histogram filtered and binary converted as performed in Figures 4.11 and 4.12 to eliminate noise. The energy for the convolved image is $\varepsilon =$ 1445 or much larger than expected for a 1.0"

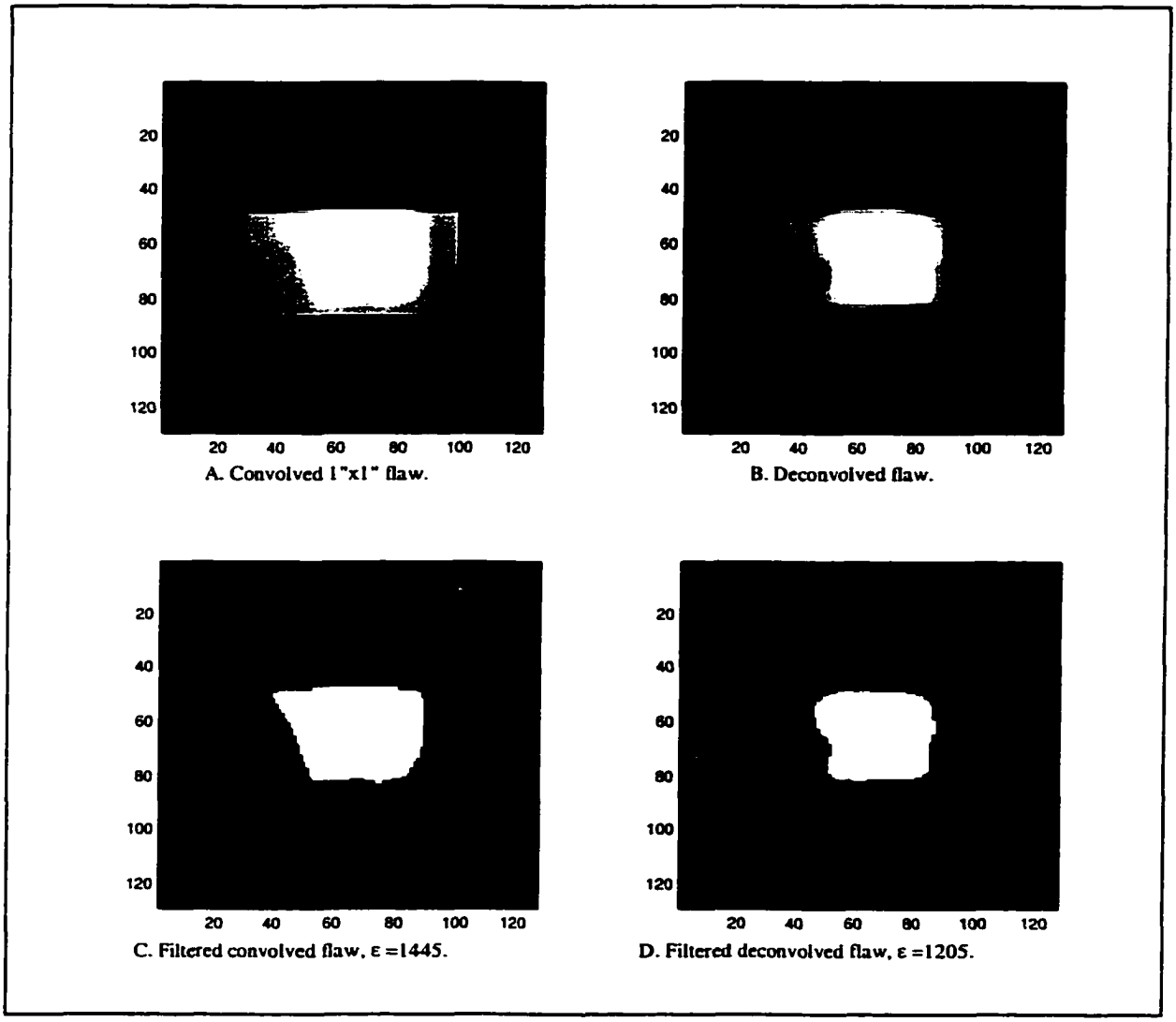

Figure 4.27: Flaw comparisons.

square flaw. Figure 4.27B shows the flaw after deconvolution and 4.27D shows the same flaw after histogram filtering and binary conversion to eliminate noise. After deconvolution by the direct method, $\varepsilon = 1205$, or very close to the expected value of 1024. The foam tape applied to simulate a flaw is 1.0" square. While the deconvolved flaw shown is not perfectly square, the image does represent a 1.0" square more accurately than the un-convolved image in 4.27C. This shows the system PSF for the aircraft tire is significant but recoverable. There is a 20% reduction in image energy with the energy of the deconvolved flaw very close to the actual value.

5. Conclusions.

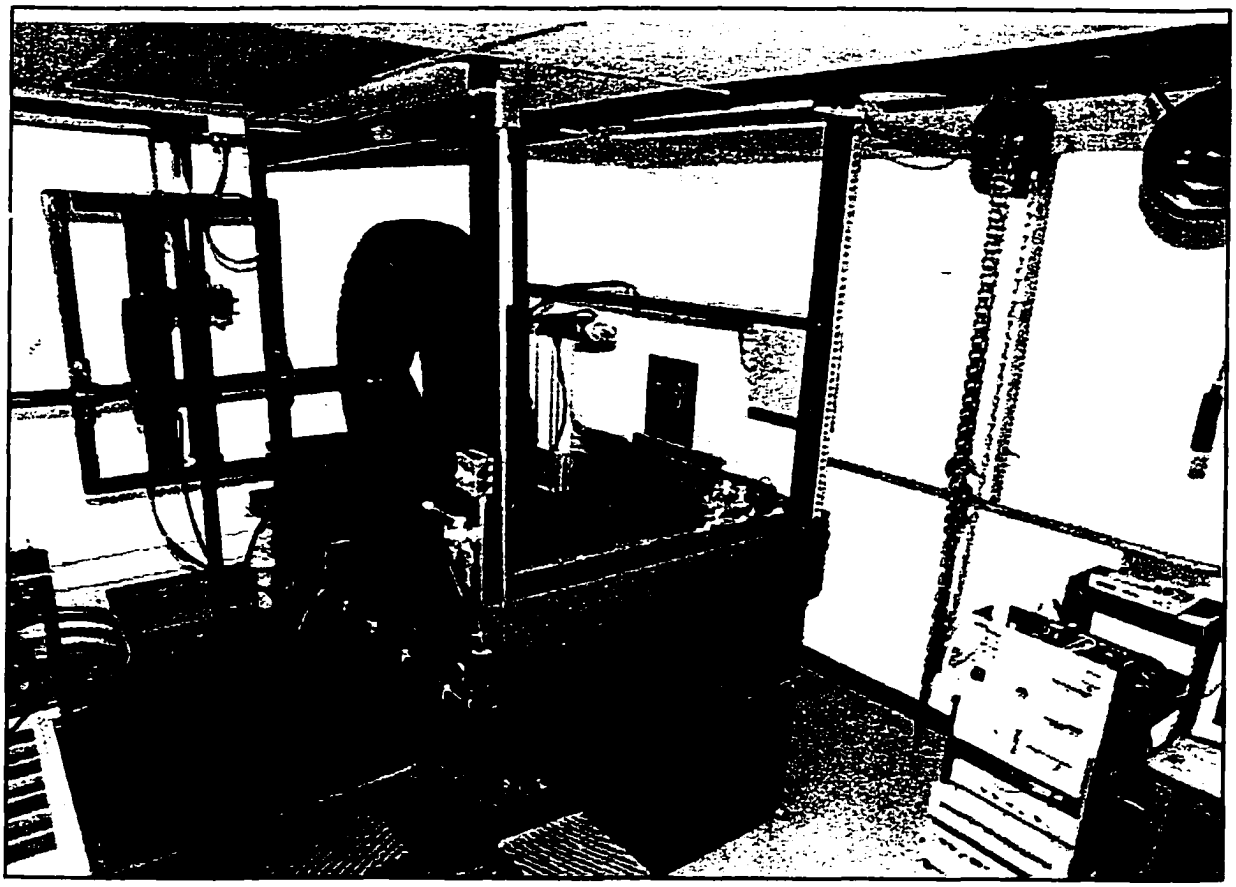

Figure 5.1: The CSU scanner.

In the work described here, a complete mechatronic system design for tire inspection was produced. In the course of this work two tire inspection scanners were constructed. One resided in the Advanced Inspection and Monitoring Laboratory at Colorado State University and is shown in Figure 5.1. The CSU scanner was relocated to the University of Maine in 1998. The second, shown in Figure 5.2, is currently in use on the production floor at Bandag Tire Corporation in Muscatine, Iowa. Tire scanning results performed using both machines during the period January, 1996 to October,

Figure 5.2: Bandag scanner.

1997 were presented in Sections 3.7 and 4.3. This system design is in production use at Bandag and demonstrates the efficacy of such a system in real applications.

tire inspection problem. Specifically, previous methods of tire inspection were slow needing 12 hours to complete a partial scan of only the tire crown region, or offered high speed only at a low resolution with 1" stepping. A completely functional system was developed and demonstrated, on simulated flaws, that allows high-speed, high-resolution data-acquisition for ultrasonic tire scanning. The design allows 1/8" or 1/16" stepping, coverage of the entire tire, and high speed scans of less than 10 minutes per tire. The design is based on a standard PC with plug-in cards that use embedded processors to control independent functions of the system. In this fashion, a central processor is not

obliged to perform all the duties of a data-acquisition and motion control system. The system architecture is easily extensible to other problems.

Additionally, a signal processing technique was demonstrated that allows significant reduction in the effects of the system point spread function in ultrasonic through-transmission tire inspection. While signal processing is not the primary focus of this work, it does demonstrate the veracity of enhancing ultrasonic tire images. The technique was applied to experimental tire inspection data. The technique employed a double Wiener filter to recover the system PSF and enhance ultrasonic signal quality. A direct filter algorithm dispensing with the double Wiener technique was demonstrated. The direct algorithm eliminates several calculation steps from the double Wiener implementation.

5.1 **Future work.**

As a complete design, the work presented here stands by itself. There are however several issues unresolved by this work that require future development. For the most part, this is due to relocation of the CSU scanner to the University of Maine prior to completion of this work. Due to the great distance involved, further development and testing of the system was no longer possible for this thesis. Additionally, use of the Bandag scanner was no longer possible due to availability and the lack of funding. Because of these facts, further testing and development was unable to progress. Areas still requiring development are detailed below.

First and foremost, a study should be undertaken to demonstrate the scanner's ability to detect actual flaws in real tires. This study showed the scanner to be capable of detecting simulated flaws in tires provided by Bandag. The tires were constructed with

embedded defects and were to be used as an example of the types of flaws and resolution required of an inspection system. The scanner met those requirements. However, little time was spent correlating the detection of simulated flaws with detection of actual flaws in tires. Such a study could begin with re-examination of the embedded defect tires and then a series of inspections of tires acquired from local tire shops. Tires with detected flaws could be sliced open to determine the nature and extent of detected damage.

The second area for future work is that the ultimate resolving capability of the inspection machine remains to be quantified. As shown in the demonstrations in Section 3.7, the machine was able to discern all flaws in the embedded defect tires provided by Bandag. Again, meeting the requirements of this study. However, a series of tests using embedded defect tires and/or foam tape flaws of various sizes would provide information on the ultimate resolving capability. Using embedded defect tires with known flaws or foam tape for attenuation provides detailed information on flaw sizing to be correlated with detected flaw images. The ultimate resolving capability can be inferred from this information.

More error handling capabilities can be developed for the system. The system is capable of performing error handling with additional effort spent on hardware-software development. There is currently no form of error checking other than the operator visually observing the b-scan display in progress. The observer is entirely responsible for setting system amplification properties.

The peak detector gating is typically fixed at the start of a scan. Gating for a tire is set wide enough to compensate for time of flight changes during movement of the receiver. It is possible that the gating and time delays for two receivers could overlap in

certain cases. This problem could be solved by an adaptive gating scheme where the gates could be reprogrammed during a scan to account for the change in time of flight characteristics. Time of flight characteristics are easily calculated knowing the geometry of the transmitter locations and the sensor head path. This could be implemented by moving the gate delay while sampling the input during a sensor head move to determine the highest level. Additionally, the peak detector gates turning on and off caused significant speckle noise in the Bandag system. This can be improved by proper time of flight gating.

Automatic gain control of the received signals, meant to be incorporated in the original software, remains to be developed. Instead, the operator needs to monitor receiver amplification through the visual display and manually change receiver gain. The system design included programmable attenuators that need only to have an appropriate control algorithm developed to provide automatic gain control.

For deconvolution, a number of areas can be addressed. The application of homomorphic deconvolution to the image enhancement should be applied. This type of deconvolution was only briefly mentioned in this work. Separation of the system point spread function knowing only the image complex cepstrum should be used. Investigation of the homomorphic deconvolution could eliminate the need for a known flaw to be placed on the material to be inspected before inspection.

Reciprocity of the focused receiving transducers was assumed. Some initial work by Achenbach indicates that reciprocity in this case is acceptable [Ach94]. Downs and Peterson also informally stated the 'gain' of the receiver could be modeled by reciprocity [Dow96]. However, these results are by no means conclusive. This was not actually

proven in fact since the system PSF recovery technique negated the need to demonstrate reciprocity. A thorough examination of focused, ultrasonic, receiving, transducer point spread functions would contribute significantly to through transmission inspection. One method that could be used to investigate this concept is operation of a phased array receiver to prove focusing and then be compared with a fixed focus receiver.

6. References

[Ach94] Achenbach, J.D., Beardsley, B., Peterson, M., Rogers, R., Tipescur, M., *Ultrasonic Testing of Truck Tires*, Progress Report to Bandag Tire Company, Center for Quality Engineering and Failure Prevention, Northwestern University, Evanston, IL, January 7, 1994.

[And77] Andrews, H.C., Hunt, B.R., *Digital Image Restoration*, Prentice-Hall, Englewood Cliffs, NJ, 1977.

[Bec97] Bechou, L., Ousten, Y., Tregon, B., Marc, F., Danto, Y., Even, R., Kertesz, P., *Ultrasonic images interpretation improvement for microassembling technologies characterization*, Microelectronics Reliability, Vol. 37, No. 10/11, 1997, pp. 1787-1790.

[Ber77] Berkhout, A.J., *Least-Squares Inverse Filtering and Wavelet Deconvolution*, Geophysics, Vol. 42, No. 7, Dec. 1977, pp. 1369-1383.

[Bol89] Bollinger, John G., Duffie, Neil A., *Computer Control of Machines and Processes*, Addison-Wesley, New York, 1989.

[Boz97] Bozarth, Martin, *1997 Retread Industry Report and Forecast For 1998*, International Tire and Rubber Association (ITRA) – The Tire Retreading/Repair Journal, Vol 41, No. 12, December, 1997, pp 4.

[Can74] Cannon, T.M., *Digital Image Deblurring by Nonlinear Homomorphic Filtering*, Ph.D. thesis, Computer Science Department, University of Utah, Salt Lake City, Utah.

[Car97] Carew, W.D., Prince, K.J., *Windows NT Workstation, the VMEbus, and real-time control*, IEEE Control Systems, Vol. 17, No. 4, August 1997, pp. 77-88.

[Che88] Chen, C.H.; Hsu, Wei-Lien; Sin, Sam-Kit; *A comparison of wavelet deconvolution techniques for ultrasonic NDT*, Proceedings, IEEE International Conference on Acoustics, Speech, and Signal processing, 1988, pp. 867-870.

[Che90] Chen, C.H., Sin, S.K., *On Effective Spectrum-based Ultrasonic Deconvolution Techniques for Hidden Flaw Characterization*, Journal of

the Acoustical Society of America, Vol 87, No. 3, March 1990, pp. 976-987.

[Che95] Cheng, Sheng-Wen, Chao, Min-Kang, *Image quality improvement of underwater synthetic aperture ultrasonic holography by deconvolution of spatial response of transducers*, Proceedings of the 1995 IEEE/MTS Oceans Conference, San Diego, October 1995, pp. 1859-1864.

[Che96] Cheng, Sheng-Wen, Chao, Min-Kang, *Resolution improvement of ultrasonic C-scan images by deconvolution using the monostatic point-reflector spreading function (MPSF) of the transducer*, NDT & E International, Vol. 29, No. 5, 1996, pp. 293-300.

[Cla86] Clark, G.A., Tilly, D.M., Cook, W.D., *Ultrasonic signal/image restoration for quantitative NDE*, NDT International, Vol. 19, No. 3, June 1986, pp. 169-176.

[Cla93] Clark, C., Meardon, K., Russell, D., *Scrap Tire Technology and Markets*, Noyes Data Corporation, Park Ridge, 1993.

[Col73] Cole, E.R, *The Removal of Unkown Image Blurs by Homomorphic Filtering*, Ph.D. thesis, Department of Electrical Engineering, University of Utah, Salt Lake City, Utah, 1973.

[Com93] Compumotor, *Positioning Control Systems and Drives*, Product literature by Parker, Inc., Compumotor Division, 1993.

[Cra97] Cravotta, N., *Real-time operating systems*, Embedded Systems Programming, Vol. 10, No. 3, March, 1997, pp.97 - 104.

[Cur55] Curtis-Wright Corp., *C-W ultrasonic tire tester*, Rubber Age, Vol76, 1955, p. 768.

[Cus90] Cushman, Charles R., Dikeman, Loren J., U.S. Patent #4,936,138, *Method and apparatus for tire inspection*, 1990.

[Dow95] Downs III, Justin G., *Re-Engineering the Denning MRV-3 with Enhanced Processing Capabilities*, MS Thesis, Colorado State University, Department of Mechanical Engineering, 1995.

[Dow96] Downs III, J., Peterson, M.L., *Theoritical, Simulated, and Experimental Resolution Enhancement of a Transducer by Deconvolution of the Point Spread Function*, in Review of Progress in Quantitative NDE, Vol. ??, 1996, pp. ??.

[Dow97] Downs III, J., *System for Non-Destructive Testing of Tire Sidewalls*, U.S. Navy SBIR #N68335-97-C-0200, Final Report, October 31, 1997.

[Dug81] Dugger, Doyle L., Ho, Morris D., U.S. Patent #4,275,589, *Method and apparatus for non-destructive inspection of tires*, 1981.

[Dun54] Dunlop Rubber Company Research Center and General Electric Co., *Tire faults can't get past this unique machine*, Tyres and Accessories, Vol. 9, 1954, pp. 13-17.

[Eic85] Eichhorn, N., Saedler, J., Wilhelmi, W., *Digital Analysis of Tyre Interferograms*, Acta Polytechnica Scandinavica, Applied Physics Series,V150, 1985, ppg88-91.

[Ell96] Ellis, Mike R., *Advanced visualization and automated flaw detection for truck tire casing inspection*, MS thesis, Dept. of Mechanical Engineering, Colorado State University, 1996.

[Elp97] Sales literature, Elpex, Inc., www.elpex.com, 1997.

[Fre89] French, Tom, *Tyre Technology*, Adam Hilger, Bristol, 1989.

[Fro88] Frock, B.G., Martin, R.W., Moran, T.J., Shimmin, K.D., *Imaging of impact damage in composite materials*, in Review of Progress in Quantitative NDE, Vol. 7b, Plenum Press, New York, 1988, pp. 1093-1099.

[Fro90] Frock, B.G., Karpur, P., *Blur reduction in ultrasonic images using pseudo three dimensional Wiener filtering*, in Review of Progress in Quantitative NDE, Vol. 9a, Plenum Press, New York, 1990, pp.751-757.

[Fro91] Frock, B.G., Karpur, P., Ruddell, M.J., *Effects of Axial-Wiener Deconvolution on the Lateral Resolution in Ultrasonic C-scan Images*, Review of Progress in Quantitative Nondestructive Evaluation, Vol 10A, Edited by D.O. Thompson and D.E. Chimenti, Plenum Press, New York, 1991, pp 781-788.

[Gil94] Van Gilluwe, Frank, *The Undocumented PC*, Addison-Wesley Publishing Co., New York, 1994.

[Gol96] Golub, Gene H., Van Loan, Charles F., *Matrix Computations; Third Edition*, The Johns Hopkins University Press, Baltimore, 1996.

[Gre80] Greguss, Pal., *Ultrasonic imaging: seeing by sound: the principles and widespread applications of image formation by sonic, ultrasonic, and other mechanical waves*, Focal Press, New York, 1980.

[Hal68] Halsey, G.H., *The NDT of passenger tires*, Materials Evaluation, Vol. 26, 1968, pp137-142.

[Hal77] Halsey, George H., U.S. Patent #4,059,989, *Non-destructive examination of an article particularly a tire, with ultrasonic energy*, 1977.

[Hay89] Hayward, G., Lewis, J.E., *Comparison of some non-adaptive deconvolution techniques for resolution enhancement of ultrasonic data*, Ultrasonics, Vol. 27, May 1989, pp. 155-164.

[Hun80] Hundt, E.E., Trautenberg, E.A., *Digital processing of ultrasonic data by deconvolution*, IEEE Transactions on Sonics and Ultrasonics, Vol. SU-27, No. 5, September 1980, pp. 249-252.

[Irm93] iRMX III Operating Systems, Intel Corporation product and pricing literature, 1993.

[Jac93] Jacob, Gerald, *PC-based test capabilities more alluring*, Evaluation Engineering, Vol. 32, No. 6, June 1993, pp. 12-16.

[Jen92] Jensen, J.A., *Deconvolution of ultrasound images*, Ultrasonic Imaging, Vol. 14, 1992, pp. 1-15.

[Jen93] Jensen, J.A., Mathorne, J., Gravsen, T., Stage, B., *Deconvolution of in-vivo ultrasound B-mode images*, Ultrasonic Imaging, Vol. 15, 1993, pp. 122-133.

[Kar89] Karpur, P., Frock, B., *Two dimensional pseudo-Wiener filtering in ultrasonic imaging for nondestructive evaluation applications*, in Review of Progress in Quantitative NDE, Plenum Press, New York, 1989, pp. 743-750.

[Kec91] Kechter, G.E., Achenbach, J.D., *Combined linear and homomorphic deconvolution for processing bandpass measurements*, IEEE Transactions on Signal Processing, Vol. 39, No. 6, June 1991, pp. 1300-1304.

[Kra90] Krautkramer J., Krautkramer, H., *Ultrasonic testing of Materials*, Springer-Verlag, New York, 1990.

[Lan96] Landman, Ronald G., *Selecting a real-time operating system*, Embedded Systems Programming, Vol. 9, No. 4, April 1996, pp. 79-95.

[Lof93] Loftis, Donald B., Cawlfield, David W., *Direct control of large processes using a micro-computer*, Advances in Instrumentation and Control, Vol. 48, Part 1, pp.603-612.

[Ler96] Lerch, Terrence Peter, *Ultrasonic transducer characterization beam modeling for applications in nondestructive evaluation*, Ph.D. dissertation, Department of Engineering Science and Mechanics, Iowa State University, Ames, Iowa, 1996.

[Mac90] Macecek, Mirek, Allan, Dave J., Bubik, Leslie, U.S. Patent #5,095,744, *UltrasonicTire Testing Method and Apparatus*, 1990.

[Mar93] Marsh, C.E., Tucker, T.W., Streit, R.L., Moore Products Co., *Characteristics and Application of an Industrial PC in a Process Control Environment*, Proceedings of the Industrial Computing Conference, Vol. 37, Industrial Computing Conference, 1993, pp. 639-649.

[McC72] McConnell, G., Klinman, R., *The nondestructive inspection of aircraft tires by use of pulse-echo ultrasonics*, Rep. NADC-72035-VT/AD 747633, Naval Air Development Center, Warminster, PA, May 1972.

[McC75] McCauley, Porter T., U.S. Patent #3,882,717, *Self-adjusting ultrasonic tire inspection device*, 1975.

[Mec96] Coverleaf definition, *IEEE/ASME Transactions on Mechatronics*, Fumio Harashima, editor-in-chief, Vol. 1, No. 4, 1996.

[Mit92] Mitchell, K.W., Gilmore, R.S., *A true Wiener filter implementation for improving signal to noise and resolution in acoustic images*, Review of Progress in Quantitative Nondestructive Evaluation, Vol. 11, Edited by D.O. Thompson and D.E. Chimenti, Plenum Press, New York, 1992, pp. 895-902.

[Mor45] Morris, W.E., U.S. Patent #2,378,237, *Method and Apparatus for Ultrasonic Testing*, 1945.

[Mor52] Morris, W. E., Stambauch, R.B., Gehman, S.D., *Ultrasonic method of tire inspection*, Rev. Sci. Instrum. Vol. 23, 1952, pp 729-734.

[Mur78] Murakami, Y., Kuri-Yakub, B.T., Kino, G.S., Richardson, J.M., Evans, A.G., *An Application of Wiener Filtering to Nondestructive Evaluation*, Applied Physics Letters, Vol. 33, No. 8, October 15, 1978, pp 685-687.

[Nat95] National Instruments seminar attended by Justin Downs III, July 1995.

[Nat97] Instrumentation Catalog, National Instruments, Bridgeport, TX, 1997.

[Nea86a] Neal, S., Thompson, D.O., *An examination of the application of Wiener filtering to ultrasonic scattering amplitude estimation*, in Review of

Progress in Quantitative NDE, Vol. 5, Plenum Press, New York, 1986, pp. 737-744.

[Nea86b] Neal, S., Thompson, D.O., *An a priori knowledge based Wiener filtering approach to ultrasonic scattering amplitude estimation*, in Review of Progress in Quantitative NDE, Vol. 6, Plenum Press, New York, 1986, pp. 807.

[Nea88a] Neal, S.P., *A prior knowledge based optimal Wiener filtering approach to ultrasonic scattering amplitude estimation*, Ph.D. dissertation, Department of Engineering Science and Mechanics, Iowa State University, Ames, Iowa, 1988.

[Nea88b] Neal, S.P., Thompson, D.O., *Evaluation of the effects of prior flaw information on Wiener filter based ultrasonic flaw scattering amplitude estimation*, Review of Progress in Quantitative NDE, Vol. 7a, Plenum Press, New York, 1988, pp.857-864.

[Nea92] Neal, S.P., Thompson, D.O., *Utilization of prior flaw information in ultrasonic NDE: an analysis of flaw scattering amplitude as a random variable*, Journal of Nondestructive Evaluation, Vol. 11, No. 2, 1992, pp 57-67.

[Nea93] Neal, S.P., Speckman, P.L., Enright, M.A., *Flaw signature estimation in ultrasonic nondestructive evaluation using the Wiener filter with limited prior information*, IEEE Transactions on Ultrasonics, Ferroelectrics, and Frequency Control, Vol. 40, No. 4, July 1993, pp 347-353.

[Opp75] Oppenheim, A.V., Schafer, R.W., *Digital Signal Processing*, Prentice Hall, Englewood Cliffs, NJ, 1975.

[Ort88] Ortoli, David M., *How to Automate Tire Testing Laboratories*, Elastomerics, V120, No. 2, February 1988, ppg 14-18.

[Pan94] Panametrics, Inc, *Automated Ultrasonic Scanning Systems for Nondestructive Testing*, Product literature by Panametrics, Waltham, MA, 1994.

[Pan95] Panametrics, Inc., *Ultrasonic Transducers for Nondestructive Testing*, Product literature by Panametrics, Waltham, MA, 1995.

[Pat97] Patent Search Server, http://patent.womplex.ibm.com/, 1997.

[Pre89] Prejean, M., *Half-soles, Kettles, and Cures; Milestones in the Tire Retreading and Repair Industry*, published by International Tire and Rubber Association (ITRA), Louisville, KY, 1989.

[Pre97] Sales literature, Premier Tire Co. 2200 Market Street, Denver, CO, 1997.

[Rei94] Reis, H.L.M, Warmann, K.A., *Acousto-ultrasonic non-destructive evaluation of fatigue damage in steel-belted radial tyres.* Insight - Non-Destructive Testing and Condition Monitoring, Vol. 36, No. 12, December 1994, pp 958-963.

[Rei96] Reis, H.L.M., Warmann, K.A., *Acousto-ultrasonic damage evaluation of steel-belted radial tires.* Proceedings of the Seventh International Symposium on Nondestructive Characterization of Materials, Center for Nondestructive Evaluation, Johns Hopkins University, Baltimore, MD, 1996.

[Rei97] Reis, Henrique, *Prototype instrument for damage evaluation in steel belted radial tires using acousto-ultrasonics*, Proceedings of the Eighth International Symposium on Nondestructive Characterization of Materials, Center for Nondestructive Evaluation, Johns Hopkins University, Baltimore, MD, 1997.

[Rea90] Reader, Karen, *Automated NDT for Manufacturing Industry*, Metals and Materials, V6, No10, 1990, ppg 636-639.

[Rog91] Rogers, R.,, Peterson, M., Achenbach, J.D., *Ultrasonic Testing of Truck Tires*, Progress Report to Bandag Tire Company, Center for Quality Engineering and Failure Prevention, Northwestern University, Evanston, IL, July 15, 1991.

[Rog92] Rogers, R., Peterson, M., Achenbach, J.D., *Ultrasonic Testing of Truck Tires Phase II*, Progress Report to Bandag Tire Company, Center for Quality Engineering and Failure Prevention, Northwestern University, Evanston, IL, 1992.

[Rog92] Rogers, R., *Ultrasonic Testing of Truck Tires*, M.S. Thesis, Northwestern University, Evanston, IL, 1992.

[Rog94] Rogers, R., Bandag Tire Corporation Research Engineer, Correspondence with M. Peterson, August 24, 1994.

[Ros82] Rosenfeld, A., Kak, A.C., *Digital Picture Processing*, Academic Press, New York, 1982.

[Rya77] Ryan, Robert F., *A Semi-Automated Pulse-Echo Ultrasonic System for Inspecting Tires*, Report No. DOT-TSC-NHTSA-76-3, HS-802-104, U.S. Department of Transportation, Transportation Systems Center, 1977.

[Sil87] Silvia, M.T., *Deconvolution*, Handbook of Digital Signal Processing, Chapter 10, Academic Press, New York, 1987.

[Sin92] Sin, Sam-Kit; Chen, C.H.; *A comparison of deconvolution techniques for the ultrasonic nondestructive evaluation of materials*, IEEE Transactions on Image Processing, Vol. 1, No. 1, January 1992, pp. 3-10.

[Str97] Strassberg, Dan, *The Changing Shape of PC-Based Test and Measurement*, EDN, October 23, 1997, pp 53-62.

[Sub95] Subbarao, Maruli; Wei, Tse-Chung; Surya, Gopal; *Focused Image Recovery from Two Defocused Images Recorded with Different Camera Settings*, IEEE Transactions on Image Processing, Vol. 4, No. 12, December 1995, pp. 1613-1628.

[Tax95] Taxt, Torfinn, *Restoration of Medical Ultrasound Images Using Two-Dimensional Homomorphic Deconvolution*, IEEE Transactions on Ultrasonics, Ferroelectrics, and Frequency Control, Vol. 42, No. 4, July 1995, pp. 543-553.

[Tec94] Technic Systems Ltd, *Product Information Literature*, Long Whatton, Loughborough, Leicestershire, LE12 5DA, 1994.

[Tre82] Treitel, S., Lines, L.R., *Linear Inverse Theory and Deconvolution*, Geophysics, Vol. 47, No. 8, Aug. 1982, pp. 1153-1159.

[Ulr71] Ulrych, T.J., *Application of Homomorphic Deconvolution to Seismology*, Geophysics, Vol. 36, No. 4, Aug. 1971, pp. 650-660.

[Unl95] Unluturk, M.S., Saniie, J., *Deconvolution Neural Networks for Ultrasonic Testing*, in Proceedings, IEEE Ultrasonics Symposium, Vol. 1, 1995, pp. 715-719.

[Var94] Vardeman, Stephan, B., *Statistics for Engineering Problem Solving*, PWS Publishing Company, Boston, 1994.

[Vol82] Vollmann, Wolfgang, *Resolution Enhancement of Ultrasonic B-Scan Images by Deconvolution*, IEEE Transactions on Sonics and Ultrasonics, Vol. SU-29, No. 2, March 1982, pp. 78-83.

[Wei81] Weiss, Arnold, A., U.S. Patent #4,297,876, *Ultrasonic tire testing Apparatus*, 1981.

[Whi95] White, Liz, *Ultrasound 'Sees' Tyre Defects*, European Rubber Journal, V177, March 3, 1995, ppg 16-17.

[Wie42] Wiener, N., *Extrapolation, Interpolation, and Smoothing of Stationary Time Series*, MIT Press, Cambridge, 1942.

[Yov94] Yovichin, A.J., U.S. Patent #5,313,827, *Method and apparatus for detecting ply defects in pneumatic tires*, 1994.

[Zha95] Zhao, J., Gaydecki, P.A., Burdekin, F.M., *Investigation of block filtering and deconvolution for the improvement of lateral resolution and flaw sizing accuracy in ultrasonic testing*, Ultrasonics, Vol. 33, No. 3, 1995, pp. 187-194.

7. Appendix

7.1 Tire coordinate system.

Due to the shape of the surface to be inspected, (approximately a torus with open interior) using a standard X,Y coordinate system would be difficult. Instead, a cylindrical coordinate system using r, θ, and z vectors is adopted. The cylindrical coordinates allow industry tire sizes, as demonstrated in Section 3.1.2, to describe the tire profile for data acquisition and sensor control purposes.

The tire is assumed to possess a standard profile with variation only in the width, height, rim size, and bead opening (bead to bead distance). a general algorithm can be developed to describe tire profiles by the tire size. Since inspection using the current system is through transmission ultrasound, without regard to depth, the tire can be mapped as a three dimensional manifold. The tire may be considered to be a toroidal surface with part of the interior removed. It is desirable to map the 2-D profile of a slice of the manifold onto a single line. Figure A.1 shows the location of the 2-D abstraction line relative to the tire. Assume for inspection purposes there is no depth associated with the tire and the ultrasound beam is inspecting a single layer.

To describe the line mathematically, note that the line is built up with elliptic sections as in Figure A.2. Knowing the bead opening, the height, and the width of the tire, the vertical segments can be constructed. The load of a tire is actually carried in tension by the upper half of the tire and the sidewall under the tread can be modeled by extension lines dropping from tangents at the major axis of the ellipse to the bead at the rim [Fre88]. This is analogous to a gondola slung under a hot air balloon. However, under use, the tire is flexed causing the lower half to curve. When used and dismounted, the curvature remains necessitating this model where segments ***a*** and ***c*** are curved.

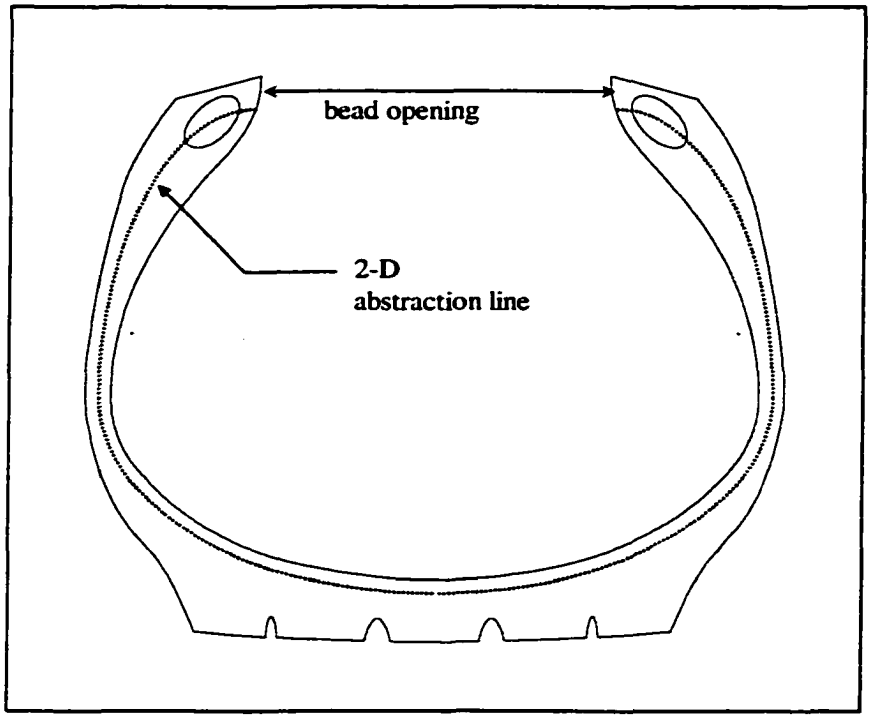

Figure A.1: 2-D abstraction line.

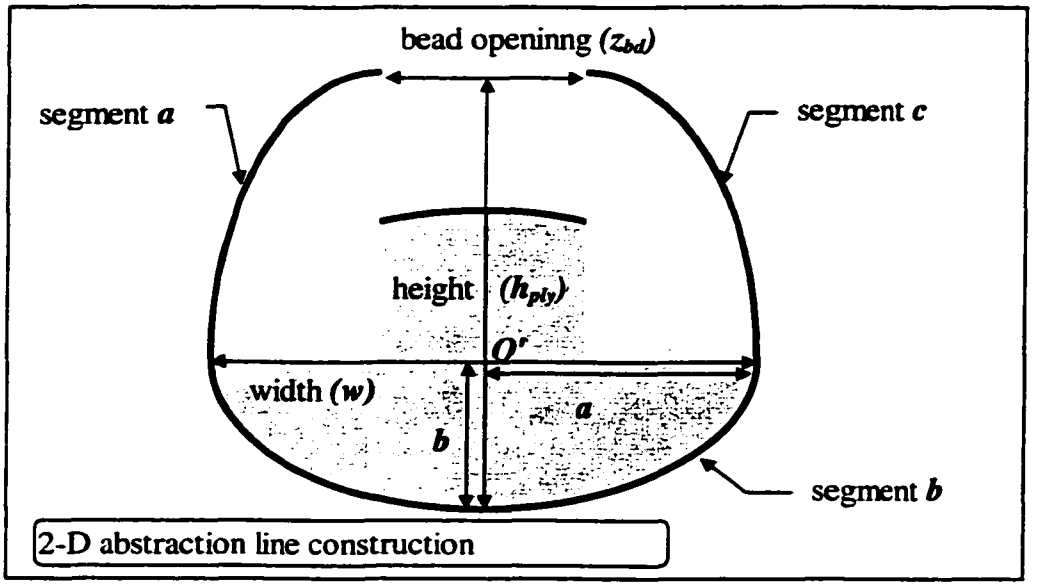

Figure A.2: Abstraction line construction.

Noting that in general tread depth is approximately 1.0", the location of the belt plies and the bottom of the ellipse for the abstraction line will be:

$$h_{ply} = h - 1.0$$
$$h = \alpha\, w$$

where: h = *original height of tire*
α = *aspect ratio*
w = *width*

The minor axis b of the ellipse is typically about 1/3 of h_{ply} and the major axis a, 1/2 the width, the half length of the axes can be calculated simply by:

$$b = \frac{1}{3} h_{ply}$$

$$a = 0.5w$$

An origin O' placed at the center of the crown ellipse will serve to locate the abstraction line elements relative to a global coordinate system.

A global coordinate system can be developed using cylindrical coordinates with r, θ, and z components that are natural for describing locations on a tire. Let the origin O of the coordinate system be located at the intersection of a line and a plane. Let the plane will bisect the tire with the intersection located at the center of the tire as shown in Figure A.3. Using cylindrical coordinates, the center of the tire will become the global origin O.

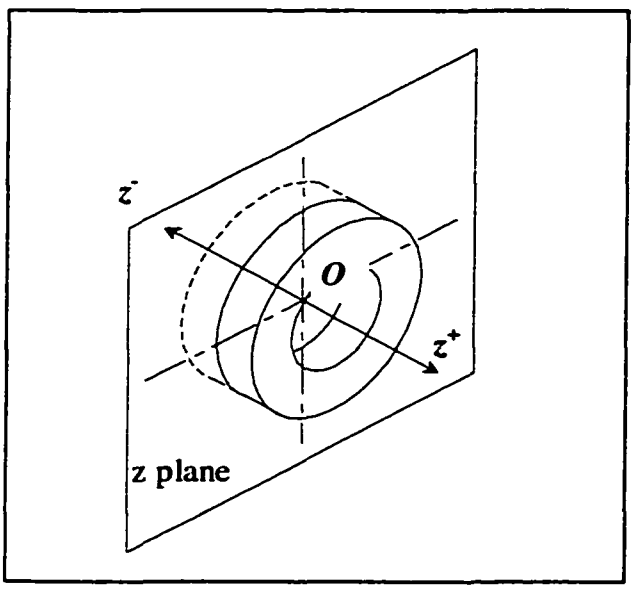

Figure A.3: Tire z plane.

All points on the tire can be described in r, θ, and z coordinates. Figure A.4 shows the

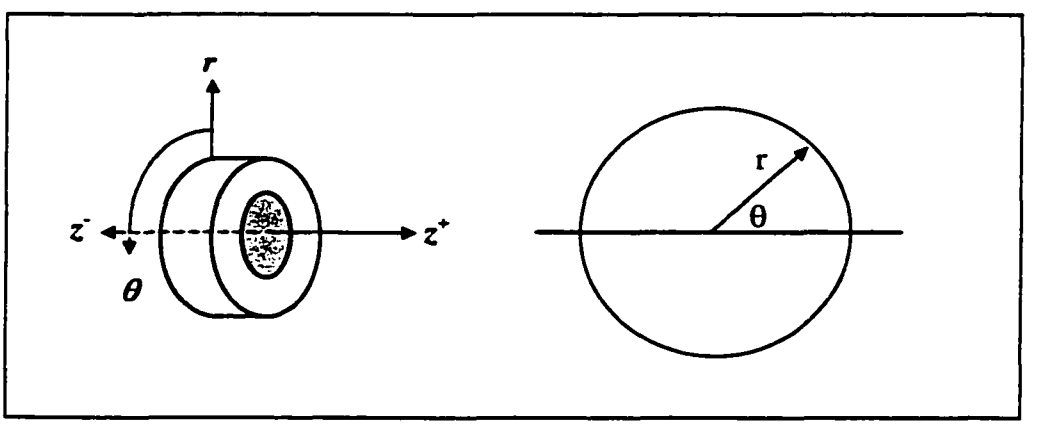

Figure A.4: Tire cylindrical coordinates.

directions for r and θ components. In this coordinate system, one side of the tire will have positive z components and the other half will have negative z components. The use of positive and negative z provides advantages in using the coordinate system due to the symmetric properties of the tire itself.

The abstraction line can then be described first in a local coordinate system O'', located at the center of the segment a ellipse, and then transferred to the global O coordinate system. Figure A.5 shows segment a relative to the local center O'' and the

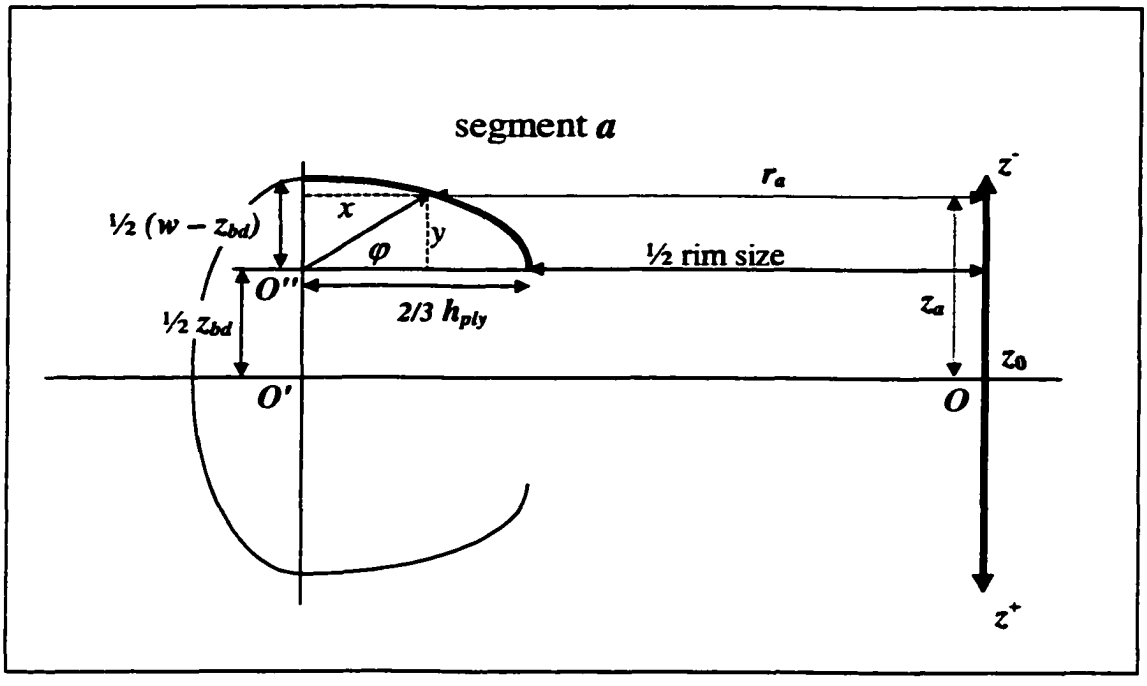

Figure A.5: Segment a relative to O'' system.

global center O. From the figure, the ellipse can be described in the O'' coordinate system by standard equations where:

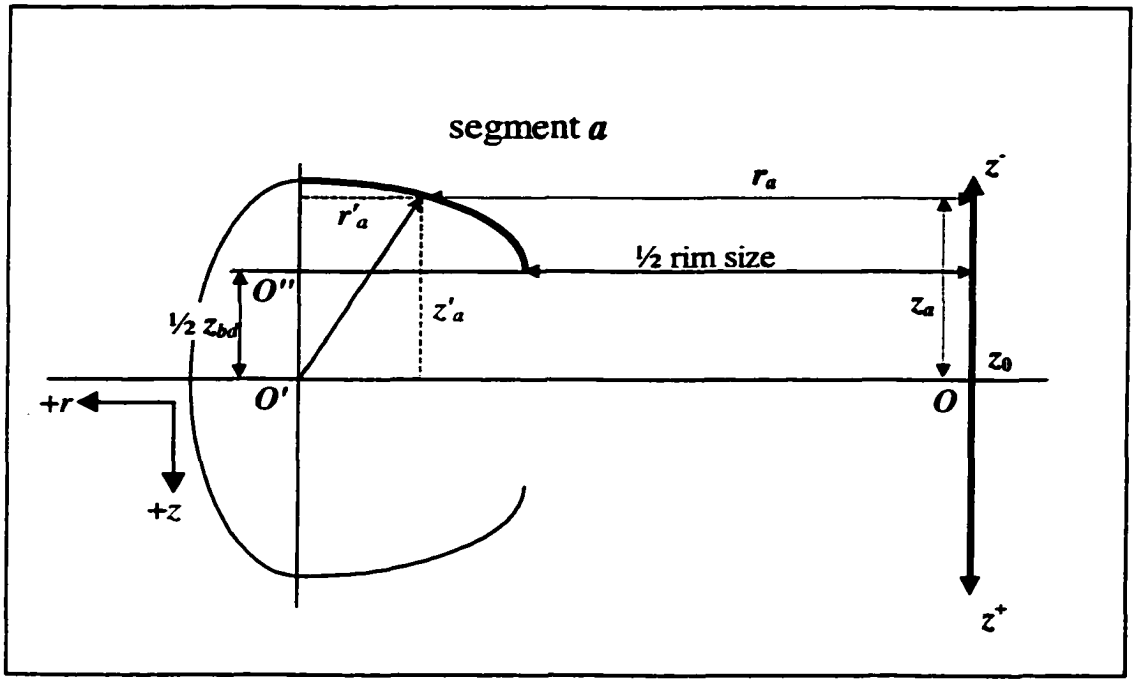

Figure A.6: Segment *a* in *O'* coordinate system.

$$x = \frac{2}{3} h_{ply} \cos\varphi$$
$$y = \frac{1}{2}(w - z_{bd})\sin\varphi \qquad 0 < \varphi < 90°$$

Coordinate transformation can be made to the *O'* system as in Figure A.6 where:

$$r'_a = -x$$
$$z'_a = -\left(y + \frac{1}{2} z_{bd}\right)$$

Where the convention for *z* is followed so *z* is negative on the segment *a* side of the tire and *r* is negative for later transformation to the *O* system. The *O'* system is located relative to the *O* system at:

$$r_{O'} = \frac{1}{2} rimsize + \frac{2}{3} h_{ply}$$
$$z_{O'} = z_0$$

So that a final coordinate transformation for segment ***a*** into the ***O*** system is:

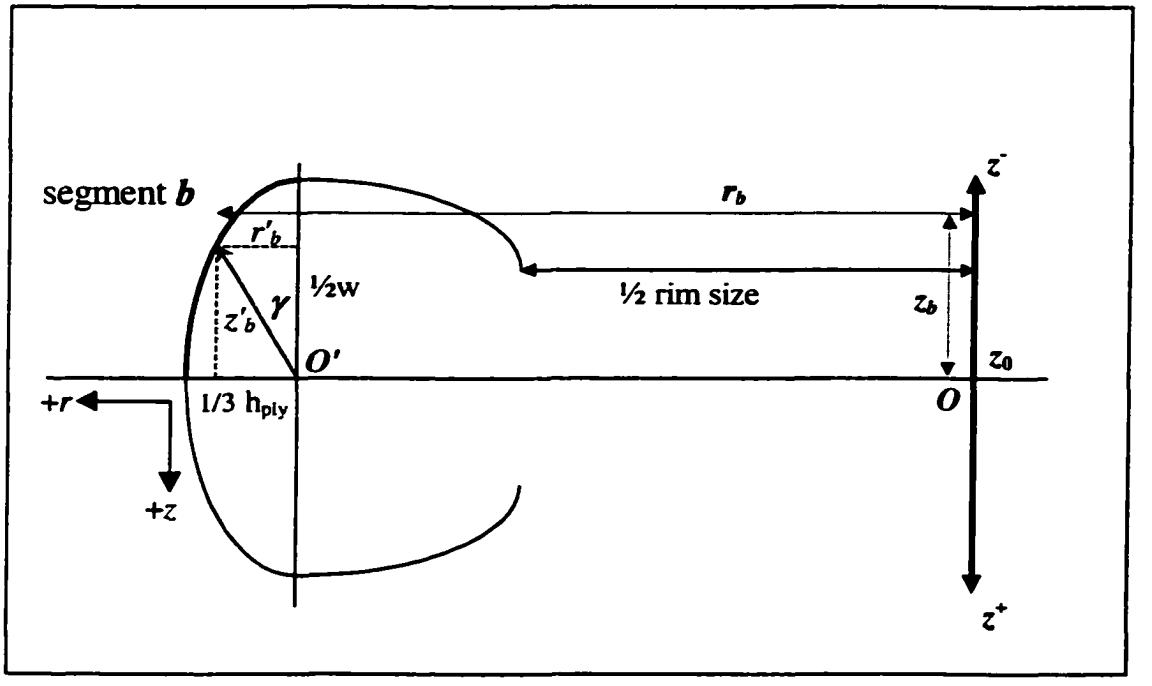

Figure A.7: Segment *b* in *O'* coordinate system.

$$r_a = \frac{1}{2} rimsize + \frac{2}{3} h_{ply}(1 - \cos\varphi)$$
$$z_a = -\left[\frac{1}{2}(w - z_{bd})\sin\varphi + \frac{1}{2} z_{bd}\right] \qquad 0 < \varphi < 90° \qquad \text{(A.1)}$$

Segment ***b*** can be described in a similar manner as shown in Figure A.7. In the local coordinate system ***O'***, the location of segment ***b*** will be at:

$$r_b' = \frac{1}{3} h_{ply} \sin\gamma$$
$$z_b' = -\frac{1}{2} w\cos\gamma \qquad 0 < \gamma < 90°$$

Where z is negative to follow the convention established. Transfer to the ***O*** coordinate system is then:

$$r_b = \frac{1}{2} rimsize + h_{ply}\left(\frac{2}{3} + \frac{1}{3}\sin\gamma\right) \qquad 0 < \gamma < 90° \qquad \text{(A.2)}$$
$$z_b = -\frac{1}{2} w\cos\gamma$$

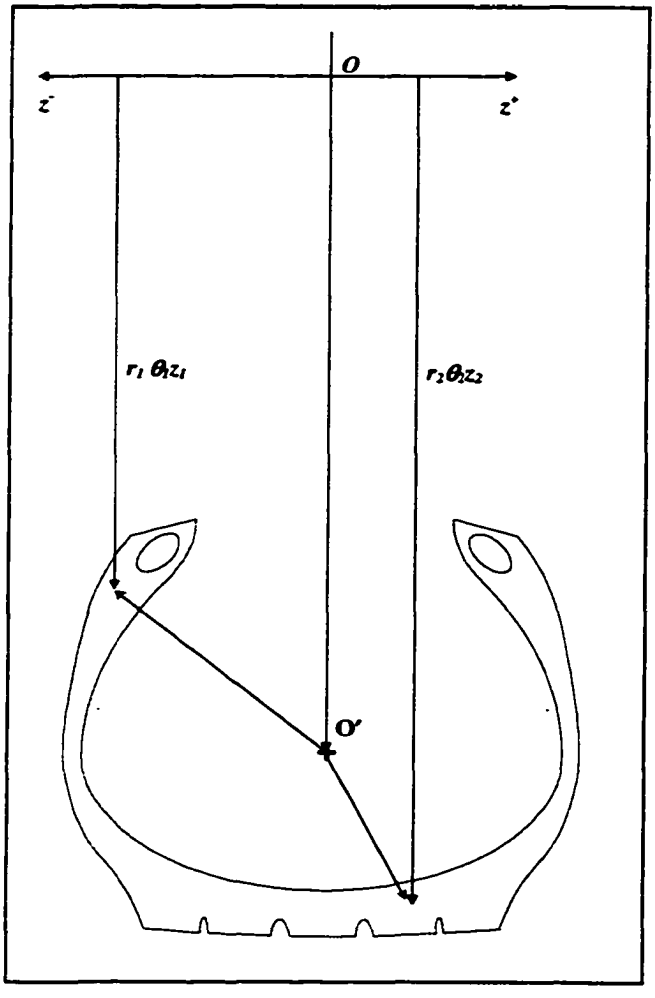

Figure A.8: Tire coordinate points.

Equations A.1,2 describe the location of the abstracted line on the negative z side of the z-plane. From the symmetric nature of the coordinate system, it is a simple matter to transfer the same coordinates to the positive side of the z-plane by multiplying the z values by (–1). The abstraction line will be called the ***inspection band*** (IB).

Figure A.8 shows how points on the IB are located using the tire coordinate system. The *tire angle* θ is relative to an arbitrary zero point picked on the tire and describes the angle between the zero point and the radial line to a point on the IB. Both the global origin O and the local origin O' will be used later.

7.2 MATLAB code for tire setpoint program.

```
% tiresets.m

% m file to generate set point information

clear

width = input('Enter tire width ') ;
rimsize = input('Enter tire rimsize ') ;
aspectratio = input('Enter aspect ratio ') ;
beadopening = input('Enter bead opening ') ;

%width = 10 ;
%rimsize = 22.5 ;
%aspectratio = 1 ;
%beadopening = 6;

stepsize = 8 ;
slowstep = .1 ;
medstep = .2 ;
faststep = .6 ;
linelength = 8 ;
armwidth = 1 ;
%rh = 15 ;
rh = 18 ;
zh = 25 -beadopening/2 ;

if width > 50
  width = width/10/2.54 ;
end
height = width*aspectratio ;
treadwidth = 0.75*width ;
hply = height - 1 ;

b = hply/3 ;
a = 0.5*width ;

z0 = 0.5*beadopening ;

rset = 0.5*rimsize - 3.0 ;
rsetsteps = rset*stepsize ;
zset = z0 ;

rinsp = 0.5*(rimsize - beadopening*tan(20/360*2*pi)) ;
rinspsteps = (rinsp-rset)*stepsize ;
zinsp = zset ;

rint = 0.5*rimsize + ...
     (height - 1)*(2/3 + sqrt(1-(treadwidth/width)^2)/3) ...
     - 0.5*treadwidth*tan(20/180*pi) ;
rintsteps = (rint-rinsp)*stepsize ;
zint = z0 ;

z1 = beadopening/2-0.125-armwidth/2 - 0.375 ;
zcrown = z1 ;
zcrownsteps = z1*stepsize ;
rcrown = 0.5*rimsize + 2*hply/3 - ...
       ((cot(20/180*pi)*(treadwidth/2-z1)) - ...
       b*sqrt((1-((treadwidth/a)^2)/4))) ;
rcrownsteps = abs((rcrown-rint))*stepsize ;
zend = -2*z1 ;
zendsteps = 2*(zcrownsteps) ;

out = [' bead opening' sprintf('%6.2f',beadopening) ;
```

```
        ' O location  ' sprintf('%6.2f',z0) ;
        ' rset        ' sprintf('%6.2f',rset) ;
        ' zset        ' sprintf('%6.2f',z0) ;
        ' rinsp       ' sprintf('%6.2f',rinsp) ;
        ' zinsp       ' sprintf('%6.2f',zinsp) ;
              ' rint        ' sprintf('%6.2f',rint) ;
             ' rcrown      ' sprintf('%6.2f',rcrown) ;
        ' zcrown      ' sprintf('%6.2f',zcrown)
        ' zend        ' sprintf('%6.2f',zend) ]

steps = [' rset steps   ' sprintf('%6d',round(rsetsteps));
        ' rinsp steps  ' sprintf('%6d',round(rinspsteps)) ;
        ' rint steps   ' sprintf('%6d',round(rintsteps)) ;
              ' rcrown steps ' sprintf('%6d',round(rcrownsteps)) ;
        ' zcrown steps ' sprintf('%6d',round(zcrownsteps)) ;
        ' zend steps   ' sprintf('%6d',round(zendsteps))]

% ---- GENERATE THE TIRE SECTIONS ----------------------------
phi = 0:.02:pi/2 ;
gamma = 0:.02:pi/2 ;
ra = rimsize/2 + hply/3*2*(1-cos(phi)) ;
za = -((width-beadopening)*sin(phi)/2 + beadopening/2) ;
rb = rimsize/2 + hply*(2/3+sin(gamma)/3) ;
zb = -width*cos(gamma)/2 ;

x1 = [za zb] ;
y1 = [ra rb] ;
xvect = [x1 fliplr(-x1)] ;
yvect = [y1 fliplr(y1)] ;

treadlinez = [-treadwidth/2 treadwidth/2] ;
treadliner = [height+rimsize/2 height+rimsize/2] ;

% ---- CALCULATE THE SENSOR HEAD ----------------------
alpha = 0:.1:pi ;
xtemp = cos(alpha) ;
ytemp = sin(alpha) ;
circx = 2*[xtemp fliplr(xtemp)] ;
circy = 2*[ytemp -ytemp] ;
sh = [circx ; circy] ;

% ----- GENERATE AUXILIARY LINES ----------------------
sidewallinex = linelength*[-cos(20/180*pi) 0 cos(20/180*pi)] ;
sidewalliney = linelength*[sin(20/180*pi) 0 sin(20/180*pi)] ;
crownx = linelength*[-cos(70/180*pi) 0 cos(70/180*pi)] ;
crowny = linelength*[sin(70/180*pi) 0 sin(70/180*pi)] ;

stinglines = [[0 0 10] ; [2 10 18]] ;
utlines1 = [sidewallinex ;-sidewalliney] ;
utlines2 = [crownx ;-crowny] ;

mntl1r = [-rimsize/2 rimsize/2] ;
mntl1z = [-beadopening/2+.125 -beadopening/2+.125] ;
mntl2r = [0 0] ;
mntl2z = [-10 -beadopening/2+0.25] ;

% ---- PLOT SECTION ------------------------------------------
clf
colordef black
p0 = plot(xvect,-yvect,'c',xvect,yvect,'c', ...
      treadlinez,-treadliner,'g',treadlinez,treadliner,'g') ;
axis([-10 30 -24 24])
set(p0(1:2),'LineWidth',2)
lm1 = line(mntl1z,mntl1r,'LineWidth',3.5,'Color','m') ;
lm2 = line(mntl2z,mntl2r,'LineWidth',14,'Color','m') ;
hold on

shloc = [sh(1,:)+zh ; sh(2,:)+rh] ;
stinglinesloc = [stinglines(1,:)+zh ; stinglines(2,:)+rh] ;
utlines1loc = [utlines1(1,:) + zh ; utlines1(2,:) + rh ] ;
```

```
utlines2loc = [utlines2(1,:) + zh ; utlines2(2,:) + rh] ;

% ---- PLOT THE SENSOR HEAD AND STING LINES ----------
p1 = plot(shloc(1,:),shloc(2,:), ...
       'LineWidth',2,'Color','r','EraseMode','xor') ;
l1 = line(stinglinesloc(1,:),stinglinesloc(2,:), ...
       'LineWidth',7,'Color','r',...
       'EraseMode','xor') ;
pause

% ---- MOVE THE SENSOR HEAD TO rset LOCATION ----------
for i = 0:-faststep:-(rset + rh)
  set(p1,'YData',shloc(2,:)+i)
  set(l1,'YData',stinglinesloc(2,:)+i)
  drawnow
end

shloc(2,:) = shloc(2,:)-(rset+rh) ;
stinglinesloc(2,:) = stinglinesloc(2,:)-(rset+rh) ;
utlines1loc(2,:) = utlines1loc(2,:)-(rset+rh) ;
utlines2loc(2,:) = utlines2loc(2,:)-(rset+rh) ;

for j = 0:-faststep:-(zh)
  set(p1,'XData',shloc(1,:)+j)
  set(l1,'XData',stinglinesloc(1,:)+j)
  drawnow
end

set(p1,'XData',shloc(1,:)-zh)
set(l1,'XData',stinglinesloc(1,:)-zh)
drawnow

shloc(1,:) = shloc(1,:)-(zh) ;
stinglinesloc(1,:) = stinglinesloc(1,:)-(zh) ;
utlines1loc(1,:) = utlines1loc(1,:)-(zh) ;
utlines2loc(1,:) = utlines2loc(1,:)-(zh) ;

pause

% ---- MOVE THE SENSOR HEAD TO rinsp LOCATION ----------
for i = 0:-medstep:-(rinsp-rset)
  set(p1,'YData',shloc(2,:)+i)
  set(l1,'YData',stinglinesloc(2,:)+i)
  drawnow
end

shloc(2,:) = shloc(2,:)-(rinsp-rset) ;
stinglinesloc(2,:) = stinglinesloc(2,:)-(rinsp-rset) ;
utlines1loc(2,:) = utlines1loc(2,:)-(rinsp-rset) ;
utlines2loc(2,:) = utlines2loc(2,:)-(rinsp-rset) ;

% ---- TURN ON SIDEWALL UT LINES ----------
l2 = line(utlines1loc(1,:),utlines1loc(2,:), ...
       'LineStyle',':', ...
       'LineWidth',1,'Color','y',...
       'EraseMode','xor') ;

pause

% ---- MOVE THE SENSOR HEAD TO rint LOCATION ----------
for i = 0:-slowstep:-(rint-rinsp)
  set(p1,'YData',shloc(2,:)+i)
  set(l1,'YData',stinglinesloc(2,:)+i)
  set(l2,'YData',utlines1loc(2,:)+i)
  drawnow
end

shloc(2,:) = shloc(2,:)-(rint-rinsp) ;
stinglinesloc(2,:) = stinglinesloc(2,:)-(rint-rinsp) ;
utlines1loc(2,:) = utlines1loc(2,:)-(rint-rinsp) ;
```

```
utlines2loc(2,:) = utlines2loc(2,:)-(rint-rinsp) ;

pause

% ---- MOVE THE SENSOR HEAD TO rcrown LOCATION ----------
for i = 0:slowstep:(rint-rcrown)
  set(p1,'YData',shloc(2,:)+i)
  set(l1,'YData',stinglinesloc(2,:)+i)
% set(l2,'YData',utlines1loc(2,:)+i)
  drawnow
end

shloc(2,:) = shloc(2,:)+(rint-rcrown) ;
stinglinesloc(2,:) = stinglinesloc(2,:)+(rint-rcrown) ;
utlines1loc(2,:) = utlines1loc(2,:)+(rint-rcrown) ;
utlines2loc(2,:) = utlines2loc(2,:)+(rint-rcrown) ;

% ---- MOVE THE SENSOR HEAD TO zcrown LOCATION ----------
for j = 0:slowstep:zcrown
  set(p1,'XData',shloc(1,:)+j)
  set(l1,'XData',stinglinesloc(1,:)+j)
  drawnow
end

shloc(1,:) = shloc(1,:)+(zcrown) ;
stinglinesloc(1,:) = stinglinesloc(1,:)+(zcrown) ;
utlines2loc(1,:) = utlines2loc(1,:)+(zcrown) ;

% ---- TURN ON CROWN UT LINES ------------------------
l3 = line(utlines2loc(1,:),utlines2loc(2,:), ...
        'LineStyle',':', ...
        'LineWidth',1,'Color','y',...
        'EraseMode','xor') ;

pause

set(l2,'Visible','off')

% ---- MOVE THE SENSOR HEAD TO zend LOCATION ----------
for j = 0:-slowstep:zend
  set(p1,'XData',shloc(1,:)+j)
  set(l1,'XData',stinglinesloc(1,:)+j)
  set(l3,'XData',utlines2loc(1,:)+j)
  drawnow
end

shloc(1,:) = shloc(1,:)+(zend) ;
stinglinesloc(1,:) = stinglinesloc(1,:)+(zend) ;
utlines2loc(1,:) = utlines2loc(1,:)+(zend) ;

set(l2,'Visible','on')
pause

% ---- RETURN TO z0 AND RETRACT ----------------------
set(l2,'Visible','off')
set(l3,'Visible','off')

for j = 0:medstep:z1
  set(p1,'XData',shloc(1,:)+j)
  set(l1,'XData',stinglinesloc(1,:)+j)
  set(l3,'XData',utlines2loc(1,:)+j)
  drawnow
end

shloc(1,:) = shloc(1,:)+(z1) ;
stinglinesloc(1,:) = stinglinesloc(1,:)+(z1) ;

for i = 0:medstep:(rcrown-rset)
  set(p1,'YData',shloc(2,:)+i)
  set(l1,'YData',stinglinesloc(2,:)+i)
```

```
  drawnow
end

shloc(2,:) = shloc(2,:)+(rcrown-rset) ;
stinglinesloc(2,:) = stinglinesloc(2,:)+(rcrown-rset) ;

for j = 0:faststep:(zh)
  set(p1,'XData',shloc(1,:)+j)
  set(l1,'XData',stinglinesloc(1,:)+j)
  drawnow
end

shloc(1,:) = shloc(1,:)+(zh) ;
stinglinesloc(1,:) = stinglinesloc(1,:)+(zh) ;

for i = 0:faststep:(rset + rh)
  set(p1,'YData',shloc(2,:)+i)
  set(l1,'YData',stinglinesloc(2,:)+i)
  drawnow
end
```